Laser-written solid state defects in wide-bandgap semiconductors

Xingrui Cheng

Wolfson College
University of Oxford

A thesis submitted for the degree of Doctor of Philosophy

Michaelmas 2024−2025

Abstract

The development of quantum networks relies on precise control of quantum systems and scalable methods to create spin–photon interfaces. Defect centres in wide-bandgap semiconductors provide a promising way to achieve stable quantum states and efficient light coupling. However, challenges remain in fabricating individual defects of various types in different host materials and improving photon extraction under high refractive index mismatches.

Ultrafast laser writing, combined with laser annealing, has demonstrated the ability to produce highly coherent NV^- centres with near-unity yield; however, these annealing protocols have not yet been systematically applied to other defects at the single-defect level. In this thesis, I present a site-controlled fabrication methodology for SnV^- centres that leverages in-situ spectral monitoring to investigate, for the first time, the real-time dynamics of defect formation. Notably, a precursor state is identified prior to the emergence of stable SnV^- centres, providing new insights into the underlying physics of defect formation.

Two complementary approaches are presented to enhance photon collection from diverse solid-state defects across various host materials, achieved through the integration of SILs with laser writing. The first employs a top-down integration of micro-transfer-printed GaN SILs onto laser-written NV^- centres. The second adopts a bottom-up strategy, wherein monolithic hemispherical SILs fabricated via greyscale lithography are pre-defined, followed by laser writing to align defect centres precisely within these structures. Demonstrations of both schemes at the single-emitter level constitute a significant innovation for on-chip quantum photonics, paving the way for versatile integration strategies.

Finally, this thesis describes a fully optical technique for fabricating device electrodes using femtosecond laser pulses. This method is exploited to investigate Frenkel defect generation during laser writing, thus merging device manufacturing and defect engineering in a single platform.

Overall, the underlying theme of the thesis is using laser processing to develop scalable quantum devices. The focus spans three key areas: defect generation, defect generation with enhanced light extraction, and the integration of new device electrodes, all achieved through ultrafast laser. These investigations also provide valuable insights into how ultrafast laser pulses interact with the host materials. Collectively, the results represent significant progress toward scalable solid-state platforms for quantum technologies.

Laser-written solid state defects in wide-bandgap semiconductors



Xingrui Cheng

Wolfson College

University of Oxford

A thesis submitted for the degree of

Doctor of Philosophy

Michaelmas 2024–2025

Acknowledgements

This thesis would not have been possible without the support and guidance of many individuals and groups, to whom I owe my deepest gratitude.

Firstly, I want to deliver my heartfelt thanks to the Photonic Nanomaterials Group and the Dynamic Optics and Photonics Group. To all group members, past and present, thank you for fostering such a fun and inspiring working environment over the past four years. In particular, I am grateful to Laiyi Weng, Shazeaa Ishmael, Ben Griffiths, Jiahe Cui, Jiangrui Qian, Yumeng Yin, Shamil Mirkhanov, and Guangzhao Chen for their collaboration, camaraderie, and shared knowledge. I also wish to thank Amit Dhawan for warmly welcoming me at the start of this fantastic DPhil journey and for being a mentor and friend during the challenging early days of the COVID-19 pandemic. My thanks also go to Andrew Kirkpatrick for his excellent teaching on the laser writing system. Special mention goes to Matt Mai and Gareth Jones, who stood by my side throughout my entire DPhil, through both the highs and lows. Your friendship, encouragement, and unwavering support, both inside and outside the lab, have meant the world to me.

Beyond groups at Oxford, I would like to acknowledge my collaborators. To Gavin Morley, Collin Stephen, and Yashna Lekhai at the University of Warwick; Nils Freier (formerly Wessling), Martin Dawson, and Michael Strain at the University of Glasgow; Mete Atatüre, Cathryn Michaels, Rachel Oliver, and Saptarsi Ghosh at the University of Cambridge; Richard Curry, Mason Adshead, and Maddison Coke at the University of Manchester; Cristian Bonato, Christiaan Bekker, and Alexander Jones at Heriot-Watt University—thank you for your invaluable collaboration and mentorship throughout my research. Special thanks to Nils Freier for his friendship and for making our collaborative work such a rewarding experience.

I am particularly grateful to the members of the Quantum Engineering Group, now based at the University of Cambridge, past and present. Working together in the lab has been an incredible experience, and I have learned so much during our time together. In particular, I wish to thank Dorian Gangloff, Andreas Thurn, Zhe Xian (Zak) Koong, Christian Schimpf, and Adam Martinez. Andreas Thurn and Dorian Gangloff, your scientific guidance, inspiration, and rigorous attitudes have profoundly shaped my approach to research and contributed immensely to my growth as a scientist.

My deepest gratitude goes to my supervisors, Jason Smith and Patrick Salter, for their exceptional mentorship, patience, and friendship. Your thoughtful lessons, companionship, scientific guidance, and unwavering support throughout my DPhil journey have been indispensable. This thesis would not have been possible without you.

I am grateful to Hannah Stern and Mark Newton for their careful reading of this thesis and for the incisive questions posed during the viva, which have materially improved the final text.

I am also grateful to my friends for their encouragement, unwavering support, and the joyful moments we have shared. Special thanks to Dingming Zhang, Lishen Jiang, Houze Zhang, Xikang Yuan, Liwei Dai, Kairan Huang, Ye Chen and Xincheng Jiang. I wish to express my sincerest gratitude to my dearest friend, Xinqian Jiang, for her companionship, emotional and mental support, patience, and understanding.

I am deeply grateful to my family, to whom I owe everything. I dedicate this work to the memory of my grandmother, Mingchu Ding, whose love and support profoundly shaped who I am today. Completing this thesis is the fulfillment of a promise I once made to you; though you are not here to witness this moment, I know you would be proud and happy. To my sister, Ming Yang, thank you for your constant encouragement and motivation—you have always been a source of strength for me. And most importantly, to my parents, Lizhong Cheng and Fang Hu: your unwavering support, inspiration, and understanding have carried me through every step of this journey. Thank you for always believing in me.

Thank you

Where the spring breezes wander for ten gentle miles, may all your endeavors surpass your deepest desires

Chún fēng shí lǐ, wàn shì shèng yì.

Abstract

The development of quantum networks relies on precise control of quantum systems and scalable methods to create spin–photon interfaces. Defect centres in wide-bandgap semiconductors provide a promising way to achieve stable quantum states and efficient light coupling. However, challenges remain in fabricating individual defects of various types in different host materials and improving photon extraction under high refractive index mismatches.

Ultrafast laser writing, combined with laser annealing, has demonstrated the ability to produce highly coherent NV^- centres with near-unity yield; however, these annealing protocols have not yet been systematically applied to other defects at the single-defect level. In this thesis, I present a site-controlled fabrication methodology for SnV^- centres that leverages in-situ spectral monitoring to investigate, for the first time, the real-time dynamics of defect formation. Notably, a precursor state is identified prior to the emergence of stable SnV^- centres, providing new insights into the underlying physics of defect formation.

Two complementary approaches are presented to enhance photon collection from diverse solid-state defects across various host materials, achieved through the integration of SILs with laser writing. The first employs a top-down integration of micro-transfer-printed GaN SILs onto laser-written NV^- centres. The second adopts a bottom-up strategy, wherein monolithic hemispherical SILs fabricated via greyscale lithography are pre-defined, followed by laser writing to align defect centres precisely within these structures. Demonstrations of both schemes at the single-emitter level constitute a significant innovation for on-chip quantum photonics, paving the way for versatile integration strategies.

Finally, this thesis describes a fully optical technique for fabricating device electrodes using femtosecond laser pulses. This method is exploited to investigate Frenkel defect generation during laser writing, thus merging device manufacturing and defect engineering in a single platform.

Overall, the underlying theme of the thesis is using laser processing to develop scalable quantum devices. The focus spans three key areas: defect generation, defect generation with enhanced light extraction, and the integration of new device electrodes, all achieved through ultrafast laser. These investigations also provide valuable insights into how ultrafast laser pulses interact with the host materials. Collectively, the results represent significant progress toward scalable solid-state platforms for quantum technologies.

Contents

List of Figures **xi**

List of Tables **xvii**

List of Abbreviations **xix**

1 Literature review **1**

1.1 Introduction 1
1.2 Introduction to solid-state quantum networks 2
1.2.1 Quantum Key Distribution Systems 3
1.2.2 Entangled quantum networks 4
1.3 Solid-state platforms 4
1.3.1 Diamond substrate 7
1.3.2 SiC substrate 15
1.4 Colour centre fabrication techniques 17
1.4.1 Overview 17
1.4.2 Laser writing and laser annealing 18
1.4.3 Thermal annealing 20
1.5 Enhancing light extraction 23
1.5.1 Optical cavity 24
1.5.2 Solid immersion lenses 25
1.6 Summary 27

2 Theoretical background **29**

2.1 Introduction 29
2.2 Gaussian beam optics 30
2.3 Solid-state defects 34
2.3.1 Group theory and symmetry of solid-state defects 34
2.3.2 Hamiltonian formalism for energy levels 37
2.3.3 Spin-orbit interations 38
2.3.4 Zeeman splitting and magnetic field effects 39
2.3.5 Strain and Jahn-Teller effects 40
2.3.6 Franck Condon analysis 41

2.4 Ultrafast laser fabrication . . . 43
2.4.1 Light-matter interaction . . . 44
2.4.2 Mechanism of Frenkel defects generation . . . 45
2.4.3 Laser annealing . . . 47
2.5 Aberration corrections . . . 49
2.5.1 Zernike Polynomials: a framework for describing aberrations 49
2.5.2 Correcting aberrations in high-index mismatch systems . . . 51

3 Experimental methods 55
3.1 Laser writing and annealing system . . . 55
3.2 Optical characterisation . . . 59
3.2.1 Confocal imaging system . . . 59
3.2.2 In-situ spectral monitoring . . . 63
3.2.3 Hanbury Brown Twiss measurement . . . 65
3.2.4 Power saturation measurement . . . 67
3.2.5 Polarisation measurement . . . 68

4 Laser activation of Group IV defects in diamond 71
4.1 Introduction . . . 72
4.2 Negatively charged tin vacancy center SnV^- in diamond . . . 73
4.2.1 Introduction . . . 73
4.2.2 Fabrication process flow . . . 74
4.2.3 Optical characterisation . . . 77
4.3 Effect of Pulse energy and annealing time . . . 84
4.3.1 Activation of single SnV^- centre . . . 90
4.3.2 Local strain study of SnV^- centres . . . 93
4.4 Type II Sn centre in diamond . . . 96
4.4.1 Introduction . . . 96
4.4.2 Frank Condon study . . . 98
4.4.3 Spectral analysis . . . 101
4.4.4 Summary . . . 104
4.5 Distribution and yield of SnV^- and Type II Sn . . . 105
4.6 In-situ monitoring . . . 107
4.6.1 In-situ spectral monitoring . . . 108
4.6.2 SPAD trace . . . 112
4.7 Positioning accuracy . . . 113
4.8 Negatively charged silicon vacancy centre SiV- in diamond . . . 116
4.8.1 Array with Poissonian 256 ions/implantation site . . . 117
4.8.2 Array with Poissonian 64 ions/implantation site . . . 118
4.9 Discussion . . . 122

5 Laser writing of wide bandgap materials with enhanced light extraction 131
5.1 Introduction . . . 132
5.2 Transfer-printed SIL integrate with laser written NV^- . . . 133
5.2.1 Introduction . . . 133
5.2.2 Fabrication of GaN SILs . . . 134
5.2.3 Laser writing of NV^- centre . . . 136
5.2.4 SIL integration . . . 139
5.2.5 Optical compatibility . . . 140
5.3 Enhanced light extraction efficiency . . . 145
5.3.1 Simulation . . . 145
5.3.2 Experimental . . . 149
5.3.3 Background analysis . . . 153
5.3.4 Summary . . . 156
5.4 Laser writing through monolithic SILs in 4H-SiC . . . 157
5.4.1 Introduction . . . 157
5.4.2 Scalable fabrication of monolithic SILs . . . 158
5.4.3 Laser writing process . . . 161
5.4.4 Characterisation of laser written array with 532 nm excitation source . . . 163
5.4.5 Characterisation of laser written array with 780 nm excitation source . . . 173
5.4.6 Summary . . . 176
5.5 Discussion . . . 177

6 Laser written interdigitated electrode devices 181
6.1 Introduction . . . 181
6.2 Device Fabrication . . . 183
6.2.1 Design . . . 183
6.2.2 Device characterisation . . . 186
6.3 Surface electrode patterning . . . 188
6.4 Discussion . . . 195

7 Conclusion and outlook 197
7.1 Conclusion . . . 197
7.2 Outlook . . . 199

8 Appendix 201
8.1 List of publications . . . 201
8.1.1 Journal Articles . . . 201
8.1.2 Conference Presentations . . . 202

References **203**

List of Figures

1.1 Binary image processing and contour identification for electrode patterns . . . 9
1.2 Simulation of phonon-limited coherence times for group-IV vacancy centres in diamond . . . 12
1.3 Geometrical structure of the SnV^- centres . . . 13
1.4 Electronic structure and cryogenic spectrum of SnV^- centre in diamond 14

2.1 Orbital configuration of the SnV^- centres . . . 37
2.2 Electronic structure and cryogenic spectrum of SnV^- centre in diamond 44
2.3 Electronic structure and cryogenic spectrum of SnV^- centre in diamond 45
2.4 Key mechanisms in Frenkel defect formation and temporal evolution of key parameters . . . 48
2.5 Schematic of ray path change when focusing into different refractive index materials . . . 52

3.1 Schematic of the custom build laser fabrication system . . . 56
3.2 Schematic of laser writing and annealing modules . . . 58
3.3 Schematic of the WASPS setup . . . 61
3.4 Schematic of the Montana setup . . . 62
3.5 Schematic of laser writing and annealing system's confocal module . 64

4.1 Process schematic . . . 74
4.2 SRIM simulation . . . 75
4.3 Transmission microscope image . . . 77
4.4 2D PL map post ion implantation . . . 78
4.5 2D PL map post preliminary laser treatment . . . 80
4.6 PL maps for array P1−P4 post preliminary laser treatment . . . 80
4.7 2D PL map post extended laser annealing . . . 81
4.8 PL spectra from ensemble Type II Sn centres annealed at different temperatures . . . 82
4.9 Spectrum upon different treatment . . . 84
4.10 PL emissions contributions post extended laser annealing . . . 85

4.11 Spectrally integrated emission for Type II Sn−related, SnV^-−related, and GR1−related defects 85
4.12 Example spectra of other Sn−related defect centres activated in arrays with 5 ions per implantation site 86
4.13 Study of the effects of annealing laser pulse energy 87
4.14 Study of the effects of laser annealing time 88
4.15 Example data processing for study of laser annealing time and pulse energy 88
4.16 Average FWHM and Peak Height vs Pulse Energy and Diffusion Time 89
4.17 Normalised PL spectra of the samples implanted with varying dosages of Sn atoms per implantation site 91
4.18 Characterization of a typical laser-activated single SnV^- centre . . . 92
4.19 Example spectra of SnV^- centres activated in arrays with 10 ions per implantation site 94
4.20 Lorentzian fitted ZPL distribution 97
4.21 Type II Sn emission spectrum 98
4.22 Room temperature experimental and simulated spectra of Type II Sn 99
4.23 Cryogenic experimental and simulated spectra of Type II Sn 100
4.24 Spectral study of a typical single Type II Sn centre 101
4.25 Second-order autocorrelation measurement with background correction and corresponding four-level fit for the single Type II Sn emitter 102
4.26 Example spectra of Type II Sn emission activated taken from low dosage arrays 103
4.27 Distribution statistics of SnV^- and Type II Sn centres 106
4.28 Sequence of 2D PL maps monitoring the laser annealing process . . 108
4.29 In situ spectral monitoring of the temporal evolution of single SnV^- centre during laser annealing 110
4.30 Spectrum tracking of the SnV^- centre 111
4.31 SPAD trace of the temporal evolution of single SnV^- centre during laser annealing 111
4.32 PL image of a post-laser activation Sn-implanted array with dosage of 500 ions/site 114
4.33 Histogram of radial discrepancies for array with a dosage of 500 ions/site 115
4.34 Positioning accuracy study of an array with a dosage of 10 ions/site 115
4.35 2D PL images of post ion implantation and post laser activation for a Si-implanted array with a dosage of 256 ions/site 117
4.36 Example SPAD trace of the temporal evolution of a Si implanted site during laser annealing 118

4.37 2D PL images of post ion implantation for a Si-implanted array with a dosage of 64 ions/site 119
4.38 2D PL images of post laser activation with various pulse energy for a Si-implanted array with a dosage of 64 ions/site 120
4.39 Count rate increment during laser activation as a function of annealing pulse energy 120
4.40 Cryogenic PL spectra taken from sites treated with different annealing pulse energies 121
4.41 Simulation of spatiotemporal thermal dynamics in ultrapure diamond 125
4.42 DFT simulation of C_i configurations relative to the implanted SnV defect in diamond 129

5.1 Schematics describing the process flow of additive GaN solid immersion integrated with laser written NV^- centres 134
5.2 Microscope Image and profile analysis of an GaN SIL 136
5.3 Optical transmission microscope image of laser written alignment boxs and marks 138
5.4 Sets of PL maps taken before transfer printing with various collection optics 138
5.5 Alignment marks aiding SIL transfer printing 139
5.6 PL maps of regions B and D with integrated GaN SILs 141
5.7 Zoomed in PL images of GaN SILs on NV^- centres 141
5.8 PL images illustrating the effect of GaN SILs on enhanced light extraction via enhanced emitter visibility 142
5.9 Second−order autocorrelation measurement of a NV^- centre in the lower quadrant of Region D after GaN SILs placed on 143
5.10 Second−order autocorrelation measurement of a NV^- centre in the lower quadrant of Region B prior to and post GaN SILs placed on acquired with same experimental parameters 144
5.11 PL spectrum of the NV^- centre in the lower quadrant of Region B post GaN SILs placed on 144
5.12 FDTD simulation of three scenarios: (i) a flat diamond substrate without any lens, (ii) a flat diamond substrate with an added GaN micro-lens, and (iii) a monolithic hemispherical SIL fabricated around the emitter 147
5.13 FDTD simulation of the transmission data for comparing GaN SILs and planar interface 148
5.14 FDTD simulation of the influence of x and y displacement on the expected collection efficiency from the two dipole emitter 150

5.15 FDTD simulation of the influence of z displacement on the expected collection efficiency from the two dipole emitter 151
5.16 Fitted power saturation measurements of two suspected NV^- centre pairs with and without GaN SIL using an objective with NA = 0.95 152
5.17 Raw power saturation measurements data of NV^- centre pairs and NV^- ensembles with and without GaN SIL using an objective with NA = 0.95 153
5.18 Room temperature photoluminescence spectra of transferprinted GaN lenses on AlGaN/AlN mesa structures on a single crystalline CVD grown polished diamond sample 155
5.19 SEM characterisation of fabricated SIL arrays 160
5.20 Schematic illustrating the process of femtosecond laser writing through planar and SIL interfaces 162
5.21 CCD images for single seed pulse and additional diffusion pulses during the writing through a 4H−SiC monolithic SIL with corresponding SPAD trace recorded 163
5.22 2D PL images of laser written defect centres through SIL interface excited with 532 nm CW laser 164
5.23 2D PL mapping of SIL arrays under 532 nm excitation with various written pulse energy 166
5.24 2D PL map showing laser-written defect arrays through a planar interface 167
5.25 Room temperature photoluminescence spectra of transferprinted GaN lenses on AlGaN/AlN mesa structures on a single crystalline CVD grown polished diamond sample 168
5.26 Normalised PL spectra of laser written defect centres with single seed pulse and seed pulse followed by diffusion pulses 173
5.27 Characterisation of a single seed pulse laser written defect centre through SIL interface at 4 K using 780 nm CW excitation 174
5.28 Normalised cryogenic PL spectrum of a single seed pulse laser written defect centre through SIL 175
5.29 Second−order autocorrelation measurement of a V_{Si}^- centre inside SIL 175

6.1 Schematic representation of the device configuration 185
6.2 Top view of conductive layer and electrode pad configuration 186
6.3 Optical profilometry surface map and profile of junction regions in the surface of the device 188
6.4 IV curves for different pad connections of the device 189
6.5 Surface roughness comparison between pristine and redeposited regions 190
6.6 Optical microscope images of laser-patterned electrode dose test . . 191

6.7 Visualisation of actual and ideal contours with pixel-based axes in original image. 192
6.8 Binary image processing and contour identification for electrode patterns 192
6.9 RMS roughness distributions for patterned arrays 194

List of Tables

1.1 Single Photon emitter properties in SiC, reproduced from source [53] 16

2.1 First 13 Zernike polynomials and their commonly associated aberrations. 51

5.1 Comparison of material parameters and calculated threshold energies for diamond and 4H-SiC 169

6.1 Array parameters and resulting pattern characteristics 191

List of Abbreviations

1D, 2D, 3D . . One-, two- or three-dimensional, referring in this thesis to spatial dimensions in an image.

AO . . . . . Adaptive optics.

AOM . . . . . Acousto-optic modulator.

CVD . . . . . Chemical vapour deposition.

CW . . . . . Continuous wave.

DFT . . . . . Density functional theory.

DPSSL . . . . Diode-pumped solid-state laser.

FDTD . . . . . Finite difference time domain.

FIB . . . . . Focused ion beam.

FPGA . . . . . Field programmable gate array.

FSM . . . . . Fast steering mirror.

FWHM . . . . Full width half maximum.

HBT . . . . . Hanbury Brown Twiss

HPHT . . . . . High pressure, high temperature.

LDA . . . . . Local density functional.

MPI . . . . . Multiphoton ionisation.

NA . . . . . Numerical aperture.

NV^- . . . . . Negatively charged nitrogen vacancy centre.

ODMR . . . . Optically detected magnetic resonance.

PLE . . . . . Photoluminescence excitation spectroscopy.

PL . . . . . Photoluminescence.

PSB . . . . . Phonon side band.

SHG . . . . . Second harmonic generation.

SiV^- . . . . . Negatively charged silicon vacancy centre.

SLM . . . . . Spatial light modulator.

SnV$^-$ . . . . . Negatively charged tin vacancy centre.

SPAD . . . . . Single photon avalanche detector.

V$^-_{Si}$ . . . . . Negatively charged silicon vacancy centre in SiC.

ZPL . . . . . Zero phonon line.

1 Literature review

Contents

1.1 Introduction 1
1.2 Introduction to solid-state quantum networks 2
1.2.1 Quantum Key Distribution Systems 3
1.2.2 Entangled quantum networks 4
1.3 Solid-state platforms 4
1.3.1 Diamond substrate 7
1.3.2 SiC substrate 15
1.4 Colour centre fabrication techniques 17
1.4.1 Overview 17
1.4.2 Laser writing and laser annealing 18
1.4.3 Thermal annealing 20
1.5 Enhancing light extraction 23
1.5.1 Optical cavity 24
1.5.2 Solid immersion lenses 25
1.6 Summary 27

1.1 Introduction

Quantum information science [1–3], computing [4], and sensing [5, 6] are emergent fields that have garnered significant attention in recent years. Advances in materials engineering have played a pivotal role in this progress, enabling a pathway towards realisable quantum technologies. At the forefront of these developments lies the

concept of quantum networks, which aim to interconnect quantum nodes using entanglement as a resource for communication, computation, and distributed sensing.

Quantum networks hold the potential to revolutionise secure communication through quantum key distribution [7], enable distributed quantum computing, and facilitate advanced metrological techniques. Unlike classical networks, quantum networks leverage the principles of quantum mechanics, such as superposition and entanglement, to achieve tasks that are otherwise infeasible. Realising such networks demands precise control over quantum systems, scalable methods to generate and distribute entanglement, and strategies to mitigate decoherence and noise.

He we focus on the foundational components of quantum networks, particularly solid-state platforms, which have emerged as a leading candidate for realising practical implementations. By leveraging defect centres in materials such as diamond and silicon carbide, researchers have demonstrated promising results in generating and manipulating entanglement, preserving coherence over extended periods, and coupling quantum states to photonic channels. These advancements highlight the intersection of quantum science and materials engineering in driving the field forward.

The following sections explore the underlying principles, fabrication techniques, and challenges associated with quantum networks. Particular emphasis is placed on the role of solid-state defect centres, the methodologies for fabricating and enhancing these systems, and the critical advancements required to bridge the gap between laboratory demonstrations and scalable quantum technologies.

1.2 Introduction to solid-state quantum networks

Building on the foundational principles of quantum information science, quantum networks represent a pivotal step toward the practical realisation of advanced quantum technologies. These networks aim to interconnect quantum nodes through the distribution of entanglement, enabling transformative applications such as secure communication, distributed quantum computing, and enhanced metrology. Unlike classical bits, which encode information as 0 or 1, quantum information employs qubits that exploit quantum superposition to encode both 0 and 1 simultaneously.

Furthermore, entanglement between qubits facilitates the exponential scaling of memory capacity with the number of qubits. This inherent scalability and the unique properties of quantum systems underpin their superior performance in specific tasks, offering unprecedented opportunities in computation, communication, and beyond.

Qubits can be realised in various physical systems, including the optical degrees of freedom of single photons, the electronic energy states of atoms, the spin states of electrons or nuclei, and the electrodynamical states of superconducting circuits [8, 9]. Among these platforms, solid-state systems, such as nitrogen-vacancy (NV) centres in diamond, stand out due to their compatibility with current information technologies. These systems offer advantages such as minimal physical resource requirements and the potential for scalable integration and cost-effective fabrication [10].

Quantum networks can be broadly conceptualised in two paradigms: quantum key distribution (QKD) systems, which enable secure communication without entanglement [11, 12], and entangled quantum networks, which directly leverage entanglement to transmit quantum information [13, 14].

1.2.1 Quantum Key Distribution Systems

Quantum key distribution (QKD) systems, such as the Micius satellite network, rely on protocols like *BB84* [15, 16], which encode quantum information onto the states of single photons. These systems exploit the Heisenberg uncertainty principle and the no-cloning theorem to ensure security:

- Measurement of a quantum state inherently disturbs it, enabling the detection of eavesdropping.
- The no-cloning theorem prevents adversaries from replicating quantum states, preserving the integrity of transmitted keys.

By encoding quantum information onto single-photon states, QKD systems provide secure key exchange and have demonstrated practical applications on a global scale. However, scalability remains a challenge due to transmission losses and distance limitations. Unlike classical communication, where amplifiers

can compensate for signal loss, quantum signals cannot be amplified due to the no-cloning theorem. Consequently, QKD systems, particularly those relying on fibre-based channels, are limited to ranges of a few hundred kilometres without additional infrastructure.

1.2.2 Entangled quantum networks

Entangled quantum networks represent a significant advancement by enabling the transfer of quantum information through mechanisms such as quantum teleportation and supporting distributed quantum processing. These networks rely on entangled quantum states shared between nodes, allowing tasks such as quantum teleportation and distributed quantum computation. The security of entangled networks is also underpinned by the no-cloning theorem, which protects the integrity of transmitted quantum states.

A key advantage of entangled networks is their ability to overcome distance limitations using quantum repeaters and quantum memories. Quantum repeaters extend the range of entanglement by dividing the communication distance into shorter segments and connecting them through entanglement swapping. Quantum memories store quantum states temporarily, preserving coherence and compensating for transmission losses caused by decoherence and environmental noise. These components enable the creation of long-distance entanglement, essential for scalable quantum networks. However, entangled quantum networks face significant challenges. Their implementation requires advanced quantum hardware, including high-efficiency single-photon sources, quantum memories, and repeaters, as well as precise synchronisation across nodes. Despite these challenges, entangled networks hold immense potential, forming the foundation for a future quantum internet capable of secure communication, distributed computation, and quantum-enhanced sensing.

1.3 Solid-state platforms

While significant advancements have been made in various paradigms of quantum networks, this thesis focuses on the solid-state platform. Solid-state systems,

particularly those employing spin qubits, hold unique potential for advancing quantum networks and technologies. Spin qubits leverage the quantum properties of electron or nuclear spins in solid-state materials, offering several key advantages, including long coherence times, precise control, and compatibility with scalable fabrication techniques. These attributes make spin qubits especially well-suited for achieving distributed entanglement, a foundational element of robust and scalable quantum networks. Distributed entanglement enables critical tasks such as quantum teleportation and distributed quantum computation, positioning solid-state platforms as a cornerstone for the future of quantum technologies.

This thesis specifically focuses on defect-based solid-state platforms. A critical aspect of advancing solid-state quantum systems lies in the careful selection of deep defect centres and their host materials. Deep defect centres serve as the foundational qubit elements in these systems, and their properties directly influence the efficiency and fidelity of quantum operations. According to the criteria proposed by Weber et al. [2], an optimal deep defect centre should satisfy the following conditions:

(D1) *A bound state suitable for qubit functionality*: The defect must exhibit a paramagnetic state with energy splitting between spin sublevels to enable qubit manipulation.

(D2) *An optical pumping cycle for qubit state polarisation*: This cycle typically involves an optical transition from the ground state to an excited state, followed by a spin-selective decay path to achieve state polarisation.

(D3) *Spin-dependent luminescence*: The optical emission intensity or wavelength must vary based on the qubit sublevel, enabling state readout. A comparable read-out can be achieved electrically, using spin-dependent photocurrent or spin-to-charge conversion mechanisms, which dispense with the need for optical detection.

(D4) *Minimised interference from host electronic states*: The optical transitions of the defect must avoid overlap with the electronic states of the host material, ensuring a clean signal.

(D5) *Thermally stable energy levels*: The defect states should have sufficiently large energy separations to prevent thermal excitation between them at operational temperatures. This is particularly important for transitions that strongly couple to phonons, such as in the ground state of SiV^- centres. In contrast, systems like the NV^- centre, where spin transitions exhibit weak phonon coupling, are less constrained by this requirement, enabling operation at higher temperatures.

Equally important is the choice of host materials, which significantly impacts the performance of the defect centres. Host materials should adhere to the following criteria to optimise their compatibility with deep defect centres:

(i) *Wide bandgap*: The bandgap must accommodate the defect's electronic structure while preventing interference from the host's band edges, fulfilling condition (D4).

(ii) *Low spin-orbit coupling*: Small spin-orbit splitting minimises spin-flipping and enhances the defect's spin coherence.

(iii) *Nuclear spin-free lattice*: To extend electron spin coherence times, the host lattice should ideally consist of spin-zero isotopes to reduce decoherence effects from nuclear spins.

(iv) *High-quality single crystals*: Defect-free, pure crystals are critical to minimising background fluorescence and avoiding qubit degradation caused by imperfections or paramagnetic impurities.

(v) *High Debye temperature*: A high Debye temperature (θ_D) reduces spin-phonon interactions, thereby limiting undesired spin-flipping events. A large θ_D shifts the phonon cut-off to higher energies, leaving little phonon density at the qubit's microwave splitting and thus lengthening the spin-lattice relaxation time T_1. Diamond, with $\theta_D \approx 1860\,\mathrm{K}$, exemplifies this benefit, giving NV^- centres second-scale T_1 values at cryogenic temperatures. By contrast, the

orbital splittings of Group-IV split-vacancy centres remain within the residual phonon band—e.g. 48 GHz for SiV^-—so single-phonon relaxation is efficient and limits their spin coherence to ∼40 ns even at 4 K.

Host materials can be broadly classified into those with and without spin-zero isotopes. Each class serves distinct purposes in quantum technologies, and their advantages will be addressed in subsequent sections.

In addition to these criteria, host materials must also meet practical requirements for fabrication and characterisation. Transparency in the optical range ensures efficient writing and readout of defect states using optical microscopy. A low dielectric constant, indicative of low lattice polarisability, reduces electromagnetic noise, thereby preserving the qubit states. Finally, defects with spin-triplet or spin-doublet ground states are preferred, as these enable the definition of long-lived spin qubits, which are essential for quantum applications. These states also allow for efficient manipulation of spin states through optical excitation.

This systematic selection of defect centres and host materials provides a robust foundation for realising solid-state platforms in quantum technologies.

1.3.1 Diamond substrate

Diamond has emerged as a premier platform for solid-state quantum systems, owing to its exceptional material properties. Its wide bandgap of 5.5 eV supports the formation of deep electronic states [17], enabling the creation of defect centres that are both optically and electronically isolated. These defect states are stable and well-separated from the conduction and valence bands, ensuring minimal thermal excitations and robust quantum behaviour.

Advances in CVD (Chemical Vapour Deposition) techniques have enabled the production of high-purity diamond [18], significantly reducing noise from impurities. This purity is essential for preserving the coherence of quantum states, as it minimises the effects of unwanted interactions. Diamond also possesses high thermal conductivity, facilitating efficient heat dissipation and maintaining defect stability during intensive quantum operations. Its strong covalent bonds result in a stiff

lattice that suppresses phonon-induced decoherence, further enhancing the quantum coherence of embedded defect centres.

The optical properties of diamond are suitable for solid state defect platform. Its transparency across a wide spectral range allows precise optical addressing and manipulation of defect centres. Many defects in diamond exhibit sharp ZPL emission, which are critical for optical readout and photonic integration. Additionally, diamond's low environmental sensitivity and high chemical stability ensure consistent performance under a variety of operational conditions.

Notably, diamond can support quantum operations at room temperature. This unique capability arises from its intrinsic properties, such as reduced spin-lattice interactions and minimal coupling to the environment [19], which help preserve spin coherence even at ambient temperatures.

NV centre

Among the various deep defect centres, nitrogen-vacancy (NV) centres in diamond are the most extensively studied and serve as a standard in quantum systems. An NV centre forms when a single substitutional nitrogen atom replaces a carbon atom in the diamond lattice, adjacent to a vacant lattice site, aligned along one of the <111> crystallographic orientations, as illustrated in Fig. 1.1b [20].

NV centres in diamond exist in two common charge states: the neutral NV^0 and the negatively charged NV^-. The NV^0 state consists of five unpaired electrons—three from the surrounding carbon atoms and two from the nitrogen atom—while NV^- contains an additional electron trapped at the defect site, resulting in six unpaired electrons. Both charge states exhibit broad PSBs that dominate their emission spectra.

NV^- centres are distinguished by their electron spin-triplet ($^3A_2$) ground state and an optically allowed transition to a ^3E spin-triplet excited state [21]. The spin sublevels ($m_s = 0$ and $m_s = \pm 1$) exhibit distinct decay pathways:

- $m_s = \pm 1$: These sublevels exhibit a branching ratio of approximately 70% radiative decay and 30% inter-system crossing (ISC) to an intermediate singlet

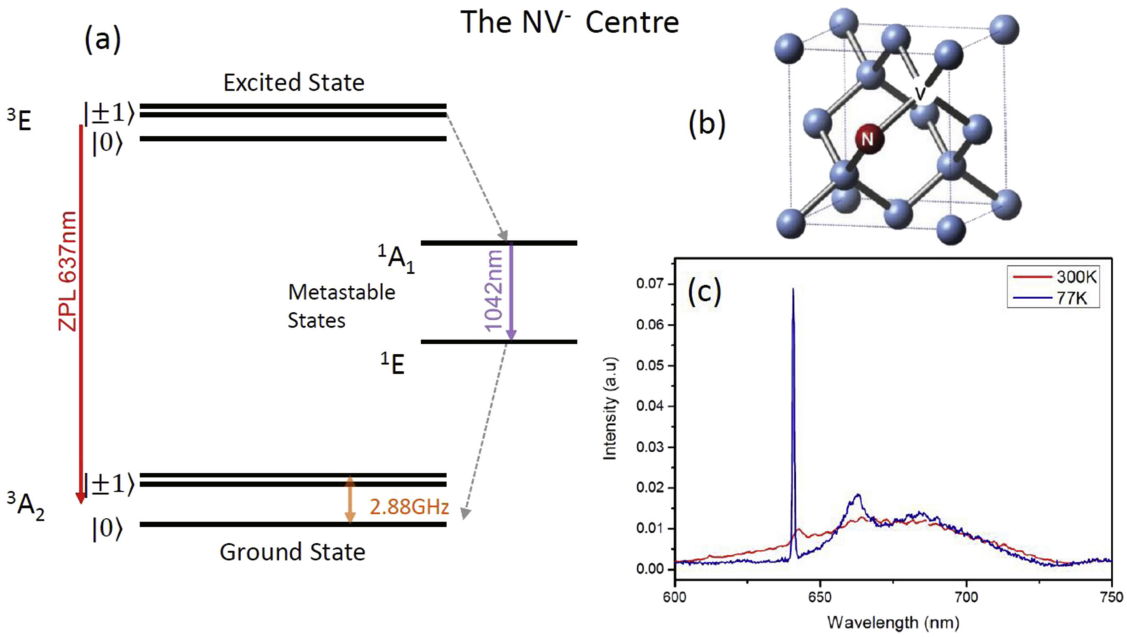


Figure 1.1: NV$^-$ centres background. This figure is reproduced from source [20] with permission. a The energy level structure of NV$^-$ centre. The magnetic dipole-dipole interaction splits the triplet sub-levels of the ground and excited states. **b** Crystal structure of NV centre aligning along the <111> crystallographic orientations. **c** PL spectrum of NV$^-$ centre at 300 K (red) and 77 K (blue). Reduction in temperature narraows the ZPL at 637 nm.

state. While the probability of ISC is significantly higher for $m_s = \pm 1$ compared to $m_s = 0$ (where ISC probability is closer to 0.1%), the majority of the decay remains radiative.

- $m_s = 0$: This sublevel predominantly decays via a radiative pathway, emitting a photon and returning directly to the ground state.

This spin-dependent decay mechanism yields two functionalities for quantum operations [22]:

1. **Spin initialisation and polarisation**: The non-radiative decay pathway facilitates efficient polarisation of the NV$^-$ centre into the $m_s = 0$ state, establishing a well-defined initial state for quantum operations.

2. **Spin-photon entanglement**: The radiative decay pathway enables photon emission that is entangled with the spin state of the NV$^-$ centre, forming the foundation for quantum communication protocols.

Spin-spin entanglement is experimentally realised using measurement-based protocols [23]. The process typically involves the following steps [24]:

1. **Photon emission**: Two NV centres (labelled NV-A and NV-B) are optically pumped into the $m_s = 0$ sublevel using a green laser. Microwave pulses are applied to create a quantum superposition state:

$$|\psi\rangle = \frac{1}{\sqrt{2}}(|0\rangle + |+1\rangle).$$

   Optical excitation drives the NV centres to their ^3E excited states, resulting in photon emission during radiative decay.

   The $^3E \rightarrow ^3A$ transitions primarily couple to linearly polarised photons. While the ^3A state in the excited configuration can couple to circularly polarised photons, this is distinct from the spin-photon entanglement mechanism. In this configuration, the emitted photons are not entangled with the spin states. Instead, the entanglement pertains to the spins of the NV centres themselves:

$$|\Psi\rangle = \frac{1}{\sqrt{2}}(|0\rangle_A|0\rangle_B + |+1\rangle_A|+1\rangle_B),$$

   where $|0\rangle$ and $|+1\rangle$ denote the spin states of NV centres A and B, respectively.

2. **Photon interference**: Photons emitted from NV-A and NV-B are directed to an interferometric setup, such as a beam splitter. Quantum interference of indistinguishable photons at the beam splitter facilitates the projection of the system onto an entangled state through measurement.

3. **Heralded entanglement**: Coincidence detection of photons at the beam splitter's output ports using single-photon detectors signals successful entanglement. This projects the NV centres into a spin-entangled Bell state:

$$|\Phi^+\rangle = \frac{1}{\sqrt{2}}(|0\rangle_A|0\rangle_B + |+1\rangle_A|+1\rangle_B).$$

The efficiency of entanglement generation (η) can be quantified as [20]:

$$\eta = \eta_{\text{ex}}\eta_{\text{em}}\eta_{\text{co}}\eta_{\text{tr}}\eta_{\text{det}}, \tag{1.1}$$

where η_{ex} is the excitation probability, η_{em} is the emission probability, η_{co} is the collection efficiency, η_{tr} is the transmission probability, and η_{det} is the detection efficiency. Maximising both collection and emission efficiencies into the ZPL is crucial for improving entanglement fidelity.

However, the Debye-Waller factors for NV^0 (1.4%) [25] and NV^- (4%) [26] reveal that most photoluminescence is emitted into the PSB rather than the ZPL, limiting the optical efficiency of NV centres for quantum information processing. To mitigate this, NV centres are often integrated into optical cavities. Optical cavities enhance photon emission into specific optical modes via the Purcell effect, increasing spontaneous emission rates and improving photon collection efficiency, indistinguishability, and the overall fidelity of spin-photon entanglement [27–30]. Other techniques, such as nanostructuring [31, 32] and SILs [33, 34], further enhance photon collection efficiencies, which will be covered in later sections. These combined techniques significantly improve the practicality of NV centres for quantum communication and computation applications.

SnV centre

As previously discussed, the NV^- centre exhibits a low ZPL contribution of only 4% to its total fluorescence due to its prominent PSB. Additionally, the NV^- centre's optical transition energy is highly sensitive to external noise, leading to spectral instability. To address these limitations, group-IV colour centres, such as silicon-vacancy (SiV^-) [35] and germanium-vacancy (GeV^-) [36], have garnered significant attention. These centres offer several advantages, including higher ZPL contributions, structural symmetries that suppress sensitivity to external noise, and quantum emission from single centres.

Unlike NV^- centres, which lack low-energy orbital levels for phonons to couple with, the electronic spin coherence of group-IV centres is limited by phonon scattering to higher ground-state orbitals. For most group-IV centres, achieving long coherence times requires extremely low temperatures (< 100 mK) using dilution refrigerators. Despite this, group-IV centres demonstrate several promising features.

For instance, studies of SiV^- and GeV^- centres [37–39] have revealed limited spin coherence times, typically in the submicrosecond range even at cryogenic temperatures (2−5 K). This is significantly shorter than the coherence times observed in NV^- centres [40]. However, these group-IV centres can support longer coherence times at millikelvin temperatures, making them suitable for specific low-temperature quantum technologies.

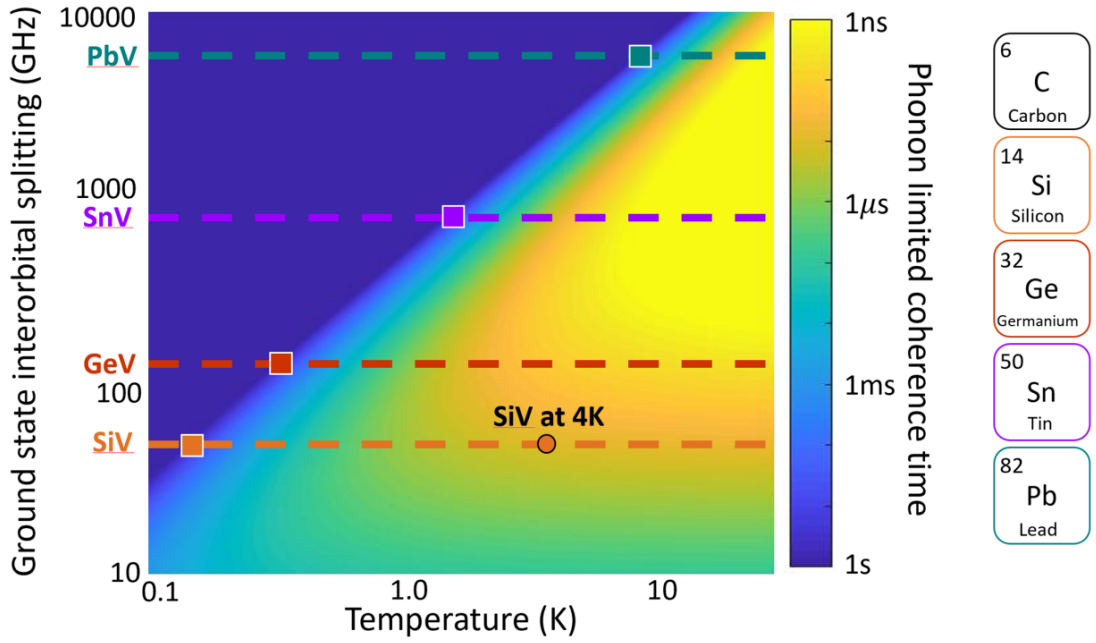


Figure 1.2: Simulation of phonon-limited coherence times for group-IV vacancy centres in diamond. This figure is reproduced from source [41]. The colour bar represents the interorbital phonon limit on coherence time, the y-axis indicates the ground-state splitting, and the x-axis maps the operating temperature. The square indicates the predicted operating temperature of different group-IV defects at which a coherence time of 1 second is achieved.

Among group-IV defects, negatively charged tin-vacancy (SnV^-) centres stand out due to their exceptionally large ground-state orbital splitting of approximately 850 GHz [42], which exceeds that of both SiV^- [35] and GeV^- [36]. This large splitting suppresses phonon scattering to upper ground-state orbitals, enabling longer coherence times at liquid helium temperatures [39, 43]. Simulations by Debroux et al. [41] (shown in Fig. 1.2) show that SnV^- centres maintain coherence times exceeding 1 microsecond at temperatures above 1 K. This improved performance is

attributed to the heavier tin atom's stronger spin-orbit coupling, which better isolates spin states and suppresses phonon scattering even at moderate temperatures [39, 44].

SnV^- centres also exhibit a remarkably high Debye-Waller factor of approximately 0.6 [45], indicating that 60% of their emission occurs in the ZPL at 620 nm. This is a significant improvement over NV^- centres (4%).

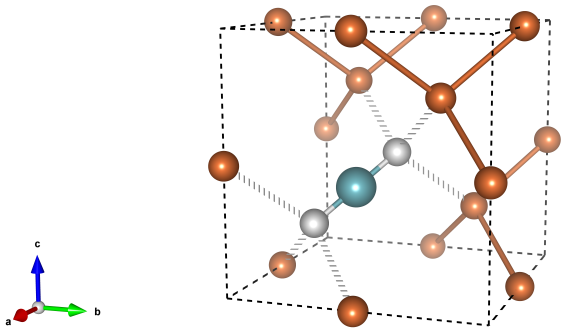


Figure 1.3: Geometrical structure of SnV^- centres. The Sn atom (blue) occupies an interstitial position between two vacant (light grey) lattice sites aligned along the ⟨111⟩ crystallographic direction. The six nearest-neighbour carbon atoms (orange), each contributing one electron to the defect centre, are depicted. Relative sizes of the impurity and carbon atoms are not drawn to scale.

The structural symmetry of group-IV defects plays a crucial role in their electronic level structures and sensitivity to environmental magnetic and electric fields. Group-IV centres consist of an impurity atom (X) and a lattice vacancy (V) in a split-vacancy configuration. For example, the SiV^- centre [46] features an impurity atom situated interstitially between two vacant carbon lattice sites along the ⟨111⟩ crystallographic direction (shown in Fig. 1.3). This configuration provides centrosymmetric symmetry around the impurity atom, eliminating a permanent electric dipole and rendering the centre insensitive to first-order electric field fluctuations. As a result, these centres produce highly stable and coherent photon emissions, predominantly into the ZPL [47].

In the case of SnV^- centres, the high spectral stability of the ZPL ensures indistinguishable photons, a critical property for quantum entanglement. The

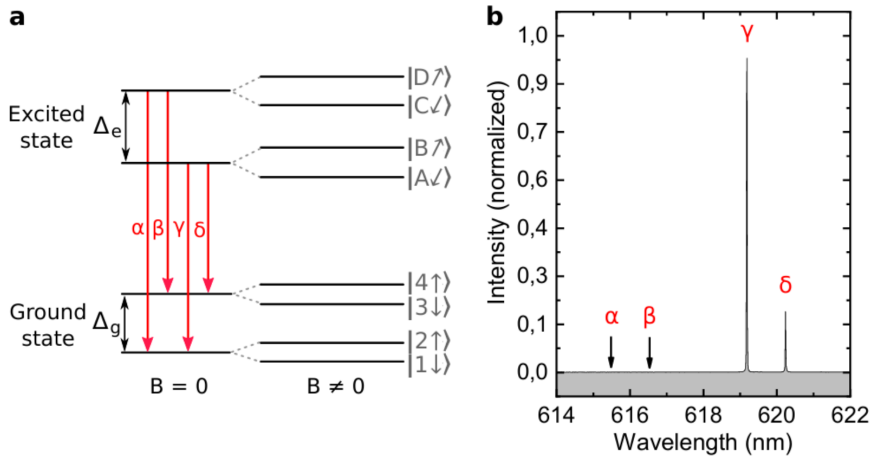


Figure 1.4: Electronic structure and cryogenic spectrum of SnV^- centre in diamond. This figure is reproduced from source [47] with permission. **a** SnV^- energy level diagram without external magnetic field is shown in the left. When a magnetic field is applied, it will split each level into two as depicted on the right. **b** PL spectrum of a single SnV^- without magnetic field.

symmetry also introduces doubly degenerate ground and excited orbital states split by spin-orbit interaction. At cryogenic temperatures (e.g., 4 K), rapid thermalisation in the excited state ensures that transitions from the lower-energy branches (γ and δ) dominate under non-resonant excitation, as shown in Fig. 1.4b.

The quantum efficiency (or the efficiency of entanglement generation as shown in Eqn 1.1) of SnV^- centres is further enhanced by their substantial ZPL emission. This high ZPL fraction facilitates efficient coupling to optical cavities and waveguides, enabling effective photon collection and routing [20]. These features, combined with their superior coherence times and emission stability, make SnV^- centres a promising platform for quantum communication and computation applications.

SiV centre

Despite having a smaller ground-state orbital splitting compared to SnV^- centres, SiV^- centres possess unique advantages that make them appealing for specific quantum applications. The D_{3d} structural symmetry of SiV^- centres provides remarkable insensitivity to external electric noise [35, 48], making them highly stable in varying environments.

SiV^- centres also exhibit a PSB compared to SnV^- centres, with a DWF of approximately 70% [49]. This high DWF is attributed to the smaller atomic size of silicon, which induces less lattice distortion and weaker coupling to phonon modes. Ab initio calculations by Thiering et al. [44] support this observation, showing a lower Huang-Rhys factor of 0.27 for SiV^- centres compared to 0.89 for SnV^- centres. This weak phonon coupling enhances the optical efficiency of SiV^- centres, making them ideal for photon-based quantum technologies.

Another significant advantage of SiV^- centres is their brightness in single-photon emission at room temperature. These centres exhibit minimal inhomogeneous broadening, with a room-temperature linewidth as narrow as 0.7 nm [50, 51]. At cryogenic temperatures, their linewidth further narrows, enabling the generation of indistinguishable photons for quantum applications that rely on photon entanglement [4].

1.3.2 SiC substrate

SiC substrates offer complementary advantages for quantum technologies, including integration potential with existing semiconductor infrastructure and stable defect centres suitable for quantum applications. SiC is a wide bandgap semiconductor composed of silicon and carbon sublayers arranged in a tetrahedral bonding configuration. The stacking sequence of these sub-lattices creates different polytypes, each with unique optical and electronic properties. Among the more than 200 known SiC polytypes [52], 3C, 4H, and 6H are the most commonly utilised due to their superior crystal quality and ease of growth [53].

SiC hosts a variety of point defects, including carbon vacancies, silicon vacancies, divacancies, and transition-metal-related complexes, some of which exhibit optically and spin-active properties that are highly relevant for quantum applications. These defects can act as single-photon emitters, essential components for quantum communication and sensing technologies. Table 1.1 summarises the diverse range of defect types in SiC, which provide emissions across visible and near-infrared

wavelengths and high photon count rates. Such characteristics make SiC-based defects well-suited for quantum systems operating at cryogenic temperature.

Notably, divacancies and silicon vacancies in 4H- and 6H-SiC have demonstrated excellent spin coherence properties [54–56], further illustrating SiC's potential as a versatile host material for qubits. The wide bandgap of SiC, combined with the availability of nuclear spin-free isotopes, helps minimise decoherence caused by interactions with the surrounding lattice. These attributes, along with the material's ability to support a range of defect configurations, make SiC a valuable platform for solid-state quantum systems.

Table 1.1: Single Photon emitter properties in SiC, reproduced from source [53]

Defect type	**Material**	**Peak wavelength (nm)**	**Spectral width (nm)**	**Lifetime (ns)**	**Count rate (c s^{-1})**	**Reference**
$C_{Si}G_V$ (bulk)	4H-SiC	670-710	>100	1.8	2 M	[57]
$C_{Si}G_V$ (nanoparticles)	3C-SiC	600-800	>100	2.1	7 M	[58]
Surface-related (PL)	3C, 4H, 6H-SiC	520-800	Variable	1-3	340-820 k	[59]
Surface-related (EL)	4H-SiC	545-850	Variable	2-5	>300 k	[60]
V_{Si}	4H, 6H-SiC	860-910	>100	5.3	10-40 k	[54, 56]
$C_{Si}V_C$	4H-SiC	648-710	50	1.2	2 M	[61]
$(V_{Si}V_C)^0$	4H-SiC	1079-1131	2	14	3-5 k	[55]

The polytype variability of SiC allows for the optimisation of defect-specific properties without requiring extensive material modifications. This intrinsic flexibility supports a broad spectrum of quantum applications, including sensing, communication, and computation. SiC's combination of scalability, material stability, and tunable defect properties ensures its continued prominence in the development of robust and scalable quantum technologies.

1.4 Colour centre fabrication techniques

1.4.1 Overview

The creation and control of colour centres in solid-state materials require precise fabrication techniques to ensure high quality and scalability. Many technologically significant colour centres are defect complexes comprising at least one impurity atom and one lattice vacancy, bound together in a thermodynamically stable configuration. The formation of these defect complexes generally involves three main steps: the introduction of impurities, the creation of lattice vacancies, and an annealing process to mitigate defect migration and the formation of stable bound states [62].

Impurities can be introduced into the substrate lattice through two primary methods: chemical vapour deposition (CVD) and ion implantation. Each method differs in mechanism and application while offering unique advantages for tailoring defect properties.

CVD is a bottom-up synthesis technique in which dopant precursors are introduced directly into the growth plasma so that impurity atoms are incorporated as each atomic layer is laid down. Provided that temperature, pressure and gas flow are carefully stabilised, the dopant concentration remains reasonably uniform across the grown layer and the crystal forms with negligible lattice damage [62]. The method yields low-defect single-crystal films and centimetre-scale wafers; however, its relatively slow growth rate still makes the manufacture of large-volume substrates both time-consuming and costly.

In contrast, ion implantation is a top-down approach in which high-energy ions are accelerated into the substrate's surface. This method displaces atoms within the local lattice, creating lattice vacancies in close proximity to the implanted impurities. Ion implantation provides excellent control over dopant concentration and spatial positioning through techniques such as masking or focused ion beams [63]. The implantation depth follows the Bragg curve of the incoming ions, which can extend to micrometre scales depending on ion energy. However, high-energy implantation can cause significant lattice damage [62, 64] and reduce lateral positional accuracy [65].

As a result, ion implantation is typically more suitable for surface modifications rather than bulk alterations.

Localised electron beam irradiation (EBI) offers a top-down route to generating lattice vacancies without introducing foreign atoms. A beam of high-energy electrons is driven through the crystal, and knock-on collisions displace host atoms to leave vacancies behind. Because electrons are several orders of magnitude lighter than typical implanted ions, they lose energy only slowly and can traverse the full thickness of standard diamond plates. At energies of a few mega-electron-volts the vacancy-production profile remains nearly uniform over depths of several hundred micrometres [66], far deeper than is attainable with ion implantation—yet the overall lattice disruption is still markedly lower than that caused by heavy ions. This combination makes EBI particularly attractive when deep, bulk-scale defect creation is required but extensive damage must be avoided.

1.4.2 Laser writing and laser annealing

Ultrafast laser processing presents an alternative and versatile method for generating defects in diamond, leveraging its ability to precisely modify bulk structures in transparent materials. This well-established technique has been widely employed for optical applications, such as creating waveguides through refractive index modifications and surface structuring [67–69]. More recently, ultrafast laser processing has been explored as a controlled approach for forming defect complexes and colour centres in diamond and other wide bandgap materials.

Laser writing has emerged as a precise tool for engineering colour centres through vacancy generation [70–73] and annealing [74, 75]. This technique enables deterministic creation of NV^- centres with live fluorescence monitoring [74] and improves SiV^- formation during thermal annealing [76]. Studies also suggest that sub-bandgap lasers can facilitate charge-state switching and local atomic mobilisation in SiC [77, 78], while femtosecond laser pulses induce atomic displacement [79], indicating broader applicability to emitters in wide bandgap materials.

The first demonstration of using femtosecond laser pulses to generate NV^- centres in diamond was reported by Liu et al. [80]. In their work, femtosecond laser pulses were focused 1–2 μm above the surface of type Ib diamond to induce surface damage. Subsequent annealing and oxidation at 680°C converted these regions into NV^- centres. This process relied on indirect laser processing, where the femtosecond laser ionised nitrogen and oxygen in the surrounding air, producing free electrons that generated vacancies within the diamond lattice [81].

In contrast, direct laser writing involves focusing the laser within the material to induce modifications via high focal intensities. This approach employs sub-bandgap laser light to interact non-linearly with valence electrons through multiphoton absorption [82, 83]. The interaction excites a high density of carriers into the conduction band, producing a dense plasma of hot carriers that quickly cool to form excitons and, at higher carrier densities, biexcitons. When these biexcitons (or their self-trapped counterparts) relax non-radiatively, their excess energy is transferred to the lattice and can displace host atoms, creating paired vacancies and self-interstitials, known as Frenkel defects, throughout the focal volume. Pimenov et al. [84] demonstrated the creation of NV^- ensembles in type IIa CVD diamond using picosecond laser pulses. Their work also marked the first use of lasers for annealing, where laser heating facilitated the migration of vacancies to form NV^- ensembles. However, this method introduced significant residual damage, unwanted charge states, and other defect centres.

Further optimisation was achieved by Kurita et al. [85], who reduced pulse duration and exploited the high non-linearity of ultrafast lasers to improve the ratio of NV ensembles to graphitic formations. This method enabled the generation of high-density NV ensembles with reduced graphitisation. However, it was largely confined to surface regions, limiting its applicability for bulk defect creation.

A breakthrough in the direct laser writing of high-quality NV^- centres within bulk type IIb diamond was demonstrated by Chen et al. [70]. Using a spatial light modulator for aberration correction, femtosecond laser pulses delivered high pulse energy uniformly across depths, enabling the fabrication of defect centres in three

dimensions. Carbon vacancies were generated at depths of 30 μm, confirmed by the GR1 PL signal. Subsequent thermal annealing produced single NV^- centres with Poissonian statistics, achieving spin coherence times comparable to native defect centres ($\sim$ 800 μs).

Building on this, Chen et al. [74] combined direct laser writing with laser annealing to mitigate Poissonian yield limitations. In this method, a femtosecond seed pulse created carbon vacancies in a nitrogen-enriched diamond (1.8 ppm), followed by diffusion laser pulses with lower energy to facilitate vacancy migration. The high non-linearity confined both the seed and diffusion zones, enabling precise defect formation. Using a fluorescence feedback loop, the yield of single NV^- centres reached 96%. Additionally, Gadalla et al. [78] demonstrated that below-bandgap laser annealing enables charge state conversion in SiC, further highlighting the versatility of laser-based annealing approaches.

This direct laser writing technique has since been extended to other wide bandgap materials, producing single and ensemble defects such as V_{Si} centres in silicon carbide [86], boron vacancies in hexagonal boron nitride [87], and RL centres in gallium nitride [88, 89]. These advances demonstrate the potential of ultrafast lasers as a route to creating vacancies or optically coherent single defects in wide bandgap materials, motivating further exploration of laser processing for quantum and photonic applications.

1.4.3 Thermal annealing

An annealing process is commonly applied after the introduction of impurities into the substrate lattice to achieve the following objectives:

(i) **Control diffusion**: Annealing promotes the formation of stable defect complexes by facilitating interactions between impurities and local vacancies. This process stabilises the system and reduces the likelihood of random defect diffusion.

(ii) **Lattice repair**: The process helps repair residual damage introduced during impurity implantation or vacancy creation. By enabling the material to reorganise into a more crystalline structure, annealing reduces defect density and improves overall crystal quality. This involves the diffusion and recombination of vacancies and interstitial atoms, as well as the dispersal of residual lattice damage through thermal diffusion. A low level of residual damage is critical for achieving high optical and spin coherence from defect centres.

(iii) **Electrical and optical activation**: Annealing enhances structural quality and facilitates the formation of defect centres in states that improve electrical and optical properties. This process often complements other methods, such as charge state manipulation.

Annealing, or heat treatment, involves heating a sample to a temperature specific to the material and the type and depth of defects being treated. This process facilitates the diffusion of vacancies and interstitial atoms, enabling the lattice to reorganise and stabilise defect complexes. The energy required for defect diffusion varies depending on the substrate material and defect type, and it can be modelled using thermodynamic and kinetic principles.

Taking diamond as an example, the thermal diffusion of point defects is governed by the Arrhenius relationship, which describes the temperature dependence of the diffusion coefficient, D:

$$D = D_0 e^{-\frac{E_a}{k_B T}} \tag{1.2}$$

where D_0 is the pre-exponential factor dependent on defect type and lattice properties [90], E_a is the activation energy for diffusion, k_B is the Boltzmann constant, and T is the absolute temperature.

In diamond, neutral vacancies exhibit an activation energy of $2.3 \pm 0.3\,\text{eV}$ [91], with a diffusion coefficient normalisation of $31 \times 10^{-6}\,\text{cm}^2/\text{s}$, allowing for diffusion at temperatures above 600°C [92]. Substitutional nitrogen (N_s), commonly involved in nitrogen-vacancy (NV) centre formation, has a much higher activation energy

of $5.0 \pm 0.3\,\text{eV}$, making nitrogen diffusion negligible under typical annealing conditions [92, 93]. Self-interstitial carbon atoms, in contrast, have a lower activation energy of 1.7 eV [90], allowing them to diffuse even at room temperature with a diffusion coefficient of $1 \times 10^{-6}\,\text{cm}^2/\text{s}$. These interstitials and their aggregates can be fully annealed out at temperatures between 400 and 600°C [94] via recombining with vacancies nearby.

The spatial distribution of defects during annealing can be modelled under the assumption of isotropic diffusion using:

$$N(r,t) = N_0 r \exp\left(-\frac{r^2}{4Dt}\right) \tag{1.3}$$

where $N(r,t)$ is the defect concentration at distance r and time t, N_0 is a normalisation constant, and D is the diffusion coefficient. The diffusion distance during annealing can be approximated as:

$$\Delta r \approx \sqrt{D \cdot t} \tag{1.4}$$

where t is the annealing duration.

For example, in electronic-grade diamond, annealing is typically performed at 1000°C for 3 hours under nitrogen flow [34, 70, 95]. Using Eqn 1.4, the diffusion distance is estimated to be on the micron scale. Given an intrinsic doping level of 1 ppb, the average separation distance between intrinsic nitrogen atoms is approximately $d = \sqrt[3]{\left(\frac{10^9}{8}\right) \times (3.57\ \text{Å})^3} \approx 178\,\text{nm}$. This implies that vacancies created during annealing are likely to encounter intrinsic nitrogen atoms and form NV^- centres.

However, annealing at temperatures above 1200 °C can lead to dissociation of the NV^- centre complex [96]. Thus, annealing can also be used to destroy colour centres and heal the lattice to a pure state. This is important as annealing can also be used to break apart other agglomerations of defects in the lattice, such as dislocations, which would lead to decoherence of spin qubits.

1.5 Enhancing light extraction

To enhance entanglement generation efficiency according to Eqn 1.1, the most effective and practical approach is to increase η_{em} the emission efficiency and η_{co} the collection efficiency. Solid-state platforms, particularly those utilising defect centres in wide-bandgap materials such as diamond and silicon carbide, have shown significant promise as components for quantum networks. However, these platforms face inherent challenges in photon collection due to the high refractive indices mismatch with collection optics and associated scattering losses of these materials. In the case of diamond, the mismatch between its high refractive index and that of the surrounding medium results in substantial internal reflection. This leads to a significant portion of emitted photons being trapped within the crystal, reducing the effective signal from emitters.

To address this limitation, several techniques have been developed to enhance the efficiency of photon collection from atomic defects within diamond or other platforms. These include:

(i) **Cavity coupling**: Integrating defect centres with optical cavities enhances the spontaneous emission rate (increasing η_{em} the emission efficiency) into specific optical modes via the Purcell effect, improving photon collection and directionality [27–30].

(ii) **Nanostructuring**: Fabricating nanoscale structures such as nanopillars, gratings, and photonic crystal cavities around defect centres increases photon extraction efficiency by directing emitted photons into desired modes. These methods have demonstrated significant improvements in brightness and emission rates [31, 32, 97–100].

(iii) **Solid immersion lenses (SILs)**: SILs focus and collect photons more effectively by reducing the divergence angle of emitted light, thereby overcoming the refractive index mismatch. This technique is particularly effective for

enhancing photon collection from individual defect centres [33, 101] (increasing η_{co}, the collection efficiency.).

These approaches collectively address the photon collection inefficiencies inherent to wide-bandgap materials, enabling improved signal extraction and enhancing the viability of solid-state platforms for scalable quantum networking applications.

1.5.1 Optical cavity

Optical cavities enable resonant coupling between defect centre emission and cavity modes, significantly enhancing the spontaneous emission rate into the ZPL while suppressing the PSB. This coupling improves both the emission efficiency and the indistinguishability of emitted photons, which are critical for quantum applications. Cavity designs, such as distributed Bragg reflector (DBR) cavities are often optimised to match the emission wavelengths of specific defect centres [28].

The optical microcavity supports only specific photon frequencies that resonate within its structure, determined by its dimensions and material properties. The allowed frequencies are given by:

$$\omega_m = \frac{m\pi c}{nL}, \tag{1.5}$$

where ω_m is the resonant frequency, m is the number of antinodes, c is the speed of light, n is the refractive index of the cavity, and L is the cavity length [102].

The enhancement of ZPL emission in a microcavity is quantified by the Purcell factor $F_\mu(\lambda)$, which represents the wavelength-dependent emission enhancement for a dipole μ coupled to a cavity mode centred at wavelength λ_{cav}:

$$F_\mu(\lambda) = \xi_\mu F_{\max} \cdot \frac{1}{1 + 4Q^2 \left(\frac{\lambda}{\lambda_{\text{cav}}} - 1\right)^2}. \tag{1.6}$$

Here, the maximum rate enhancement $F_{\max}$ is given by:

$$F_{\max} = \frac{3}{4\pi^2} \left(\frac{\lambda_{\text{cav}}}{n}\right)^3 \frac{Q}{V_{\text{mode}}},$$

where Q is the cavity quality factor, and V_{mode} is the mode volume. The spatial overlap and orientation factor ξ_μ measures the alignment between the dipole μ and the cavity's electric field $\mathbf{E}$:

$$\xi_\mu = \left(\frac{|\mu \cdot \mathbf{E}|}{|\mu||\mathbf{E}_{\text{max}}|} \right)^2,$$

where $\mathbf{E}_{\text{max}}$ is the maximum electric field. If the emitter is positioned at the electric field maximum, $\mathbf{E} = \mathbf{E}_{\text{max}}$, the overlap factor simplifies to $\xi_\mu = \cos^2(\theta)$, where θ is the angle between the dipole and the cavity plane [28, 103].

Experimental demonstrations have shown the effectiveness of cavity coupling for single solid-state defect centres. For instance, coupling a single NV^- centre in a diamond membrane to a cavity achieved an increment of the Debye-Waller factor from 3% to 44.7% [104]. Similarly, coupling single SiV^- centres in nanodiamonds to microcavities demonstrated a lower-bound Purcell factor of 1.61 [105].

Despite these successes, cavity coupling is often constrained to thin membranes due to the trade-off between mode volume and the Purcell factor. Longer optical paths required for cavity resonance increase potential loss channels and scattering, further limiting efficiency. Consequently, thin membranes are preferred to optimise cavity performance, offering enhanced emission and coupling capabilities while mitigating loss. However, the fabrication and handling of such membranes still remains challenging.

1.5.2 Solid immersion lenses

Solid immersion lenses (SILs) provide an effective method for improving light collection efficiency from solid-state defect centres. By increasing the NA of the optical system, SILs reduce refraction losses caused by total internal reflection, a significant issue in high-refractive-index materials such as diamond. Unlike cavity coupling, SILs rely solely on optical enhancement, improving the collection efficiency term (η_{co}) without requiring cavity-based resonant interactions. This makes SILs particularly compatible with bulk substrates. SILs are typically fabricated directly on the host material using precision techniques like laser ablation or focused ion

beam (FIB) machining, allowing for a wide range of geometries and scales. Common SIL geometries include hemispherical SILs and Weierstrass SILs [106], although the latter is less suitable for spectrally broad emitters due to chromatic aberrations.

Fabrication methods depend on the desired scale of the SIL. Millimetre-scale SILs are produced through laser ablation and mechanical processing [107], while micrometre-scale SILs, the focus of this thesis, are created using FIB techniques [108, 109]. Additive methods, such as positioning hemispherical caps on diamond or other materials like gallium phosphide, have also been demonstrated [107, 110]. A standard FIB milling process takes approximately one hour per lens [109], presenting challenges for scalability. Nevertheless, significant collection enhancements, up to 10×, have been reported. While no detrimental effects on the coherence properties of solid-state defect centres have been observed [111], concerns remain about potential strain induced by ion bombardment around the defect of interest [112, 113]. Recent advancements in NV-based quantum computing and quantum networking highlight the practical significance of SILs, with reports of faster measurement times and reduced error rates due to enhanced signal-to-noise ratios [114, 115].

The hemispherical SIL is a prominent example of how light collection efficiency can be enhanced by increasing the effective NA of the optical system [116]. In a conventional setup, the NA is defined as:

$$\mathrm{NA} = n \sin(\theta), \tag{1.7}$$

where n is the refractive index of the medium between the emitter and the lens (typically air, with $n \approx 1$), and θ is the maximum half-angle of the light cone collected by the lens. The resolution (R) of the optical system is inversely proportional to the NA:

$$R \propto \frac{\lambda}{\mathrm{NA}}, \tag{1.8}$$

where λ is the wavelength of the emitted light. Introducing a hemispherical SIL with a refractive index n_{SIL} increases the effective NA:

$$\mathrm{NA}_{\mathrm{eff}} = n_{\mathrm{SIL}} \sin(\theta), \tag{1.9}$$

which directly improves the resolution:

$$R_{\mathrm{SIL}} = \frac{\lambda}{n_{\mathrm{SIL}} \sin(\theta)}. \tag{1.10}$$

For example, a diamond SIL with $n_{\mathrm{SIL}} \approx 2.4$ achieves a resolution enhancement factor of 2.4 compared to conventional air-based systems.

To further optimise performance, anti-reflective coatings are often applied to SILs to minimise Fresnel reflection losses, enhancing photon transmission into the collection optics [117]. Although materials with higher refractive indices provide greater enhancements, they also introduce challenges, such as increased Fresnel reflections and optical aberrations, necessitating careful optimisation of SIL design and integration.

1.6 Summary

Solid-state defects have emerged as strong candidates for enabling quantum technologies, offering stable and coherent spin properties suitable for applications in sensing, communication, and computation. Among solid-state platforms, diamond and silicon carbide (SiC) stand out due to their unique material properties and ability to host various defect centres. This chapter discusses the quantum potential of these platforms, focusing on nitrogen-vacancy (NV^-), silicon-vacancy (SiV^-), and tin-vacancy (SnV^-) centres in diamond, alongside silicon-vacancy (V_{Si}) centres in SiC, which demonstrate exceptional promise for quantum applications.

A variety of engineering techniques for generating solid-state defects is summarised, highlighting the advantages and limitations of each approach. Ion implantation, followed by annealing, has been extensively used to produce highly coherent colour centres with precise positional control. However, this method suffers from low yield, shallow implantation depths, and residual damage along the implantation track, making it less suitable for large-scale device fabrication.

Electron irradiation offers an alternative, producing defect centres with rivalled quality to native defects. Despite this, it provides little to no positional control, limiting its applicability in highly structured quantum devices.

Laser writing, combined with laser annealing, has shown promise for generating defects with in-situ feedback and three-dimensional spatial control enabled by adaptive optics. This method is particularly effective for NV^- centres and offers scalability advantages. However, its applicability to group-IV defects, which require extrinsic doping typically achieved through ion implantation, remains undemonstrated. The focus on NV^- centres in existing work also limits the technique's versatility for fabricating a broader range of defect types.

Several techniques for enhancing light extraction from solid-state defects are also reviewed. Cavity coupling and SILs are explored for their ability to improve photon collection efficiency and emission quality. Cavity coupling enhances emission into the ZPL and photon indistinguishability through resonant interaction but often requires thin membranes, posing fabrication challenges. SILs, on the other hand, increase NA and light collection efficiency without requiring resonant coupling, offering better compatibility with bulk substrates. While both methods have their respective strengths, their limitations in scalability and fabrication complexity necessitate careful optimisation for specific quantum applications.

In summary, the combined advancements in defect engineering and optical enhancement techniques underscore the growing potential of solid-state defects as scalable platforms for quantum technologies. However, further research is needed to overcome existing challenges in fabrication yield, positional accuracy, and defect versatility to fully realise the promise of these systems.

2

Theoretical background

Contents

2.1 Introduction 29
2.2 Gaussian beam optics 30
2.3 Solid-state defects 34
2.3.1 Group theory and symmetry of solid-state defects . . . 34
2.3.2 Hamiltonian formalism for energy levels 37
2.3.3 Spin-orbit interations 38
2.3.4 Zeeman splitting and magnetic field effects 39
2.3.5 Strain and Jahn-Teller effects 40
2.3.6 Franck Condon analysis 41
2.4 Ultrafast laser fabrication 43
2.4.1 Light-matter interaction 44
2.4.2 Mechanism of Frenkel defects generation 45
2.4.3 Laser annealing 47
2.5 Aberration corrections 49
2.5.1 Zernike Polynomials: a framework for describing aberrations 49
2.5.2 Correcting aberrations in high-index mismatch systems 51

2.1 Introduction

This chapter outlines the theoretical framework that underpins the research presented in this thesis. It begins with an introduction to Gaussian beam optics, providing the foundation for understanding the laser systems used in this work.

The discussion then transitions to the photophysics of solid-state defect systems, highlighting their unique properties and relevance to quantum technologies. Following this, the processes of laser writing and laser annealing are examined in detail, showing their roles in the fabrication and optimisation of defect centres. Finally, the chapter concludes with an overview of aberration correction techniques employed during the laser fabrication process.

2.2 Gaussian beam optics

Gaussian beam optics provides a mathematical framework for understanding the propagation and focusing of laser beams, making it indispensable for applications in confocal imaging, spectroscopy, and the precise laser writing of defects in solid-state substrate. The detection or creation of atomic-scale defects demands an optical focus that is not only tight but also well-characterised to achieve high spatial resolution and optimise light–matter interactions.

While traditional ray optics can offer a first-order approximation for simple lens systems, it falls short when dealing with diffraction-limited beams and the finer details of the electric field distribution at the focal point. In confocal imaging and spectroscopy, the scale at which we aim to resolve and manipulate individual defects is well below the regime where rays provide an accurate description. Consequently, Gaussian beam optics is employed to fully capture the beam's intensity profile, phase-front curvature, and the influence of the wavelength on the achievable focus. Such precision is especially vital in single photon sources from single solid-state defect imaging, where the fluorescent signals emanate from a spatially localised region, and in laser writing, where the precise positioning and density of created defects depend critically on the beam's characteristics.

Drawing on the principles of Gaussian beam optics, one can design optical systems that maximise NA and ensure efficient light collection and coupling. By selecting the appropriate beam waist and focusing geometry, it is possible to attain an optimal balance between resolution and throughput. This careful tuning directly impacts the performance of confocal imaging and spectroscopic systems,

leading to sharper images, improved signal-to-noise ratios, and more reliable defect creation and characterisation.

Maxwell's equations govern the dynamics of electric and magnetic fields, encapsulating the fundamental laws of electromagnetism. They are expressed as:

$$\nabla \cdot \mathbf{E} = \frac{\rho}{\epsilon_0}, \quad \nabla \cdot \mathbf{B} = 0 \tag{2.1}$$

$$\nabla \times \mathbf{E} = -\frac{\partial \mathbf{B}}{\partial t}, \quad \nabla \times \mathbf{B} = \mu_0 \mathbf{J} + \mu_0 \epsilon_0 \frac{\partial \mathbf{E}}{\partial t} \tag{2.2}$$

Here:

- $\mathbf{E}$ and $\mathbf{B}$ are the electric and magnetic fields, respectively,
- ρ is the charge density,
- $\mathbf{J}$ is the current density,
- ϵ_0 is the permittivity of free space,
- μ_0 is the permeability of free space.

In free space, where $\rho = 0$ and $\mathbf{J} = 0$, these equations simplify, and combining them yields the wave equation for the electric field:

$$\nabla^2 \mathbf{E} = \frac{1}{v^2} \frac{\partial^2 \mathbf{E}}{\partial t^2} \tag{2.3}$$

where $v = 1/\sqrt{\mu_0 \epsilon_0}$ is the speed of light in vacuum.

For monochromatic waves, the solution can be written as:

$$E(\mathbf{r}, t) = E(\mathbf{r}) e^{i\omega t}. \tag{2.4}$$

This expression is valid because monochromatic waves have a single frequency, ω, and their time dependence can be factored out as $e^{i\omega t}$, leaving a spatial component $E(\mathbf{r})$ to satisfy the wave equation. Substituting this solution into the wave equation yields the Helmholtz equation:

$$\left[\nabla^2 + k^2\right] E(\mathbf{r}) = 0 \tag{2.5}$$

where $k = \omega/v$ is the wave number.

For a beam propagating predominantly along the z-direction, the electric field can be expressed as:

$$E(\mathbf{r}) = a(x, y, z)e^{ikz} \tag{2.6}$$

Here, $a(x, y, z)$ represents the slowly varying envelope of the beam's amplitude in the transverse (x, y) directions, and e^{ikz} captures the rapid phase oscillations along z. This form is appropriate because in optical systems such as confocal imaging, the z-axis is typically aligned with the optical axis, which defines the primary direction of beam propagation. This alignment ensures that the beam's wavefronts are mostly perpendicular to the optical axis.

Using the paraxial approximation, where $\partial^2 a/\partial z^2 \ll 2k\,\partial a/\partial z$, the Helmholtz equation reduces to the paraxial wave equation:

$$\nabla_\perp^2 a + 2ik\frac{\partial a}{\partial z} = 0, \qquad \text{with } \nabla_\perp^2 \equiv \frac{\partial^2}{\partial x^2} + \frac{\partial^2}{\partial y^2}. \tag{2.7}$$

One solution to the paraxial wave equation is the Gaussian beam:

$$E(r, z) = E_0\frac{\omega_0}{\omega(z)}e^{i(kz-\omega t)}e^{-i\alpha(z)}e^{-\frac{r^2}{\omega(z)^2}}e^{i\frac{kr^2}{2R(z)}} \tag{2.8}$$

where:

- E_0: Amplitude at $z = 0$,
- ω_0: Beam waist at $z = 0$,
- $\omega(z)$: Beam radius at distance z, defined as:

$$\omega(z) = \omega_0\sqrt{1 + \left(\frac{z}{z_r}\right)^2} \tag{2.9}$$

- $z_r = \pi\omega_0^2/\lambda$: Rayleigh range,
- $\alpha(z) = \arctan(z/z_r)$: Gouy phase shift,
- $R(z) = z\left[1 + (z_r/z)^2\right]$: Radius of curvature of the wavefront.

Here, $z = 0$ represents the position of the beam waist, which in confocal systems corresponds to the focal plane where the beam achieves its minimum spot size. The focal plane is crucial for achieving high resolution in imaging and optimal coupling in spectroscopy.

Gaussian optics plays a vital role in confocal imaging and spectroscopy through the following aspects:

1. **Matching the Numerical Aperture (NA):** In confocal imaging and spectroscopy, matching the beam's numerical aperture to the focal number of the spectrometer or imaging system ensures efficient light collection and minimises aberrations. The NA can be related to the beam waist ω_0 via:

$$\mathrm{NA} = n \sin\theta \approx n\frac{\lambda}{\pi\omega_0} \tag{2.10}$$

   where n is the refractive index of the medium and θ is the divergence angle. This expression assumes that the divergence angle θ of the Gaussian beam is small. For small angles, the approximation $\sin\theta \approx \tan\theta$ is valid, allowing the numerical aperture to be directly related to the wavelength and the beam waist. Under the paraxial approximation, where the beam propagates predominantly along the optical axis and angular deviations from the axis are small, this relationship highlights the importance of the beam waist in determining the focusing and resolution capabilities of optical systems.

2. **Resolution of Confocal Imaging and Spectroscopy:** The resolution of a confocal imaging system depends on the beam waist ω_0, as smaller waists provide tighter focusing, leading to higher spatial resolution. In spectroscopy, the resolution improves by optimising the beam waist and spot size to match the spectrometer's entrance slit or pinhole. Under the Rayleigh criterion, an objective of numerical aperture of 0.95 excited at 532 nm typically delivers a lateral resolution of about 0.34 μm (with an axial resolution close to 1 μm in air).

3. **Efficient Light–Matter Interaction:** Gaussian beams provide a predictable intensity profile, which is essential for precise spatial resolution in confocal microscopy and controlled excitation in spectroscopy. The focusability of Gaussian beams ensures strong light–matter interactions at the focal point, enhancing signal strength and data quality.

In conclusion, Gaussian beam optics offers a comprehensive understanding that goes beyond the approximations of ray optics, providing the means to control and optimise beam parameters for advanced imaging, spectroscopy, and laser-based fabrication techniques required in solid-state defect research, including the creation and study of NV centres.

2.3 Solid-state defects

The properties of solid-state defects arise from their electronic structure, governed by the symmetry of the defect and its interaction with external fields. While the NV^- centre has been extensively studied, this thesis focuses on the group-IV vacancy centres, particularly the SnV^- centre, due to its high D_{3d} symmetry and strong spin-orbit coupling. This section develops a theoretical framework for understanding the photophysical properties of such centres, using SnV^- as a representative example.

2.3.1 Group theory and symmetry of solid-state defects

The electronic structure of solid-state defects is fundamentally determined by their symmetry, which can be systematically described using group theory. Group theory provides a framework to characterise symmetry operations, such as rotations, reflections, and inversions, that leave the defect configuration invariant. These operations collectively form a point group that defines the defect's symmetry.

For group-IV vacancy centres, the symmetry elements include:

- A principal threefold rotational axis (C_3) through the impurity and vacancy sites.
- Three perpendicular C_2 axes providing 180° rotation symmetry.

- A centre of inversion (i), relating every point to its opposite counterpart.
- Horizontal and vertical mirror planes (σ_h and σ_d) reflecting symmetries around the C_3 axis.
- Improper rotation axes (S_6), combining rotations with reflections to further constrain the defect's symmetry.

These symmetry elements collectively define the D_{3d} point group. Group theory further allows the classification of electronic states through representations of the point group. Representations that can be reduced into sums of lower-dimensional components are called reducible, while those that cannot are irreducible representations (irreps). Irreps label quantum mechanical functions, such as orbitals and wavefunctions, transforming under the D_{3d} point group.

Irreps for D_{3d} are conventionally labelled using specific notations:

- **Irreps A and E:** A denotes non-degenerate (single-level) states, often associated with ground-state configurations, while E represents doubly degenerate (two-level) states, commonly describing excited states. Degeneracy arises because an E irrep accommodates two orthogonal basis functions transforming identically under symmetry operations, leading to energetically equivalent states.
- **Subscripts g and u:** The subscripts g (gerade) and u (ungerade) describe the behaviour of wavefunctions under inversion. A g state remains invariant ($\psi(\mathbf{r}) = \psi(-\mathbf{r})$), while a u state changes sign ($\psi(\mathbf{r}) = -\psi(-\mathbf{r})$).
- **Subscripts 1 and 2:** For one-dimensional irreps (A_1 and A_2), the subscripts distinguish symmetry responses. A_1 is totally symmetric under all operations, while A_2 changes sign under at least one operation.

The electronic states of group-IV centres can be classified using these irreps:

- a_{1g} (A_{1g}): Non-degenerate, fully symmetric, and even under inversion. Typically resides deep within the valence band and is fully occupied.

- a_{2u} (A_{2u}): Non-degenerate, odd under inversion, and interacts with valence band states.
- e_g (E_g): Doubly degenerate, even under inversion, and located near the valence band edge. Its position varies across group-IV impurities.
- e_u (E_u): Doubly degenerate, odd under inversion, and partially filled in the ground state within the bandgap.

These states form the foundation of the defect's electronic structure. Symmetry-adapted linear combinations (SALCs) of atomic orbitals [118] assign each electronic level to an irrep, elucidating how symmetry governs energy alignments and occupancies.

Group-IV centres have 11 electrons distributed among four orbital states: six from carbon dangling bonds, the four valence electrons of the Group-IV atom itself, and one additional electron supplied by the lattice to achieve a negatively charged charge state. These electrons occupy four symmetry-adapted orbitals, a_{1g}, a_{2u}, e_u and e_g, giving the ground-state configuration

$$a_{1g}^2\, a_{2u}^2\, e_u^4\, e_g^3.$$

Thus the two a singlets and the bonding e_u doublet are completely filled, while the antibonding e_g doublet is only partly occupied. With three electrons shared between two degenerate orbitals the centre has a spin-$\frac{1}{2}$ ground term, (^2E_g), which is four-fold degenerate (orbital $\times$ spin). Optical excitation lifts one electron from e_u to e_g, producing the excited configuration (^2E_u) shown in Fig. 2.1. Any perturbation that lowers the ideal D_{3d} symmetry—static strain, spin–orbit coupling or the Jahn–Teller effect—lifts this orbital degeneracy and splits both the ground and excited manifolds, giving rise to the fine structure seen in optical and spin-resonance spectra.

The positioning of these levels varies across group-IV centres. For example, e_g levels lie slightly below the valence band edge for SiV and GeV, align with it for SnV, and are slightly above it for PbV. Excitation shifts the e_u level into the bandgap, enabling optical transitions vital for quantum applications.

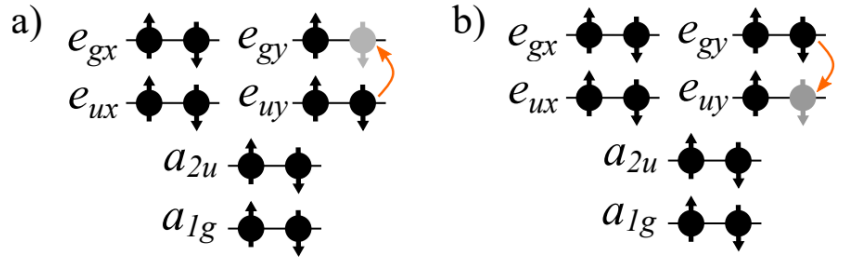


Figure 2.1: Orbital configuration of the SnV^- centres. Reproduced from [119]. **a** Ground state of SnV^- orbital configuration. **b** Excited state of SnV^- orbital configuration. The transition, denoted by the orange arrow, shows the e_u level is partially filled with fourfold degeneracy.

2.3.2 Hamiltonian formalism for energy levels

To describe the splitting and interactions of the electronic states of the SnV^- centre, as demonstrated by Hepp et al. [48], the total Hamiltonian is expressed as:

$$H = H_0 + H_{\mathrm{SO}} + H_{\mathrm{JT}} + H_{\mathrm{strain}} + H_{Z,L} + H_{Z,S} \tag{2.11}$$

The terms in the Hamiltonian are defined as follows:

- H_0: Represents the unperturbed orbital levels (e_g, e_u), describing the system in the absence of external perturbations.
- $H_{\mathbf{SO}}$: The spin-orbit coupling term, which mixes the spin and orbital angular momentum of the electrons. It splits the e_g and e_u states based on the spin-orbit interaction strength $\lambda_{g,e}$, which depends on the atomic number of the impurity.
- $H_{\mathbf{JT}}$: Models the Jahn-Teller interaction, which accounts for lattice distortions arising from electronic degeneracy. This effect introduces coupling constants Γ_x and Γ_y, lifting the degeneracy of states such as e_g and e_u.
- $H_{\mathbf{strain}}$: Represents strain-induced distortions that modify the electronic structure similarly to the Jahn-Teller effect. Strain effects are characterised by coefficients α and β.

- $H_{Z,L}$ **and** $H_{Z,S}$: Describe the orbital and spin Zeeman interactions, which lift the degeneracy of energy levels under an external magnetic field.

Solving this Hamiltonian yields the eigenvalues and eigenstates of the system. The eigenvalues represent the stationary energy levels, while the eigenstates describe the quantum states associated with those energies, encompassing the probability distributions of the electrons and their spin configurations.

2.3.3 Spin-orbit interations

The spin-orbit component of the Hamiltonian plays a particularly significant role in the behaviour of group-IV colour centres, as it is the primary element that varies between these centres. The spin-orbit coupling term is expressed as:

$$H_{\mathrm{SO}} = \begin{bmatrix} 0 & 0 & -i\lambda_{g,e} & 0 \\ 0 & 0 & 0 & i\lambda_{g,e} \\ i\lambda_{g,e} & 0 & 0 & 0 \\ 0 & -i\lambda_{g,e} & 0 & 0 \end{bmatrix} \tag{2.12}$$

where $\lambda_{g,e}$ is the spin-orbit coupling constant in the ground or excited state, quantifying the interaction strength between the electron's spin and its orbital motion. This constant varies significantly between different group-IV colour centres.

As we move down the group-IV column of the periodic table, the implanted ions in the diamond lattice become larger, leading to stronger relativistic effects. These effects enhance the spin-orbit coupling constant $\lambda_{g,e}$, which increases the energy level splitting between the electronic states e_u and e_g. This progression results in larger spin-orbit interaction strengths for heavier group-IV elements, such as Sn and Pb.

Incorporating H_{SO} into the Hamiltonian reduces the fourfold degeneracy of the ground and excited states, resulting in twofold spin degeneracy for each. This reduction occurs because the spin ($\mathbf{S}$) and orbital angular momenta ($\mathbf{L}$) couple to form total angular momentum states ($\mathbf{J} = \mathbf{L} + \mathbf{S}$). The size of the splitting between the two ground states and two excited states is directly proportional to $\lambda_{g,e}$.

This spin-orbit interaction is a critical factor in determining the optical and spin properties of group-IV defects, for example, the enhanced spin-orbit coupling in heavier group-IV centres such as SnV^- and PbV^- leads to larger energy

separations, which can suppress phonon-mediated decoherence, improving their quantum coherence properties.

2.3.4 Zeeman splitting and magnetic field effects

The Zeeman Hamiltonian isolates the effects of magnetic fields, providing insights into the splitting of degenerate energy levels. For the SnV^- centre, the Zeeman effect describes how an external magnetic field **B** lifts the degeneracy of the ground and excited states. The Hamiltonian for the Zeeman interaction is given by:

$$H_Z = H_{Z,L} + H_{Z,S} \tag{2.13}$$

The terms $H_{Z,L}$ and $H_{Z,S}$ represent the orbital and spin contributions, respectively, which depend on the magnitude and direction of the applied magnetic field **B**. The orbital Zeeman interaction is expressed as:

$$H_{Z,L} = q\gamma_L \begin{bmatrix} 0 & 0 & iB_z & 0 \\ 0 & 0 & 0 & iB_z \\ -iB_z & 0 & 0 & 0 \\ 0 & -iB_z & 0 & 0 \end{bmatrix}, \tag{2.14}$$

where γ_L is the orbital gyromagnetic ratio, and q is the quenching factor, describing the reduction in effective orbital angular momentum due to the crystal environment.

The spin Zeeman interaction is given by:

$$H_{Z,S} = \gamma_S \begin{bmatrix} B_z & B_x - iB_y & 0 & 0 \\ B_x + iB_y & -B_z & 0 & 0 \\ 0 & 0 & B_z & B_x - iB_y \\ 0 & 0 & B_x + iB_y & -B_z \end{bmatrix}, \tag{2.15}$$

where γ_S is the electron gyromagnetic ratio, describing the magnetic moment's sensitivity to spin angular momentum. The splitting magnitude depends on the magnetic field's direction and strength, allowing for precise control over the defect's electronic and spin properties in quantum applications.

2.3.5 Strain and Jahn-Teller effects

The Jahn-Teller and strain Hamiltonians contribute to the splitting of the degenerate e_g and e_u states. These effects arise from intrinsic and extrinsic distortions that alter the crystal field environment and energy levels. The Jahn-Teller effect describes an intrinsic mechanism where a spontaneous distortion of the molecular or crystal structure surrounding an ion or molecule with electronically degenerate states lifts the degeneracy, lowering the overall energy and stabilising a specific electronic configuration. In the case of the SnV^- centre, the large size of the Sn atom prevents it from occupying a regular carbon lattice site. Instead, it resides between two vacant carbon sites along $\langle 111 \rangle$, forming an elongated, symmetric split-vacancy geometry. This unique configuration redistributes local strain and inherently avoids simple Jahn-Teller distortions, stabilising the configuration while maintaining symmetry.

The Jahn-Teller effect lifts the degeneracy of the e_g and e_u levels through lattice distortions. The magnitude of this splitting is proportional to the Jahn-Teller coupling constants Γ_x and Γ_y [120]. The Hamiltonian for the Jahn-Teller effect is expressed as:

$$H_{\mathrm{JT}} = \begin{bmatrix} \Upsilon_x & 0 & \Upsilon_y & 0 \\ 0 & \Upsilon_x & 0 & \Upsilon_y \\ \Upsilon_y & 0 & -\Upsilon_x & 0 \\ 0 & \Upsilon_y & 0 & -\Upsilon_x \end{bmatrix}, \tag{2.16}$$

where Υ_x and Υ_y represent the Jahn-Teller coupling strengths along the x- and y-directions, respectively. Similar to the spin-orbit term H_{SO}, the introduction of H_{JT} reduces the fourfold degeneracy of the ground and excited states to twofold, with splitting magnitudes of $2\Upsilon_x$ or $2\Upsilon_y$.

Strain effects, which arise from external or lattice-induced mechanical distortions, further modify the electronic structure by shifting and splitting energy levels. Strain alters the local crystal field, effectively changing the density of states (DoS) and contributing to energy-level splitting. The strain Hamiltonian is described as:

$$H_{\text{strain}} = \begin{bmatrix} \varepsilon_x & 0 & \varepsilon_y & 0 \\ 0 & \varepsilon_x & 0 & \varepsilon_y \\ \varepsilon_y & 0 & -\varepsilon_x & 0 \\ 0 & \varepsilon_y & 0 & -\varepsilon_x \end{bmatrix}, \tag{2.17}$$

where ε_x represents the effective strain along the x-direction, combining the symmetric strain α and the anisotropic strain δ as $\varepsilon_x = \alpha - \delta$. The term ε_y corresponds to the shear strain along the y-direction, represented by the parameter β. Here, α is the symmetric strain component that contributes uniformly to energy splitting, β is the shear strain component that introduces non-uniform interactions, and δ captures the directional asymmetry in the strain field. For low-strain environments, such as high-quality bulk diamond, these coefficients may often be approximated as zero, simplifying the Hamiltonian. However, in highly strained systems, such as nanodiamonds, these terms become significant and must be explicitly included to account for strain-induced effects.

The combined contributions of Jahn-Teller and strain effects modify the transition energies. Transitions between split states in the ground and excited levels result in distinct PL peaks. The energy difference between levels, such as $\Delta E = E(e_{ux}) - E(e_{gx})$, can be directly related to frequency splitting via $E = h\nu$. Splitting magnitudes are typically calculated from the eigenvalues of H_{JT} and H_{strain}, yielding energy differences observed as GHz-level transitions in PL spectra for the SnV^- centre.

2.3.6 Franck Condon analysis

The Franck−Condon principle [25, 121] provides a fundamental framework for understanding vibronic transitions, where both electronic and vibrational energy levels contribute to optical processes. Since electronic transitions occur on timescales much shorter than nuclear motion, the atomic configuration is effectively 'frozen' during excitation or emission. The overlap of vibrational wavefunctions between initial and final electronic states, quantified by Franck−Condon factors, determines the intensity distribution among vibrational transitions.

This principle is essential in analysing PL spectra of solid-state systems, where emission features include a sharp ZPL and PSBs. The relative intensities of these features reveal information about electron−phonon coupling and lattice distortion associated with different electronic states. By applying the Franck−Condon principle, one can quantify these effects using parameters such as the Huang−Rhys factor and the Debye−Waller factor, which describe the coupling strength and ZPL prominence, respectively.

The PL emission intensity $I(E)$ as a function of photon energy E is given by:

$$I(E) \propto E^3 \sum_{n=1}^{\infty} I_n(E_v)|M_{0n}|^2 \tag{2.18}$$

where $I_n(E_v)$ represents the lineshape for creating n phonons with vibrational energy E_v, and $|M_{0n}|^2$ is the Franck−Condon factor (the squared overlap integral). This expression captures the contributions from all phonon sidebands, each weighted by its Franck−Condon factor and modulated by the photon density of states.

The Franck−Condon factor quantifies the probability of emission into the n-phonon vibrational level of the ground state:

$$|M_{0n}|^2 \propto \frac{S^n}{n!} \tag{2.19}$$

where S is the Huang−Rhys factor, reflecting the strength of electron−phonon coupling. A larger S indicates stronger coupling and more prominent phonon sidebands.

The Debye−Waller factor (DW) is defined as:

$$DW = e^{-S} \tag{2.20}$$

where DW represents the fraction of optical intensity in the ZPL (vibration-free transitions), while $1 - DW$ corresponds to the phonon sidebands. A smaller S results in a sharper ZPL, emphasising the ZPL over PSBs.

The lineshape for a transition involving n-phonon creation, $I_n(E_v)$, is determined recursively as:

$$I_n(E_v) = \int_0^{E_{\max}} I_1(x) I_{n-1}(E_v - x)\, dx \tag{2.21}$$

where E_v denotes the vibrational energy after the optical transition, and $E_{\max}$ is the maximum energy of the n-phonon distribution. This recursive convolution aggregates contributions from successive phonon interactions to form the overall phonon sideband lineshape.

The emission spectrum $I(E)$ is the cumulative result of weighted contributions from each phonon sideband. Each term in the sum reflects the likelihood of a specific phonon transition, modulated by Franck−Condon factors and photon density of states.

Understanding these theoretical constructs is vital for interpreting and simulating vibronic emission spectra in colour centres and other solid-state systems.

2.4 Ultrafast laser fabrication

Ultrafast, usually femtosecond scale, laser micromachining offers unique advantages for creating defect qubits and single-photon sources in solid-state point defects compared to other post-growth methods. The nonlinear interaction confines induced changes to the focal volume [122], which, combined with laser-beam focusing, enables deterministic three-dimensional generation of localized defects. Additionally, the non-linear absorption process is material-independent, allowing photonic device fabrication across various host materials.

Laser writing results from laser-induced optical breakdown, where optical energy transfers to materials, ionizing electrons that further transfer energy to the lattice [82], producing localized bond breaking, cracking, void formation, or melting. The damage site generation follows a sequential process [62]:

- Generation of hot charge carriers
- Multiple-Photon ionization (MPI) or Zener breakdown
- Further heating of excitons via free-carrier absorption
- Relaxation delivering energy to the lattice

2.4.1 Light-matter interaction

In transparent materials, no linear absorption of the incident laser pulse occurs [89]. The ionization process involves non-linear absorption mechanisms in two intensity-dependent regions: MPI and Zener breakdown. In the MPI regime, electrons simultaneously absorb multiple photons until the total energy equals or exceeds the material bandgap [89]. In the tunnelling regime, the laser's electric field suppresses the coulomb well, allowing electrons to tunnel through barriers into the conduction band [69].

The Keldysh parameter describes the balance between MPI and Zener breakdown [123]:

$$\gamma = \omega \sqrt{\frac{mcn\varepsilon_0 I_p}{q^2 I}} \tag{2.22}$$

where ω is laser frequency, I is focal laser intensity, m is the effective electron mass, q is the elementary charge, c is light speed, n is material refractive index and I_p is the ionisation potential (equal to the band-gap energy for a dielectric). MPI dominates when $\gamma \gg 1.5$, while Zener breakdown dominates when $\gamma \ll 1.5$.

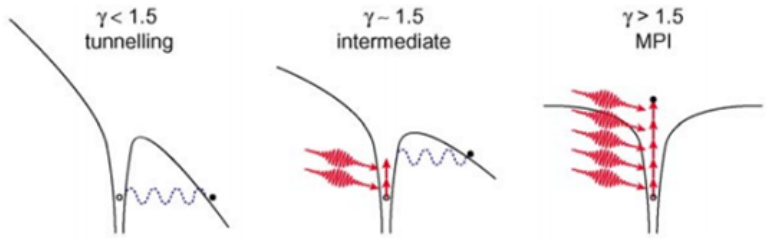


Figure 2.2: Schematic diagram of electron photoionization in an atomic potential for different Keldysh parameter values. This figure is reproduced from source [69] with permission. It demonstrats Zener breakdown and MPI. The electron promotes from valence to conduction band rather than ionization in a solid.

Some literature [70, 74] attributes solid-state defect formation to MPI regime nonlinearity. The MPI model can calculate vacancy generation spatial distribution functions and corresponding FWHM in radial and axial directions, providing insight into the writing process once the multiple photon ionization type is confirmed. Multiple laser pulses can affect defect fabrication, with pulse energy determining

defect type and pulse number determining defect concentration. Pulse repetition rate effects require consideration, as frequency variations lead to different lattice interaction mechanisms and influences.

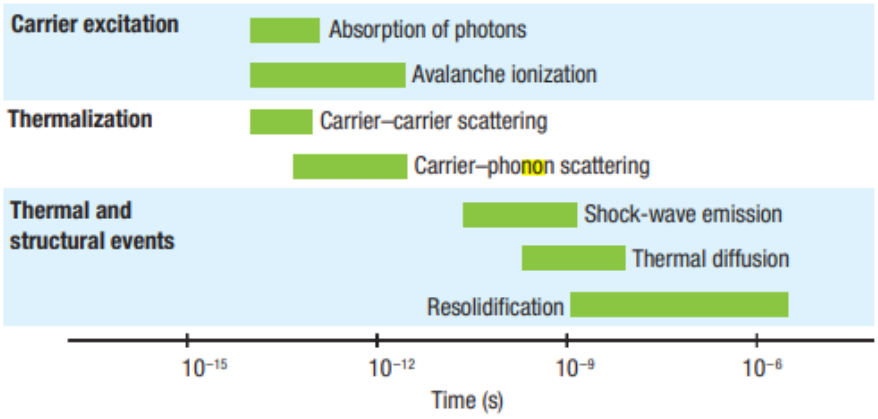


Figure 2.3: Timescale of physical phenomena associated with laser pulse interaction at different time scales with transparent materials. This figure is reproduced from source [82] with permission. Despite femtosecond-scale light absorption, material changes can continue microseconds later.

Understanding damage generation timescale effects is crucial. Fig. 2.3 shows material-light interaction across different timescales. Femtosecond laser pulse damage fundamentally differs from damage caused by pulses exceeding 1 picosecond [82]. Since electron-phonon scattering time approximates 1 ps, femtosecond pulses can conclude before electrons thermally excite nearby ions, minimizing the heat-affected zone beyond the focal volume and improving fabrication precision [124]. Heat confinement and repeatability make femtosecond laser pulses ideal for creating single defects in bulk materials.

2.4.2 Mechanism of Frenkel defects generation

Recent work by Griffiths et al. [83] offers a comprehensive analysis of Frenkel defect formation during femtosecond direct laser writing in diamond. These mechanisms are governed by coupled nonlinear rate equations that describe the interaction of pulsed laser fields with diamond and the non-equilibrium dynamics of charge carriers.

Photoionisation—principally through multiphoton absorption and Zener breakdown—creates a dense plasma of hot charge carriers. Carrier–carrier scattering

rapidly amplifies the density, and the electron population peaks ≈ 0.25 ps after the laser-pulse maximum. At that instant the carrier temperature rises to several-thousand kelvin, far exceeding the lattice temperature. Over the subsequent ~ 30 ps electron–phonon scattering transfers this excess energy to the lattice, raising the local lattice temperature and establishing a quasi-equilibrium that sets the stage for defect formation.

As the plasma cools, electrons and holes first bind into excitons and, at higher density, into biexcitons. Self-trapped biexcitons (STbXs) localise on individual C–C bonds, releasing ≈ 1.7 eV of lattice-relaxation energy and stretching the bond by ≈ 0.04 nm, thereby pre-weakening it. Each STbX resides at an adiabatic minimum 8.9 eV above the perfect lattice—well above the 7.14 eV required to form a neutral Frenkel pair. When the two electrons recombine non-radiatively with the two holes, their energy is deposited locally, completing the bond rupture and propelling one carbon atom into a nearby interstitial site. The process thus renders Frenkel-pair formation not merely possible but energetically favourable.

The dynamics of carrier densities during laser-diamond interaction are described by the following rate equations:

$$\begin{aligned}\frac{d\rho_e}{dt}(r,z,t,E) = &\frac{\delta\rho_e}{\delta t_{\text{epp}}} + \frac{\delta\rho_e}{\delta t_{\text{ep}}} + \frac{\delta\rho_e}{\delta t_{\text{eh}}} \\ &+ \frac{\delta\rho_e}{\delta t_{\text{PI}}} + \frac{\delta\rho_e}{\delta t_{\text{Casc}}} + \frac{\delta\rho_e}{\delta t_{\text{Auger}}} \\ &+ \frac{\delta\rho_e}{\delta t_{\text{Rad}}} + \frac{\delta\rho_e}{\delta t_{\text{SRH}}} + \frac{\delta\rho_e}{\delta t_{\text{Exc}}} \\ &+ \frac{\delta\rho_e}{\delta t_{\text{Diff}}}.\end{aligned} \tag{2.23}$$

Each terms indicates:

- $\frac{\delta\rho_e}{\delta t_{\text{epp}}} + \frac{\delta\rho_e}{\delta t_{\text{PI}}} + \frac{\delta\rho_e}{\delta t_{\text{Casc}}}$: Accounts for energy changes due to collisions, incorporating mechanisms such as free carrier absorption through electron-phonon-photon interactions, electron-phonon coupling, and carrier-carrier scattering.

- $\frac{\delta\rho_e}{\delta t_{\text{PI}}}$: Describes the photoionisation of electrons across the bandgap, demonstrating the influence of photons on electron density.

- $\frac{\delta \rho_e}{\delta t_{\text{Casc}}}$: Represents the cascade multiplication of carrier density, resulting in an increased population of hot carriers.

- $\frac{\delta \rho_e}{\delta t_{\text{Auger}}} + \frac{\delta \rho_e}{\delta t_{\text{Rad}}} + \frac{\delta \rho_e}{\delta t_{\text{SRH}}}$: Accounts for losses in electron density through Auger and radiative recombination processes. Negligible Shockley-Read-Hall recombination is assumed for the intrinsic crystal, with consideration given to the formation and dissociation of excitons.

- $\frac{\delta \rho_e}{\delta t_{\text{Diff}}}$: Describes the diffusion of electrons, which is critical for understanding the temporal dynamics of laser-diamond interactions.

These equations, solved using finite difference time domain (FDTD) methods, model the evolution of carrier densities, lattice temperatures, and Frenkel defect concentrations during and after laser pulse interaction.

Fig. 2.4a illustrates primary scattering and recombination mechanisms, including carrier-carrier scattering, phonon scattering, free carrier absorption, and impact ionisation. It also highlights recombination pathways, such as Auger and radiative recombination, alongside exciton formation and defect-assisted recombination processes. These mechanisms describe energy transitions and carrier dynamics during laser interaction.

Fig. 2.4b shows the temporal evolution of key parameters. The electron temperature rises sharply during carrier excitation and transfers energy to the lattice, resulting in gradual lattice heating. Frenkel defect formation correlates strongly with the STbX population, emphasising the role of self-trapped biexcitons in lattice deformation and defect generation.

2.4.3 Laser annealing

The detailed mechanism underlying the laser annealing process remains unclear. It is widely believed that the process is not purely thermal, as even a few minutes of annealing with MHz laser pulses can result in significant defect mobilization [74]. According to Eqn 1.4, if the process were purely thermal, a few minutes of annealing would only yield a diffusion radius of less than 0.1 Å. This estimate does not account

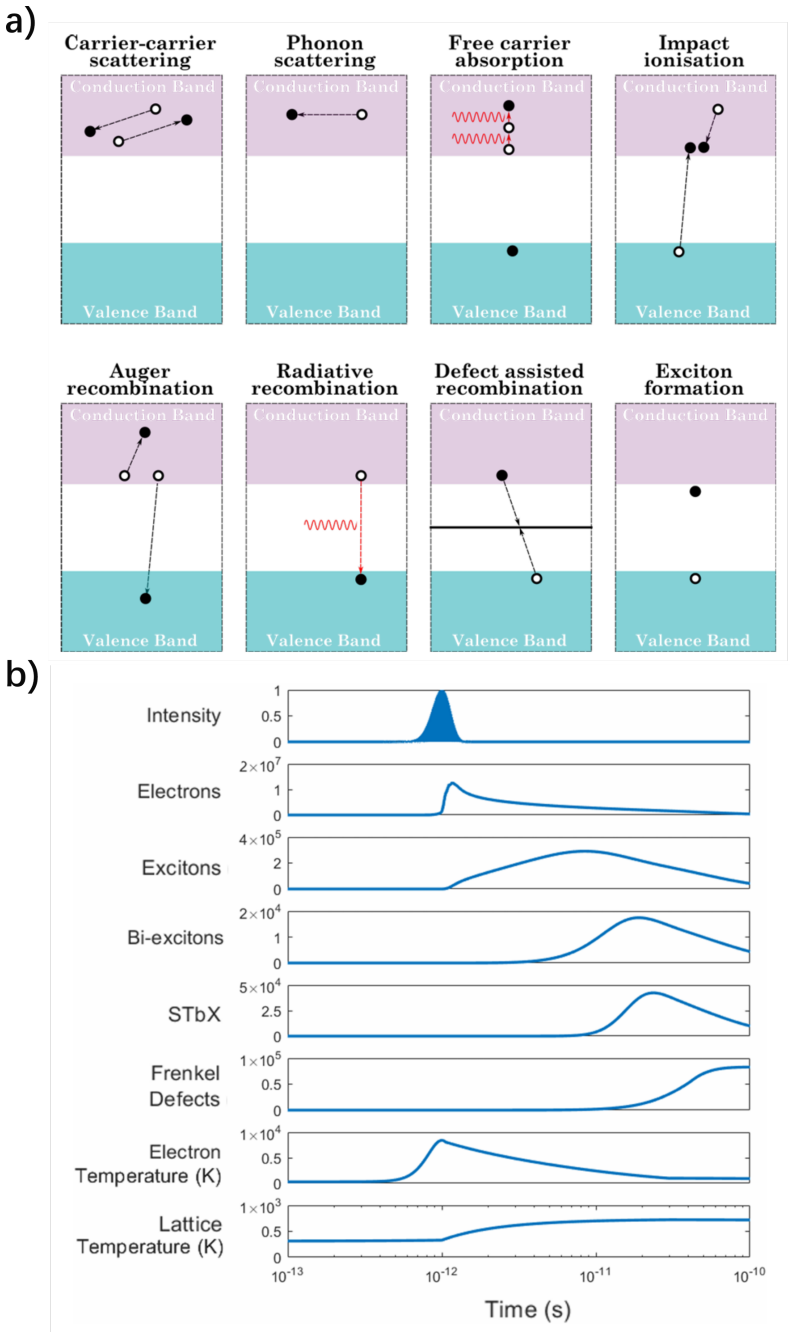


Figure 2.4: Key mechanisms in Frenkel defect formation and temporal evolution of the system. a, Reproduced from [125]. Schematic of scattering and recombination processes during femtosecond laser interaction with materials. **b**, Temporal evolution of parameters including laser intensity, carrier densities (electrons, excitons, and biexcitons), STbX concentration, Frenkel defect formation, and electron and lattice temperatures. Reproduced from [83] with permission.

for the effective annealing time of the MHz laser pulses, further supporting the hypothesis that additional mechanisms are involved.

We propose that the laser annealing process is exciton-mediated. In this hypothesis, femtosecond laser pulses generate hot carriers, which subsequently relax and form excitons [83]. These excitons act as energy carriers, delivering energy directly to the lattice. This localized energy transfer facilitates defect mobilization and annealing by overcoming energy barriers that would otherwise be insurmountable under purely thermal conditions. This exciton-mediated process could explain the observed efficiency of laser annealing over short timescales and its ability to significantly affect defect dynamics within the lattice.

2.5 Aberration corrections

Optical aberrations arise from deviations in a wavefront relative to a reference wavefront, typically a plane wave for collimated beams or a spherical wave for converging/diverging sources. These aberrations degrade focusing quality, increasing the focal spot size beyond the diffraction limit and limiting the performance of applications such as confocal imaging, single-mode fibre coupling, and high-precision optical processing. For instance, when using femtosecond lasers to induce Frenkel defects in wide-bandgap semiconductors, the high refractive index mismatch between the substrate and air, combined with high NA optics, emphasising the needs of applying aberration correction to achieve high-quality defect formation.

2.5.1 Zernike Polynomials: a framework for describing aberrations

To analyse and correct optical aberrations, a systematic mathematical framework is required to represent complex wavefront deformations. Zernike polynomials provide an orthonormal basis defined over a unit circular aperture, allowing wavefronts to be decomposed into physically meaningful modes corresponding to specific aberrations.

Mathematical formulation

Any wavefront, $\psi(r,\theta)$, can be expanded using Zernike polynomials as:

$$\psi(r,\theta) = \sum_{n=0}^{\infty} \sum_{m=-n}^{n} a_n^m Z_n^m(r,\theta), \tag{2.24}$$

where (r,θ) are normalised polar coordinates in the pupil plane, and a_n^m are the expansion coefficients (this represent the magnitude of each aberrations).

The Zernike polynomials $Z_n^m(r,\theta)$ are defined as:

$$Z_n^m(r,\theta) = \begin{cases} R_n^m(r)\cos(m\theta) & \text{if } m \geq 0, \\ R_n^m(r)\sin(|m|\theta) & \text{if } m < 0, \end{cases} \tag{2.25}$$

with the radial polynomial $R_n^m(r)$ given by:

$$R_n^m(r) = \sum_{l=0}^{\frac{n-m}{2}} \frac{(-1)^l (n-l)!}{l!\left(\frac{n+m}{2}-l\right)!\left(\frac{n-m}{2}-l\right)!} r^{n-2l}. \tag{2.26}$$

Here, n and m are integers, where $n \geq |m|$ and $n - |m|$ is even. The quantity $\rho = r/R$ is the normalised radial coordinate: r is the physical distance from the pupil centre, R is the pupil radius, and thus $0 \leq \rho \leq 1$. Hence ρ simply measures what fraction of the pupil radius a point lies at—$\rho = 0$ is on the optical axis and $\rho = 1$ sits on the pupil rim. The Zernike modes $Z_n^m(\rho,\theta) = R_n^m(\rho)\cos(m\theta)$ for $m \geq 0$ and $Z_n^{-m}(\rho,\theta) = R_n^m(\rho)\sin(m\theta)$ for $m > 0$ are orthogonal over the unit disc and form a complete basis for circular wavefronts.

Lower-order Zernike polynomials correspond to familiar optical aberrations. Table 2.1 summarises the first 13 Zernike modes and their associated aberrations, including piston (Z_0^0), tilt ($Z_1^{\pm 1}$), defocus (Z_2^0), astigmatism ($Z_2^{\pm 2}$), coma ($Z_3^{\pm 1}$), and spherical aberration (Z_4^0). To build Table 2.1 one assigns each mode index i the unique (n,m) pair given by Noll's scheme; evaluates the radial polynomial $R_n^m(\rho)$ from the factorial expression; multiplies by $\cos(m\theta)$ for $m \geq 0$ or $\sin(|m|\theta)$ for $m < 0$ to obtain the full two-dimensional polynomial; and finally identifies the aberration whose physical symmetry matches the resulting wavefront shape.

Mode Index (i)	Zernike Polynomial	Corresponding Aberration
1	$Z_0^0 = 1$	Piston
2	$Z_1^1 = 2\rho\cos\theta$	Tip
3	$Z_1^{-1} = 2\rho\sin\theta$	Tilt
4	$Z_2^0 = \sqrt{3}(2\rho^2 - 1)$	Defocus
5	$Z_2^2 = 2\sqrt{3}\rho^2\cos(2\theta)$	Astigmatism
6	$Z_2^{-2} = 2\sqrt{3}\rho^2\sin(2\theta)$	Astigmatism
7	$Z_3^1 = 2\sqrt{2}(3\rho^3 - 2\rho)\cos\theta$	Coma
8	$Z_3^{-1} = 2\sqrt{2}(3\rho^3 - 2\rho)\sin\theta$	Coma
9	$Z_3^3 = 2\sqrt{2}\rho^3\cos(3\theta)$	Trefoil
10	$Z_3^{-3} = 2\sqrt{2}\rho^3\sin(3\theta)$	Trefoil
11	$Z_4^0 = \sqrt{5}(6\rho^4 - 6\rho^2 + 1)$	Spherical Aberration
12	$Z_4^2 = \sqrt{10}(4\rho^4 - 3\rho^2)\cos(2\theta)$	Secondary Astigmatism
13	$Z_4^{-2} = \sqrt{10}(4\rho^4 - 3\rho^2)\sin(2\theta)$	Secondary Astigmatism

Table 2.1: First 13 Zernike polynomials and their commonly associated aberrations.

2.5.2 Correcting aberrations in high-index mismatch systems

When focusing deep into high-refractive-index materials, such as diamond ($n \approx 2.4$) from air ($n \approx 1.0$), significant aberrations arise due to the refractive index mismatch. These aberrations are further exacerbated by high NA optics, particularly when the focus is positioned deep within the material to avoid surface graphitisation and ensure subsurface modifications.

The aberration function caused by the refractive index mismatch can be described as:

$$\Psi_{\mathrm{RIM}}(d, \rho) = k(n_2 l_2 - n_1 l_1), \tag{2.27}$$

where $k = 2\pi/\lambda$ is the wavenumber, n_1 and n_2 are the refractive indices of the lower- and higher-index media, respectively, and l_1 and l_2 are the optical path lengths in each medium, as illustrated in Fig. 2.5. This function quantifies the phase distortion introduced by the refractive index mismatch as a function of the focusing depth d and radial coordinate ρ.

The optical path lengths l_1 and l_2 depend on the geometry of the focusing system and are functions of d and ρ. This makes the aberration depth-dependent

and radially asymmetric. The aberrated wavefront, $\Psi_{\text{original}}(\rho, \theta)$, which serves as the basis for wavefront correction, can be derived from $\Psi_{\text{RIM}}(d, \rho)$ by modelling the spatially varying phase shifts introduced by the refractive index mismatch.

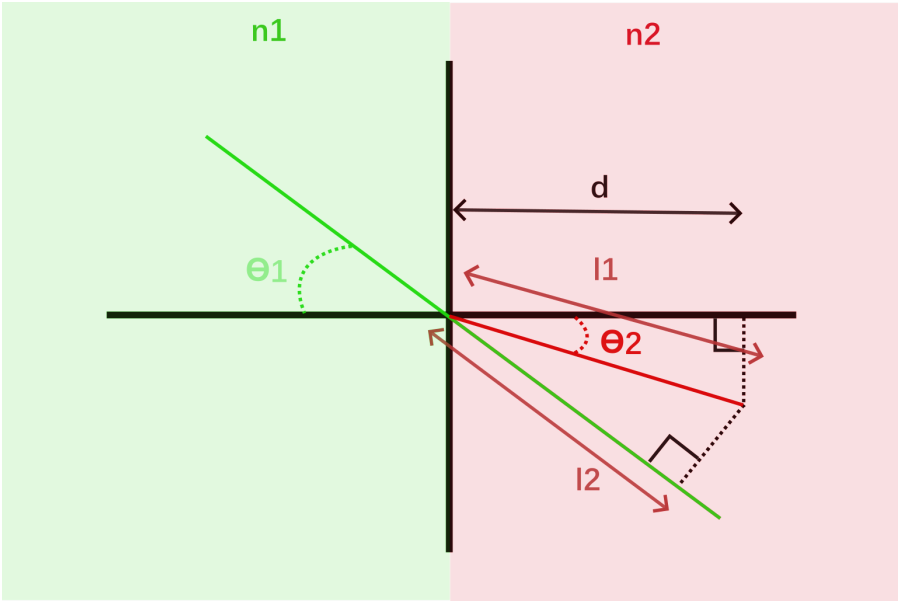


Figure 2.5: Schematic of ray path change when focusing into different refractive index materials. Two different media are shown, with the lower-index medium (n_1) highlighted in green and the higher-index medium (n_2) in red. The distance d represents the depth from the interface to the focal point.

Adaptive optics using a Spatial Light Modulator

To counteract these aberrations, adaptive optics techniques employing spatial light modulators (SLMs) can be utilised. SLMs introduce corrective phase profiles onto the incoming beam, effectively compensating for distortions caused by the refractive index mismatch. This process involves measuring the aberrated wavefront, decomposing it into Zernike modes, and determining the dominant aberration terms. The SLM then applies a phase pattern to cancel these distortions, described mathematically as:

$$\Psi_{\text{corrected}}(\rho, \theta) = \Psi_{\text{original}}(\rho, \theta) - \sum_i a_i Z_n^m(\rho, \theta), \tag{2.28}$$

where $Z_n^m(\rho, \theta)$ represents the Zernike polynomial modes, a_i are the coefficients for each mode, and $\Psi_{\text{corrected}}(\rho, \theta)$ is the resulting corrected wavefront. By aligning

the corrective phase profile with the aberration profile, SLMs can restore focus and enhance the precision of subsurface modifications, even in high-index-mismatch systems, allowing fabricating deep below the surface with a diffraction limited spot inside diamond or other solid-state defects.

3
Experimental methods

Contents

3.1 Laser writing and annealing system 55
3.2 Optical characterisation 59
3.2.1 Confocal imaging system 59
3.2.2 In-situ spectral monitoring 63
3.2.3 Hanbury Brown Twiss measurement 65
3.2.4 Power saturation measurement 67
3.2.5 Polarisation measurement 68

3.1 Laser writing and annealing system

The ultrafast laser writing and annealing were performed using a custom-built system comprising three main modules:

1. **Confocal Fluorescence Microscope**: This module was extensively used for the optical characterisation of fabricated samples before, during, and after laser fabrication. It includes functionalities such as two-dimensional PL mapping, in-situ fluorescence feedback, in-situ spectral monitoring, and spectroscopy. A detailed discussion of this module will be presented in the next section.

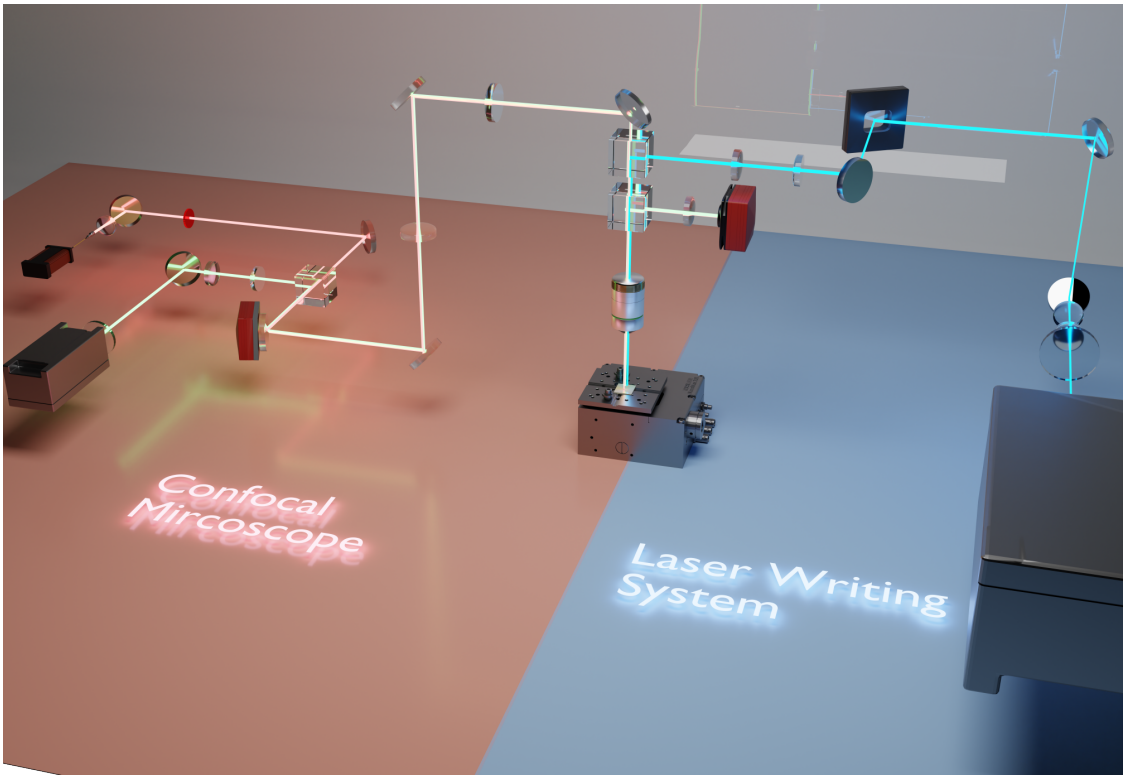


Figure 3.1: Schematic of the custom build laser fabrication system. Overview of the system showing the Confocal Microscope (left) and the Laser Writing System (right), illustrating the optical paths and key components.

2. **Regeneratively Amplified Ti:Sapphire Laser System**: This module consists of a Spectra Physics Mai Tai laser and a Spectra Physics Solstice amplifier, operating at 790 nm with a maximum repetition rate of 1 kHz, equipped with a SLM (Hamamatsu Photonics X10468−02). Owing to the low-energy photons emitted, these femtosecond laser pulses offer a wider operational pulse energy window for non-linear light–matter interactions in wide-bandgap semiconductors. This module was frequently used to generate single defects during the research presented in this thesis.

3. **Yb:KYW Laser System with Frequency Doubling**: This module utilises a 1040 nm Yb:KYW laser (Spectra Physics Spirit) with a frequency-doubling module to produce a 520 nm laser source. Both lasers have a maximum repetition rate of 1 MHz and are equipped with an SLM (dual-band Meadowlark Optics HSP1920−500−1200−HSP8). The high repetition rate

of this module makes it suitable as the laser annealing light source for most of the research conducted in this thesis. It minimises wasted dead time—the interval after the disturbance from the previous pulse has settled and before the next pulse interaction. According to Griffiths' simulation, this timescale is on the order of nanoseconds [83]. Since the pulse duration of the femtosecond laser is shorter than the timescale of thermal diffusion (nanoseconds), most of the pulse energy is delivered to the focal volume before it can diffuse away as heat, resulting in feature sizes smaller than the focal volume of the pulsed laser beam.

An overview schematic of the custom-built system is illustrated in Fig. 3.1, while detailed schematics of the laser writing and annealing modules are shown in Fig. 3.2. Given the similarities between the kHz and MHz modules, a shared optical schematic is used for simplicity; however, in practice, the optical paths and components differ. The high peak intensity of femtosecond laser pulses, compared to CW lasers, necessitates the use of optical components that can withstand higher damage thresholds.

Power control in both modules was achieved using a $\lambda/2$ waveplate (HWP) and a Glan-laser polariser. Since the SLMs are polarisation-sensitive, the polariser was oriented to align with the fast axis of the respective SLM. By adjusting the angle of the $\lambda/2$ waveplate, the linearly polarised output laser pulses could be modulated in power, as described by Malus's Law:

$$P = P_0 \cos^2(2\theta) \tag{3.1}$$

where P_0 is the power before the $\lambda/2$ waveplate, and θ is the angle between the $\lambda/2$ waveplate and the polariser's fast axis. The angle between them is controlled by a DC servo motor (Thorlabs PRM1Z8) with a resolution of 0.03°.

To achieve uniform (top-hat) illumination on the SLM instead of a Gaussian profile to match the pixels on the SLM, the beam was expanded using a set of plano-concave lenses. While this configuration inherently sacrifices some laser power,

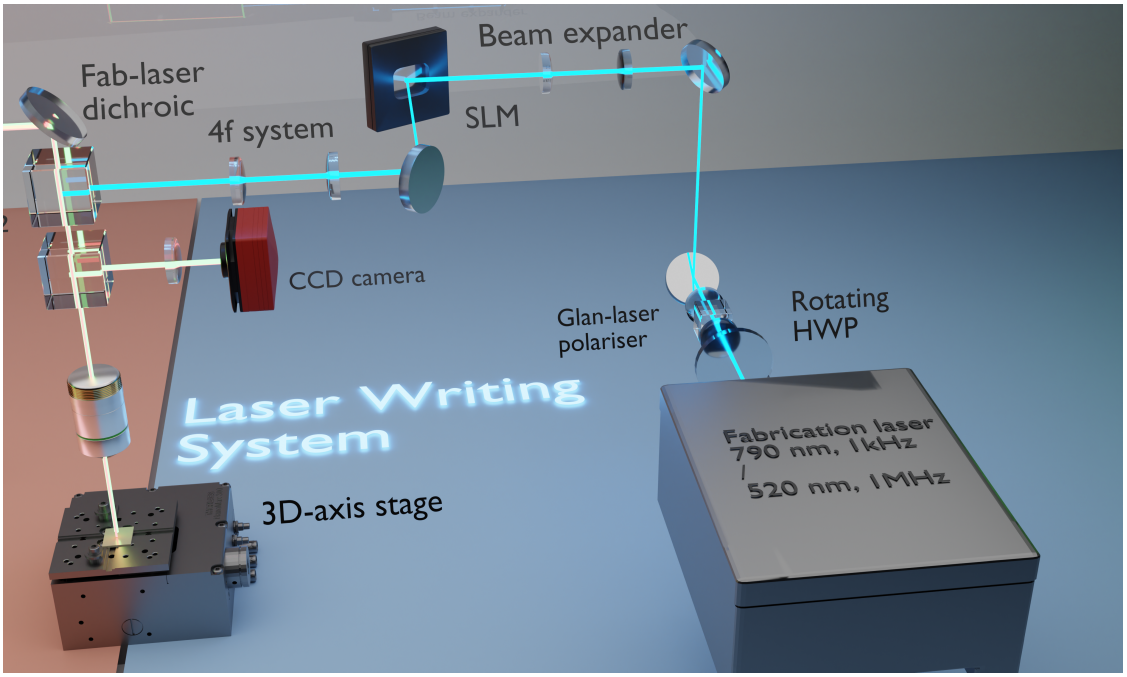


Figure 3.2: Schematic of laser writing and annealing modules. Detailed view of the Laser Writing System, including the fabrication laser for both kHz and MHz, SLM, $\lambda/2$ waveplate, Glan-laser polariser, CCD camera, 4f system, and translation stages for sample positioning.

it still provided sufficient power for the experiments conducted in this thesis. After modulation by the SLM, the beam was imaged onto the back aperture of the objective lens using a 4f lens system, ensuring phase-only modulation of the pupil.

The pulse duration of the fabrication lasers was measured using an intensity autocorrelator (APE Pulsecheck) and generally ranged between 250 and 350 fs. The Ti:Sapphire laser source includes a compressor capable of modulating the pulse length (using a chirped pulse amplifier), allowing remote control of the pulse duration via a motorised stage. The Yb:KYW laser had a fixed pulse length of 330 fs at 1040 nm for the fundamental mode and 250 fs for the second harmonic generation (SHG) at 520 nm. Importantly, the system was built so that both fabrication lasers could not operate simultaneously, thereby avoiding unnecessary laser hazards associated with multiple class-4 laser systems within a single enclosure.

Samples were mounted on translation stages (Aerotech x˘y: ABL10100; z: ANT95−3−V) to provide three-dimensional control. Additionally, a piezoelectric stage (Piezosystem Jena Tritor 102) was mounted atop the Aerotech stage to

facilitate precise movements in the x and y directions. This setup ensured that experimental work could continue even when the Aerotech stage was temporarily unavailable.

Illumination of the samples was achieved using an LED embedded within the translation stages for widefield transmission microscopy, or an external LED placed in the confocal microscope optical path for reflection microscopy. A variety of objective lenses were used and could be interchanged between experiments:

- **60x, 1.4 NA Olympus PlanApo Oil Immersion Lens**: Used for generating single defects in bulk diamond.
- **50x, 0.95 NA Olympus LMPlanFL N Air Lens**: Employed for laser annealing and fabrication on diamond membranes.
- **20x, 0.5 NA Olympus UPlanFL N Air Lens**: Utilised for surface electrode patterning.

Electronic control of the laser fabrication systems and the confocal microscope was managed through custom-built code written for a Field Programmable Gate Array (FPGA) (NI PCI-7830R), with a user interface developed in LabVIEW.

3.2 Optical characterisation

3.2.1 Confocal imaging system

All experiments involving confocal scanning microscopy were performed using several custom-built confocal microscope systems. Three types of confocal microscopes were used: (i) a room-temperature laser scanning confocal microscope with various excitation sources and objective lenses (WASPS setup), (ii) a cryogenic-temperature laser scanning microscope (Montana setup), and (iii) a stage-scanning confocal microscope. Confocal microscopy offers higher spatial resolution compared to widefield microscopy by incorporating a pinhole in the detection path. This pinhole ensures that only light from the focal plane is collected, rejecting out-of-focus light.

The confocal spot is rastered across the sample either by scanning mirrors to move the laser focus or by rastering the sample stage relative to the objective lens.

The schematic of the WASPS setup is shown in Fig. 3.3. A CW 532 nm laser (GEM 532) serves as the primary excitation source for off-resonance excitation. The beam is collimated and expanded using a set of planar-concave lenses. A variable neutral density filter, mounted on a rotational motor, is used to modulate the laser power, and a 532 nm clean-up filter ensures that only the desired laser wavelength passes through. A 90/10 beam splitter (10% reflection, 90% transmission) deflects the laser beam towards the FSM while allowing the fluorescence emission to pass to the collection end. The beam splitter was chosen instead of a dichroic mirror to provide flexibility for alternative excitation sources, such as a 795 nm laser, for substrates other than diamond. Although this configuration sacrifices 90% of the excitation power, sufficient power levels of up to 4 mW are still achievable.

A Newport FSM 300 fast steering mirror is used to raster the laser focus across the sample to build a 2D PL image. A relay lens module in a 4f configuration ensures that the deflection of the FSM is mapped onto the back aperture of the objective lens, corresponding to lateral displacement on the focal plane. Two objective lenses were used for imaging and excitation: a 50x, 0.8 NA Olympus MPlanFI air lens and a 100x, 1.25 NA Olympus PlanC N oil-immersion lens.

For fluorescence collection, the system operates in an epifluorescent configuration, where light is collected through the same objective lens used for excitation. The collected fluorescence travels back through the optical path but is transmitted through the beam splitter. Additional filters, including a 532 nm notch filter and either a 650/150 nm bandpass or a 550 nm long-pass filter, are used to suppress residual excitation light. The filtered signal is then coupled into a single-mode fibre (SM600) and directed to one of three detection systems: a single-photon avalanche diode (SPAD) (Excelitas SPCM-AQRH-14-FC) for photoluminescence measurements, a spectrometer for spectral analysis, or a second SPAD for HBT measurements to determine photon statistics. The spectra data is aquired with a 300 nm Kymera 193i-A spectrograph and a low noise Newton CCD. Samples

are mounted on a 3-axis stage (Thorlab Nanomax 3-axis stage) with controller electronics. Widefield transmission microscopy is achieved using an LED placed behind the sample mount for illumination.

The stage-scanning confocal microscope operates similarly to the WASPS setup, except that the sample stage is rastered relative to the confocal spot instead of scanning the laser beam. This eliminates the need for the 4f relay lens system, simplifying the optical layout.

Electronic control of the WASPS setup, including laser scanning and data acquisition, is managed through custom-built code written for a National Instruments DAQ system (NI-DaQ), with a user interface developed in LabVIEW.

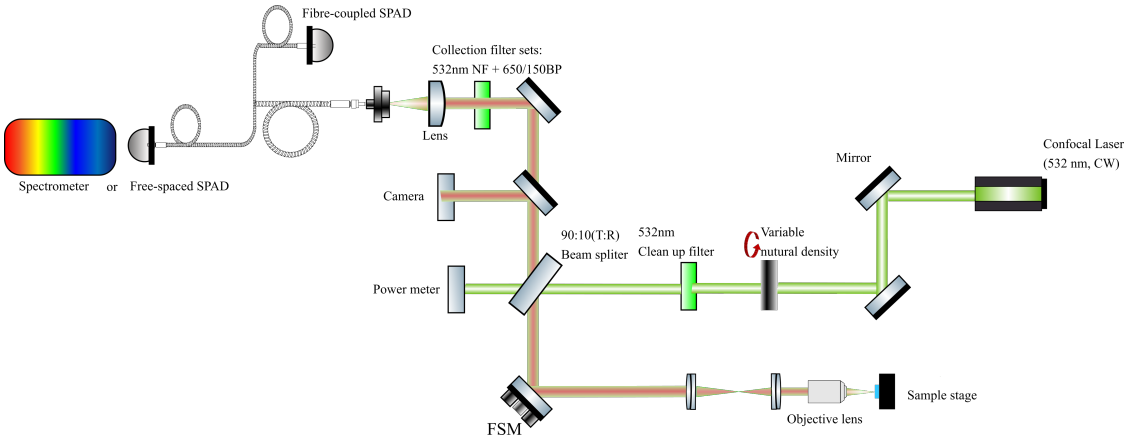


Figure 3.3: Schematic of the WASPS setup. A home-built room-temperature confocal microscope configured with multiple objective lenses and excitation sources for optical characterisation.

The Montana setup, illustrated in Fig. 3.4, integrates a Montana S-50 closed-cycle liquid helium cryostat with a customised beam-scanning confocal microscope. Samples were mounted on a 4 mm^2 piece of thermal-grade diamond using Apiezon thermal N-grease and silver dag. The thermal-grade diamond was thermally coupled to a cold finger using thermal N-grease, ensuring efficient heat transfer. The cold finger was connected to a three-stage open-loop piezoelectric actuator for navigation. Imaging was conducted using a Zeiss EC Epiplan X100, 0.85 NA, 0.87 mm working distance objective lens. This lens was mounted within the cryostat housing under vacuum and maintained at room temperature with an internal heater.

Beam scanning was performed using a Newport FSM 300 FSM combined with a relay lens module in a 4f configuration. This setup allowed precise lateral positioning of the beam. The filter set was customised for measurements on solid-state defects in diamond, including a 532 nm notch filter to block the excitation laser line and a 600 nm long pass filter tilted at an angle of incidence (AOI) to function as a 580 nm long pass filter. This configuration enabled the acquisition of spectra from Type II Sn defects, a defect type related to SnV^- centres in diamond, which will be studied in details in Chapter 4. For specific SnV^- centre measurements, a 620/5 bandpass filter was used to isolate the ZPL.

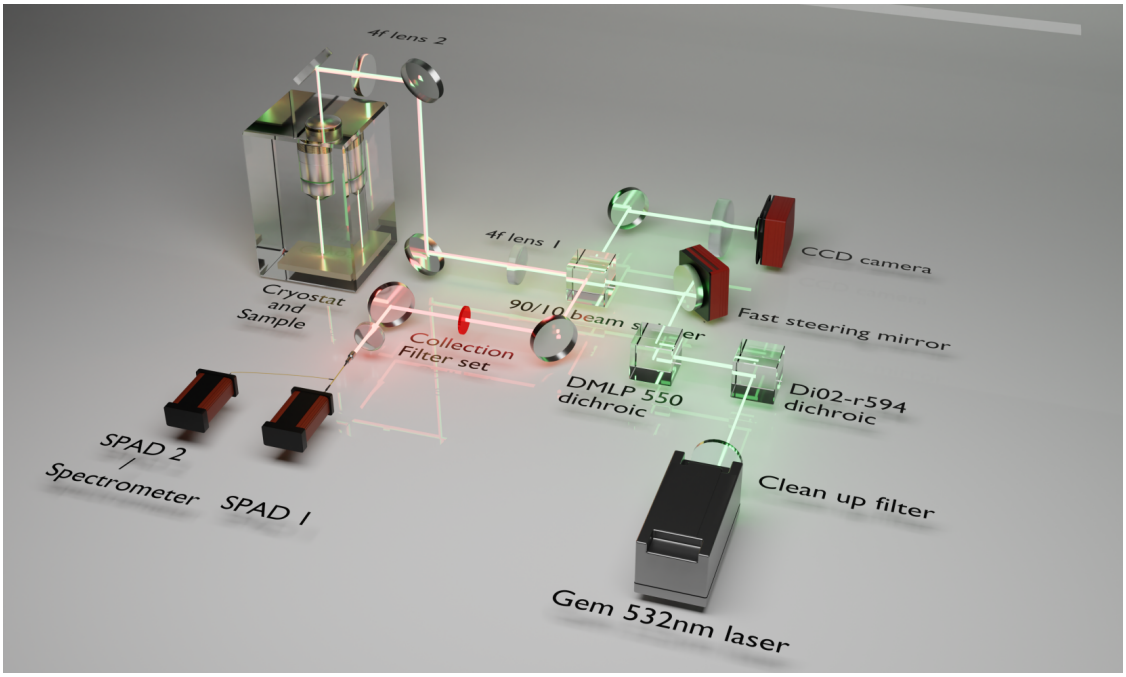


Figure 3.4: Schematic of the Montana setup. A customised cryogenic-temperature confocal microscope integrated with a Montana S-50 closed-cycle liquid helium cryostat and a 0.85 NA objective lens.

The schematic of the confocal microscope used in the laser writing and annealing system is shown in Fig. 3.5. The excitation source was a 532 nm CW diode-pumped solid-state laser (DPSSL) (Cobalt Samba). PL was collected in an epiconfiguration and detected through a confocal pinhole using a SPAD (Excelitas SPCM-AQRH-14-FC) at a sampling frequency of 1 kHz. A bandpass spectral filter transmitting wavelengths between 650 and 750 nm isolated fluorescence from NV^- centres,

cutting out light from the excitation laser and the Raman signal associated with the confocal source. For SnV^- centre measurements, a 600 nm long pass filter with AOI tilted to function as a 580 nm long pass filter was used for PL imaging and spectral acquisition, while a 620/5 bandpass filter was employed during fluorescence feedback in laser annealing processes.

A significant challenge of using the confocal microscope in-situ with the laser fabrication system was ensuring that the excitation and collection regions were confocal with the focal volume of the writing or annealing laser. To achieve a flat intensity profile (top-hat function) at the pupil (back aperture), the beam was expanded 50x using an objective lens. This expansion improved resolution and contrast and facilitated subsequent optical manipulations, such as relay lensing, albeit at the expense of laser power.

The same FSM was used in this setup as in the previous systems, enabling independent lateral position control of both the microscope and fabrication focal spots. On the collection side, signals were coupled into a multi-mode fibre, where the mode field diameter (MOD) of the fibre effectively acted as the pinhole. This configuration reduced sectioning accuracy but allowed the collection of signals from areas outside the focal point. Such a setup was crucial for fluorescence feedback during laser annealing, as it enabled detection of pre-fabricated vacancy defects that may have migrated from their original positions.

(The spectra data is aquired with a 300 nm Kymera 193i-A spectrograph and a low noise Newton CCD.)

3.2.2 In-situ spectral monitoring

This work represents the first demonstration of in-situ spectral monitoring during the laser annealing process, offering unprecedented insights into the mechanisms of defect formation. These measurements were conducted using the custom-built laser writing and annealing system, integrated with a confocal microscope module. Spectral data were acquired with a 300 mm blaze spectrograph (SpectraPro HRS-300) and a low-noise camera (PIXIS 100 from Princeton Instruments).

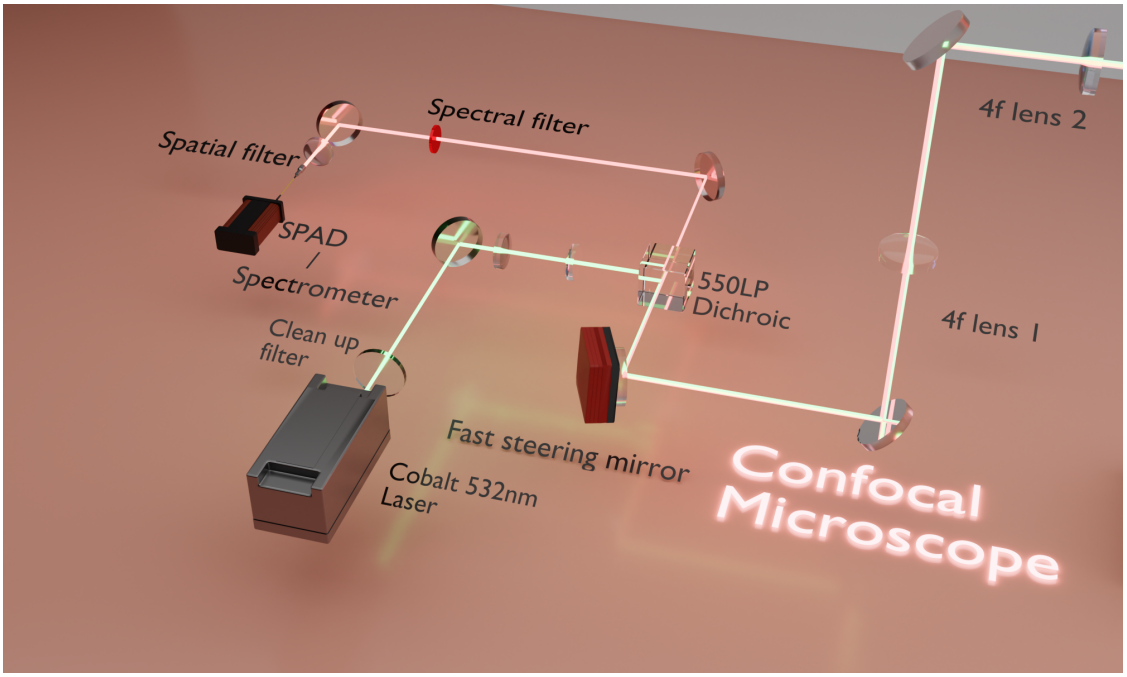


Figure 3.5: Schematic of laser writing and annealing system's confocal module. Detailed view of the confocal module, including the excitation laser, beam rastering module with FSM and 4f configuration relay lenses, and the collection system for SPAD or spectrometer detection.

Given the focus of this thesis on studying the laser activation process of SnV^- centres in diamond, PL was collected using a high-numerical-aperture (50x, 0.95 NA Olympus LMPlanFL N Air Lens) air objective shared with the femtosecond laser activation beam. A tailored 582 nm long-pass filter (created by tilting a 600 nm long-pass filter at a specific angle of incidence) was used during PL imaging to block the first-order Raman emission of diamond while highlighting the Type II Sn feature near 595 nm.

To monitor defect evolution during the annealing process, a 2D PL map of the laser annealing region was first captured prior to any laser treatment, with background spectra recorded for comparison. The laser annealing process was then performed iteratively, alternating between 1 minute of annealing and PL mapping of the treated region. This approach allowed the identification of discrete emitters as they formed, and the spectrum of each emitter was recorded to build a temporal profile of the spectral evolution over successive annealing steps. While a default

time interval of 2 minute was used between spectral measurements, this interval could be adjusted to suit specific experimental requirements.

For deterministic modification of specific defects, such as converting Type II Sn to SnV^- centres, live SPAD traces were recorded during laser annealing using a 620/5 bandpass filter to isolate the SnV^- ZPL. Whenever a sharp increase in SPAD counts was detected, the annealing laser was immediately terminated, and the defect's spectrum was recorded. By combining spectra acquired through the iterative protocol with the live SPAD data, a time-ordered sequence of photoluminescence spectra was generated, capturing the defect's transformation to the SnV^- state.

3.2.3 Hanbury Brown Twiss measurement

To analyse the photon statistics of solid-state defects, auto-correlation measurements were performed using Hanbury Brown and Twiss (HBT) interferometry. The emission from the defect centre was split by a 50/50 beam splitter and directed towards two single-photon avalanche diodes (SPADs). The time differences between photon detection events at the two detectors were recorded as a histogram using a time tagger (Swabian Instruments Time Tagger 20). This measurement is characterised by the second-order correlation function, $g^{(2)}(\tau)$, defined as:

$$g^{(2)}(\tau) = \frac{\langle I_A(t) I_B(t+\tau) \rangle}{\langle I_A(t) \rangle \langle I_B(t+\tau) \rangle} \tag{3.2}$$

where $\langle \dots \rangle$ denotes the time average, $I_A(t)$ and $I_B(t)$ are the instantaneous count rates at detectors A and B, respectively, and τ is the time delay between detections. The time-averaged count rates, $\langle I_A(t) \rangle$ and $\langle I_B(t+\tau) \rangle$, can be related to experimentally measurable quantities as:

$$\langle I_A(t) \rangle \langle I_B(t+\tau) \rangle = I_A \cdot I_B \cdot \delta t \cdot t_{\text{total}} \tag{3.3}$$

where $I_A = \langle I_A(t) \rangle$ and $I_B = \langle I_B(t) \rangle$ are the average count rates at detectors A and B, δt is the time bin size, and t_{total} is the total measurement time. The second-order correlation function $g^{(2)}(\tau)$ quantifies the statistical correlation between photon detection events at detectors A and B. The numerator, $\langle I_A(t) I_B(t+\tau) \rangle$,

represents the coincidence rate, while the denominator normalises this value by the product of the independent count rates.

For a three-level system, such as NV^- or SnV^- centres, where a metastable state is present, $g^{(2)}(\tau)$ can be expressed as:

$$g^{(2)}(\tau) = 1 - (1+\alpha)e^{-\frac{|\tau|}{\tau_1}} + \alpha e^{-\frac{|\tau|}{\tau_2}} \tag{3.4}$$

where α is a coefficient, and τ_1 and τ_2 represent the radiative lifetimes of the excited and metastable states, respectively. For a four-level system, where electrons are initially pumped to a higher-energy state and non-radiatively decay to the metastable state before undergoing stimulated emission to a lower-energy state (not the ground state), $g^{(2)}(\tau)$ is given by:

$$g^{(2)}(\tau) = 1 + \alpha_1 e^{-\frac{|\tau|}{\tau_1}} + \alpha_2 e^{-\frac{|\tau|}{\tau_2}} - (1+\alpha_1+\alpha_2)e^{-\frac{|\tau|}{\tau_3}} \tag{3.5}$$

where τ_1, τ_2, and τ_3 are the lifetimes of the upper excited state, metastable state, and lower lasing state, respectively. The $g^{(2)}(0)$ value is determined for different emitter types using n-photon Fock states:

$$g^{(2)}(0) = 1 - \frac{1}{n} \tag{3.6}$$

where n is the number of emitters. For a single emitter, the expected $g^{(2)}(0)$ is ideally 0, whilst for two emitters (doublets), $g^{(2)}(0)$ is 0.5.

In practice, the measured intensity comprises both the quantum signal and uncorrelated background contributions from sources such as Raman scattering, detector dark counts, and optical leakage:

$$I_{\text{measured}}(t) = I_{\text{signal}}(t) + I_{\text{background}}(t) \tag{3.7}$$

For notational simplicity, we denote $I_{\text{signal}}(t)$ as $I_s(t)$ and $I_{\text{background}}(t)$ as $I_b(t)$. The measured second-order correlation function becomes:

$$g_m^{(2)}(\tau) = \frac{\langle [I_s(t) + I_b(t)][I_s(t+\tau) + I_b(t+\tau)] \rangle}{\langle I_s + I_b \rangle^2} \tag{3.8}$$

To derive the background correction, we employ standard quantum optics assumptions: the background is uncorrelated with the signal, meaning $\langle I_s(t) I_b(t+$

$\tau)\rangle = \langle I_s\rangle\langle I_b\rangle$, and the background follows Poisson statistics with $\langle I_b(t)I_b(t+\tau)\rangle = \langle I_b\rangle^2$ for $\tau \neq 0$.

Defining ρ as the background-to-total intensity ratio:

$$\rho = \frac{\langle I_b\rangle}{\langle I_s + I_b\rangle} \tag{3.9}$$

and noting that $\langle I_s(t)I_s(t+\tau)\rangle = g_s^{(2)}(\tau)\langle I_s\rangle^2$, the measured correlation function can be expressed as:

$$g_m^{(2)}(\tau) = g_s^{(2)}(\tau)(1-\rho)^2 + 2\rho(1-\rho) + \rho^2 \tag{3.10}$$

Solving for the true signal correlation function yields:

$$g_s^{(2)}(\tau) = \frac{g_m^{(2)}(\tau) - 2\rho + \rho^2}{(1-\rho)^2} \tag{3.11}$$

For experimental setups with low background levels where ρ^2 is negligible compared to 2ρ, this simplifies to:

$$g^{(2)}_{\text{corrected}}(\tau) = \frac{g^{(2)}_{\text{measured}}(\tau) - \rho}{(1-\rho)^2} \tag{3.12}$$

This correction formula ensures accurate determination of photon statistics by accounting for noise contributions, enabling precise characterisation of single-photon sources and other quantum optical phenomena.

3.2.4 Power saturation measurement

The power saturation measurement of a defect centre is performed by measuring the SPAD count rates as a function of the excitation power. The excitation power is determined at the back aperture of the objective lens. The relationship between the count rate and the excitation power can be described by the power saturation equation:

$$I(P) = \frac{I_{\text{sat}} \cdot P}{P + P_{\text{sat}}} \tag{3.13}$$

where $I(P)$ is the count rate at excitation power P, I_{sat} is the saturation intensity, and P_{sat} is the saturation power.

To ensure accurate measurements, the count rates used in this equation must be background-subtracted. The background baseline is determined by measuring the vicinity background count rate level near the defect centre. By subtracting this background contribution from the measured count rates, the derived parameters I_{sat} and P_{sat} accurately represent the intrinsic properties of the defect centre.

3.2.5 Polarisation measurement

To characterise the polarisation properties of the light emitted by the solid state defect centres, a motorised HWP was placed in the detection beam path. The HWP was rotated to precisely vary the polarisation state of the transmitted light. This waveplate introduces a phase shift between the orthogonal components of the light, effectively rotating its polarisation direction by twice the angle of the waveplate's rotation. Downstream of the HWP, a linear polariser was positioned to transmit only the component of the electric field aligned with its transmission axis, while blocking the orthogonal component. The linearly polarised light was then directed into a SPAD for intensity measurement.

By rotating the HWP and recording the transmitted light intensity, the polarisation response of the SnV^- centres was analysed using Malus's Law (as shown in Eqn 3.1). This law relates the transmitted light intensity to the angle between the light's polarisation direction and the polariser's axis. The measured polarisation data provide insights into the symmetry properties and dipole alignment of the SnV^- centres.

PL emission intensity was calculated by integrating the spectrum over the ZPL wavelength range. For Type II Sn defects, this integration was performed over the range of $593 - 595$ nm. For SnV^- centres, the integration was carried out over $619 - 622$ nm for the γ transition and $622 - 625$ nm for the δ transition. These wavelength ranges ensure that the analysis captures the distinct emission characteristics of each defect type while excluding contributions from phonon sidebands or other emission features.

The degree of polarisation provides information about the alignment of the emitter's dipole. A high degree of polarisation indicates that the dipole axis lies predominantly within the plane of the objective lens, whereas a low degree suggests that the dipole is either oriented out of plane or that multiple dipoles contribute to the emission. Polarisation measurements also reveal the orientation of the defect's symmetry axis relative to the observation plane, the site symmetry of the defect within the crystal lattice, and the possible presence of multiple dipole transitions.

Anisotropic polarisation suggests the influence of a low-symmetry crystal field, whereas isotropic polarisation indicates a higher symmetry. The angular dependence of the polarisation response can provide insights into the rotational symmetry of the defect, while variations in polarisation under external perturbations, such as strain or electric fields, reveal symmetry-breaking influences. These analyses enable a deeper understanding of the intrinsic and extrinsic symmetry properties of the defect centres.

4

Laser activation of Group IV defects in diamond

Contents

4.1 Introduction 72
4.2 Negatively charged tin vacancy center SnV^- in diamond 73
4.2.1 Introduction 73
4.2.2 Fabrication process flow 74
4.2.3 Optical characterisation 77
4.3 Effect of Pulse energy and annealing time 84
4.3.1 Activation of single SnV^- centre 90
4.3.2 Local strain study of SnV^- centres 93
4.4 Type II Sn centre in diamond 96
4.4.1 Introduction 96
4.4.2 Frank Condon study 98
4.4.3 Spectral analysis 101
4.4.4 Summary 104
4.5 Distribution and yield of SnV^- and Type II Sn 105
4.6 In-situ monitoring 107
4.6.1 In-situ spectral monitoring 108
4.6.2 SPAD trace 112
4.7 Positioning accuracy 113
4.8 Negatively charged silicon vacancy centre SiV- in diamond 116
4.8.1 Array with Poissonian 256 ions/implantation site 117
4.8.2 Array with Poissonian 64 ions/implantation site 118
4.9 Discussion 122

4.1 Introduction

Building on the theoretical background covered in Chapters 1 and 2, this chapter focuses on the experimental creation and activation of single SnV^- centres in diamond. As previously discussed, SnV^- centres are particularly promising among group-IV defects for quantum applications due to their large spin-orbit coupling, high ZPL fraction, and reduced sensitivity to spectral diffusion [45, 47, 126]. However, scaling up their use in quantum devices remains a challenge, especially when precise spatial placement and reliable activation protocols are required.

To address these challenges, we combine site-selective ion implantation of tin—achieved with sub-50 nm accuracy [63]—with femtosecond laser processing and live PL monitoring. Unlike traditional post-implantation annealing methods, this laser-based approach enables localised and tunable heat treatment, mitigating lattice damage while preserving nanofabricated features. The use of in situ PL feedback allows real-time observation of the emergence and interconversion of Sn-related defects, including a previously under-studied centre that earlier investigations considered to be insufficiently annealed. Here I refer to this centre as 'Type II Sn', which is hypothesised to correspond to SnV–C_i [39, 127, 128]; however, an SnV–V_C complex or substitutional tin cannot be ruled out. These reversible spectral transitions provide new insights into the formation mechanisms of tin-related colour centres and enable deterministic activation of SnV^- centres.

By integrating site-specific ion implantation with femtosecond laser annealing and live PL monitoring, this work establishes a pathway to create high-quality SnV^- centres at targeted locations. This advancement paves the way for more scalable and precisely engineered quantum devices based on group-IV colour centres.

4.2 Negatively charged tin vacancy center SnV^- in diamond

4.2.1 Introduction

Negatively charged Tin-vacancy (SnV^-) centres are particularly noteworthy among group IV defects due to their large ground-state orbital splitting, which is significantly greater than that of other defects such as silicon-vacancy (SiV) [48] and germanium-vacancy (GeV) [36]. This large splitting suppresses phonon scattering to the upper ground-state orbital, giving long coherence time at liquid helium temperature [39, 43], which facilitates operation without requiring the extremely low temperatures of a dilution refrigerator (<100 mK) [39].

Despite their promising attributes, including longer coherence times at liquid helium temperatures [39, 43] compared to other group-IV defects and a remarkably high Debye-Waller factor relative to NV^- centres, the precise creation and manipulation of SnV^- centres—and group-IV centres in general—remain significant challenges. Traditional methods, such as ion implantation followed by thermal annealing, have been widely employed [39]. However, these methods yield low formation efficiencies (1%-5%) [129], and the resulting defect centres often suffer from significant inhomogeneous broadening due to strain. Two critical hurdles on the path to scalability are the activation of single emitters and the fabrication of regular arrays of defect centres.

Alternative fabrication approaches have been explored to address these limitations. High-pressure, high-temperature (HPHT) annealing can reduce inhomogeneous broadening, but it often causes surface damage and does not allow for precise spatial control of defect centres. Chemical vapour deposition (CVD) growth techniques have successfully been used to create SiV and GeV centres, though their application to SnV^- centres remains to be demonstrated. Similarly, HPHT growth methods have produced GeV and SnV^- centres in both bulk diamond and nanodiamonds, but these methods lack site-selectivity, which limits their scalability for quantum technologies.

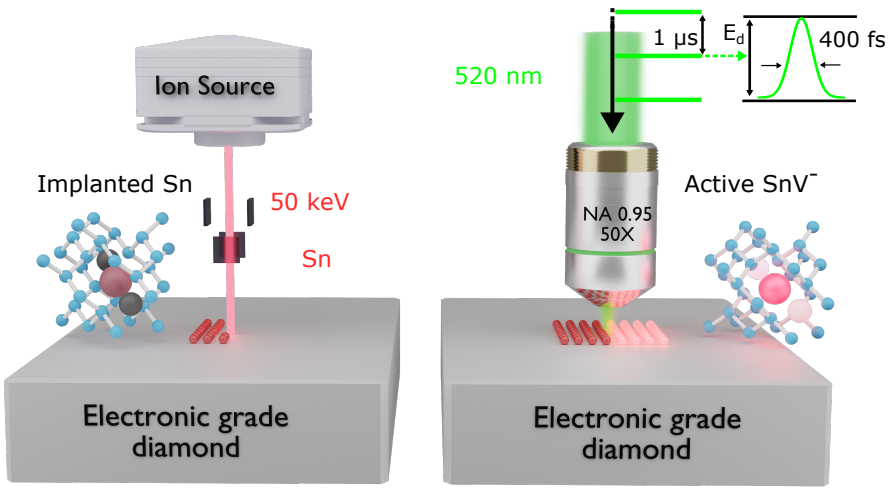


Figure 4.1: Fabrication process schematic illustrating the process of ion implantation followed by femtosecond laser annealing.

Given these constraints, laser annealing emerges as a promising alternative. Its ability to precisely activate and localise single emitters makes it an attractive approach for addressing scalability challenges. By providing control over defect formation and localisation, laser annealing has the potential to enable deterministic creation of high-quality SnV^- centres, thereby advancing the development of scalable quantum devices.

4.2.2 Fabrication process flow

The overall process flow is illustrated in Fig. 4.1. Where initially ions with varrying dosage per implanted site were implanted to different arrays in the sample surface, subsequently different laser treatment is applied to the implanted regions. Details will be covered in the following subssections.

Ion Implantation

The diamond, CVD-grown electronic-grade type IIa diamond substrates with a nitrogen concentration of less than 1 ppb, substrates were implanted using the Platform for Nanoscale Advanced Materials Engineering (P-NAME, University of Manchester, UK [63]), which has a maximum anode voltage of 25 kV. The isotopic mass resolution of the ion implantation system enables the selection of the

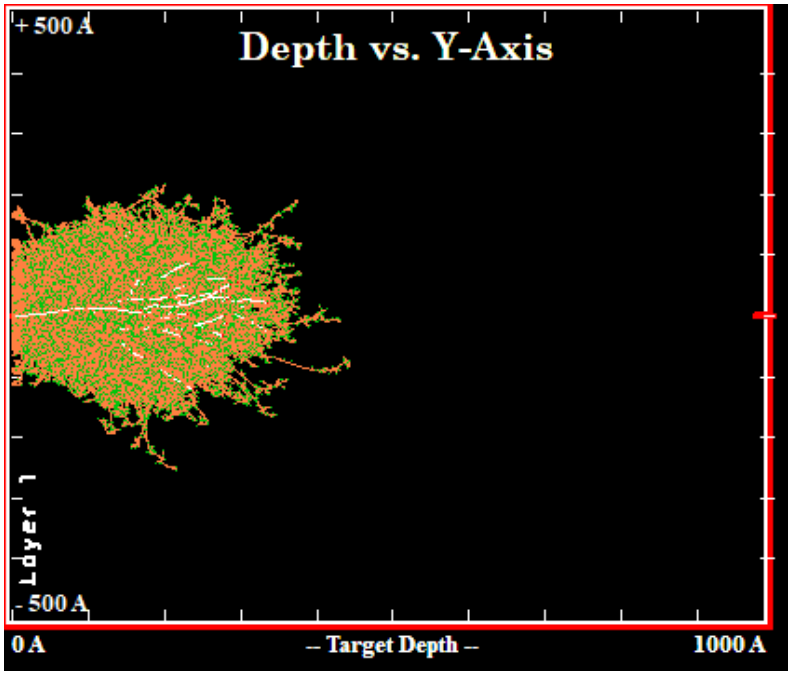


Figure 4.2: Reproduced from source [63] with permission. SRIM simulation of 50 keV Sn ion implantation into diamond (C, 3.5 g/cm^3) with a 3° offset angle using SRIM. The plot illustrates the depth (X-axis) vs. lateral Y-axis distribution of ion trajectories. The ions were implanted with a slight tilt to replicate the P-NAME system's setup. The spread of the ion trajectories within the diamond substrate is evident from the cluster of ions localized primarily around 20 nm in depth and lateral Y positions between -50 nm and +50 nm.

^{117}Sn isotope, with choice of an ionisation state of 2+ providing an energy of 50 keV, leading to an implantation depth of approximately 20 nm (as simulated using Stopping Range of Ions in Matter, SRIM). The alignment markers, designed to be the vertices of a square, were created with 25 keV bismuth ions as illustrated in Fig. 4.3.

The implantations were carried out in a Poissonian mode, with the ion beam current held constant. The pulse width of the electrostatic beam blanking was adjusted to control the average number of ions per site, following Poisson statistics. To investigate the effect of ion dosage, Arrays of 100 μm × 100 μm implantation sites, spaced 0.78 μm apart, were fabricated, with each array implanted with Poisson-distributed means of 1000, 500, 100, 50, 10, 5, and 1 Sn ion(s) per site.

Laser activation process

Traditionally, thermal annealing after ion implantation is used to activate SnV^- centres. As demonstrated in previous work [70–72], laser pulses can also be used to transfer energy into the diamond lattice to facilitate annealing. However, unlike the fabrication of NV^- centres—where annealing enables vacancies to diffuse and bond with naturally occurring substitutional nitrogen atoms—SnV^- centres exhibit a different process. During the implantation of Sn ions into the diamond lattice, the split divacancy structure of the SnV^- centre forms in significant quantities [127] as the implanted Sn atoms induce pairs of vacancies and interstitials. This structure, however, is often in a perturbed configuration due to local radiation damage, such as nearby vacancies and interstitials. The role of thermal annealing in this case is to restore the diamond's optical properties and local structure post-implantation [127], while facilitating the diffusion of interstitials and vacancies away from the SnV^- centres.

As previously discussed in Chapter 3, the laser annealing setup used in this work consisted of the frequency-doubled output from an ytterbium-doped laser (Spectra Physics Spirit), delivering a train of pulses with a duration of 400 fs at a repetition rate of 1 MHz and a central wavelength of 520 nm. The laser beam was expanded and directed onto a Meadowlark liquid crystal spatial light modulator (SLM), which was subsequently imaged in a 4f configuration onto the back aperture of an Olympus 50×, 0.95 NA objective lens. The SLM provided fine control over the position and shape of the focal intensity distribution and was used to correct for any system aberrations.

Two different approaches were carried out for the laser activation process: (a) Preliminary laser treatment and (b) Extended laser annealing. For the preliminary laser treatment, the laser focus was uniformly scanned across ion implantation regions with varying dosages. A 6 µm by 6 µm area within the each array was raster scanned at a speed of 200 nm/s, and a laser pulse energy of 1.7 nJ. Given a diffraction limited laser focal size of 330 nm, this corresponds to an effective dose at each point in the raster scan of 1.6×10^6 pulses.

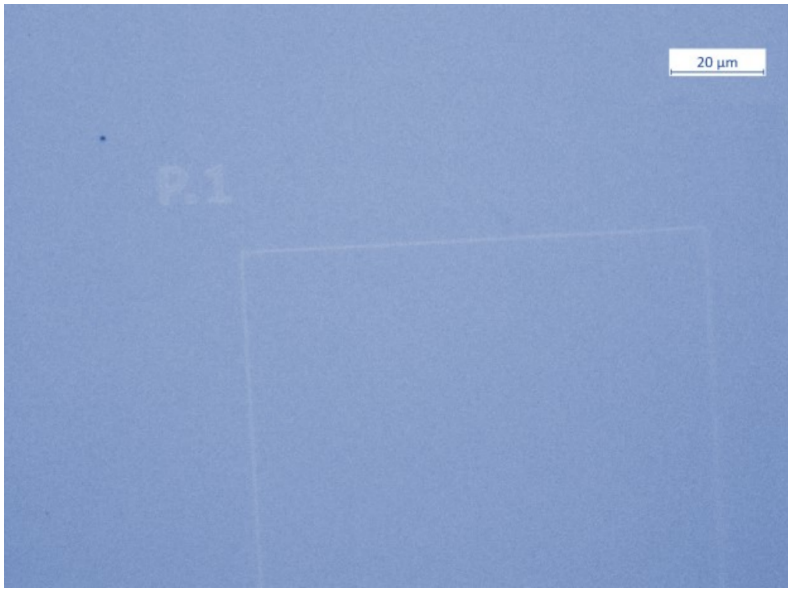


Figure 4.3: Transmission microscope image of array P1 (array with 1000 ions per implanted site). The visible square marks and letter were fabricated with implanted bismuth ions, indicating the position of implanted array.

For the extended laser annealing, the laser pulses irradiated the diamond surface with a fixed focal position. The laser focus was placed approximately at the centre of an implantation region that we intend to study. The duration of the laser exposure was determined based on live PL feedback. The pulse energy used for this process was reduced to 1 nJ and the laser slightly defocused by 1 µm from the diamond surface to avoid ablation during the extended exposure.

4.2.3 Optical characterisation

Post ion implantation

Following implantation, an optical transimision microscope and a custom-bulit scanning confocal microscope were used to characterise the sample prior to any laser treatment.

PL imaging with 1 mW 532 nm excitation with 600 nm long pass filter were applied to all arrays post ion implantation to assess the presence of bright emitters immediately after implantation. As shown in Fig. 4.4, the 2D PL image of the highest dosage array (P1, 1000 ions/site) revealed no visible implanted sites that were brighter than the background, indicating the absence of optically active sites at

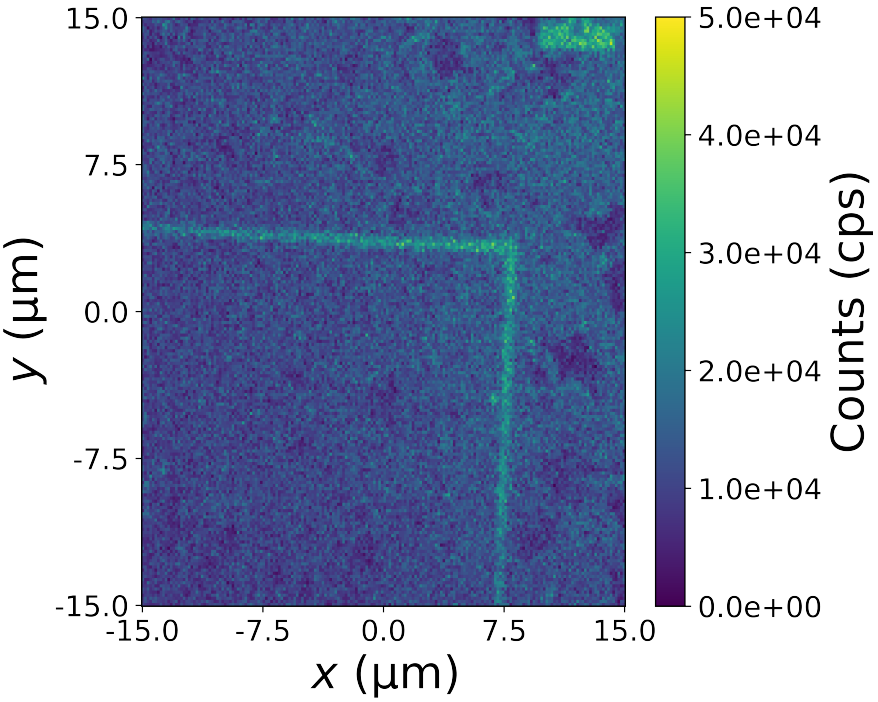


Figure 4.4: 2D PL map with fluoresent alignment marks post ion implantation of array P1 (array with 1000 ions per implanted site). The bright features correspond to implanted bismuth alignment marks.

this stage. The rest of the arrays (P2−P7), implanted with lower dosages, similarly showed no optically active sites, which is expected due to the reduced damage to the diamond lattice at these lower implantation levels.

Post laser activation

To minimise damage to the implanted arrays during initial laser treatment since excessive energy or prolonged laser annealing may locally nano-ablating the diamond surface and to investigate the possibility of locally modifying the post-implantation arrays, a preliminary laser treatment was performed. An additional motivation for this step arose from observations on a sample where GR1 defects were initially in a dark state (i.e., invisible in both the 2D PL map and spectroscopy) immediately after ion implantation (potential explanations are provided in sections later in this chapter). A brief femtosecond laser raster scan was found to locally activate these GR1 defects.

Preliminary laser treatment was performed with 400 fs pulses at a wavelength of 520 nm and a repetition rate of 1 MHz, focused at the surface of the diamond. As a preliminary activation step, the diamond was subjected to a raster scan of the activation laser across 6 µm x 6 µm regions within an implanted array (approximately 60 implantation sites) for each implantation dose, with a dwell time of about 1 second per site, at a pulse energy of 1.7 nJ. PL imaging following this preliminary step reveals fluorescent emission from the implantation sites, as shown in Fig. 4.5 for the same site. The preliminary laser treatment is observed to be well localised within the range of the raster scan, as shown in Fig. 4.5. This indicates that the preliminary laser treatment remains confined to a short range. Spectral analysis of the observed emission will be discussed in the next section. In order to confirm the presence of SnV^- centre related emission in these activated sites, a narrower spectral window is applied to the confocal imaging (615 nm−625 nm, correponds to SnV^- centre's 619nm ZPL). Fig. 4.6 shows that some SnV^- emissions were activated by the preliminary laser treatment in arrays P1−P4 (1000, 500, 100, and 50 ions/site). However, for arrays implanted with lower dosages, no bright features were observed following this treatment.

Spectral analysis (discussed in the next section) suggests that only partial annealing of the diamond lattice occurred with this preliminary laser treatment (see SI of Iwasaki et al [39]). To address this, an extended laser treatment was performed over a 2-hour period, focusing 1 nJ laser pulses on a single point near the activated arrays to ensure no further damage was introduced at the implantation sites−note that this long exposure time reduces to only an effective 3 milliseconds (due to the ultrashort pulse duration) of actual exposure with 7.2 J of energy deposited. This extended laser treatment was found to cause effects delocalised to several micrometres beyond the diffraction-limited laser spot, as illustrated in Fig. 4.7.

Spectral analysis

Fluorescence spectra were taken with the custom built confocal microscope with a collection window from 550 nm−800 nm. Fig. 4.9 shows the example spectrum taken

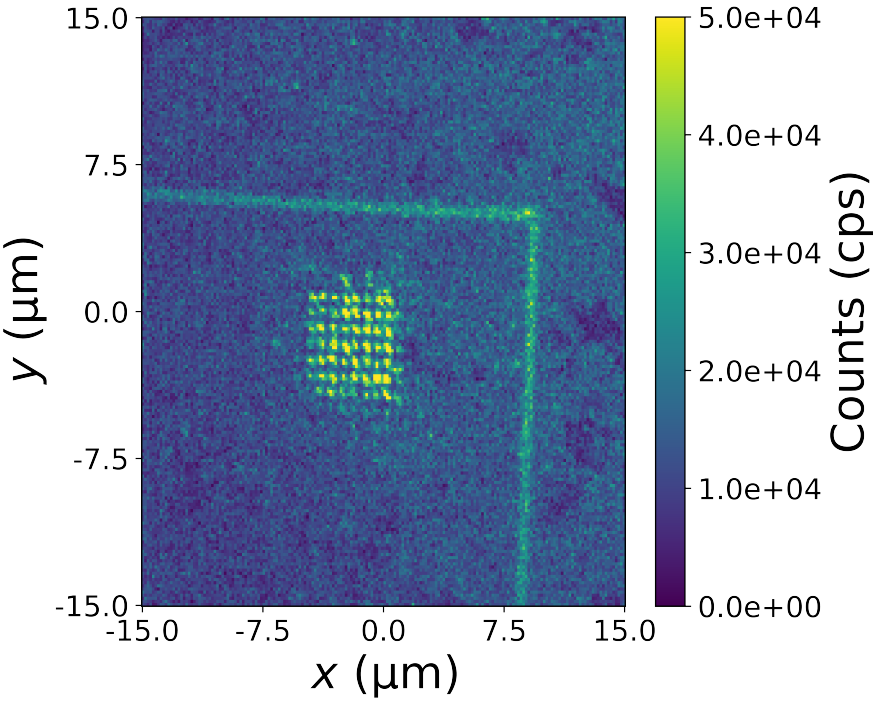


Figure 4.5: 2D PL map post preliminary laser treatment of the array P1. The bright square-shaped array was activated by laser.

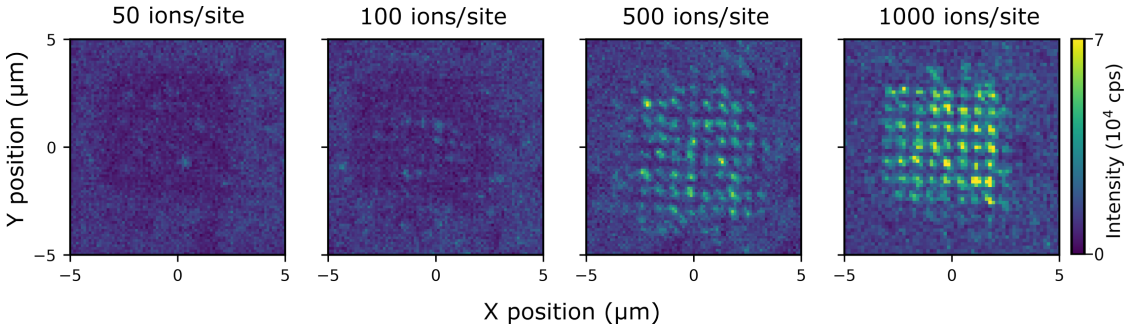


Figure 4.6: 2D PL maps of four regions with different ion implantation dosages after preliminary laser treatment. The spectral collection window is $615 - 625$ nm.

from a same implanted site in array P2 (500 ions/site) upon three different stage: immediately after ion implantation (left), after preliminary laser treatment (middle), and after 2 hours of extended laser annealing (right). Post ion implantation, as evidence of the PL image from before, no emission is presented apart from second order Raman peak (feature shown from 600 nm to 620 nm). Upon preliminary laser treatment, the observed spectrum features resemble the inhomogeneously broadened spectrum of an ensemble of SnV^- centres formed by thermal annealing at around 800 ° C (as illustrated in Fig. 4.8, reproduced with permission from the SI of Iwasaki

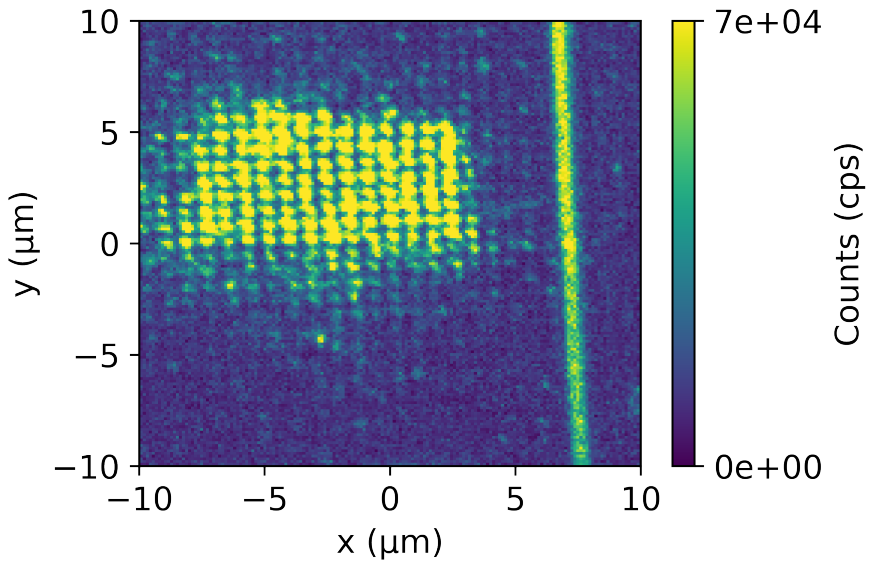


Figure 4.7: 2D PL map post extended laser annealing of the array P1. The bright centre of the square-shaped array was the focal spot of the annealing laser.

et al. [39]). Notably, a narrow peak is present centred at 595 nm (we refer it as Type II Sn) and a broad peak is observed centred at 741 nm which attributes to well-known neutral carbon vacancy (GR1) [130] emission.

These two features are not observed immediately after ion implantation. We propose that the specific spectral characteristics observed after ion implantation, where GR1 defect intensities are negligible or absent, can be explained by the preferential stabilisation of carbon vacancies as ND1 defects (negatively charged carbon vacancies). ND1 defects are not optically active under green excitation and, therefore, remain undetected in the initial spectrum. This behaviour can be attributed to the modification of the diamond surface by a graphene coating, applied to improve secondary electron detection [131]. The graphene coating shifts the Fermi level of the oxygen-terminated diamond surface, inducing band bending and resulting in n-type doping near the surface [132]. As a result, carbon vacancies tend to stabilise as ND1 defects. Subsequent laser treatment alters the charge state of these vacancies, leading to an equilibrium between ND1 and GR1 defects, with GR1 defects becoming optically detectable [130]. An alternative possibility is that, at high implantation doses, the extensive lattice damage creates additional rapid

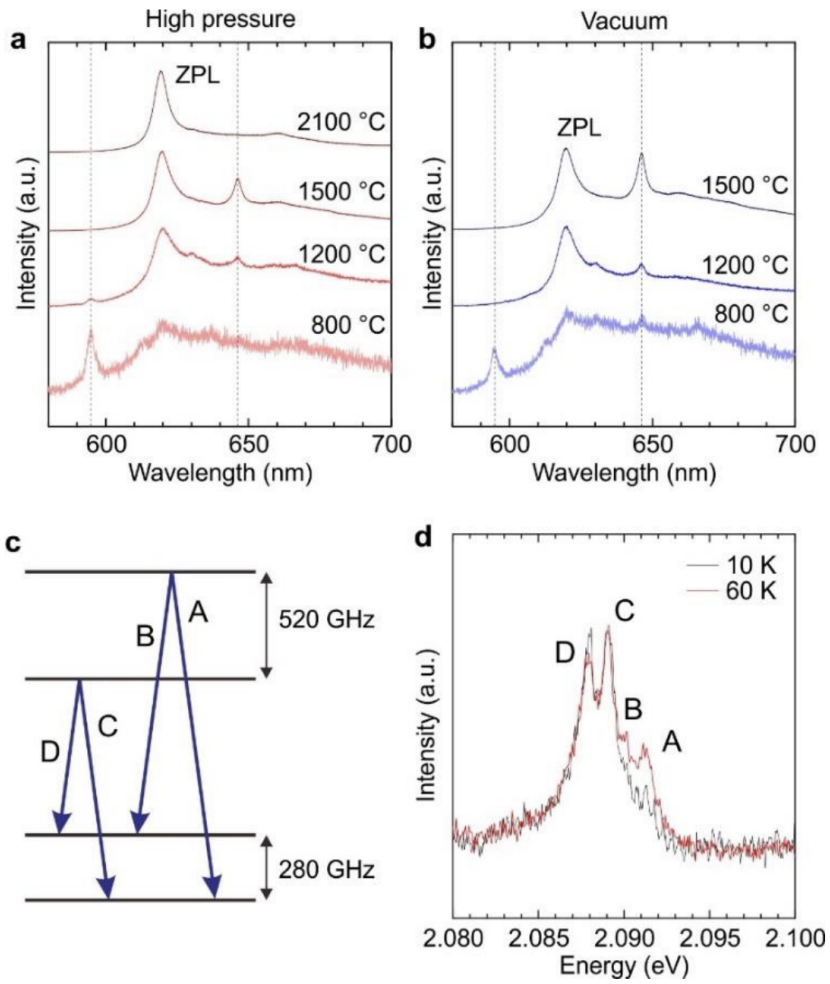


Figure 4.8: Reproduced from Iwasaki et al. [39] with permission. PL spectra from ensemble Type II Sn centres annealed at different temperatures under **a**, high pressure of 7.7 GPa, and **b**, vacuum. **c**, Possible energy levels, and **d**, low-temperature PL spectra of the defect centre.

non-radiative pathways that effectively quench the GR1 emission [133, 134].

In summary, we hypothesise that the preliminary laser treatment primarily serves to locally alter the charge state and restore the optical properties of the diamond, given that the effective interaction time at each site is only 400 ns. One possible explanation for the activation of the Type II Sn defect is that the laser treatment restores the emitter's optical properties. This is because the Type II Sn defect may initially exist in a quenched (non-radiative) state due to lattice distortion introduced during ion implantation. This reasoning also explains why GR1 defects are not observed immediately after implantation. To further confirm

this hypothesis, absorption spectroscopy could be applied to detect ND1 and GR1 defects post-ion implantation. Another contributing factor could be that ion implantation results in at least two carbon interstitials around the SnV^- centres due to the ion implantation nature. In this case, the preliminary laser treatment may remove the more weakly bound interstitials, allowing partial activation of the emitters. The fluorescence spectra shown in Fig. 4.9 support these hypotheses. This figure illustrates the spectra recorded at three distinct stages—immediately after ion implantation, following preliminary laser treatment, and after 2 hours of extended laser annealing—for an implanted array with a dosage of 50 ions/site. Post-implantation, the spectrum displays a broad background with weak or absent defect-related features, consistent with the stabilisation of carbon vacancies as ND1 defects. After preliminary laser treatment, prominent spectral peaks emerge, corresponding to GR1 and Type II Sn defects, suggesting partial activation of these emitters by altering the charge state and mitigating quenching effects. Extended laser annealing further enhances the emission, resulting in significant narrowing and intensification of the fluorescence peaks, particularly around the SnV^- ZPL at 619 nm. This improvement supports the idea that extended laser treatment reduces lattice distortion and facilitates the complete activation of the SnV^- centres.

Extended laser treatment was also observed to produce delocalised effects, reaching several micrometres beyond the diffraction-limited laser spot, and resulted in significant narrowing and strengthening of the fluorescence peaks. Fig. 4.11a, b, and c show the relationship between implantation dose and PL intensities after extended laser annealing, summed across the treated array sites, for spectral windows corresponding to Type II Sn, SnV^-, and GR1 defects, as indicated in Fig. 4.10. As expected, increasing the implantation dose leads to higher PL intensities across all three spectral windows. Interestingly, only the GR1 fluorescence intensity increases linearly with implantation dose (slope 0.89 ± 0.08). In contrast, the fluorescence intensities from Type II Sn (slope 0.31 ± 0.1) and SnV^- (slope 0.61 ± 0.05) defects exhibit sub-linear behaviour, suggesting that higher implantation doses result in

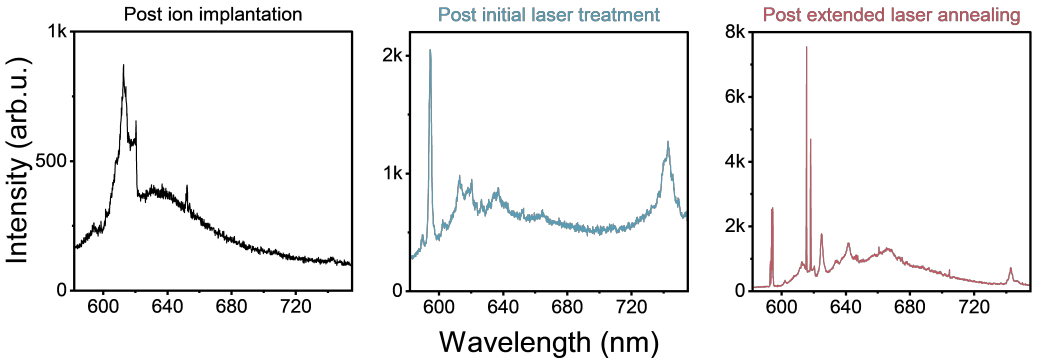


Figure 4.9: Fluorescence specturm of an array with implantation dosage of 50 ions/site, taken at cryogenic temperature (4.2 K) from a same implanted site taken immediately after ion implantation, preliminary laser treatment and 2hr extended laser annealing. The band between 610 nm and 619 nm is the second-order Raman of the diamond lattice under 532 nm excitation.

reduced fluorescence quantum yields post-activation or that a broader variety of defect structures is formed at higher doses.

Apart from the three aforementioned emissions, additional Sn-related defect centres were observed. In particular, arrays implanted with a dosage of 5 ions/site yielded two prominent types of emitters, as shown in Fig. 4.12. These emitters exhibit ZPLs centred at 663 nm and 647 nm. Both defect types display sharp ZPLs at room temperature, which narrow further under cryogenic conditions. Aside from the red shift in ZPL, their spectral features closely resemble those of typical SnV^- centres. Interestingly, the 647 nm emitter type had been previously reported as being insensitive to external electric fields, indicating the absence of any charge [135]. However, its ZPL position does not match that of the neutral SnV^0 centre, which has a ZPL at 683 nm [44]. This suggests that the 595 nm emitter, referred to as Type II Sn, is not a SnV centre of any known charge state, but rather a distinct type of emitter arising from a different defect structure.

4.3 Effect of Pulse energy and annealing time

To gain deeper insight into the laser annealing process, we investigated the effects of laser pulse energy and annealing time on the activation of implanted emitters. Fig. 4.13 shows a series of PL maps for different sites within a region implanted

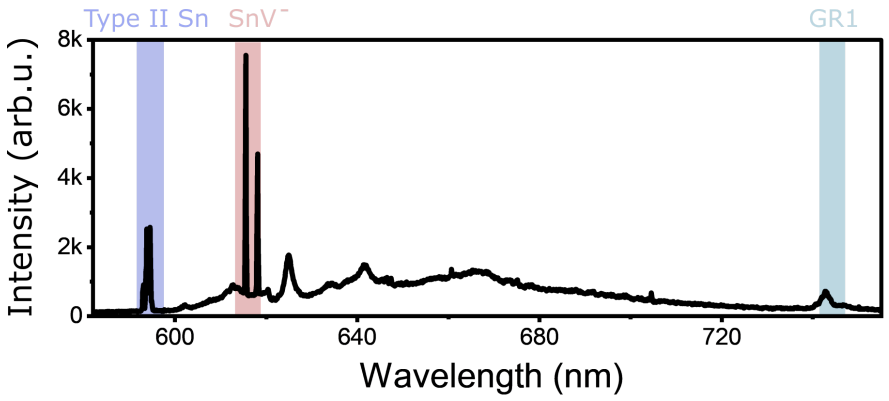


Figure 4.10: Fluorescence specturm taken at cryogenic temperature post−2hr extended laser annealing of an array with implantation dosage of 50 ions/site,. This spectrum highlights three distinct emission contributions: Type II Sn related (indicated in blue), SnV^- related (indicated in red), and GR1 related (indicated in cyan).

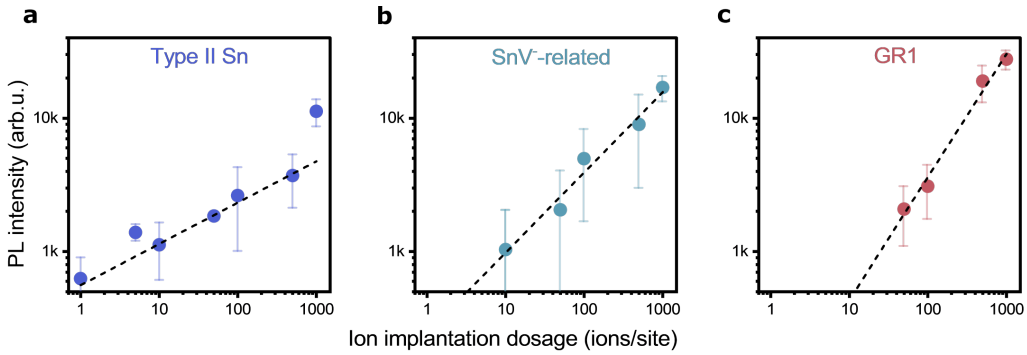


Figure 4.11: Spectrally integrated emission intensity (as ranges shown in Fig. 4.10) of Type II Sn−related, SnV^-−related, and GR1−related defects, respectively, as a function of implantation dosage following the extended laser annealing, spectrum were at 4.2 K. Error bars indicate one standard error. Dashed lines are linear fits to each data set on the double logarithmic scale with slopes 0.31 ± 0.1, 0.61 ± 0.05, and 0.89 ± 0.08, respectively.

with 1000 ions per site, recorded before and after 1 minute of laser annealing at varying pulse energies ranging from 0.93 nJ to 1.23 nJ. The laser was focused on the red circled points, and after each annealing step, it was moved to a untreated region. As expected, higher pulse energy under the same annealing duration resulted in a larger affected region.

Fig. 4.14 presents PL maps of the same site within a region implanted with 1000 ions per site, subjected to 30 minutes of laser annealing at a pulse energy of 1.05 nJ. The laser remained focused on the red circled point throughout the process. The annealing was divided into six distinct intervals, with PL images

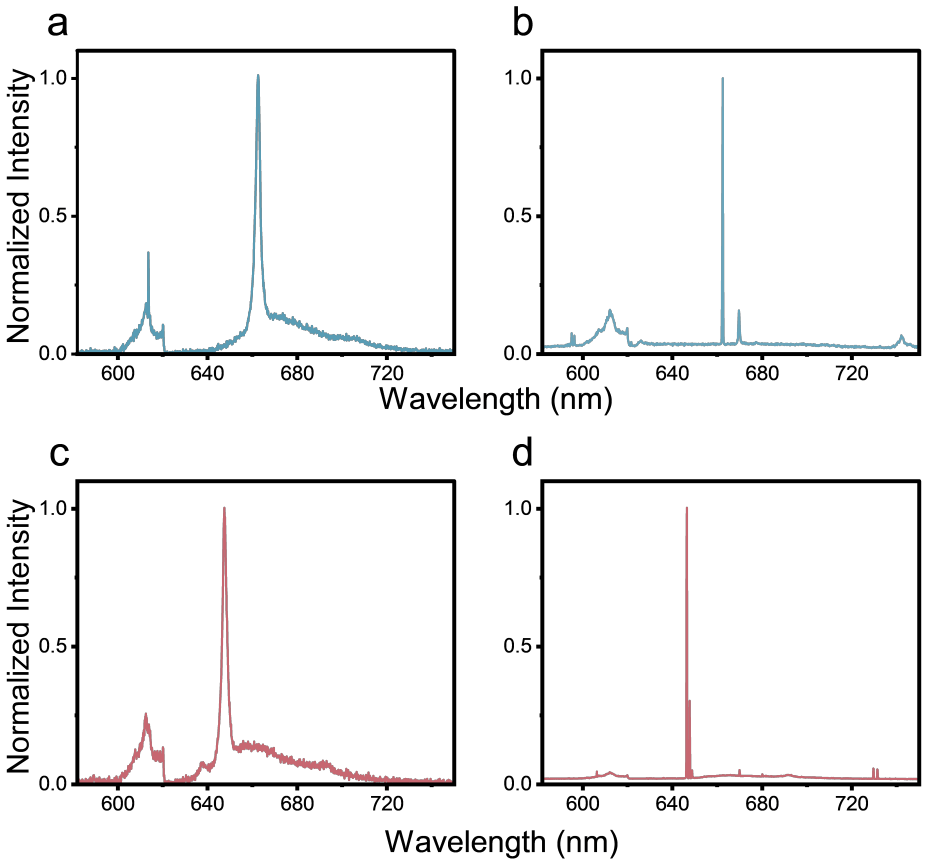


Figure 4.12: Example spectra of other Sn−related defect centres activated in arrays with 5 ions per implantation site. **a** and **b** shows the room temperature and cryogenic temperature spectrum of a typical emission with ZPL centred at 663 nm respectively. **c** and **d** shows that for the 647 nm emission.

captured after each interval under identical experimental conditions. To better visualise the radial spread of the activation, the colour scale in Fig. 4.14 is set to the same upper limit across all plots, which causes the PL intensity at the centre of the laser focus to appear saturated.

To quantify the spread and intensity of the activated area, a gaussian filter was applied to aid fitting and a Gaussian function was fitted to the PL maps (as illustrated in Fig. 4.15 for an example smoothening and fitting), treating PL intensity (here we are collecting emissions from both Sn-related defects and GR1s, and the figures displayed a min and max of brightness for better visibility, no capping was applied for any analyses) as the Gaussian height and analysing the spread across the x and y axes. The full width at half maximum (FWHM) and

Gaussian peak height were extracted and plotted against annealing time, as shown in Fig. 4.16. The FWHM along the x and y axes was determined by:

$$\mathrm{FWHM}_{x/y} = 2\sqrt{2\ln 2} \times \sigma_{x/y} \tag{4.1}$$

An average FWHM was calculated, and the peak height was taken as I.

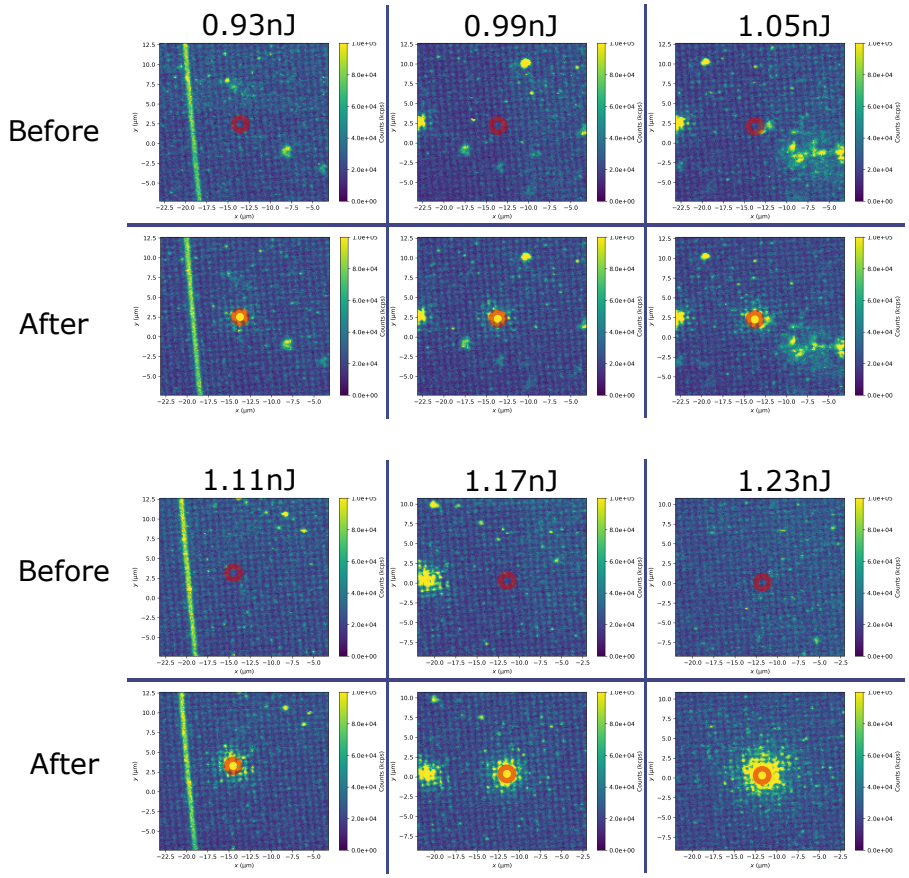


Figure 4.13: Sets of 2D PL images are presented for a region implanted with 1000 ions per site, captured before and after 1 min of laser annealing. The images progress from left to right and top to bottom, corresponding to increasing pulse energy. The laser was focused on the red circled points in the PL maps, with a slight defocus of 1 μm from the surface.

The effects of pulse energy were also investigated, with the annealing time held constant while varying the pulse energy of the annealing laser. This study was conducted in the region implanted with 1000 ions per site, where the laser was focused on the red circled points and annealed for 1 minute. Pulse energies ranging from 0.93 nJ to 1.23 nJ were applied. The PL maps were processed as

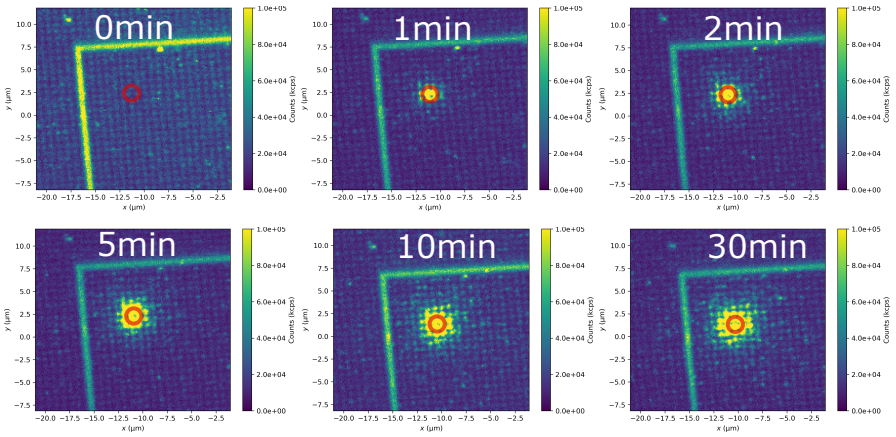


Figure 4.14: Sets of 2D PL images are shown for a region implanted with 1000 ions per site, taken at the same locations after varying annealing times (annotated in white within each PL map). The laser was focused on the red circled points in the PL maps, with a slight defocus of 1 μm from the surface.

described previously, and the variations in the spread and intensity of the activated region are presented in in Fig. 4.16.

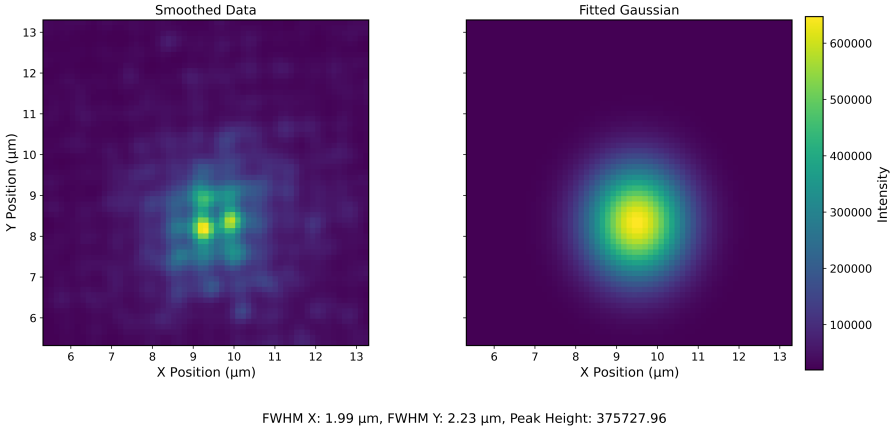


Figure 4.15: Example showing how the PL data set is treated: An Gaussian filter is applied to smoothen the data followed by a Gaussian beam fitting. The fitted parameters are extracted.

Both the peak height and spread of the activated region increase with annealing time up to 10 minutes, after which they plateau. With a laser spot size of approximately 0.4 μm, the activated region can extend up to 5 μm, which is comparable to the exciton diffusion length in high-purity diamond at 298 K [136]. This observation supports our hypothesis that the extended laser annealing process

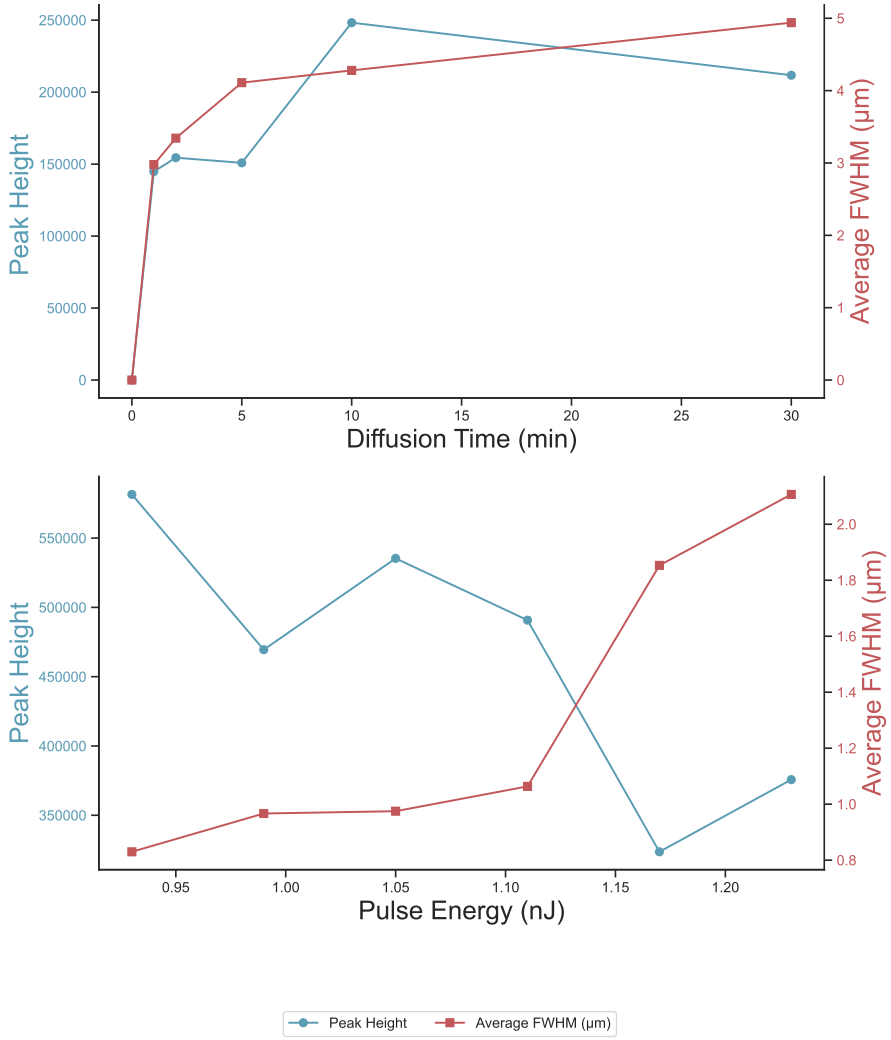


Figure 4.16: The top graph shows the relationship between diffusion time and both the Average FWHM of the activated area and the peak height of the fitted Gaussian's PL intensities for a region implanted with 1000 ions per site. The bottom graph displays the variation of the same parameters with respect to pulse energy.

is exciton-mediated, where femtosecond laser pulses generate hot carriers that relax to form excitons [83]. These excitons subsequently deliver energy to the lattice, facilitating the annealing process.

Increasing the pulse energy of the annealing laser has a minimal effect on the peak height, which is primarily constrained by the ion implantation dosage. However, higher pulse energy results in a slight increase in the spread of the activated region. Notably, at a pulse energy of 1.23 nJ, there is a significant drop in the fitted peak height and a marked increase in the fitted geometric mean. This behaviour is

attributed to graphitisation of the diamond [70], where the diamond lattice locally melts and recrystallises, reducing the number of vacancies and interstitials, leading to the observed changes in the fitted data.

4.3.1 Activation of single SnV^- centre

Correlation in Fig. 4.11 enables us to deduce the optimal dosage for activating a single SnV^- centre. Specifically, the target dosage is identified at the threshold where the GR1 PL signal is barely detectable, indicating minimal creation of GR1 defects and, hence, minimal damage to the lattice that might affect the quality of any activated SnV^- centre. Based on our experiments, the optimal implantation dosage for forming SnV^- centres was found to be 10 ions per site, as shown in Fig. 4.17. At this dosage, GR1 emission was no longer visible, while the implantation dosage remained high enough to facilitate the formation of SnV^- centres and it is not too high so that it increases the likelihood of creating single emitters.

Fig. 4.18a shows a room temperature PL spectrum (processed to remove Raman scattering) from one of the array (10 ions/implanty site) sites, with the associated PL image in the inset. The spectrum reveals a remarkably clean ZPL at 619 nm and its accompanying PSB extending to 750 nm [39], characteristic of a single SnV^- colour centre. At cryogenic temperature (4.2 K) the ZPL splits into two narrow peaks, characteristic of the γ and δ optical transitions of the ZPL (see level diagram in Fig. 4.18b) [47]. The splitting between the γ and δ lines is 1.7 THz, suggesting that the SnV^- centre is located in a highly strained environment [137].

To confirm that the activated SnV^- centre corresponds to a single emitter, we performed a Hanbury Brown-Twiss intensity auto-correlation measurement [138]. Fig. 4.18c shows the background-corrected [139] second-order autocorrelation function $g^{(2)}(\delta t)$, revealing a dip at $\delta t = 0$ with a $g^{(2)}(0)$ value of 0.1 ± 0.13, which is characteristic of a single quantum light emitter. Fitting of an analytic function for a three-level system (shown in Eqn 4.2, and details can be found in Chapter 3) [39] to the $g^{(2)}(\delta t)$ histogram reveals an excited state lifetime of $\sim 1.4 \pm 1.5$ ns.

$$g^{(2)}(\delta t) = 1 - (1+\alpha)e^{-\frac{|\delta t|}{\tau_1}} + \alpha e^{-\frac{|\delta t|}{\tau_2}} \tag{4.2}$$

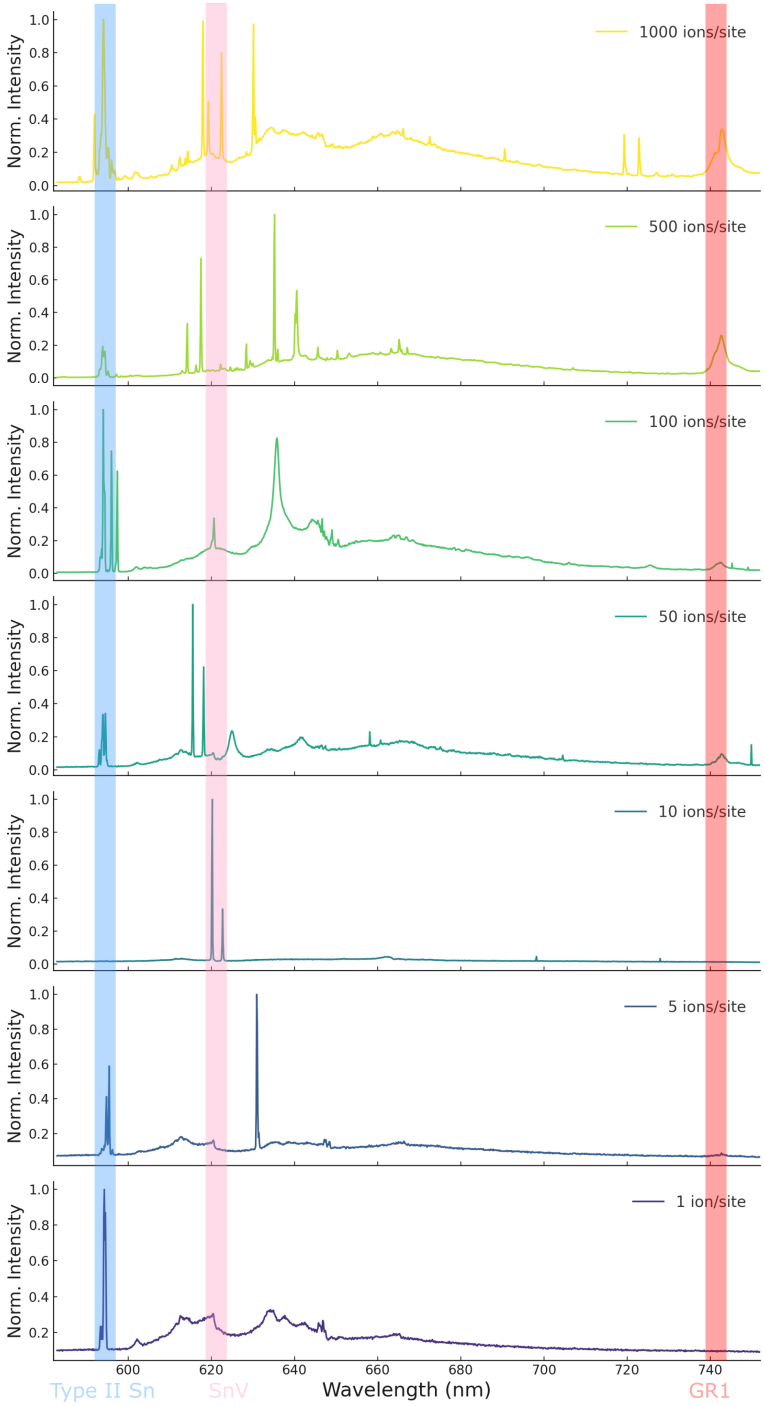


Figure 4.17: Normalised PL spectra of implanted site after the same extended laser annealing in arrays with differente implantation dosage, measured at 4.2 K. The spectra are arranged in descending order of implantation dose, from 1000 ions/site at the top to 1 ion/site at the bottom. The regions highlighted in blue, pink, and red denote the emission from Type II Sn, SnV^-, and GR1 respectively.

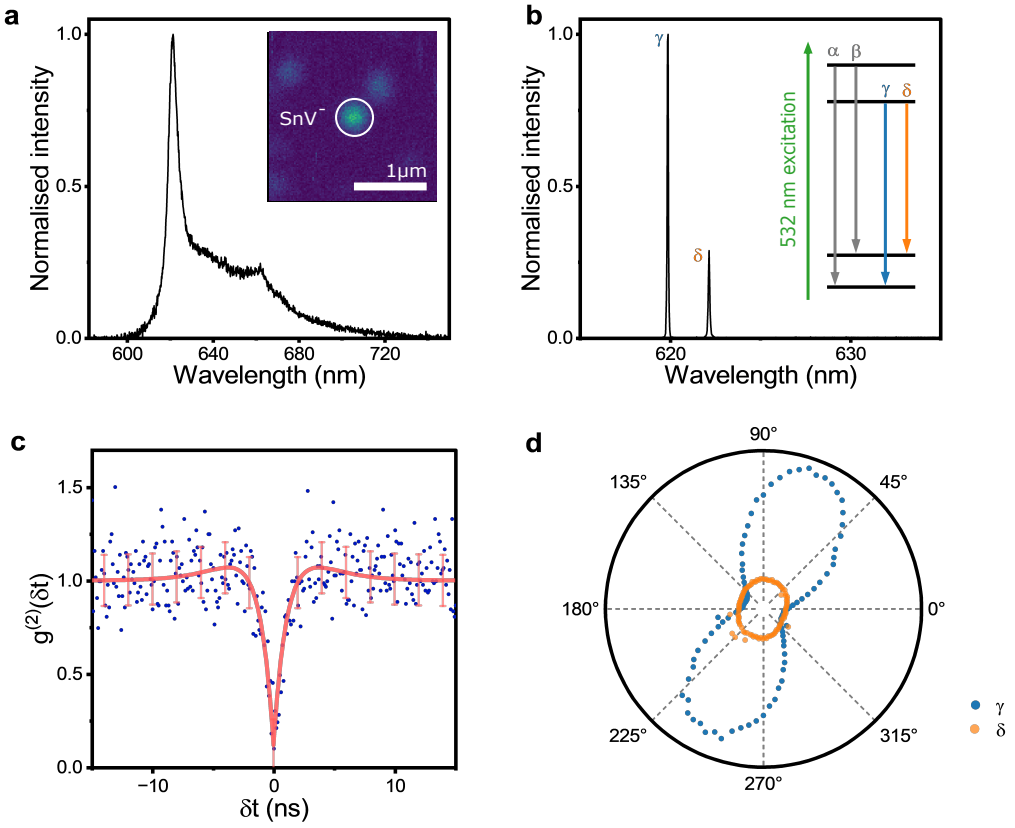


Figure 4.18: Characterization of a typical laser-activated single SnV^- centre.**a**, Room-temperature photoluminescence (PL) spectrum from a single site in the array implanted with 10 ions per site, exhibiting the characteristic SnV^- center emission. The inset shows a 2D PL image of the site and its nearby surroundings. **b**, Spectrum at 4.2 K of the same site, showing the γ and δ optical transitions typical of an SnV^- centre. **c**, Histogram showing the background-corrected second-order auto-correlation measurement of PL emitted from the same site as in panels a and b. The red curve corresponds to a three-level model $g^{(2)}(\delta t) = 1-(1+\alpha)e^{-\frac{|\delta t|}{\tau_1}}+\alpha e^{-\frac{|\delta t|}{\tau_2}}$, with fitted values $\tau_1 = 1.4 \pm 1.5$ ns and $\tau_2 = 9.7$ ns. The red shaded region represents one standard error. **d**, Polarisation dependence of the SnV^- emission. Intensity of the γ (blue) and δ (orange) transitions as a function of analysing polariser angle, normalised to the maximum value of each transition.

This value is shorter than the $5-7$ ns lifetimes reported previously for SnV^- [45, 47] which may be attributable to its close proximity to the diamond surface (20 nm depth) leading to rapid non-radiative decay [45], delays of emission [140], or the effect of high power off-resonant excitation [141, 142]. Fluorescence polarimetry, covered in detials in Chapter 3, reveals a high degree of linear polarisation of the fluorescence from the γ transition (Fig. 4.18d), also in line with previous reports [143, 144].

4.3.2 Local strain study of SnV^- centres

Fig. 4.19 presents example spectra from various sites activated within arrays implanted with 10 ions per site. Each recorded spectrum reveals variations in the ZPL positions and the degree of peak splitting, reflecting the distinct local environments surrounding the SnV^- centres. The observed γ and δ optical transitions splitting provides insights into the local strain around each SnV^- centre: sites with larger splittings likely experience greater local strain, whereas those with minimal splitting may exist in relatively strain-free conditions.

To quantify the local strain experienced by individual SnV^- centre, we analyzed the splitting between the γ and δ optical transitions. Take the SnV^- centre studied in Fig. 4.18 as an example. The energy splitting ΔE can be calculated from the observed frequency difference ν:

$$\Delta E = h\nu, \tag{4.3}$$

where $h = 4.136 \times 10^{-15}$ eV s for the Planck's constant. Given a measured splitting of $\nu = 1.7$ THz, the energy difference becomes:

$$\Delta E = (4.136 \times 10^{-15}\ \text{eV s}) \times (1.7 \times 10^{12}\ \text{Hz}) = 7.03 \times 10^{-3}\ \text{eV}. \tag{4.4}$$

Since spectrum taken at 4.2 K, higher-order effects such as temperature effect are neglected. The total observed splitting is a combination of the intrinsic splitting due to spin-orbit coupling and the dynamic Jahn-Teller effect [145], $\Delta E_{\text{intrinsic}}$, and the strain-induced splitting, ΔE_{strain}:

$$\Delta E_{\text{total}} = \Delta E_{\text{intrinsic}} + \Delta E_{\text{strain}}. \tag{4.5}$$

From the literature, the intrinsic splitting for unstrained SnV^- centres is approximately 0.85 THz [47], corresponding to an energy of:

$$\begin{aligned} \Delta E_{\text{intrinsic}} &= h\nu_{\text{intrinsic}} \\ &= (4.136 \times 10^{-15}\ \text{eV s}) \times (0.85 \times 10^{12}\ \text{Hz}) \\ &= 3.515 \times 10^{-3}\ \text{eV}. \end{aligned} \tag{4.6}$$

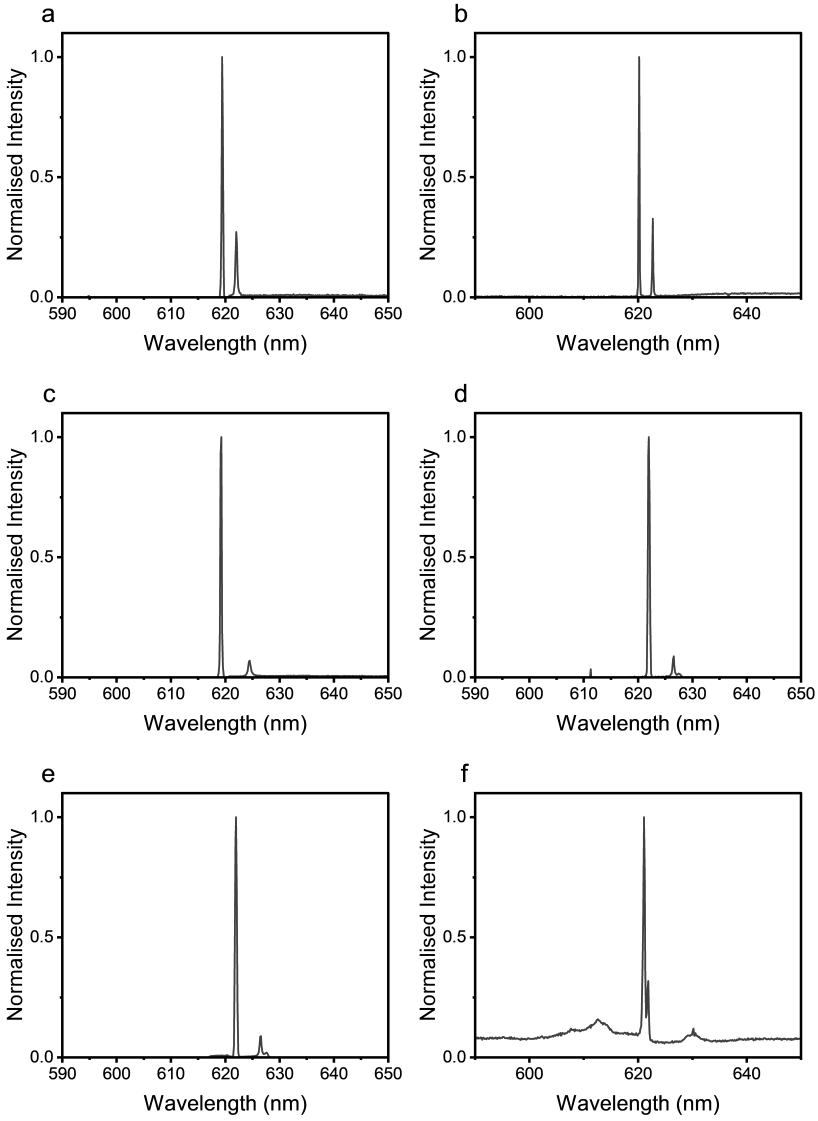


Figure 4.19: Example spectra of activated SnV^- centres in arrays with 10 ions per implantation site from different sample. Each panel displays a different activated site, illustrating variations in ZPL positions and the γ and δ transitions splitting. These differences suggest that each site is influenced by unique local conditions, with variations in splitting primarily reflecting the local strain environment of the SnV^- centres.

The strain-induced splitting is therefore:

$$\Delta E_{\text{strain}} = \Delta E_{\text{total}} - \Delta E_{\text{intrinsic}} = (7.030 - 3.515) \times 10^{-3} \text{ eV} = 3.515 \times 10^{-3} \text{ eV}. \quad (4.7)$$

The effective local strain ϵ_{eff} (a linear combination of the relevant strain tensor components, and the P here stands for peta, 10^{15}) experienced by the SnV^- centre can be calculated using the deformation potential d_e assuming relationship between strain and energy splitting is linear (The factor of 2 arises from the total splitting is twice the shift of a single level):

$$\Delta E_{\text{strain}} = 2 d_e \epsilon_{\text{eff}} \quad \Longrightarrow \quad \epsilon_{\text{eff}} = \frac{\Delta E_{\text{strain}}}{2 d_e}. \quad (4.8)$$

The deformation potential used is estimated from literature on SiV^- [137] ground state (GS) splitting, extracted from the slope of orbital spliting plot:

$$\begin{aligned} E_{gx} &= 2.2 \text{ PHz/strain} \\ E_{gy} &= 2.2 \text{ PHz/strain} \\ E_{gz} &= 1.2 \text{ PHz/strain} \end{aligned} \quad (4.9)$$

assuming isotopic strain and orthogonality (this is normally valid for small strain environment), the average deformation potential can be calcualted to be:

$$E_{avg}(\text{SiV}) = \frac{E_{gx} + E_{gy} + E_{gz}}{3} \approx 1.86 \text{ PHz/strain} \quad (4.10)$$

The SnV^- deformation potential is therefore estimated based on the ratio of bond lengths, which better reflects the local strain coupling to the defect:

$$\begin{aligned} E(\text{SnV}) &\approx E_{avg}(\text{SiV}) \cdot \frac{\text{C-Sn bond length}}{\text{C-Si bond length}} \cdot h \\ &= 1.86 \text{ PHz/strain} \cdot \frac{2.05 \text{ Å}}{1.88 \text{ Å}} \cdot h \\ &\approx 8.39 \text{ eV/strain} \end{aligned} \quad (4.11)$$

Using a estimated value of deformation potential of $d_e = 8.39$ eV, the effective local strain is calculated:

$$\epsilon_{\text{eff}} = \frac{3.515 \times 10^{-3} \text{ eV}}{2 \times 8.39 \text{ eV}} = 2.01 \times 10^{-4}. \quad (4.12)$$

This corresponds to an effective strain of approximately 0.0201%, reflects the deformation of the diamond lattice surrounding the SnV^- centre. This deformation alters the positions of the carbon atoms neighboring the defect, leading to changes in the electronic environment experienced by the SnV^- centre. Notably that this strain assumes an ideal diamond lattice apart from the local strain, neglecting other defects or impurities that might influence the energy levels. Largest splitting between γ and δ optical transitions observed is 7 THz (shown in Fig. 4.19f), which according to the previous calculations, gives a local strain of 0.152%. This SnV^- centre is from another sample with same dosage but higher implantation energy (290 keV) that grants deeper depth (90 nm) of the implanted ions, consistent with the increased depth.

4.4 Type II Sn centre in diamond

4.4.1 Introduction

During the laser activation of SnV^- centres, another type of defect is observed to be activated, exhibiting a ZPL at 595 nm. These defect appear exclusively at Sn-implanted sites and display single-photon emission characteristics, indicating that they are Sn-related defects. This Sn-related defect complex, with a ZPL in the 595 nm spectral region—referred to as 'Type II Sn'—has been reported previously [39, 127, 128] as a product of low-temperature annealed SnV^- centres. However, a comprehensive study on Type II Sn defects has yet to be conducted. In this work, we demonstrate the creation of single Type II Sn defects and perform a comparative analysis with single SnV^- colour centres.

Regarding the formation of the 595 nm emission peak and SnV^- centres, previous research has shown that approximately 40% of implanted Sn ions settle into a split-vacancy configuration [127], resulting in two carbon interstitial (C_i) defects in close proximity. An alternate hypothesis is that the resulting SnV-2C_i complex is optically inactive, but that the initial laser treatment mobilises one of the C_i defects, leaving behind an optically active SnV-C_i complex, which corresponds to the Type II Sn defect with the 595 nm ZPL. Importantly, further extended laser annealing facilitates the mobilization of the remaining C_i, which is more

strongly bound to the SnV defect. This allows the remaining C_i to migrate away, switching on the SnV^- photoluminescence.

Extended laser annealing across multiple arrays with varying implanted ion dosages revealed sharp fluorescence peaks at both 595 nm and 620 nm, corresponding to the formation of small numbers of Type II Sn and SnV^- centres, respectively. Fig. 4.20 illustrates the distribution of Lorentzian-fitted central wavelengths for the dominant spectral features observed at room temperature for activated sites. Interestingly, the Type II Sn centres at 595 nm exhibit a much narrower wavelength distribution, with a standard deviation of 1.10 nm, compared to the SnV^- centres at 620 nm, which have a standard deviation of 4.77 nm. This suggests that the Type II Sn centres are less sensitive to local strain, indicating differences in their defect structures.

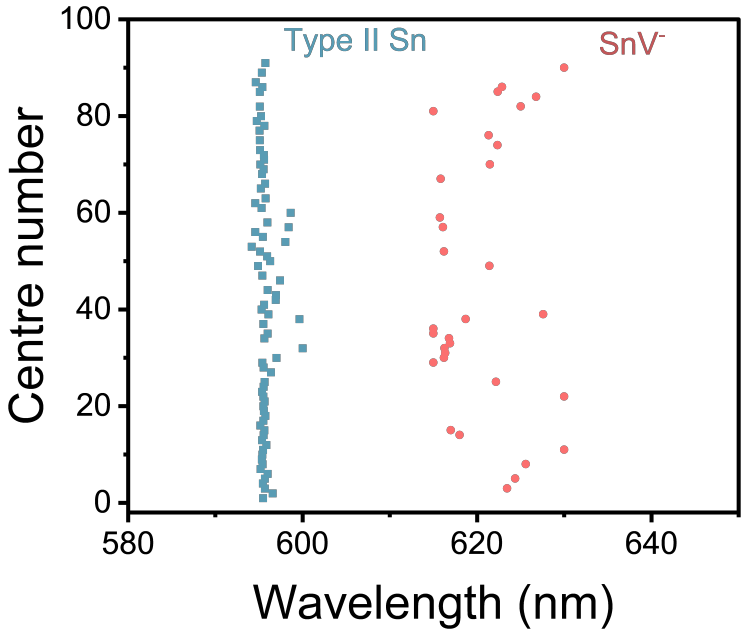


Figure 4.20: Distribution of ZPL fitted with Lorentzian of 90 sites activated by laser annealing. Where the emissions attribute to Type II Sn defects are plotted in blue and those of SnV^- are in red.

4.4.2 Frank Condon study

In order to have a detailed understanding of the Type II Sn centres, spectral analysis both at room temperature (Fig. 4.21a) and cryogenic temperature (Fig. 4.21b) were conducted. Fig. 4.21 showed a typical spectrum of Type II Sn in an array with 10 ions/implanted site. A sharp peak at 595 nm is observed with red-shifted PSB extending up to 720 nm in room temperature. This sharp peak gets narrower and more pronounced when cooled down. This narrowing indicates reduced phonon interactions at lower temperatures, which minimizes broadening and results in a sharper spectral feature, further suggest that the sharp peak observed at 595 nm is the ZPL of the Type II Sn centre.

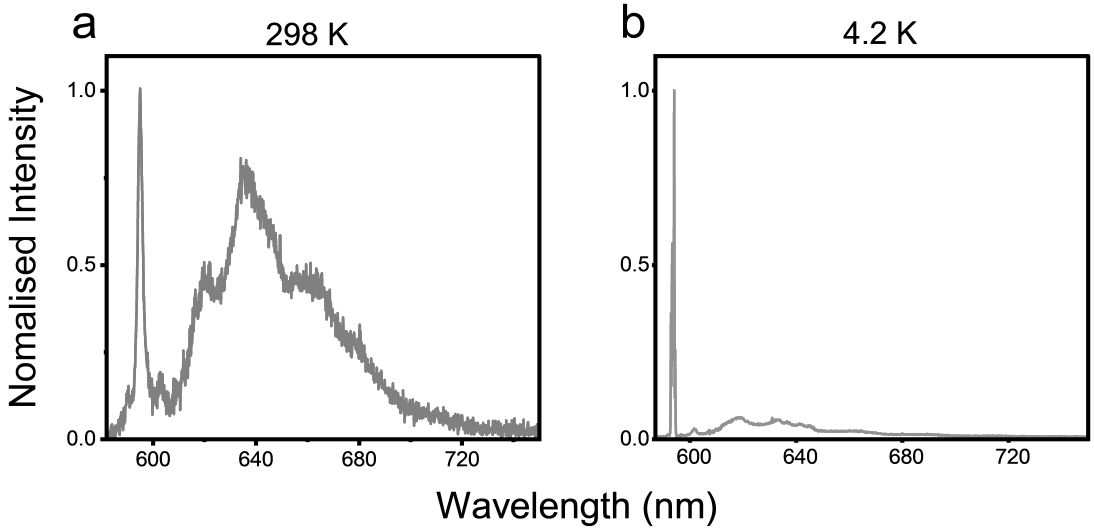


Figure 4.21: Typical emission spectra of the same Type II Sn defect centre site (from 10 ions/site array) at room and cryogenic temperatures. **a**, At 298 K, the spectrum shows a broad emission with a peak around 595 nm with red-shifted PSB extending up to 720 nm. **b**, At 4.2 K, the 595 nm ZPL becomes narrower and sharper, indicating suppressed of the phonon modes.

To model the PL emission spectrum of Type II Sn centres, the Franck-Condon principle [25, 121], described in Chapter 2, was applied. This principle explains the intensity distribution of vibronic transitions, where electronic transitions are accompanied by changes in vibrational energy. Since electronic transitions occur much faster than nuclear motions, the nuclei remain fixed during the transition, this is referred to as the vertical transition.

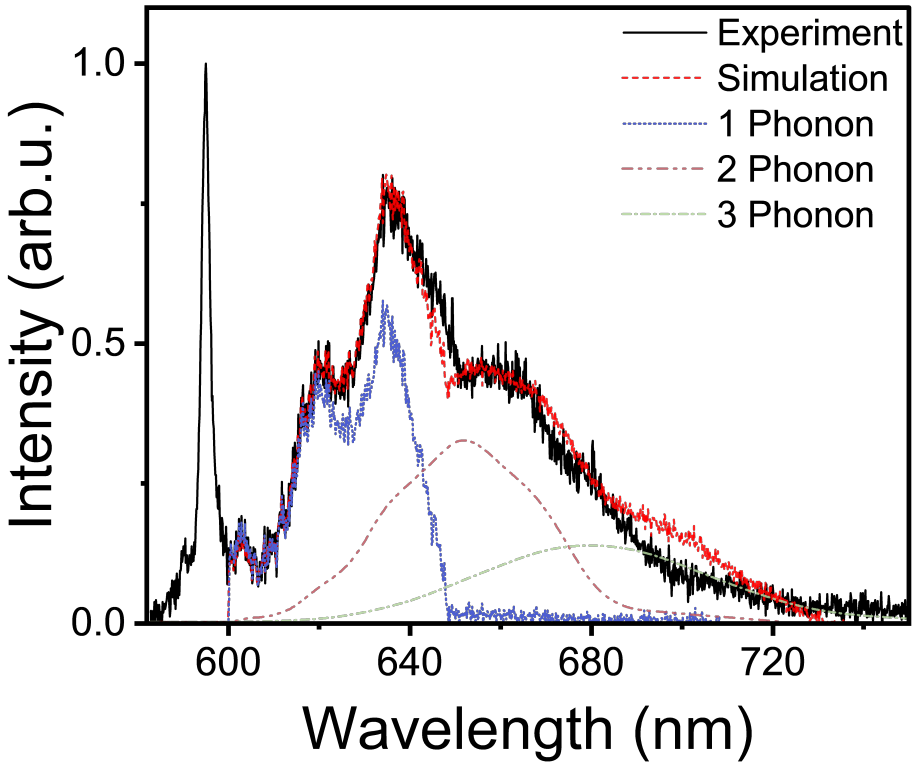


Figure 4.22: Room temperature spectrum of a Type II Sn centre in array with 10 ions/site, with simulated spectra based on single phonon coupling spectra extending to the 165 meV longitudinal optical phonon energy of diamond. The 1−, 2− and 3−phonon spectra are presented, the higher−phonon modes are not displayed due to their insignificant intensity.

Franck-Condon analysis was applied to the spectra of typical Type II Sn centres at both room and cryogenic temperatures. In diamond, the one-phonon range extends from approximately 0 meV (for acoustic phonons near the Γ point) to 165 meV (for optical phonons at the Γ point). The PSB offset from the ZPL by 165 meV matches the optical phonon energy at the Brillouin zone centre [146]. Background-subtracted spectra from 0 to 165 meV were used to represent the 1-phonon spectrum, and higher-order phonon spectra were obtained via self-convolution, as described by Eqn. 2.21. These multi-phonon spectra were then incorporated into Eqn. 2.18 to simulate the PSB.

At room temperature, the ZPL intensity is comparable to that of the PSB. The recorded spectra and Franck-Condon simulated spectra, plotted as functions

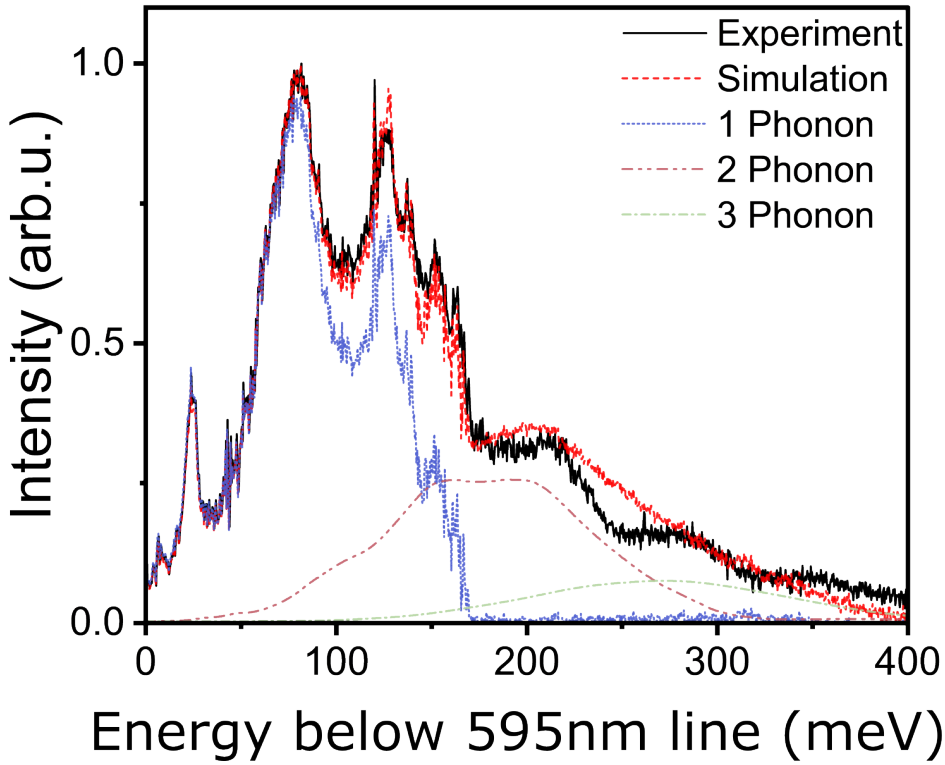


Figure 4.23: Cryogenic temperature spectrum of the same Type II Sn centre, with simulated spectra based on single phonon coupling spectra extending to the 165 meV longitudinal optical phonon energy of diamond. Since the intensity of ZPL is much higher than the PSB, here the spectra is plotted on an energy axis representing the red-shifted energy from the ZPL, with the end of the ZPL set to 0 meV.The 1−, 2− and 3− phonon spectra are presented, the higher−phonon modes are not displayed due to their insignificant intensity.

of wavelength, are shown in Fig. 4.22. Higher-order phonon modes, such as the 2-phonon mode, appear smoother due to the self-convolution of the 1-phonon mode, with a similar effect observed for the 3-phonon mode.

In contrast, spectra acquired at cryogenic temperatures are plotted on an energy axis, with the red-shifted energy from the ZPL set to 0 meV. The simulated PSB closely matches the experimental spectra and yields a Huang–Rhys factor of 1.70. This value is significantly larger than the reported value of 0.57 for SnV^- centres [45], indicating stronger electron–phonon coupling in Type II Sn centres compared to SnV^- centres.

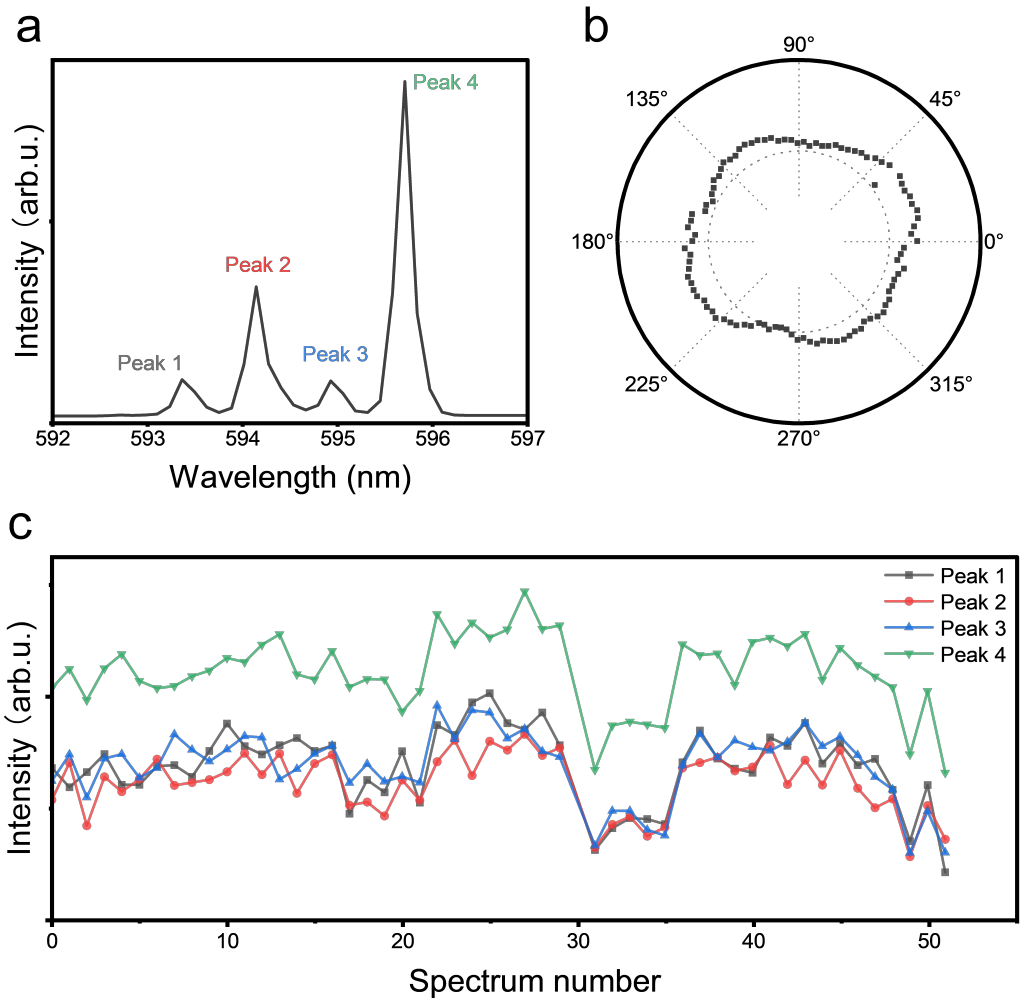


Figure 4.24: Spectral study of a typical single Type II Sn centre. **a**, magnified cryogenic spectrum focusing on the ZPL window, where 4 resolvable peaks are presented. **b**, Polarisation dependence of the Type II Sn ZPL emission measured at 4.2 K, no strong polarisation dependence observed. **c**, dynamic spectra of this Type II Sn centre that shows the correlated intensities fluctuations of each sub−peaks at individual spectrum acquired, with each spectrum of an exposure time of 1 s.

4.4.3 Spectral analysis

Fig. 4.24a presents a magnified spectrum of the previously studied Type II Sn center, revealing 4 resolvable peaks.

To confirm that the observed Type II Sn emission is from a single emitter, a HBT measurement was performed, as shown in Fig. 4.25. The second-order autocorrelation function yielded $g^{(2)}(0) = 0.3 \pm 0.12$, confirming single-photon

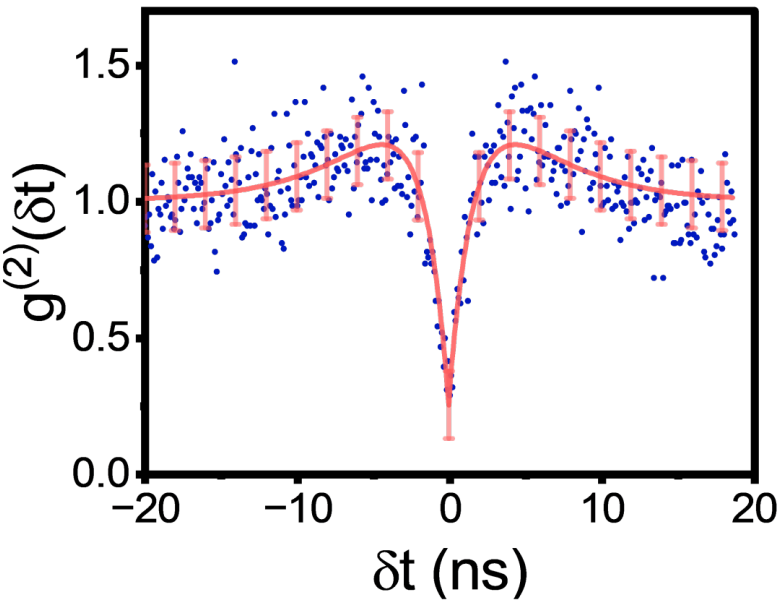


Figure 4.25: Second-order autocorrelation measurement with background correction and corresponding four-level fit for the single Type II Sn emitter shown in Fig. 4.21 and Fig. 4.24. A clear dip is observed with $g^{(2)}(0) = 0.3 \pm 0.12$. The red shaded region represents one sigma error.

emission. A fitted lifetime of 2.2 ± 0.3 ns was obtained. Notably, unlike the SnV^- centre, a four-level system provided a better fit for Type II Sn emission, this implies that a single Type II Sn centre might possess an extra metastable, giving two radiative pathways within one emitter. The additional level acts as a shelving state, lowering the saturation power and slightly extending the excited-state lifetime. The autocorrelation measurements rules out the possibility that the multiple peaks were due to the presence of multiple emitters on all the presented spectra and polarisation data. However, it is theoretically possible for a low $g^{(2)}(0)$ value to arise from multiple emitters with differing relative intensities.

To investigate the polarisation properties of the light emitted from these colour centres, we applied polarisation measurements as mentioned in Chapter 3. The PL emission intensity was determined by integrating the spectrum over the ZPL wavelength range. For Type II Sn defects, this range is 593−596 nm, and no polarisation dependence was observed. To assess the stability of each peak over time, we collected dynamic data by acquiring 50 spectra, each with a 1 second exposure

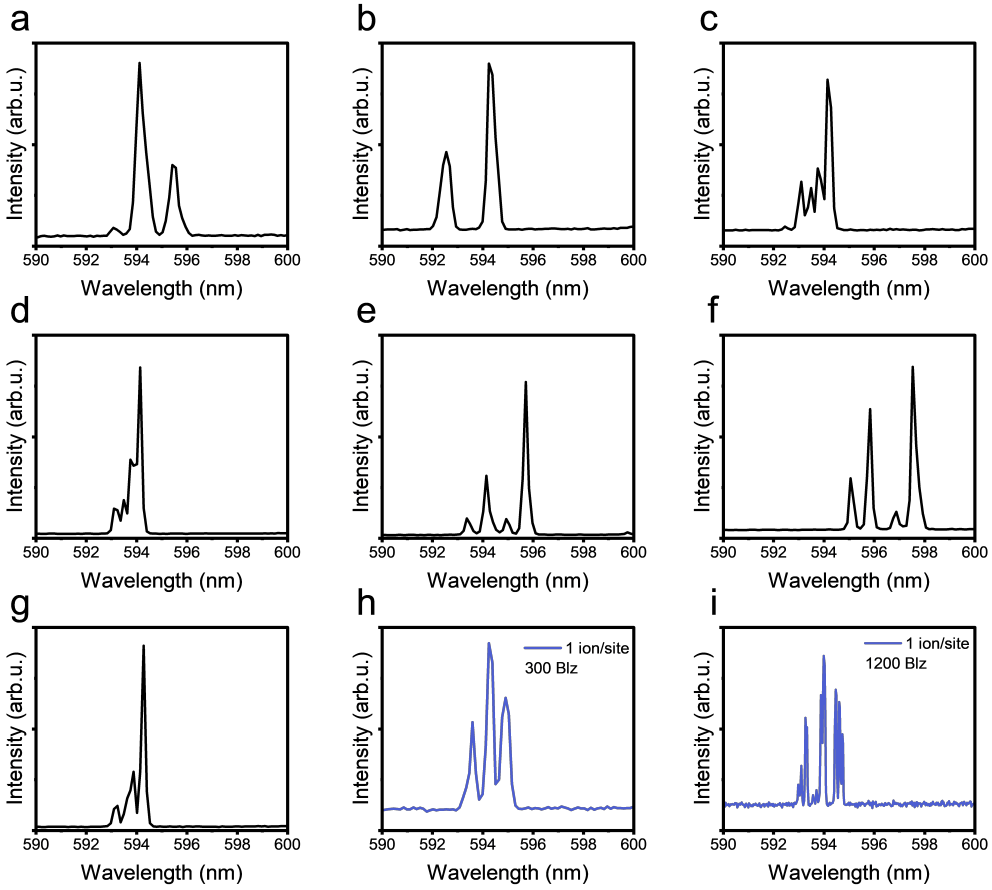


Figure 4.26: Example spectra of activated Type II Sn centres focusing inside the ZPL window. **a**−**g**, taken from array with 10 ions/site implantation dosage with 300 lines/mm diffraction grating. **h**, Type II Sn centre from 1 ion/site array with 300 lines/mm diffraction grating, and more splittings are actually presented in these three resolvable main peaks when move to 1200 lines/mm diffraction gratting displayed in **i**.

time. Lorentzian fits were applied to each peak within the ZPL window, and the intensity and central wavelength of each peak were extracted, as shown in Fig. 4.24c. While the emission peak intensities fluctuated, the relative intensities between peaks remained consistent. This constancy suggests that the defect structure responsible for the ZPL is stable. Any fluctuations in intensity likely affect all sub−peaks uniformly, indicating no significant changes in the local environment or electronic structure that could independently alter the intensity of individual sub−peaks. Throughout the characetrisation of the Type II Sn centres activated, we noticed that although the ZPL shape is consistent and the wavelength distribution is

very narrow at room temperature, the ZPLs in the cryogenic spectra are different. Fig. 4.26a−g present spectra of Type II Sn centres activated from arrays with an implantation dose of 10 ions per site. Even though the ZPL window remains narrow (593−598 nm), different number and shape of peaks are observed inside the ZPL window. Fig. 4.26h shows a Type II Sn observed in an array implanted with a Poissonian dose of 1 ion per site. To obtain detailed information on the ZPL of this centre, we employed a high-resolution spectrograph diffraction grating (1200 lines/mm) for this centre, which is displayed in Fig. 4.26i. Initially, only three peaks were resolved; however, with this higher-resolution grating, additional peaks and peak splittings were observed.

The origin of multiple peaks or splittings with a single ZPL of the PL spectrum at room temperature may include crystal field splitting [147], the fine structure splitting [148], hyperfine interactions [149] and symmetry lowering [37]. Our hypothesis on the origin of Type II Sn centres is that it originates from a carbon interstitial bound to a SnV^- centre (this will be discussed in detailed next section). Considering this, the most reasonable causes of the observed splitting and multiple peaks are symmetry lowering that generates degenerate states, fine structure splitting originated from spin−orbit interaction, and the Jahn−Teller effect modified by the presence of the carbon interstitial.

4.4.4 Summary

The observations described above — including the lower inhomogeneous broadening, the different Huang–Rhys factor, and the unpolarised emission — strongly suggest that the Type II Sn centre represents a distinct Sn complex, rather than another optically active charge state of the SnV^- defect. This interpretation aligns with theoretical predictions, which place the ZPL of the optically active neutral tin-vacancy centre at 681 nm [44].

However, recent work by James et al. within our group indicates that some Type II Sn ZPL polarisation characteristics resemble those of SnV^-, except that the spectral lines have similar strengths. When unresolved individually, these peaks

within the ZPL range may appear unpolarised. This suggests that the Type II Sn defect could be an SnV centre perturbed by strain from a nearby interstitial in a low-energy configuration, rather than an entirely different defect.

4.5 Distribution and yield of SnV^- and Type II Sn

As previously mentioned, the extended laser annealing yields both SnV^- and Type II Sn centres within the implanted arrays, Fig. 4.27a and b present yield statistics for these two types of emitters. Fig. 4.27a displays a PL map obtained after 5 minutes of laser annealing of a previously untreated area of an array with an implantation dosage of 10 ions per site. The sites where only Type II Sn emission is observed are marked in red, while sites with only SnV^- emission are marked in cyan. Fig. 4.27b presents a histogram of $g^{(2)}(0)$ values measured across all sites marked in Fig. 4.27a (region 1). The histogram also includes statistics for another similar laser-activated region within the same array (region 2). The data indicate that among the fluorescent sites in the array, the majority are single-photon emitters, and notably, all five SnV^--active sites are single photon emitters. Fig. 4.27c shows examples of HBT results discussed in Fig. 4.27b. The $g^{(2)}(0)$ values for singlet, doublet and triplet are determined via employing n−photon Fock states. The boundary $g^{(2)}(0)$ values for singlet, doublet and triplet emission would be 0.5, 0.67 and 0.75 respectively. While the total activation yield of implanted ions is still low (based on $g^{(2)}(0)$ values, 43 emitters out of an estimated 320 implanted ions or 13%), this relatively short laser anneal (which due to the low duty cycle of the pulse train in the annealing laser and rapid thermal diffusion in diamond equates to less than a second of energy transfer to the lattice) suggests that higher yields are possible, and the result clearly demonstrates the potential for site selective feedback, which will be discussed in details in the next section.

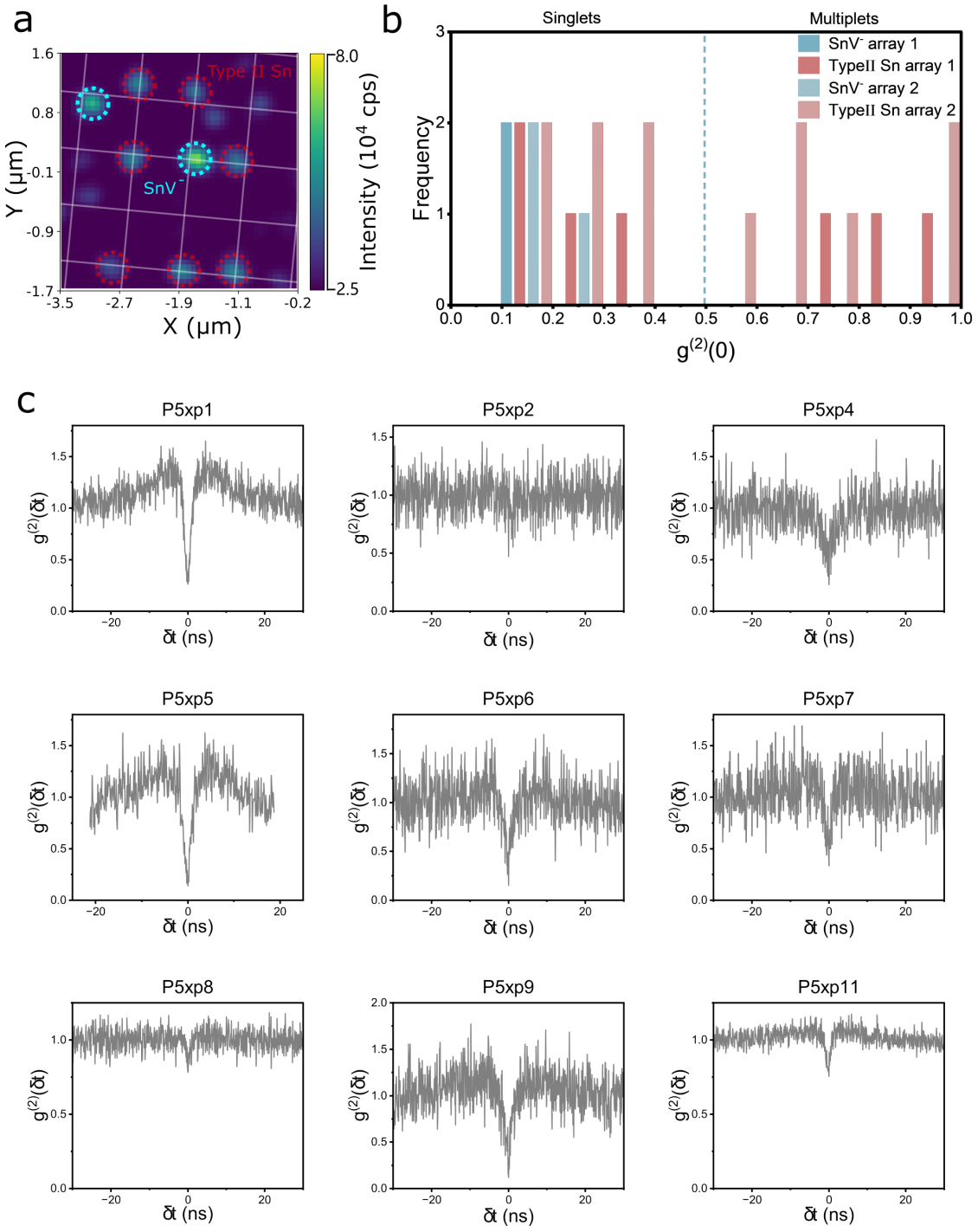


Figure 4.27: Distribution statistics of SnV^- and Type II Sn centres. **a**, 2D PL image of a 3 μm $\times$ 3 μm region of an array with a dosage of 10 ions/site, taken after 5 minutes of laser annealing. Nine stable emitting sites are identified, with SnV^- centres circled in cyan and Type II Sn centres circled in red. **b**, Histogram of $g^{(2)}(0)$ values for activated stable emitters. It shows the results for two identically sized regions of the same array. **c**, Example HBT results discussed in **b**.

4.6 In-situ monitoring

A significant advantage of using laser annealing to create solid-state defects is the ability to conduct in situ monitoring of their formation. In this study, I utilise PL imaging and spectroscopic analysis to track the formation of single SnV^- centres during the laser annealing process. The use of 2D PL map monitoring has been explored in previous studies, such as the deterministic NV centre creation reported by Chen et al. [74], where PL maps were used to identify potential emitters during annealing. However, relying solely on 2D PL maps can be insufficient for distinguishing different types of emitters, as multiple defect species can exhibit similar PL intensities. Therefore, spectral analysis is required to definitively identify SnV^- centres.

Fig. 4.28 shows a sequence of 2D PL maps captured during the laser annealing process, illustrating the emergence of discrete emitters over time. Although PL maps provide a fast method for identifying emitters, the integration time required for spectral measurements at ambient conditions is significantly longer, making real-time spectral monitoring impractical. To overcome this limitation, we adopted an iterative protocol alternating between laser diffusion for prescribed durations and the capture of 2D PL maps, followed by targeted spectral recordings at selected points of interest.

To further improve the efficiency of this process, future work could explore the use of spectral filtering as a potential live-monitoring technique, allowing real-time differentiation between SnV^- centres and other defect species based on their characteristic emission wavelengths.

To explain the origin of the Type II Sn emission, we hypothesise that it arises from a SnV^-–C_i complex. Upon implantation of ^{117}Sn ions, two carbon atoms within the diamond lattice are displaced, creating at least two adjacent carbon interstitials and carbon vacancies. The local tensile strain field around the SnV^- centre favours interaction with the compressive strain field of the carbon interstitials, thereby balancing the local strain fields. This interaction results in three emission states: an optically inactive state, Type II Sn, and SnV^-.

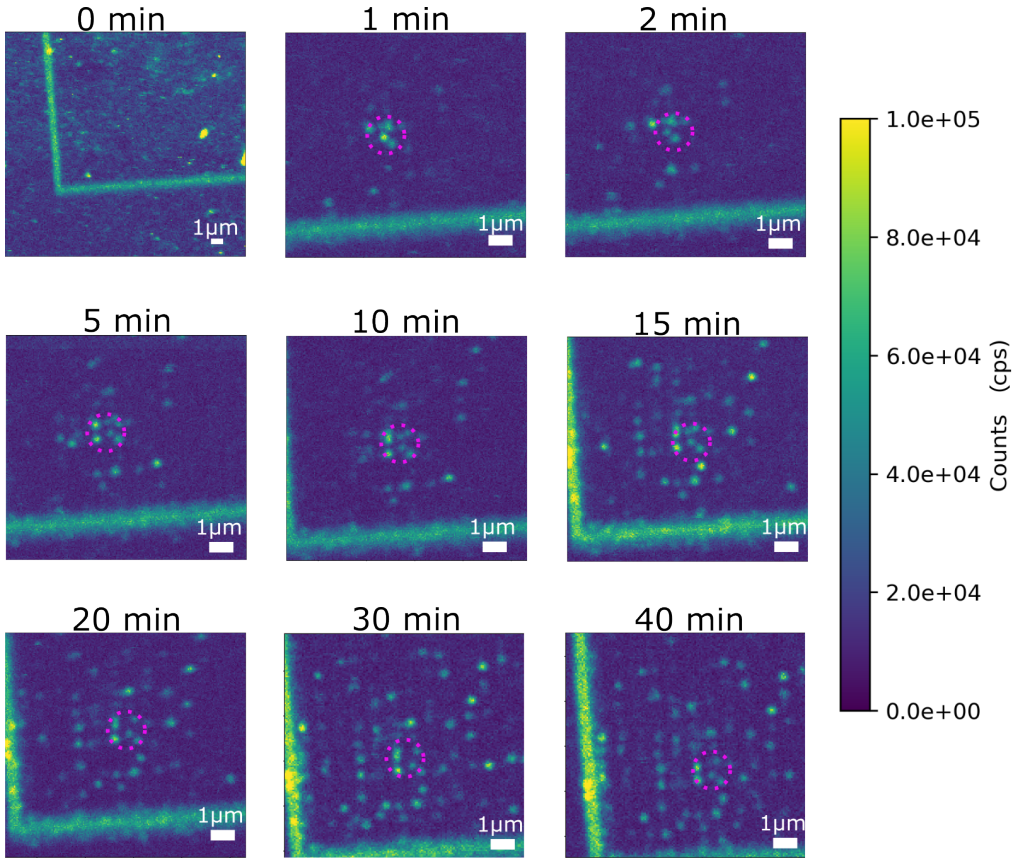


Figure 4.28: Sequence of 2D PL maps captured during the laser annealing process, showing the evolution of discrete emitters over time. The pink dashed circle indicates the focal region of the annealing laser. PL maps were acquired prior to laser annealing and at intervals during annealing for durations ranging from 0 to 40 minutes, illustrating the dynamic 'birth and death' of emitters at different implanted sites. The scale bar represents 1 µm.

4.6.1 In-situ spectral monitoring

Fig. 4.29a describes the formation of a single SnV^- centre. Initially, the spectrum displayed only the second-order Raman signature of diamond. Following 1 minute of laser annealing, a sharp ZPL appeared at 595 nm with new broad emission peaks at 617 nm, 636 nm, and 665 nm, suggesting activation of a local defect complex, attributed to the Type II Sn centre we previously hypothesized. After 3 minutes of laser annealing, the ZPL of the Type II Sn centre narrowed, indicating that the laser pulses were refining the defect structure. After 4 minutes of laser annealing, the spectra revealed the emergence of SnV^- emission from the Type II Sn centre, characterised by a prominent ZPL at 620 nm. This is attributed to

the partial dissociation of the defect complexes during the annealing process. My hypothesis suggests that the C_i diffuses around the SnV^- centre during annealing. Since C_i is highly mobile even at room temperature, it is likely that, during the 5-minute spectral acquisition, the defect complex dynamically transitions between the SnV^- state and the SnV^-–C_i complex state. This dynamic behaviour results in the simultaneous observation of spectral features corresponding to both states. After 5 minutes of laser annealing, a clean SnV^- emission spectra was observed, indicating complete dissociation of the defect complex. The annealing laser pulses had diffused the Ci far enough from the SnV centre, resulting in no further effect on the SnV^- emission. The photon autocorrelation measurement for this SnV^- is displayed as an inset, with a clear dip at $\delta t = 0$ and a $g^{(2)}(0)$ value of 0.26 confirming the presence of a single colour centre.

Fig. 4.29b depicts the transition of a SnV^- centre into a Type II Sn centre upon further laser annealing. Starting from a distorted Type II Sn, activated by previous laser treatment, 1 minute of additional annealing produced a clean SnV^- emission spectrum. After 4 minutes of laser treatment, the emission of the SnV^- was suppressed. Continued annealing for a total of 5 minutes caused formation of the Type II Sn centre, as evidenced by the PL emission spectra observed. Fig. 4.29c describes another scheme. Spectral shifting, spectral structure and intensity changes were observed upon laser annealing of the SnV^- centre,indicating the orbiting of C_is around the SnV centre and local changes in the defect environment. The final spectra shows only the diamond substrate emission, suggesting the activated defect centres can be deactivated by further laser annealing. This deactivation is likely due to transition to an optically inactive charge state of the defects (e.g. SnV^{2-} [150]) or recombination of the interstitial carbons and the vacancies within the SnV split divacancy structure. Fig. 4.30 shows the spectral shifting and intensity changes in Fig. 4.29c. Here, a Lorentzian function was fitted to the ZPL of the SnV^- centre, and the fitting parameters were extracted. The peak intensities, determined by integrating the fitted Lorentzian peaks, vary with different annealing times, suggesting that the movement of C_is around the SnV^- centre affects the

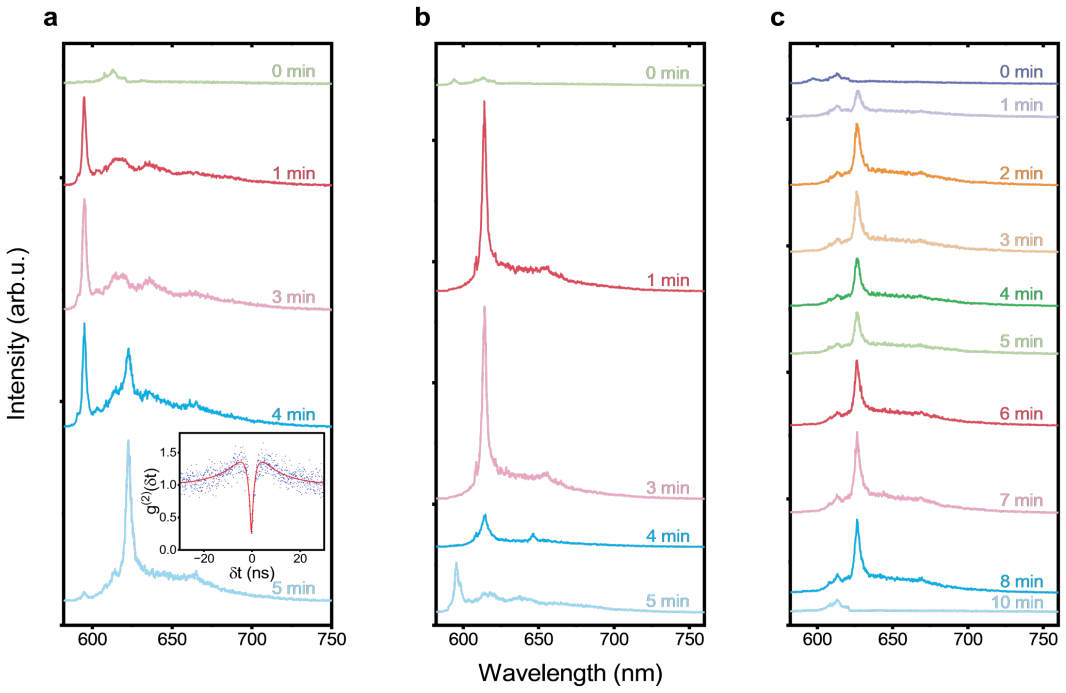


Figure 4.29: Live spectral monitoring of the temporal evolution of single SnV^- centre during laser annealing. **a**, Formation of a single SnV^- centre, starting from bare diamond background emission. The spectral evolution shows: the initial formation of a Type II Sn centre, the emergence of SnV^- centre emission peaks, and the final SnV^- centre spectrum. Inset displayed the second-order autocorrelation measurement of the SnV^- centre formed as the end state. **b**, Formation of a single Type II Sn centre, the spectrum transitions from a Type II Sn centre (weak emission) to a clear SnV^- centre, terminating to a Type II Sn centre upon further laser annealing. **c**, Deactivation of a SnV^- centre. Starting with a Type II Sn centre (weak emission), progresses to a clear SnV^- centre. Further laser annealing first leads to modification of the SnV^- emission, then deactivation into a bare diamond background emission.

degree of PL emission quenching. A correlation between peak intensity and full width at half maximum (FWHM) was observed: as the ZPL broadens, the SnV^- emission intensity decreases, indicating that the presence of a C_i suppresses the SnV^- emission. Notably, aside from the significant changes observed between 1 and 2 minutes−where both peak intensity and FWHM vary the most−the ZPL's central wavelength remains relatively stable until deactivation occurs.

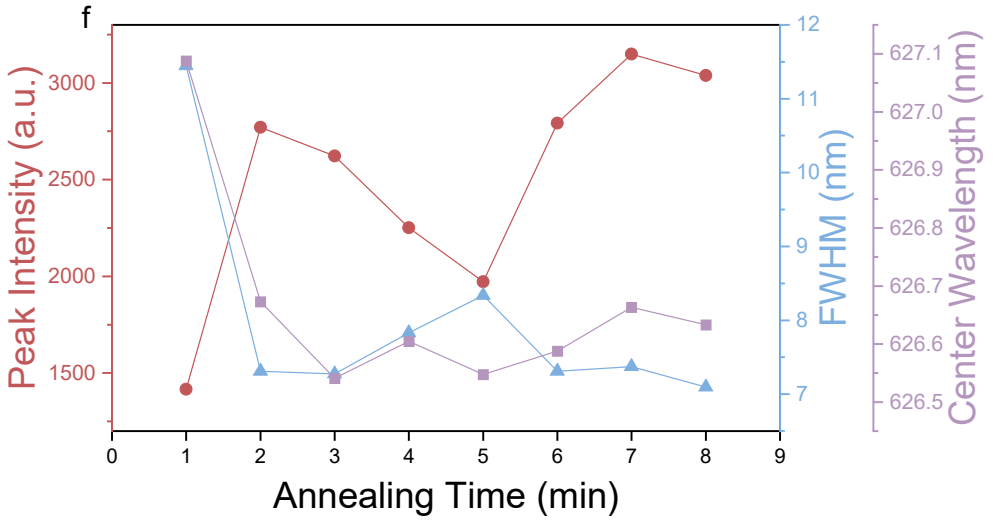


Figure 4.30: Spectrum tracking of the SnV^- centre. Where the ZPL of the SnV^- centre, as shown in Fig. 4.29c, is monitored over time during laser annealing. A Lorentzian fit is applied to the ZPL, with the fitting parameters extracted and plotted as a function of annealing time.

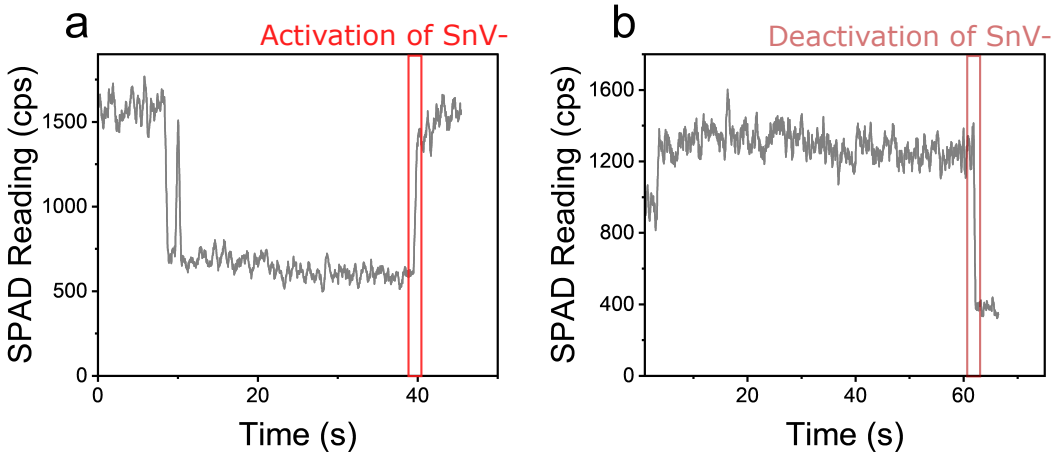


Figure 4.31: SPAD trace of the temporal evolution of single SnV^- centre during laser annealing. **a** and **b** show SPAD monitoring during laser annealing with a collection window of $615 - 625$ nm to emphasize the signal from SnV^- centres; showing a case of activation and deactivation of SnV^- centres.

4.6.2 SPAD trace

In addition to spectral monitoring, in-situ tracking of the laser annealing process can be performed using fluorescence feedback loop via SPAD (Single-Photon Avalanche Diode) traces, this provides real-time feedback control, allowing us to halt annealing as soon as SnV^- centres are activated or deactivated. SPAD readings with a binning time of 20 ms were recorded for emitters under fs-laser annealing, while simultaneously being excited by a 532 nm CW laser using a home-built confocal microscope mentioned in Chapter 3. The PL emission signal from the emitter was collected within the $615 - 625$ nm range, where the SnV^- emission is expected. Fig. 4.31a shows the SPAD trace during the $4-5$ minute interval in Fig. 4.29a. After a further 40 seconds of annealing from the 4-minute mark, a sharp increase in SPAD counts within the $615-625$ nm emission window indicates the activation of a single SnV^- centre. The initial decrease observed during the first 10 seconds of annealing, followed by a sharp spike, is not yet fully understood. This behaviour may indicate the deactivation of an SnV^- centre. Moreover, it is possible that the same SnV^- centre is reactivated, as the signal intensities before and after the spike are identical.

Fig. 4.31b shows the SPAD trace during the $3-4$ minute interval corresponding to the in-situ spectral monitoring in Fig. 4.29b. After an additional 60 seconds of annealing beyond the 3-minute mark, the SnV^- emission was deactivated, as indicated by a sharp drop in SPAD counts within the $615-625$ nm emission window. Compared to the in-situ spectral monitoring, where the temporal resolution is limited by the acquisition time required to resolve SnV or Type II Sn emission, SPAD monitoring offers significantly higher temporal resolution due to its much shorter time window.

Although the applied spectral window filtering ensures that the collected PL signal falls within the ZPL range of SnV^- centres, actual identification of the emitter requires spectroscopic verification to confirm whether the observed signal corresponds to the actual ZPL of SnV^- or an increase in broad emission intensities.

4.7 Positioning accuracy

The positioning accuracy of activated centres is critical, as it directly influences the performance and functionality of applications relying on fabricated defect centres. To establish the baseline positioning accuracy, or pointing accuracy, of the P-NAME implantation system, a PL map of an array with a relatively high implantation dose (500 ions per site) was analysed. This higher dose ensures that the sites are nearly fully activated by the femtosecond laser without the activated centres becoming excessively bright, allowing each site to be clearly resolved. Although these sites do not represent single emitters, the average position of the aggregated emissions at each site provides a reliable measure for evaluating the alignment accuracy of the fabrication system.

The analysis focused on a central $5\,\mu\text{m} \times 5\,\mu\text{m}$ area of the array, with the colour scale optimised to highlight the implantation sites while excluding background noise. Gaussian fits were applied to the emitters within the region of interest (ROI), with the centre of each fitted Gaussian used to determine the positional coordinates.

In subsequent analyses, arrays implanted at a lower dose (10 ions per site) were examined, as these yield predominantly singlets, doublets, or triplets. This approach complements the positioning accuracy assessment derived from the higher-dose array.

$$f(x, y) = \text{offset} + A \times \exp\left(-\left(\frac{(x - x_0)^2}{2\sigma_x^2}\right) - \left(\frac{(y - y_0)^2}{2\sigma_y^2}\right)\right) \tag{4.13}$$

where *offset* is the constant background level, A is the peak height of the Gaussian, x_0 and y_0 are the coordinates of the centre of the Gaussian, and σ_x and σ_y are the standard deviations in the x and y directions, respectively.

An ideal grid with a known uniform spacing of 0.78 μm, derived from the implantation mask, was fitted to the observed Sn implanted positions by optimising the x-offset (dx), y-offset (dy), and rotation angle (θ). The optimisation minimised the total discrepancy:

$$D = \sum_i w_i \min_j \sqrt{(x_{0,i} - x'_j)^2 + (y_{0,i} - y'_j)^2} \tag{4.14}$$

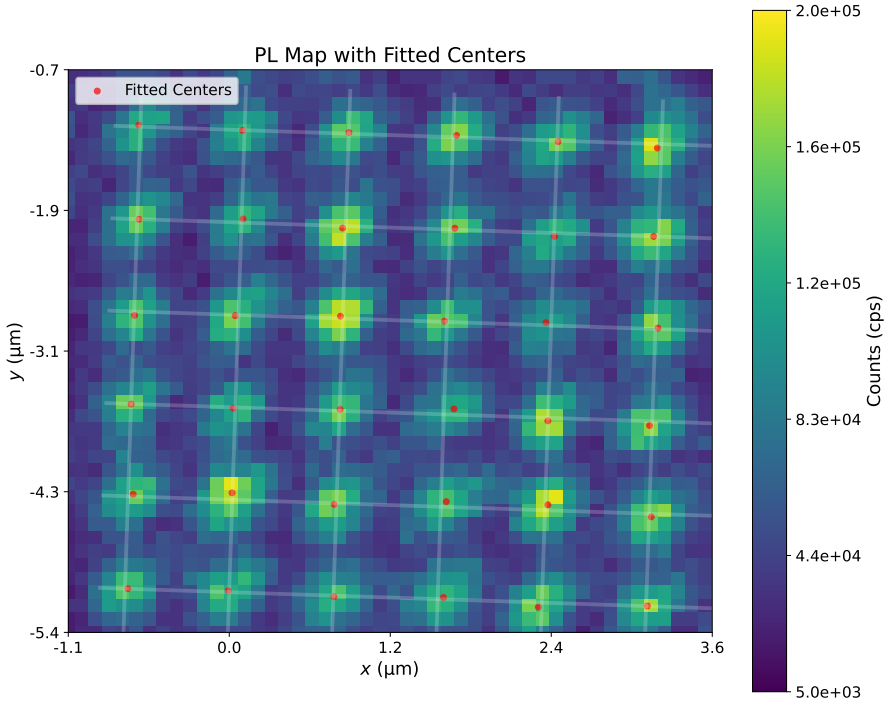


Figure 4.32: 2D PL map of an array implanted with approximately 500 Sn ions per site, following laser activation. The white grid lines correspond to the theoretically fitted positions according to the implantation mask, and the red dots correspond to centre of the fitted Gaussian of individual emitter.

where $(x_{0,i}, y_{0,i})$ are the fitted Gaussian centres of the emitters, and (x'_j, y'_j) are the nearest points on the ideal grid. Additionally, the radial discrepancy (D_r) was calculated for each centre based on the offsets in (x) and (y), where

$$D_r = \min_j \sqrt{(x_0 - x'_j)^2 + (y_0 - y'_j)^2} \tag{4.15}$$

This radial discrepancy (D_r) represents the distance between each observed centre and the ideal grid, providing a measure of how closely the observed centres align with the expected positions after accounting for the optimised offsets. As shown in Fig. 4.32, within the 5 μm x 5 μm area, 36 bright emitters (implanted sites, each site contains ensemble of emitters) were identified following Gaussian fitting, which matches the total number of emitters in the PL map. Analysis of this area revealed an average radial discrepancy of 27.6 nm. The sub-30 nm average discrepancy demonstrates the high precision of our combined implantation and activation process, closely aligning with the expected implantation positioning

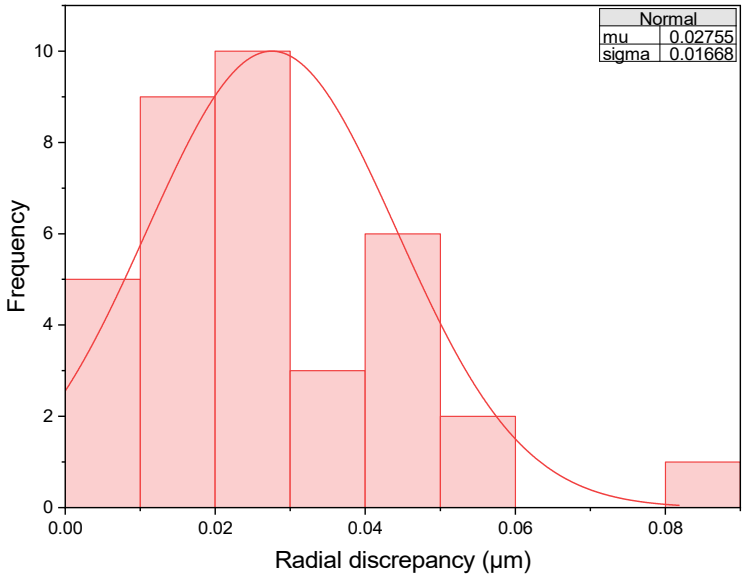


Figure 4.33: The histogram shows the distribution of radical discrepancies for array with dosage of 500 ions/site, with normal distribution fits overlaid. The fitted mean and standard deviation for the radial discrepancy are 27.6 nm and 16.9 nm, respectively.

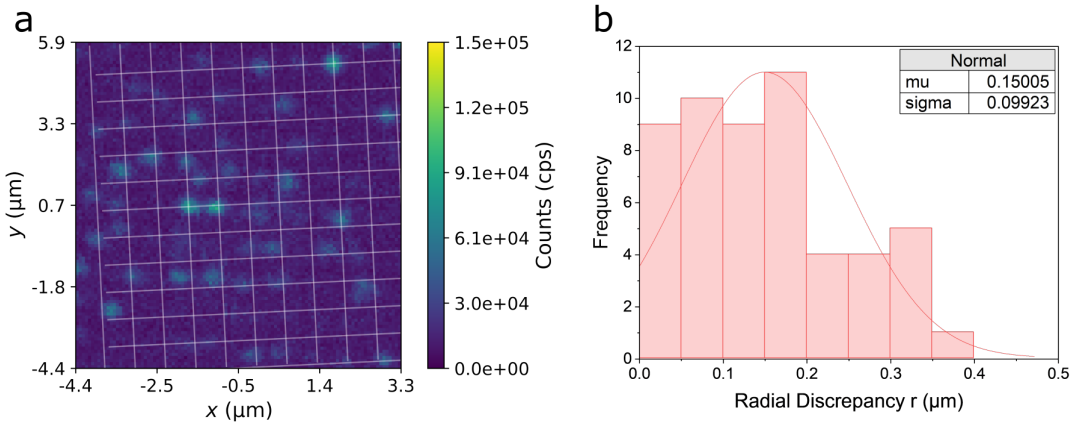


Figure 4.34: Positioning accuracy study of an array with a dosage of 10 ions/site. **a**2D PL map of an array implanted with approximately 10 Sn ions per site, following laser activation. The white grid lines correspond to the theoretically fitted positions according to the implantation mask. **b**The histogram shows the distribution of radical discrepancies for array with dosage of 10 ions/site, with normal distribution fits overlaid. The fitted mean and standard deviation for the radial discrepancy are 150 nm and 90 nm, respectively.

accuracy. According to the P−NAME implantation system, the positioning accuracy for the ion implantation is 100 nm, The observed accuracy may exceed expectations due to the high dosage region used, where each bright emitter represents an ensemble of defects. In this context, Gaussian fitting averages the distribution of ions, which will enhance the precision estimate. To achieve a more representative measure, we applied the same method to a 10 ions/site array, where laser-activated emitters (SnV^- or Type II Sn) typically appeared as singlets, doublets, or triplets as discussed in the previous section, providing a more accurate assessment of individual positioning accuracy, as shown in Fig. 4.34. Analysis for the 10 ions/site array yields an average radial discrepancy of 150 nm and standard deviation of 90 nm, which is still comparable to the P−NAME implantation system's resolution.

These results indicate that the laser activation process does not affect the positioning of the implanted Sn atoms. This is supported by the observation that the grid of bright emission sites closely aligns with the P-NAME implantation pattern. The emission sites remain within a reasonable range of the implanted locations, as confirmed by the fitted radial discrepancies. This supports the hypothesis that additional annealing after implantation is unnecessary for vacancy migration toward the implanted Sn atoms, countering the common misconception based on analogies to NV^- centres. Additional laser annealing or thermal annealing serve the role to restore the optical property by curing the diamond lattice from implantation damage [151], and to restructure the SnV centre into its ideal configuration [127].

4.8 Negatively charged silicon vacancy centre SiV- in diamond

This study demonstrates that femtosecond laser activation can be applied to other Group IV defect centres. We conducted laser annealing on an ion-implanted array, with doses of 256, 64, 16, 4 and 1 ^{29}Si ion(s) per site, following Poissonian distribution. Implantation sites were spaced 5 μm apart. To ensure precision, alignment marks were added along lateral directions, corresponding to the implantation sites. These marks enabled accurate laser focusing, allowing for site-specific annealing, which

was monitored in real-time using a fluorescence feedback loop. Here we performed the same type of techniques (preliminary laser treatment and extended laser annealing), due to the presence of well-aligned alignment marks and larger between-site seperation, the extended laser annealing is performed from site to site with the annealing laser focused at the exact position of the implanted position (based on the fluorescence feedback). The activation laser was turned off when a sharp increase in the SPAD counts was observed as shown in Fig. 4.36, indicating the activation of an emitter.

4.8.1 Array with Poissonian 256 ions/implantation site

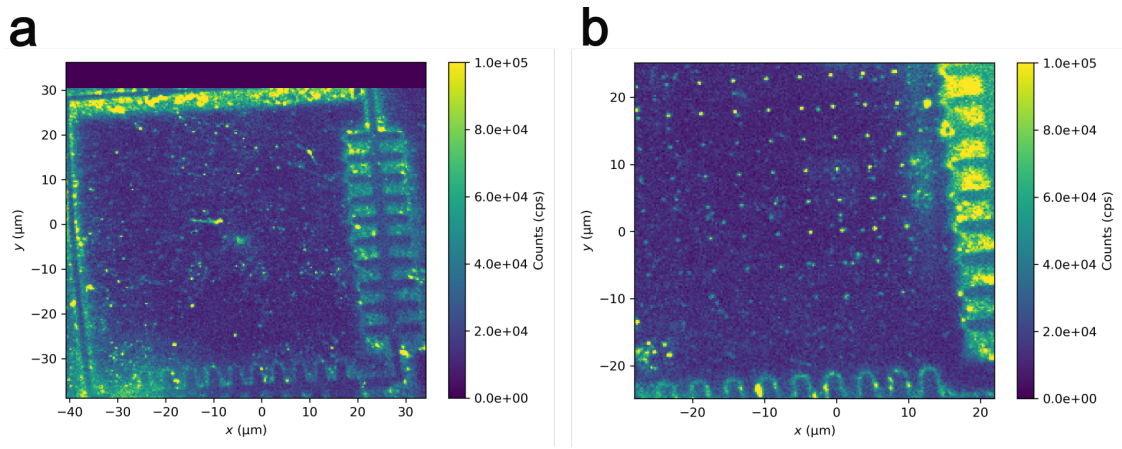


Figure 4.35: 2D PL images of a Si-implanted array with a dosage of 256 ions/site. **a** post ion implantation, where only background emission was observed. And **b** post laser activation, where arrays of emitters with between-sites spacing of 5 μm are activated.

The first array examined was the one implanted with 256 ions per site, as higher dosage of Si ions make it easier to activate colour centres. Fig. 4.35a presents a 2D PL image of the array prior to any laser processing. The square-shaped features correspond to ion-implanted Au markers.

For each site in this array, extended annealing was performed using a fluorescence feedback loop to determine the duration of treatment. The annealing laser remained on until a spike in the SPAD trace was detected, as shown in Fig. 4.36. The typical duration for laser exposure in this high-dosage array was around two minutes.

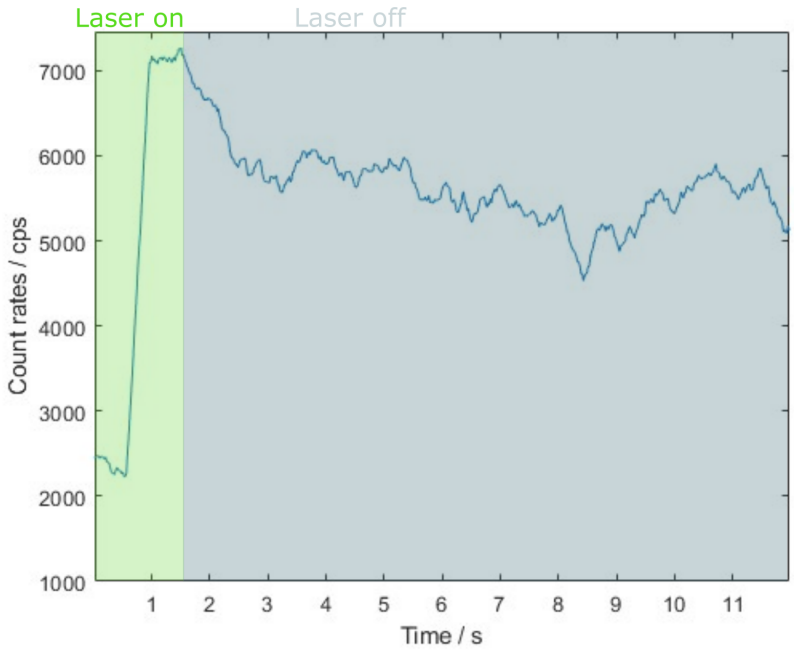


Figure 4.36: Example SPAD trace of the temporal evolution of a Si-implanted site during laser annealing, with a collection window of 700 − 800 nm. The initial spike indicates the activation of the colour centre. The SPAD trace is capped around the activation point, although the site had been annealed for 1 minute. Fluctuations are observed after the annealing laser is switched off, which may be attributed to the presence of unstable emitters within the ensemble.

Fig. 4.35b shows the same array after full laser activation. Different annealing pulse energies were applied across the rows, resulting in varying emitter brightness, despite the uniform implantation dose across the array. This suggests that the emitters formed are ensembles of defect centres. This finding prompted a shift in focus to an array with a lower implantation dose.

4.8.2 Array with Poissonian 64 ions/implantation site

Here we studied an array with dosage of Poissonian 64 Si ions per implanted site. Fig. 4.37 and Fig. 4.38 illustrate the temporal evolution of PL maps: post ion implantation and post laser treatment (however this PL map is taken cryogenic temperature during spectral analysis) with different regions treated by various pulse energy from 1.88 nJ down to 0.31 nJ. It was observed that some defects activated using the lowest pulse energy (0.31 nJ) underwent deactivation without any further treatment, while defects treated with higher pulse energies (1.88 nJ,

1.56 nJ, and 0.93 nJ) exhibited stable emission properties. This behaviour is likely due to insufficient annealing at low pulse energies, which may result in incomplete stabilization of the defects and the formation of metastable defect states. In contrast, higher pulse energies facilitate more robust lattice restructuring, leading to stable defect activation and emission properties.

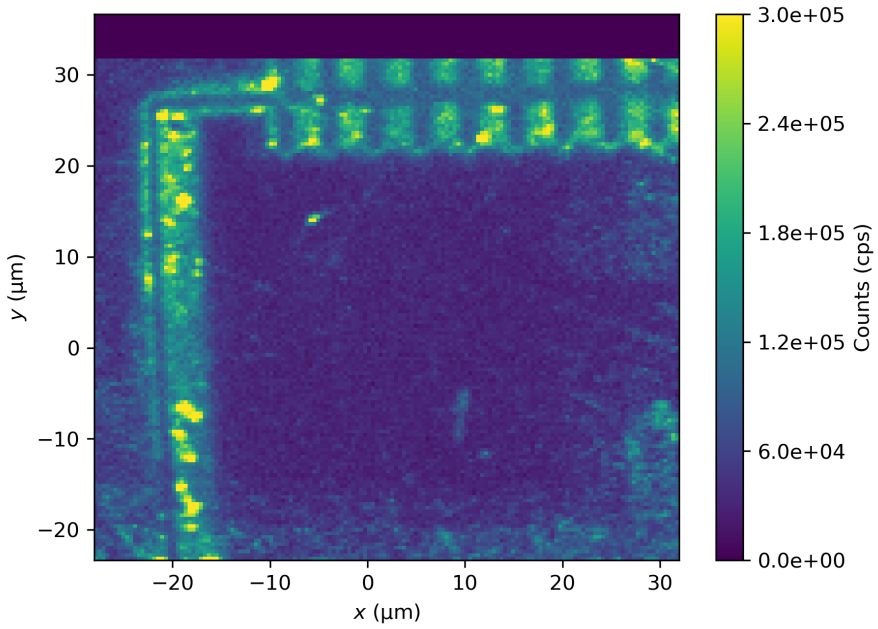


Figure 4.37: 2D PL images of a Si implanted array, with a dosage of 64 ions/site, following ion implantation. Only background emissions are visible, with no detectable array-shaped emitters present.

For each individual site, the annealing process was terminated when a spike was detected in the SPAD trace, as illustrated in Fig. 4.36. Fig. 4.39 demonstrates the relationship between the increase in count rate for the spike and the laser pulse energy used for different regions. Despite variations in annealing time, the spike observed in the SPAD trace was consistent across different pulse energies. This suggests that the same type of defects were activated. Given that the sample is a high-purity diamond implanted only with Si ions, it is likely that SiV^- centres were activated. Notably, the high implantation dosage makes it unlikely for the activated emitters to be singlets. Cryogenic spectral analysis was subsequently performed on the same array, as shown in Fig. 4.40. Each spectrum features two prominent peaks: the first at approximately 737 nm, corresponding to SiV^- emission [37, 152], and

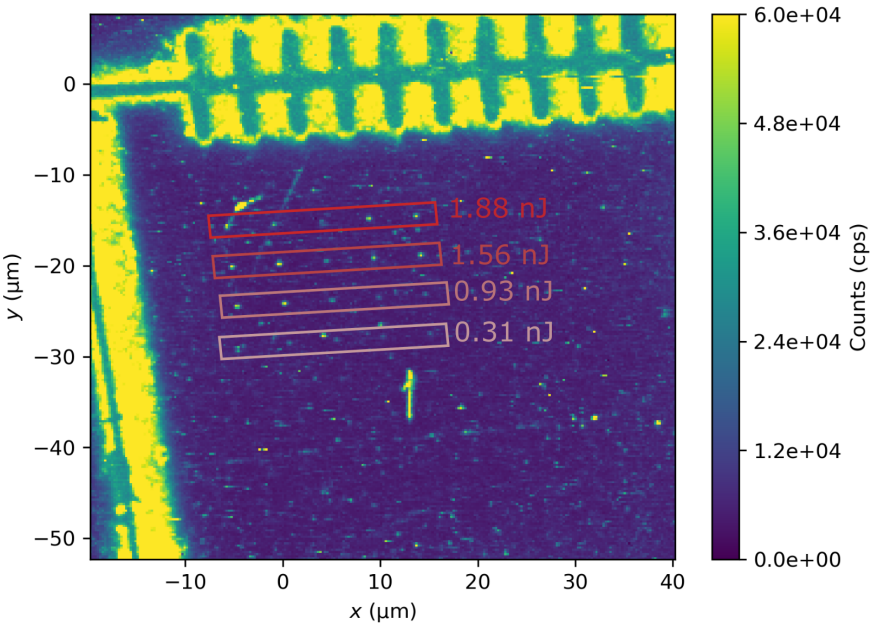


Figure 4.38: Set of 2D PL images of a Si implanted array, with a dosage of 64 ions/site, post laser activation taken at cryogenic temperature. Four rows are activated, with each row treated by different pulse energies: 1.88 nJ, 1.56 nJ, 0.93 nJ, and 0.31 nJ. The activated rows are outlined with squares of different colours to distinguish between rows treated with varying pulse energies.

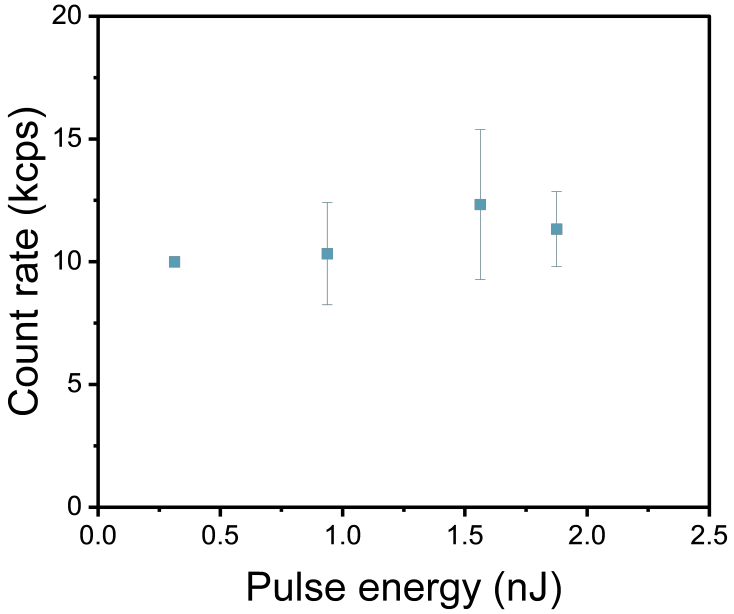


Figure 4.39: This graph illustrates the spike (increment) in count rates observed during laser activation, plotted against the annealing pulse energy. Despite variations in annealing time, the spike in the SPAD trace remained consistent across the different pulse energies. Error bars represent one−sigma uncertainties.

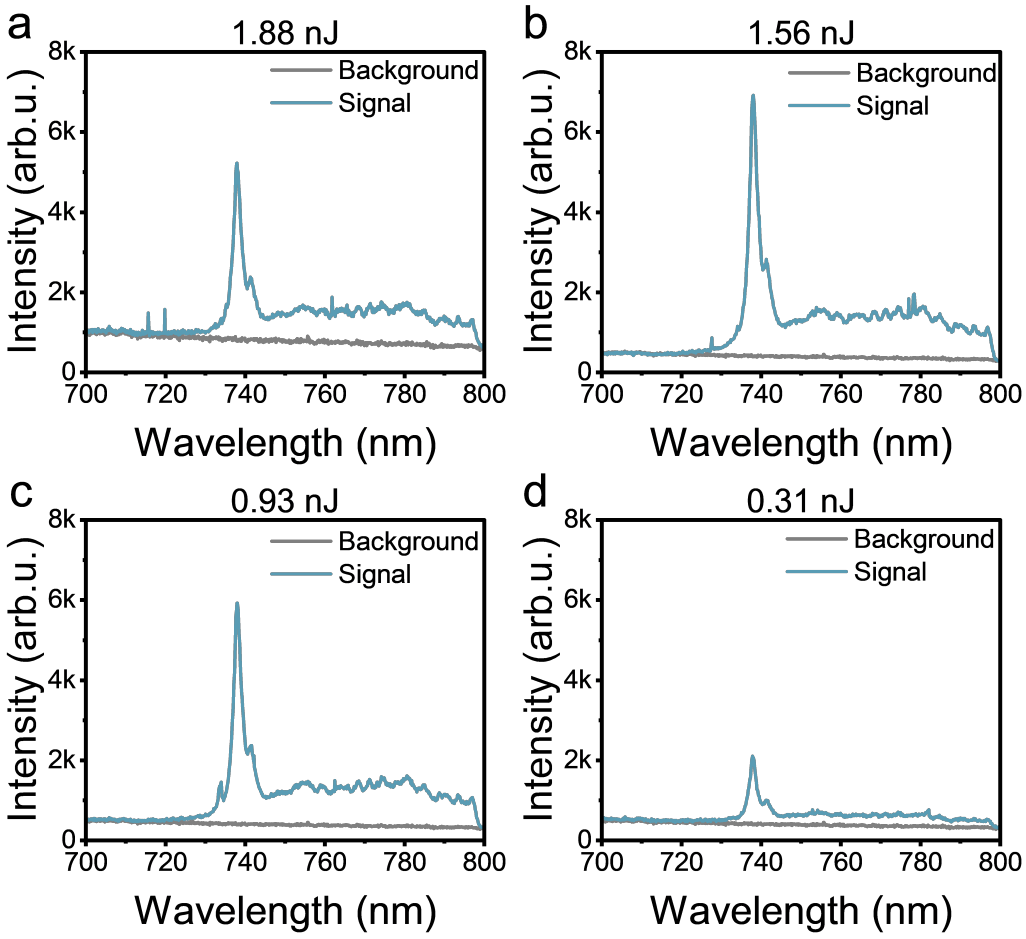


Figure 4.40: Four cryogenic (4.2 K) PL spectra taken from sites treated with annealing pulse energies of **a** 1.88 nJ, **b** 1.56 nJ, **c** 0.93 nJ, and **d** 0.31 nJ. The blue line indicates the signal, while the grey line represents the background. Two type of peaks are observed: one at 737 nm, corresponding to SiV^- emission, and another at 741 nm, corresponding to the GR1 emission. Spectra from sites treated with 1.88 nJ, 1.56 nJ, and 0.93 nJ are quite similar, whereas the SiV^- emission from the site activated with 0.31 nJ shows a lower count rate. This reduction could be due to deactivation during the laser activation process or fewer defects being activated at this pulse energy.

the second at 741 nm, associated with GR1 emission. These peaks were consistently observed across the sites, confirming the presence of these defect centres. The spectra from the sites treated with 1.88 nJ, 1.56 nJ, and 0.93 nJ pulse energies exhibit clear SiV^- emission intensity. However, for the site treated with a lower pulse energy of 0.31 nJ, both the GR1 and SiV^- emissions demonstrate reduced intensity. This reduction could indicate that fewer SiV^- centres were activated at this lower energy, or alternatively, that a deactivation process occurred during

laser activation. The consistency in the GR1 peak relative to the SiV^- peak across all pulse energies suggests that both features fluctuate together, maintaining a roughly constant ratio in peak heights.

Although the study of SiV^- centres is less detailed compared to SnV^- centres in this work, it still provides important insights into the generality of the laser activation process. The focus on SnV^- centres was driven by the fact that SnV^- ZPLs do not overlap with GR1 emission, facilitating clearer spectral analysis, and because SnV^- centres are comparatively less studied than SiV^- centres. In terms of fabrication, activating SiV^- centres is not inherently more difficult than SnV^- centres. The observed similarities in spectral behaviour suggest that the underlying activation mechanisms are analogous for both defect types. Moreover, it is expected that laser annealing in this context remains exciton-mediated, consistent with previous studies on defect activation in diamond. These preliminary results with SiV^- centres highlight the broader applicability of the laser activation technique and motivate further studies to explore this process in greater detail.

4.9 Discussion

In this section, we introduce a novel technique for activating Group IV defects in diamond using in-situ monitoring. This approach allows real-time tracking of defect activation and offers valuable insights into the mechanisms by which laser treatment modifies the diamond lattice at the atomic scale. By enabling fast, localised activation of PL, this method significantly enhances our understanding of how defect centres are formed and optimised through laser processing. The fast, localised activation of fluorescence reported in Fig. 4.6 suggests that it results from the direct optical excitation of pre-existing defects at the implantation sites. The high-energy Sn ion implantation process displaces some carbon atoms from their lattice sites, thereby generating both carbon vacancies and self-interstitials (C_i) [153]. The absence of GR1 fluorescence in the post-implantation spectra suggests that these vacancies are predominantly in the negatively charged (ND1) state, which is not optically active under green excitation and does not emit in the

measured wavelength range [154]. While this result is unexpected in electronic grade diamond [155–157], the formation of stable ND1 defects by the ion implantation process may be attributed to band bending effects near the surface [132], resulting from the relatively shallow implantation depth of approximately 20 nm. The preliminary laser treatment then converts the charge state of some of these ND1s to GR1s [130, 158–161], resulting in the emergence of the corresponding luminescence feature centred at 741 nm. As noted earlier, the extensive lattice damage produced by high ion-implantation doses can create additional rapid non-radiative pathways that effectively quench the GR1 emission [133, 134]; this possibility cannot be dismissed. Such a mechanism also explains why, immediately after heavy implantation, no GR1 luminescence is detected, yet following a femtosecond-laser pulse that locally heals the diamond, the GR1 emission once again becomes observable.

The appearance of Type II Sn and SnV^- photoluminescence on short time scales may also be related to charge state modification, although this is not the hypothesis we deem most plausible based on our observations. Indeed, the femtosecond laser pulses trigger both linear and nonlinear absorption mechanisms at these implantation sites [70, 75], creating free charge carriers and excitons via multi-photon band-to-band transitions and defect ionization [70, 82, 83]. The resulting charge carriers can then transfer their energy to the diamond lattice through electron-phonon scattering and recombination processes, leading to localized lattice heating [83, 162, 163].

Despite the energy transfer, previous studies show that lattice temperatures remain below 700 K during laser annealing ($I_S \approx 3.01 \times 10^{15}$ W cm^{-2}, similar to Kononenko et al. [163] when accounting for differences in wavelength and focal spot size), indicating that the process of activating SnV^- is not solely thermal [83]. To better understand the thermal dynamics, I modelled heat diffusion using the thermal diffusion equation:

$$\frac{\partial T(\mathbf{r},t)}{\partial t} = \alpha \nabla^2 T(\mathbf{r},t), \tag{4.16}$$

where $\alpha = k/(\rho c_\mathrm{p})$ is the thermal diffusivity, with initial conditions given by a three-dimensional Gaussian temperature distribution:

$$T(\mathbf{r}, 0) = T_\mathrm{b} + (T_\mathrm{h} - T_\mathrm{b}) \exp\left[-\left(\frac{x^2}{2\sigma_\mathrm{x}^2} + \frac{y^2}{2\sigma_\mathrm{y}^2} + \frac{z^2}{2\sigma_\mathrm{z}^2}\right)\right], \tag{4.17}$$

with standard deviations determined by the laser focusing conditions.

We considered two limiting cases: room-temperature diffusivity ($\alpha_\mathrm{rt} = 1.22 \times 10^{-3}\,\mathrm{m}^2/\mathrm{s}$) and high-temperature (930°C) diffusivity ($\alpha_\mathrm{hot} = 0.06 \times 10^{-3}\,\mathrm{m}^2/\mathrm{s}$) [164, 165]. Our simulations (Fig. 4.41) reveal that heat dissipates within $\sim 10\,\mathrm{ns}$ in either case—two orders of magnitude faster than the time between consecutive annealing pulses (1 µs)—precluding cumulative heating effects. Furthermore, the temperature distribution spreads to at most a few micrometres in diameter within the first nanosecond before cooling to ambient conditions.

Although multi-photon absorption coefficients for femtosecond laser pulses at 520 nm in diamond are not well characterised, we can estimate an upper bound for absorption. Using the three-photon absorption coefficient at 400 nm ($\beta_{3,400\mathrm{nm}} = 2.3 \times 10^{-22}\,\mathrm{cm}^3\mathrm{W}^{-2}$) [166], the fraction of absorbed pulse energy is:

$$\frac{\Delta E}{E_0} \approx -\beta_{3,400\mathrm{nm}} I_0^2 \Delta z = 16\,\%, \tag{4.18}$$

where $I_0 = 3 \times 10^{12}\,\mathrm{Wcm}^{-2}$ is the peak intensity and $\Delta z = 790\,\mathrm{nm}$ is the confocal parameter. Since $\beta_{3,520\mathrm{nm}} << \beta_{3,400\mathrm{nm}}$, the actual absorption is significantly lower, supporting our conclusion that peak temperatures remain well below the diamond graphitisation threshold of ~ 1050°C [167]—the maximum temperature used in our simulations (Fig. 4.41a). The absence of graphitisation despite extended exposure (>12 h) confirms this assessment.

We hypothesise that exciton formation, coupled with these limited thermal effects, mediates the annealing process. Hot carriers generated by the laser pulses relax into excitons [83], which then deliver energy to the lattice, facilitating defect annealing. Concurrently, the energy contained in the electronic and phononic subsystems diffuses over an area several μm in diameter within nanoseconds [163]. Our observation that extended laser treatment effects are delocalised beyond the

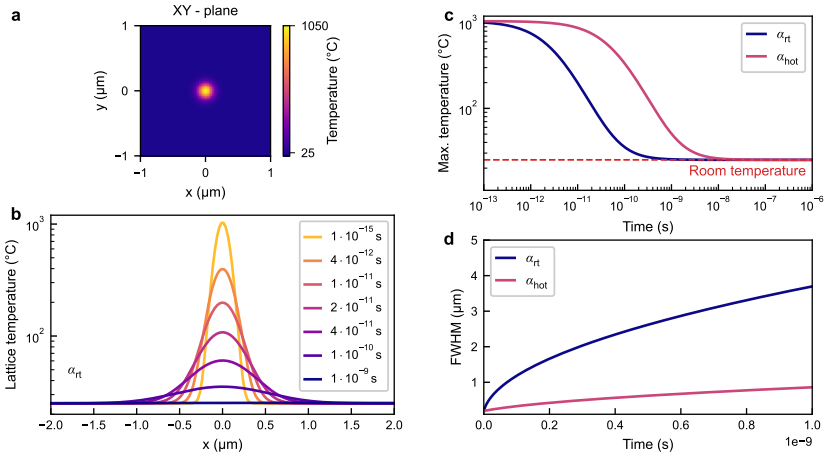


Figure 4.41: Simulation of spatiotemporal thermal dynamics in ultrapure diamond. **a**, Cross-sectional temperature distribution in the XY plane immediately after excitation. The initial peak temperature is set to 1050 °C. At such a temperature, diamond graphitises within minutes under steady-state conditions. As no graphitisation is observed over extended periods, the peak temperatures reached in our study are likely significantly lower. **b**, X-axis temperature profiles at successive timepoints assuming room-temperature (α_{rt}) diffusivity, demonstrating nanosecond-scale thermal equilibration. **c**, Maximum temperature as a function of time for room-temperature (α_{rt}) and high-temperature (α_{hot}) diffusivity parameters. **d**, Time evolution of the full width at half maximum (FWHM) for both cases.

diffraction-limited laser spot (Fig. 4.13) is consistent with both the thermal diffusion simulations (Fig. 4.41d) and the occurrence of such processes, facilitating defect migration. Consequently, some limited structural modification resulting from the preliminary laser treatment cannot be ruled out. Notably, carbon interstitials in diamond are highly mobile and may diffuse short distances as part of the activation process, potentially contributing to the observed delocalised effects.

Regarding the formation of the 595 nm emission peak and SnV^- centres, previous research has shown that $\sim$ 40% of implanted Sn ions already settle into a split vacancy configuration [127], necessarily resulting in two C_i defects being present in the near vicinity. Rather than focusing solely on those interstitials, it is instructive to consider the behaviour of vacancies in the vicinity of substitutional tin. A vacancy must approach the substitutional site in order to create the SnV complex, and vacancies remain mobile in diamond, with an activation energy for migration of 2.3 eV. Interstitials close to substitutional tin are also possible, but the local

compressive strain is expected to drive them away. Further calculations are required to confirm these scenarios. A further plausible configuration is the SnV–V_C complex (tin–vacancy bound to a carbon vacancy); see the Supplementary Information of Ref. [145]. An alternate hypothesis is therefore that the resultant SnV-2C_i complex is optically inactive, but that the preliminary laser treatment is sufficient to mobilise one of the C_is, and could leave behind an optically active SnV-C_i complex −− the Type II Sn with a feature at 595 nm. Importantly, subsequent extended laser treatment further facilitates the mobilization of the remaining C_i, which is more strongly bound to the SnV defect, allowing it to migrate away from the SnV defect and switching on the SnV^- photoluminescence.

To investigate aspects of this hypothesis, Zhao performed density functional theory (DFT) calculations of a single C_i near a SnV^- centre. Simulations were conducted using a 3×3×3 supercell containing an SnV^- and a C_i. The models were constructed using CrystalMaker [168] and subjected to DFT geometry optimisation with the CASTEP code [169], employing the Perdew−Burke−Ernzerhof (PBE) exchange-correlation functional [170] and ultrasoft pseudopotentials. A cutoff energy of 900,eV was used, and the Monkhorst−Pack (MP) grid spacing was specified as 0.05. Upon introducing a single interstitial carbon into the diamond lattice, it optimises to form split-⟨100⟩ interstitial carbon pair. Various configurations were explored with the interstitial placed at different lattice sites relative to the SnV^- centre, as shown in Fig. 4.42. The calculations reveal that a single C_i can form a stable complex with SnV^- without undergoing recombination. As can be seen in Fig. 4.42, we find that the energy of the SnV^- centre complexed with a C_i one or two lattice sites away is around 2 eV lower than that of configurations where the carbon interstitial is either more distant from or directly adjacent (but not bound) to the Sn^-V centre.

The emerging picture of laser annealing mobilising C_i defects to create different defect complexes is consistent with previous work on nitrogen-vacancy defects [171] and with other aspects of the experimental results presented here. The larger inhomogeneous distribution of spectral lines from SnV^- compared to Type II Sn,

shown in Fig. 4.20, would be a natural result of the varying strain field experienced by the SnV^- defect as a result of the range of positions that the dissociated C_i could occupy in the nearby lattice. Continued annealing leads to a clearer SnV^- spectrum, as the C_is diffuse away from the SnV^- centres, and creates a more stable environment that favours consistent emission characteristics. However, further annealing can also reintroduce the C_is into the vicinity of the SnV^- centres. In some cases, a C_i will once again bind to the SnV^- centre, producing Type II Sn emission or, if two C_is migrate close enough, deactivate the SnV^- centres entirely (as seen in Fig. 4.29c).

If correct, our model may also shed light on the low yield of SnV^- centres in undoped diamond, despite the high initial formation efficiency of split-vacancy configurations [127, 143]. During the thermal annealing process, a significant proportion of SnV centres would likely remain bound to surrounding carbon interstitials, leading to the frequent formation of stable SnV-C_i complexes emitting at 595 nm. Only if sufficient energy is provided to overcome the SnV-C_i binding energy, by e.g. a 2000°C anneal (requiring high pressure), a large portion of SnV-C_i will remain, as corroborated by previous work [39].

Other Group IV defects, such as SiV^-, have also been generated through the laser activation process. Preliminary results for SiV^-, though not as extensively studied as SnV^- in this thesis, suggest that the SiV^- spectral feature is more easily obtained via laser activation, with no intermediate states observed during the process. The structural similarity between SiV and SnV centres suggests that this disparity arises primarily from the atomic size of the respective Group IV elements.

The larger atomic radius of tin compared to silicon induces greater tensile strain within the diamond lattice. For instance, the Si−C bond length in SiV centres is 1.96 Å, whereas the Sn−C bond in SnV centres extends to 2.08 Å [145]. Similarly, the C−C distance across the vacancy increases from 2.67 Å in SiV to 2.83 Å in SnV^-, compared to the typical C−C bond length of 1.54 Å in pristine diamond. This represents a 73% increase in lattice spacing for SiV^- centres and an 84% increase for SnV centres$^-$, with an 11% difference in lattice expansion highlighting the more pronounced tensile strain introduced by SnV defects. This strain likely

contributes to the lower yield and more complex fabrication process associated with SnV^- centres compared to SiV^- centres.

The larger strain field surrounding SnV defects not only affects activation efficiency but also influences their photoluminescence properties. While both defect types share a split-vacancy configuration, the smaller silicon atom causes less lattice distortion upon incorporation into the diamond matrix, reducing the formation energy of the defect and streamlining the charge-state conversion process. In contrast, the larger tin atom induces significant lattice relaxations, potentially creating additional pathways to metastable configurations or transient charge states. These extra relaxation channels may explain the presence of intermediate states and the more complex activation dynamics often observed with SnV^- centres.

Although a detailed comparison of formation energies and phonon sidebands would require additional *ab initio* modelling or higher-resolution experimental studies, these preliminary findings are consistent with prior reports indicating that larger Group IV elements lead to more intricate defect-formation behaviours and optical characteristics in diamond. A systematic investigation encompassing photoluminescence spectroscopy, defect yield measurements, and charge-state interconversion analyses for both SiV^- and SnV^- would further validate these trends and clarify the structure-property relationships underlying their distinct optical properties.

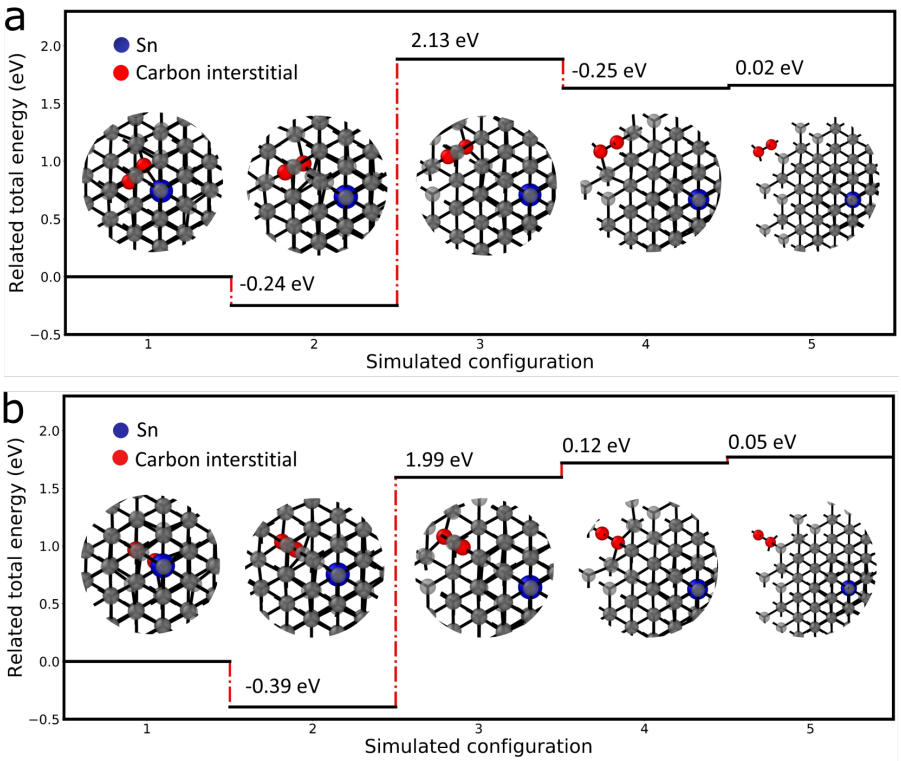


Figure 4.42: The figure illustrates the total energy of the system for various simulated configurations of the C_i, **a** and **b** shows two orientation that the C_i travels. In configuration 2, the C_i is in a stable state, occupying a second-nearest neighbour site to the SnV defect without recombining with the vacancy. The energy landscape shows an energy barrier that must be overcome to move the C_i away from the SnV complex, leading to the formation of a pure SnV^- defect.

5

Laser writing of wide bandgap materials with enhanced light extraction

Contents

5.1 Introduction 132
5.2 Transfer-printed SIL integrate with laser written NV^- 133
5.2.1 Introduction 133
5.2.2 Fabrication of GaN SILs 134
5.2.3 Laser writing of NV^- centre 136
5.2.4 SIL integration 139
5.2.5 Optical compatibility 140
5.3 Enhanced light extraction efficiency 145
5.3.1 Simulation 145
5.3.2 Experimental 149
5.3.3 Background analysis 153
5.3.4 Summary 156
5.4 Laser writing through monolithic SILs in 4H-SiC . . . 157
5.4.1 Introduction 157
5.4.2 Scalable fabrication of monolithic SILs 158
5.4.3 Laser writing process 161
5.4.4 Characterisation of laser written array with 532 nm excitation source 163
5.4.5 Characterisation of laser written array with 780 nm excitation source 173
5.4.6 Summary 176
5.5 Discussion 177

5.1 Introduction

In this chapter, we explore the combined effect of solid immersion lenses (SILs) and femtosecond laser writing on enhancing photon collection from solid-state quantum defects. As aforementioned in Chapter 1, quantum defects, such as nitrogen-vacancy (NV^-) centres in diamond, play a vital role in quantum information science, quantum sensing, and quantum imaging due to their stability at room temperature, long spin coherence times, and potential for scalable fabrication. However, the efficient collection of photons from these defects is often compromised by the high refractive index of diamond, which causes internal reflection and photon loss. This reduction in collection efficiency leads to longer acquisition times, decreased fidelity, and lower signal-to-noise ratios (SNR).

To address this challenge, several techniques have been developed, including surface treatments, cavity coupling [27–30], and surface nanostructuring [31, 32, 97–100]. Among these, SILs have been developed as an effective solution. SILs are hemispherical or super-hemispherical lenses made of high refractive index materials, designed to be placed on or near quantum emitters. By reducing internal reflection and increasing the effective numerical aperture, SILs improve photon extraction from the solid state defect centres.

This chapter examines the underlying principles of the synergistic technique used for enhancing light extraction efficiency, outlines the fabrication process, and evaluates the resulting improvements. These advancements play a crucial role in the broader development of quantum technologies.

Two different scenarios for integrating and aligning SILs with solid-state quantum defect centres are explored in this chapter. The first approach is a top-down method, where defect centres are first fabricated and well-registered to alignment marks, followed by the integration of SILs using these alignment marks to ensure precise positioning. The second approach is a bottom-up method, where defect

centres are created through the SIL interface and directly aligned with the SIL's focal point during fabrication.

5.2 Transfer-printed SIL integrate with laser written NV^-

5.2.1 Introduction

As previously mentioned, SILs can be applied to enhance light collection from NV^- centres, traditional methods like focused ion beam (FIB) milling have been used to directly carve SILs into diamond substrates [33, 35, 101, 109]. While this method has demonstrated up to a 10 times improvement in light collection, it is time intensive, taking approximately one hour per lens [109], and presents scalability challenges. Even though no detrimental effects of the milling process on the coherence properties of NV^- centres are reported [111], there are some concerns that the ion bombardment might cause additional strain around the defect of interest [112, 113].

To overcome these limitations, we demonstrated an approach that combines laser written NV^- centres with gallium nitride (GaN) SILs, integrated using a transfer printing technique. This method separates the creation of NV^- centres from the fabrication of the lenses, enabling faster, scalable production through wafer−compatible wet and dry etching. The GaN lenses are formed using inductively coupled plasma (ICP) etching [172], taking advantage of the high etch selectivity between photoresist and GaN to produce lenses with high aspect ratios−geometries that are difficult to achieve with diamond. With the NV^- centres fabricated through laser writing, position of defects can be aligned well with laser written alignment marks that further aid the transfer print process towards a higher positioning accuracy. Furthermore, refractive index of GaN is well−matched to diamond at the NV^- emission wavelength, reducing reflection losses and improving photon extraction efficiency. Crucially, this approach avoids damage to the diamond crystal, preserving the integrity and coherence of the NV^- centres.

In this section, the preparation of GaN SILs and the transfer printing process were primarily conducted by our collaborators at the University of Strathclyde. The

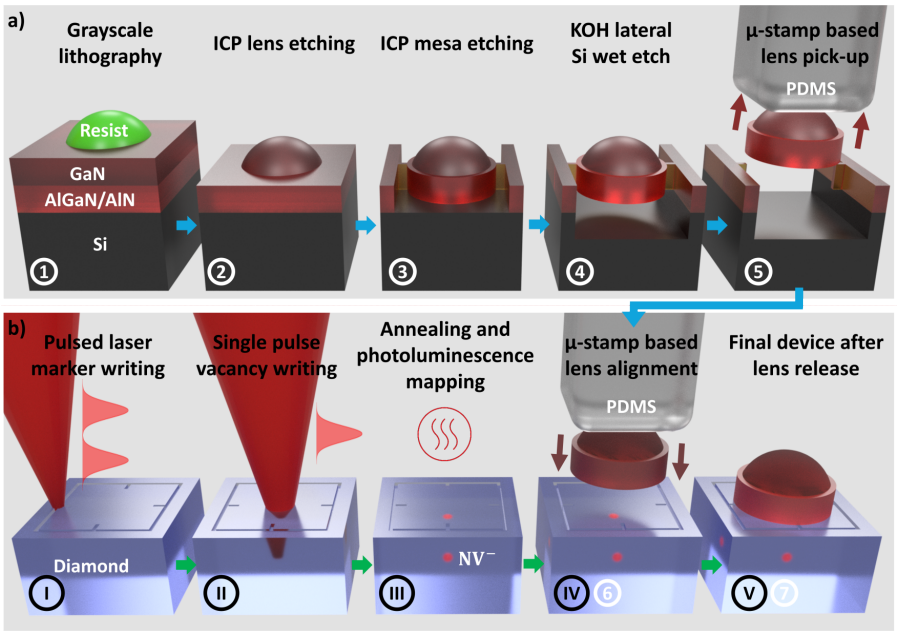


Figure 5.1: Schematics describing the process flow of additive GaN solid immersion integrated with laser written NV^- centres. **a** suspended GaN solid immersion lenses are fabricated by parallel plasma dry and wet etching techniques, **b** after initial marker writing, a NV^- defect centre is generated in single crystalline diamond by pulsed laser writing and subsequent thermal annealing, and the suspended GaN lenses are assembled above the defect centre with micro-transfer printing.

simulation work was a collaborative effort, with equal contributions from both teams. All optical characterisation was performed by the author, while the defect writing was carried out jointly by the author and Andrew Kirkpatrick. The annealing of the diamond sample was performed by our collaborator at the University of Warwick.

Fig. 5.1 presents a schematic of the complete process flow, which is divided into three main stages: the fabrication of GaN SILs, the laser writing of NV^- centres, and the integration of SILs with the diamond substrate through transfer printing. Each of these stages will be discussed in detail throughout this section.

5.2.2 Fabrication of GaN SILs

As illustrated by Fig. 5.1a, the GaN solid immersion lenses are defined and suspended on a strain-optimised heteroepitaxially grown GaN−on−Si chip [173–175] based on the wafer-scale compatible microfabrication process as described in [172]. The process begins with the creation of polymer resist lenses through grayscale

lithography and thermal reflow. This technique allows precise control over lens dimensions and ensures a smooth surface finish (1). These polymer lenses are then transferred to the 2 μm thick GaN top layer using inductively coupled plasma (ICP) dry etching. An Ar/Cl_2-based etch recipe, with selective etching rates, is employed to accurately shape the GaN material (2).

Next, a mesa structure is defined around the lens through lithography, which is then etched into the approximately 2 μm thick AlGaN/AlN buffer layer using an additional ICP etch step. This reveals the underlying silicon substrate, creating the suspension anchors (3). To suspend the lens and mesa laterally, a SiO_x hard mask—deposited via plasma-enhanced chemical vapor deposition (PECVD)—is employed for its durability. An anisotropic potassium hydroxide (KOH) wet etch selectively removes the silicon beneath the mesa along specific crystal planes while preserving the micro-lens features protected by the hard mask. The mask is subsequently removed by reactive ion etching (RIE), restoring the lens surface with minimal roughness (4).

The prefabricated GaN SILs are then lifted from their growth substrate using a modified dip−pen lithography system [176] with white light illumination for precise alignment (5). A patterned polydimethylsiloxane (PDMS) micro-stamp, made from 6:1 Sylgard 184 PDMS, with approximately 35 μm extrusion height and 30 μm square lateral dimensions, was used. This polymer−based micro−transfer printing technique allows for accurate placement of the suspended semiconductor components with sub−micron lateral precision. The reversible adhesion properties of PDMS enable precise positioning and easy detachment [176–178], ensuring that the GaN SILs are transferred onto the target substrate without compromising their structural integrity.

The GaN SIL dimensions are optimized for efficient light focusing, with a diameter of 11 μm, a height of 2 μm, and a radius of curvature of 8.3 μm. An example SIL is shown in Fig. 5.2. AFM data confirms the actual dimensions and verifies a smooth, spherical profile. The design targets a radius of 8−9 μm to align

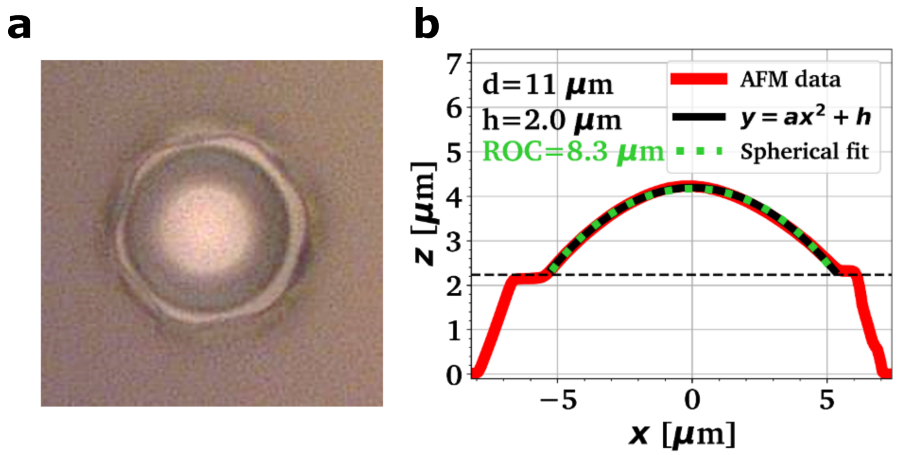


Figure 5.2: This figure, provided by our collaborators Wessling et al. from the University of Strathclyde, has been reproduced here with permission. An example GaN SIL. **a**, Optical microscope image of the SIL. The lens has a circular, convex shape, and appears as a bright, raised feature against a contrasting background, indicating its smooth, well-defined surface. **b**, AFM profile of the SIL showing the lens's cross-sectional height. The measured data (red line) closely follows a quadratic fit (black line) and aligns with a spherical approximation (green dashed line), indicating a smooth, spherical surface with a radius of curvature of 8.3 μm. The measured height and diameter are 2 μm and 11 μm respectively.

with the emitter depth of 5 μm, ensuring optimal photon extraction enhancement (detailed simulation results would be discussed in later section).

5.2.3 Laser writing of NV^- centre

The fabrication process of NV^- centres in diamond is illustrated in Fig. 5.1b. A commercially available electronic-grade single crystalline ⟨100⟩ diamond (from Element Six) grown by chemical vapour deposition with nitrogen density < 5 ppb is used as substrate. As described in Chapter 3, laser writing is implemented using a regeneratively amplified Ti:Sapphire source producing laser pulses with 250 fs duration, 790 nm wavelength and a repetition rate of 1 kHz which is focused using a high-NA oil immersion objective lens (Olympus 60×, 1.4 NA).

Initially square shaped alignment marks were fabricated via high pulse energy laser pulses Fig5.1b(I). These pulses disrupt the sp^3 carbon bonds, causing a rearrangement into sp^2 bonds, leading to localised graphitisation. These surface markers are clearly visible under an optical microscope, assisting in the precise

localisation of the writing sites and facilitating the later transfer printing process. As demonstrated in Fig. 5.3, 6 alignment squares were created, each containing lateral alignment teeth, resulting in 5x5 addressable positions per quadrant, with 100 addressable positions for laser-written defects within each alignment square.

Next, arrays of NV^- centres are fabricated. A single femtosecond laser pulse is focused within the diamond substrate at a depth of 5 μm, introducing an ensemble of Frenkel defects at the target positions defined by the alignment markers (Fig. 5.1b(II)). Optical aberrations related to refraction at the diamond interface are corrected using a liquid crystal spatial light modulator[67, 83] as discussed in Chapter 3. Within each alignment square, the writing pulse energy decreases from top to bottom, leading to a higher concentration of bright features, such as defect ensembles or graphitised points, in the upper quadrants, while fewer Frenkel defects are expected in the lower quadrants.

The sample is then annealed at 1000 °C for three hours in a nitrogen atmosphere, allowing vacancies to become mobile and combine with intrinsic substitutional nitrogen atoms in the diamond lattice, forming stable NV^- centres (Fig5.1 b(III)) [70, 95]. An optimal concentration of Frenkel defects in the lower quadrant is crucial for maximising the likelihood of forming single NV^- centres after the thermal annealing process.

Sets of PL maps were taken after laser processing and thermal annealing, but before transfer printing, using a 532 nm excitation source at a power of 1 mW with a collection window from 600 to 700 nm. A range of objective lenses with NA of 1.25, 0.95 and 0.5 were used to compare the resolution of the laser-fabricated array across regions A to F. Fig 5.4 shows PL maps of Region B as an example, taken with different objective lenses focusing on the same area. Arrays of emitters, well-aligned with the laser-written alignment markers, were observed. Using the NA = 0.5 objective lens, only emitters from the upper two quadrants were distinguishable. As expected, resolution and signal collection improved with increasing NA, and for both NA = 0.95 and 1.25, emitters in the lower two quadrants also became visible.

Spectral analysis and photon autocorrelation measurements were then conducted to identify promising NV^- centre singlets or doublets. The relative positions of the selected emitters were recorded for subsequent integration with the GaN SILs.

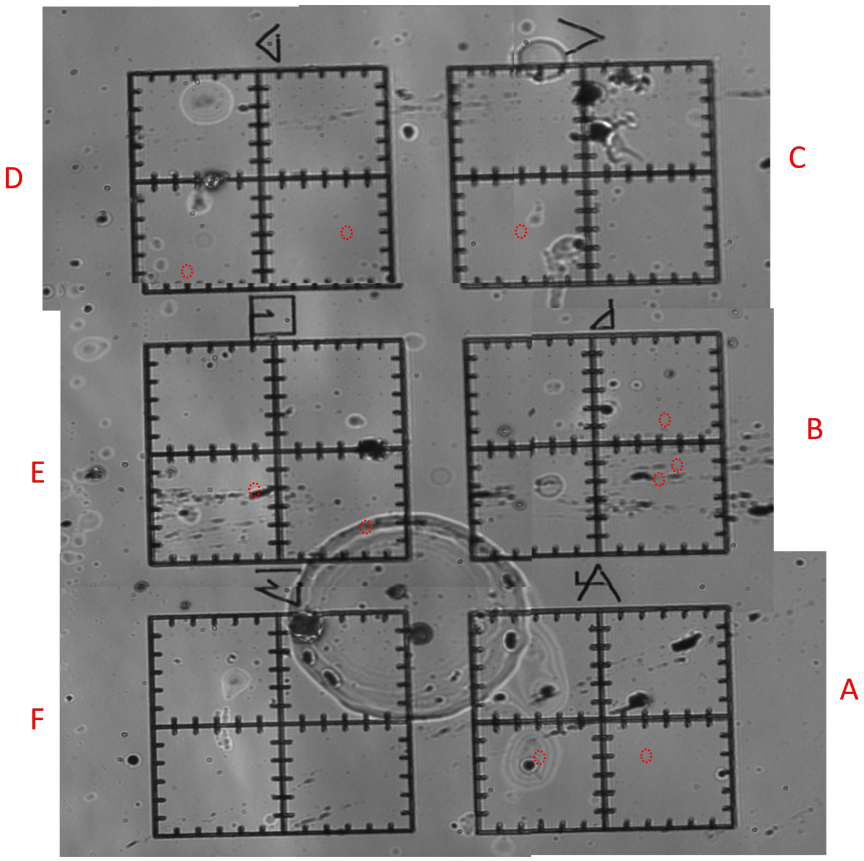


Figure 5.3: Optical transmission microscope image of region A to F, taken at a depth of 5 μm below the diamond substrate surface. The visible square marks and lateral teech were laser written graphitic alignment boxs and marks. Single pulses of fabrication laser were focused at the point of intersection of the extensions of each two teeth. The pulse energy decreased from top to bottom.

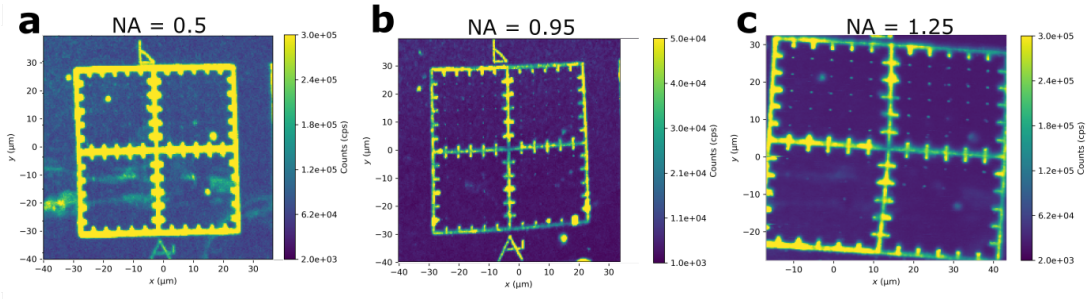


Figure 5.4: PL images of the same region after the initial laser writing and thermal annealing, taken with the same excitation source but different objective lenses with different NA: **a** 0.5, **b** 0.95 and **c** 1.25.

5.2.4 SIL integration

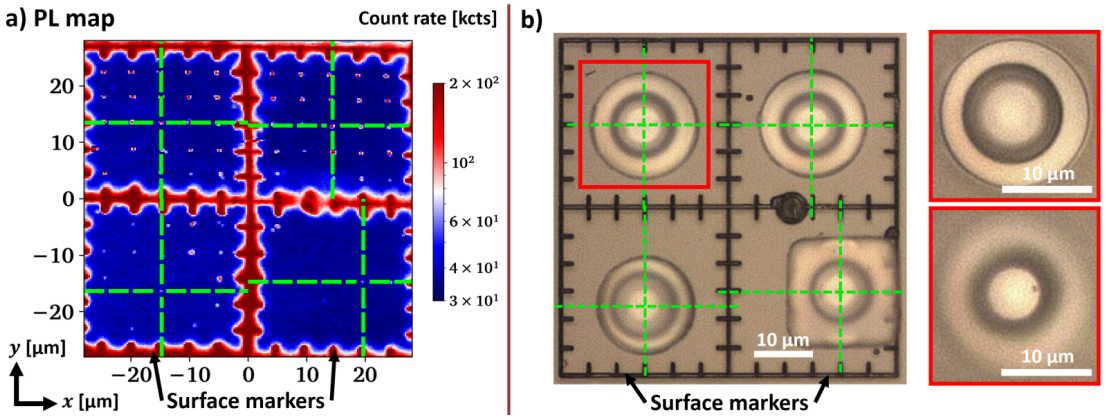


Figure 5.5: Alignment marks aiding SIL transfer printing. **a**, PL image of an example region (Region D) after laser writing and annealing. The image was recorded using an oil immersion objective with NA=1.25. Targeted emitter locations are marked with green crosses. **b**, Microscope images of the assembled GaN SILs above the marked emitters in **a**.

Using the detailed spatially resolved precharacterisation of the emitters, GaN SILs with a radius of ROC matching the emitter depth are preselected, removed from their growth substrate and deterministically placed above targeted NV^- centres using the laser written marker structures as alignment guide, as illustrated in Fig. 5.1b IV and Fig. 5.5. Multiple micro-lenses are integrated within a compact area, with one GaN lens placed in each quadrant of the pre-characterised marker region. The corresponding PL map shown in Fig. 5.5a is used to adjust the print position according to the most promising emitter locations. Alignment accuracy is primarily constrained by distortions in the PL map, with markers serving as visual references without the use of computational or mathematical alignment methods. Prior to transfer printing, the diamond surface is cleaned with an ultrasonic solvent and then treated with boiling acid, using 95% sulfuric acid mixed with 30% H_2O_2 with 3:1 volume ratio, to remove residual debris from the laser written markers. The GaN micro−lenses adhere to the diamond surface purely through Van−der−Waals forces. This bonding relies on both micrometre−scale flatness and nanometre−scale local roughness of the surfaces. The micro lens height is confined to the 2 μm thick GaN epilayer to ensure a flat bottom surface [172].

After integrating the GaN SILs, PL measurements were performed to assess the enhancement in emitter visibility and the impact on the optical properties of the NV^- centres. As illustrated in Fig. 5.6, PL maps of two example regions (B and D) were captured using objective lenses with NAs of 0.95 and 0.5, respectively. The integration of the SILs essentially extends the optical path length before reaching the emitters, requiring a deeper focal adjustment into the diamond for these measurements. The observed high brightness of the SILs in the PL maps is attributed to their auto-fluorescence, which will be discussed later in this chapter.

To highlight the effect of the SILs, two selected SILs, outlined with dashed black and red lines in Fig. 5.6, were examined in detail. The zoomed and refocused PL images of these SILs are shown in Fig. 5.7. The SIL marked in black targets NV ensembles in the upper quadrant of the region and was captured using an NA of 0.5. The SIL marked in red focuses on an NV doublet in the lower quadrants and was captured using an NA of 0.95. This latter case will be analysed further in the subsequent sections. Both images show enhanced visibility compared to the pre-integration state.

Fig. 5.8 compares PL images of the same emitter before and after the integration of the GaN SILs, illustrating the dependence on the numerical aperture of the collection optics. Line profiles along the green lines in the PL maps highlight improvements in signal intensity and resolution. The original PL maps were acquired with consistent exposure times and a step size smaller than the diffraction limit for each optic. These results confirm that integrating GaN SILs significantly enhanced the emitters' visibility.

5.2.5 Optical compatibility

To verify the compatibility of the GaN SILs for measurements in the optical quantum regime, spectral analysis and photon autocorrelation measurements were conducted. As mentioned in Chapter 3, intensity autocorrelation is a well-established method for identifying single−photon sources in solid state physics, originating from the work of Hanbury Brown and Twiss (HBT) [179–181]. For these measurements the

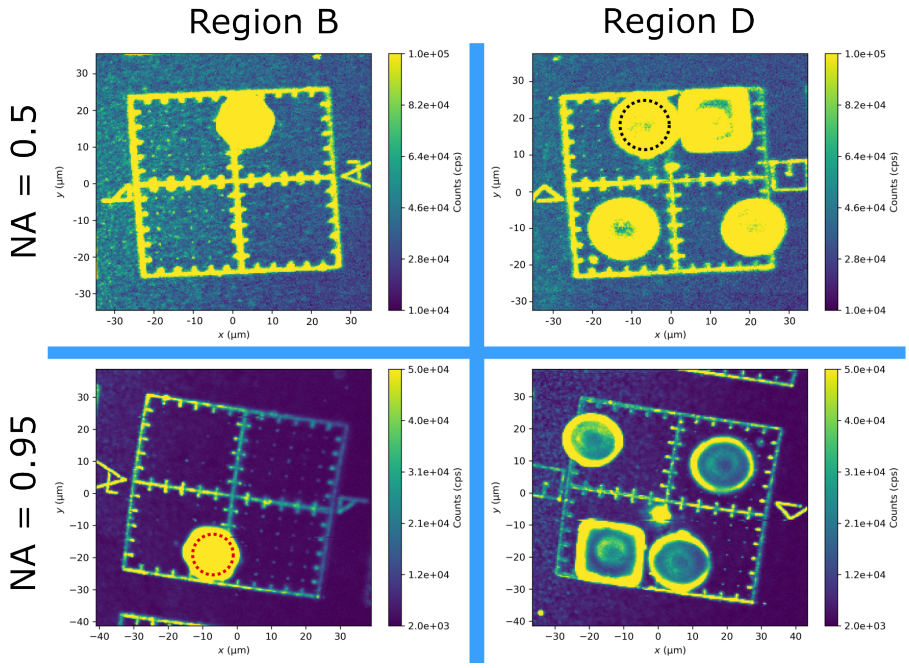


Figure 5.6: PL maps of two example regions (Region B and D) after the integration of GaN SILs, taken with objective lenses with NA of 0.95 and 0.5. Two SILs, circled with dashed lines in black and red, are zoomed in the next figure for better visibility. The oil immersion objective lens with an NA of 1.25 was not used due to the incompatibility between the immersion oil and the GaN SILs.

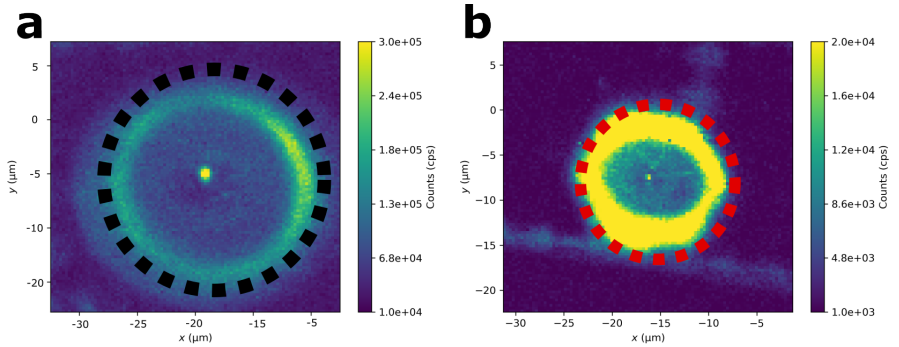


Figure 5.7: The introduction of GaN SILs effectively elongates the optical path length before reaching the emitters, resulting in the emitters covered by SILs being at different virtual depths; thus, the focus is moved further into the diamond for these images. Both images show increased visibility compared to before the integration of the SILs. **a**, SIL circled in black from Fig. 5.6, focusing on NV ensembles, taken with an objective lens of NA = 0.5. **b**, SIL circled in red, focusing on an NV doublet, captured with an objective lens of NA = 0.95.

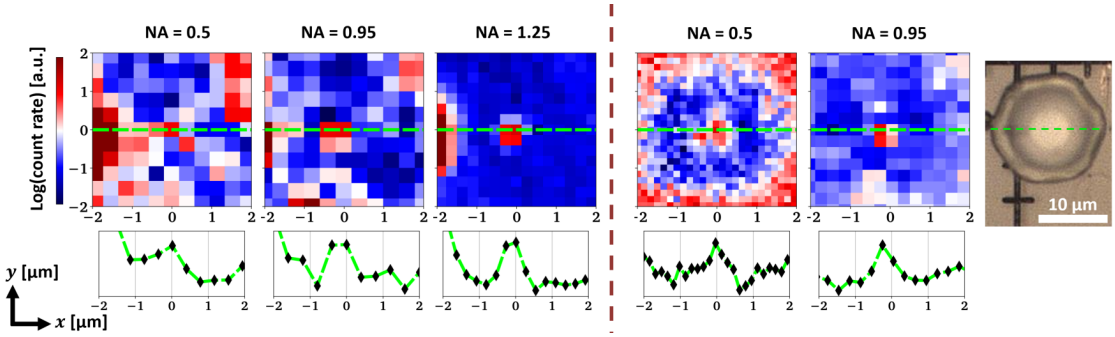


Figure 5.8: PL images of the same emitter after the initial laser writing and annealing (left), and after the integration of a GaN SIL (right), demonstrating the dependence on the numerical aperture of the collection optics. Line profiles were taken along the green lines in the maps. The original PL maps were acquired with identical and sufficient exposure times at each step, and the step size was smaller than the diffraction limit for each collection optic.

objective lens with NA=0.95 is used. A spectral filter in the optical path of one SPAD prevents potential optical cross-talk due to the breakdown flash commonly observed in Si APDs and SPADs[182]. HBT measurements were carried out on NV centres of interest prior to and post GaN SIL placement. Fig. 5.9 shows the second order autocorrelation function $g^{(2)}(\delta t)$ for an NV^- centre in Region D following integration with the GaN SILs. A dip at at $\delta t = 0$ with a $g^{(2)}(0)$ value of 0.67 suggests that the ensemble consists of two closely spaced NV^- centres, which cannot be resolved separately. Fitting the autocorrelation function to a three−level system (shown in Eqn 3.4) yields $\tau_1 = 9.4$ indicating a estimated lifetime of 9.4 ns, matching the literature value of NV^- centre in bulk diamond [183].

Fig. 5.10 compares the second-order autocorrelation functions for the same NV^- centre in Region B prior to (Fig. 5.10a) and post GaN SILs placement (Fig. 5.10b). In both cases, dips $\delta t = 0$ are observed, with $g^{(2)}(0)$ value of 0.68 before SIL integration and 0.56 after. These values confirm that the measured NV^- centre is a doublet emitters, while the variation in the $g^{(2)}(0)$ values reflects differences in signal to noise ratio (SNR) between the measurements. The high pitch around 30 ns time delay attributes to a electric signal crosstalk between the SPADs. The normalised intensity of this peak is lower in the data taken with the GaN SILs, suggesting an improved

SNR with the SILs in place. Fitting the data to a three-level model produced a similar lifetime estimate of 9 ns, reinforcing the consistency of the measurements.

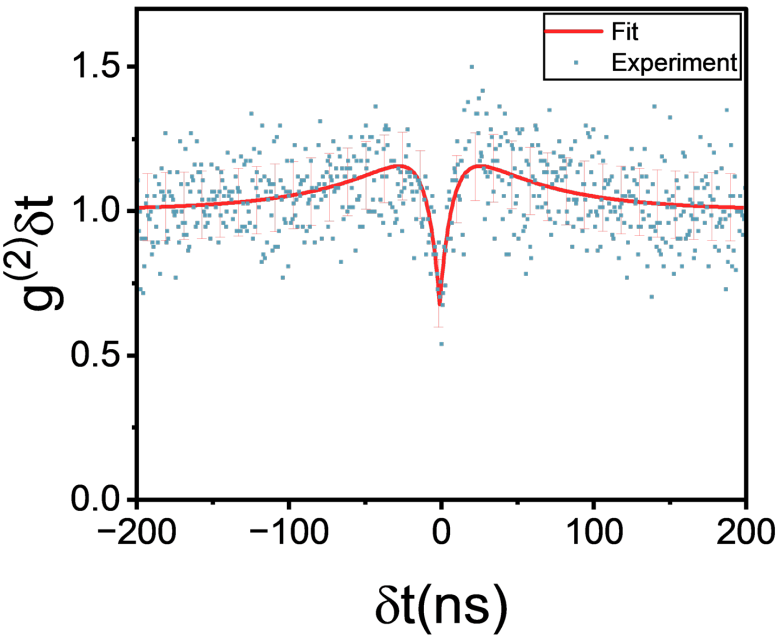


Figure 5.9: Second−order autocorrelation measurement and corresponding three−level fit for a NV^- centre in the lower quadrant of Region D after GaN SILs placed on. A dip is observed with $g^{(2)}(0) = 0.67$. The red curve correponds to a three−level model fitting with fitted values $\tau_1 = 9.4$ ns. The red shaded region represents one sigma standard error.

Fig. 5.11 shows a background corrected spectral measurement of the discussed emitter taken through the lens, exhibiting a sharp ZPL centred at 637 nm and a phonon sideband of approximately 100 nm width, as is characteristic of the NV^- centre in diamond [184, 185].

So far in this section, we have experimentally demonstrated the successful transfer printing of SILs using laser-written alignment marks, with previously fabricated defect centres registered to these marks. Despite the intrinsic auto-fluorescence of the SILs, a clear enhancement in the visibility of the defect centres was observed. Additionally, the results indicate that the SILs provide good optical and quantum compatibility with the defect centres.

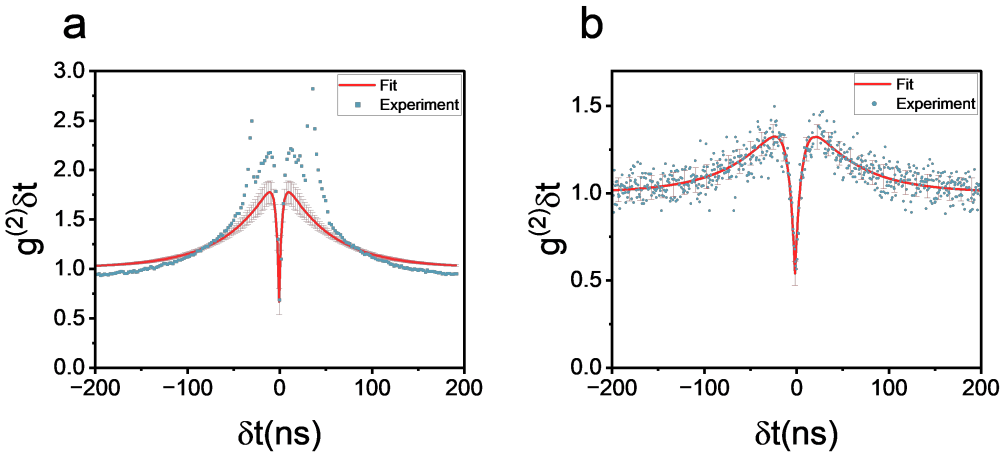


Figure 5.10: Second−order autocorrelation measurement and corresponding three−level fit for a NV^- centre in the lower quadrant of Region B prior to and post GaN SILs placed on acquired with same experimental parameters, the difference attributes to different SNR. The red curve correponds to a three−level model fitting and the red shaded region represents one sigma standard error. **a**, measurements before SILs integration, a dip is observed with $g^{(2)}(0) = 0.68$, the high pitch around 30 ns time delay attributes to a electric signal crosstalk between the SPADs. **b**, measurements after integration of GaN SILs, a dip is observed with $g^{(2)}(0) = 0.56$ with a fitted value of $\tau_1 = 9$ ns.

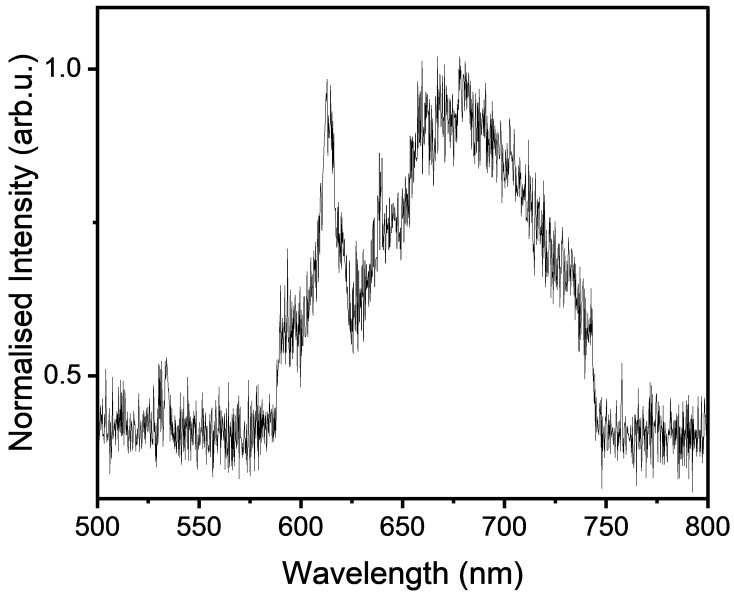


Figure 5.11: PL spectrum of the NV^- centre mentioned in Fig. 5.10 post GaN SILs placed on, a ZPL at 637 nm is observed confirming the identity of the NV^- centre, and the peak at 612-619 nm corresponds to second order Raman of from the diamond with 532 nm excitation.

5.3 Enhanced light extraction efficiency

5.3.1 Simulation

To quantify the potential improvement in collection efficiency from NV^- centres due to the transfer-printed GaN SILs, three different scenarios are investigated with finite difference time domain simulations (FDTD) performed with the commercial software 'Ansys lumerical': (i) a flat diamond substrate without any lens, (ii) a flat diamond substrate with an added GaN micro-lens, and (iii) a monolithic hemispherical SIL fabricated around the emitter, which can typically be achieved by focused ion beam milling. In all scenarios, the emitter position is set to match the focal point (i.e., the geometric centre of the lens sphere [186]) of the SILs. Fig. 5.12a illustrates all three scenarios.

Based on previous photon autocorrelation measurements, the NV^- centres involved in the lower pulse energy quadrant are composed of closely spaced emitter pairs that cannot be separately resolved. Therefore, two dipole emitters were used as the simulated light sources for all three scenarios. Each NV^- centre was modelled with two electric dipoles perpendicular to the tilted NV^- symmetry axis at a depth of 5 μm below the (100) diamond surface. To account for the two distinct dipole orientations, two separate simulations were performed and their results averaged. One of the dipoles is tilted by $90° - 54.7°$ with respect to the surface normal (since the NV^- axis aligns with one of the $\langle 111 \rangle$ crystallographic directions in the diamond lattice, which has a fixed angle of 54.7° relative to the (100) surface normal), while both dipoles remain perpendicular to the NV^- axis. Cross sections and far field projection are taken at $\lambda = 700\,\text{nm}$ wavelength. The expected collection efficiency is calculated by averaging the transmission through the detector surface above the lens (indicated in green) multiplied with the projected far field distribution from the same detector, choosing $\lambda = 650 - 750$ nm wavelength to match the spectral emission region of the NV^- centre. Both transmission and far field projection are found to be insensitive towards wavelength changes in this spectral regime, allowing us to ignore the spectral density distribution of the emission spectrum. In each

case, the substrate is a diamond with a (100) surface orientation. The monolithic SIL was modelled using the same diamond material as the substrate to maintain material continuity. For the GaN transfer−printed SILs, the AlGaN/AlN buffer layer possesses a similar refractive index to GaN, so the GaN SIL complex was approximated with a refractive index of $n = 2.4$. Fig. 5.12b illustrates the intensity cross−section through each simulation region.

In the case of the flat diamond surface (scenario i), the emitted wavefront shows significant curvature after passing through the diamond−air interface, indicating large angles of the k−vector with respect to the surface normal due to refraction at the interface. This leads to total internal reflection (TIR), trapping a substantial portion of the upwards travelling light within the diamond slab, thereby reducing external light collection. In contrast, both GaN (scenario ii) and monolithic SILs (scenario iii)preserve the shape of the wavefront after passing through the semiconductor materials, as their curvature is matched to the dipole emitter's position, effectively collimating the emitted light. The GaN SILs visibly mitigates the negative effects of TIR, while the monolithic diamond SIL fabricated by FIB milling nearly eliminates TIR entirely. The upwards directed far−field emission pattern is recorded using monitors positioned at the green lines in Fig. 5.12b. This setup allows us to assess the theoretical collection efficiency and its dependence on the NA of the collection optics. The results of the far-field projections are displayed in Fig. 5.12c.

As expected, without a SIL (scenario i), the intensity distribution is relatively weak and dispersed over wide angles. In contrast, both types of SILs (scenarios ii and iii) increase the maximum light intensity by approximately one order of magnitude. Due to the buffer layer thickness and the additive nature of the assembly process, the far-field above the GaN micro-lens shows a significant improvement, especially with collection optics of low numerical aperture (NA < 0.6). For optics with NA > 0.6, the absolute collection efficiency gains are less pronounced, as illustrated in Fig. 5.13. Employing lower numerical aperture optics could facilitate addressing multiple quantum emitters across a larger field of view, offering a potential path

to scaling quantum systems using spatial light modulators and free-space photonic integrated circuits for beam delivery [187].

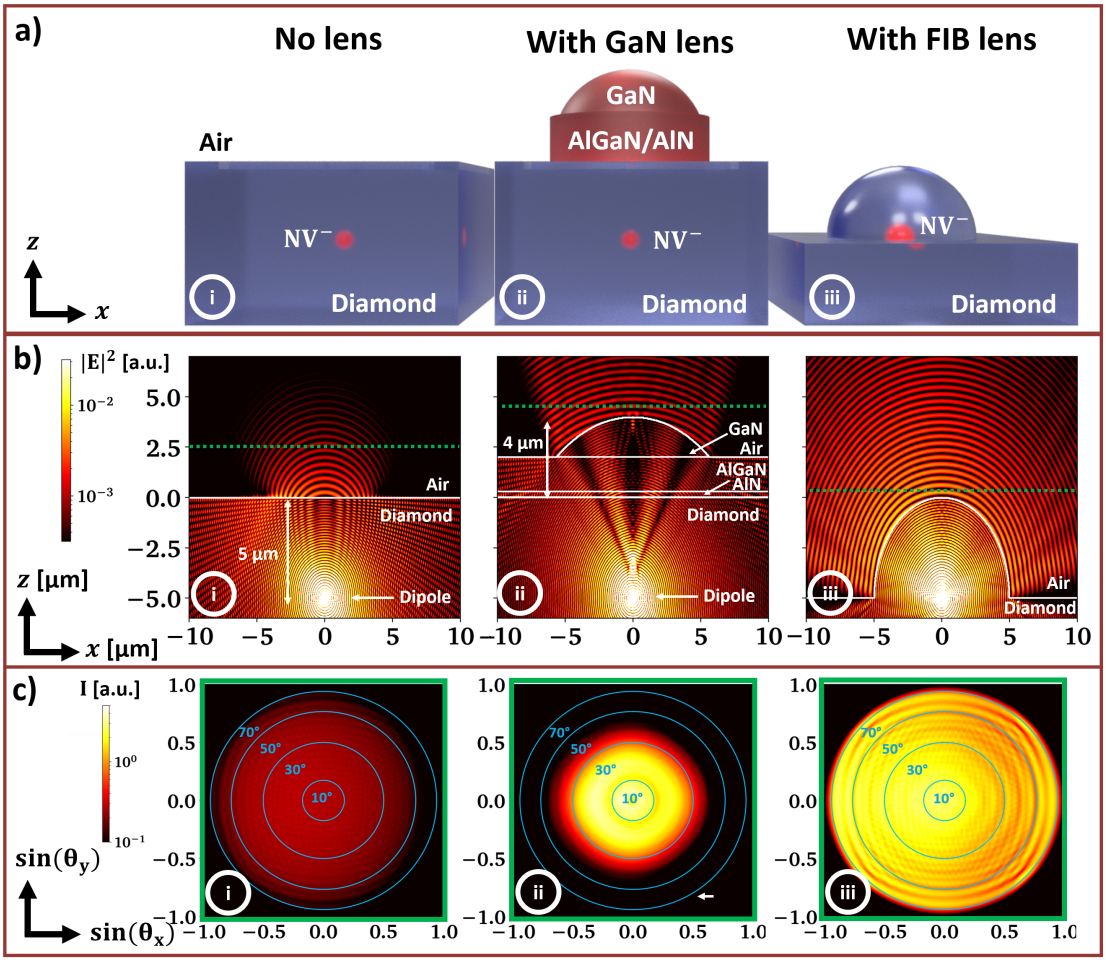


Figure 5.12: This figure is reproduced from source [34]. **a**, Schematics introducing three different cases of NV-to-free-space coupling with **b**, corresponding device cross sections from finite difference time domain simulations at $\lambda = 700\,\text{nm}$ wavelength with two dipole emitters mimicking the NV defect centre in $5\,\mu\text{m}$ depth. **c**, the far field projection in free-space above the emitter derived from the simulations in **b**, similarly taken at $\lambda = 700$ nm wavelength.

Fig. 5.13 provides detailed FDTD results for the scenario involving GaN SILs placed above NV^- doublets (pair of NV^- centres) (black line), compared to a flat diamond surface (red line). The integrated intensity at the monitor height is plotted against the far−field light cone angle, which effectively models the use of objective lenses with different numerical apertures for collection. The enhanced efficiency maximised around NA= $<$ 0.5 which gives approximately 6x of enhancement

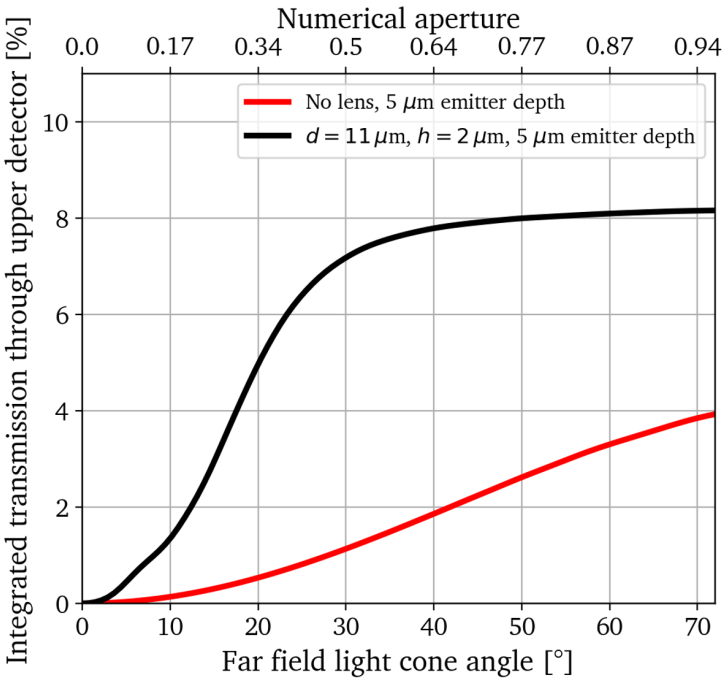


Figure 5.13: FDTD simulation results of transmission data averaged between 650−700 nm for the scenario involving GaN SILs placed above NV^- doublets (black line), compared to a flat diamond surface (red line).

factor. This enhanced efficiency saturated for higher NA and reachs around 2x of enhancement factor at NA= $<$ 0.95. These results will be compared with experimental data in the subsequent section.

Up to this point, all the simulations have assumed perfect geometrical match of the emitters and the SILs. Fig. 5.14 and Fig. 5.15 show the effect of lateral and depth displacement respectively of the emitter with respect to the focal point of the transfer-printed SIL.

Simulation results indicate that lateral displacement of emitters from the SIL focal point has different impacts depending on the NA of the objective lens used. For high NA lenses (NA = 0.95), the enhancement factor remains nearly constant within a 2 μm displacement. This stability is due to the large acceptance angles of high NA lenses, which allow them to collect light emitted across a broad range of angles. Consequently, even with a 2 μm lateral displacement, the high NA lens can capture most of the emitted light, maintaining a consistent enhancement factor. The wide angular acceptance compensates for small emitter displacements

by encompassing light paths from these off-centre positions.

In contrast, low NA lenses (NA = 0.5) experience a significant drop by about a factor of 2x in the enhancement factor for the same lateral displacement. This reduction occurs because low NA lenses have smaller acceptance angles, limiting their ability to capture light emitted at larger angles. As a result, when the emitter is displaced laterally, much of the emitted light falls outside acceptance angle of the low NA lens, leading to a decrease in the enhancement factor.

Similarly, axial (z−axis) displacement of the emitter relative to the SIL focal point affects the enhancement factor differently for low and high NA lenses. When using a low NA lens, defocusing the emitter by 2 μm along the optical axis leads to a roughly twofold decrease in the enhancement factor. In contrast, with a high NA lens, moving the emitter 2 μm deeper into the diamond substrate results in a 30% reduction, while shifting 2 μm closer to the surface increases the enhancement factor by approximately 40%. As seen in the wavefront diagrams in Fig. 5.15a, this variation arises from the angular collection characteristics of the lenses. For low NA lenses, the narrower acceptance angle cannot accommodate the shifted emission, leading to a suppression of the enhancement factor when the emitter is axially displaced. High NA lenses, however, capture a broader angular distribution, meaning that even with some spherical aberration, a shallower NV^- centre position brings more of the emission within the acceptance angle of the objective lens, resulting in an increased enhancement factor.

5.3.2 Experimental

To quantify the enhancement caused by the SILs, power saturation measurements are taken on two NV^- centre pairs in the lower quadrant of Region B before and after SIL transfer-printing using the air objective lens with NA= 0.95. The results are shown in Fig. 5.16, and as expected, the count rates of the NV centres increase with increasing laser power up to a certain saturation level, after which the count rates plateau. Pair 1 corresponds to the emitter discussed in Fig. 5.10, while pair 2 corresponds to the emitter discussed in Fig. 5.9. The data is fitted with the sum of

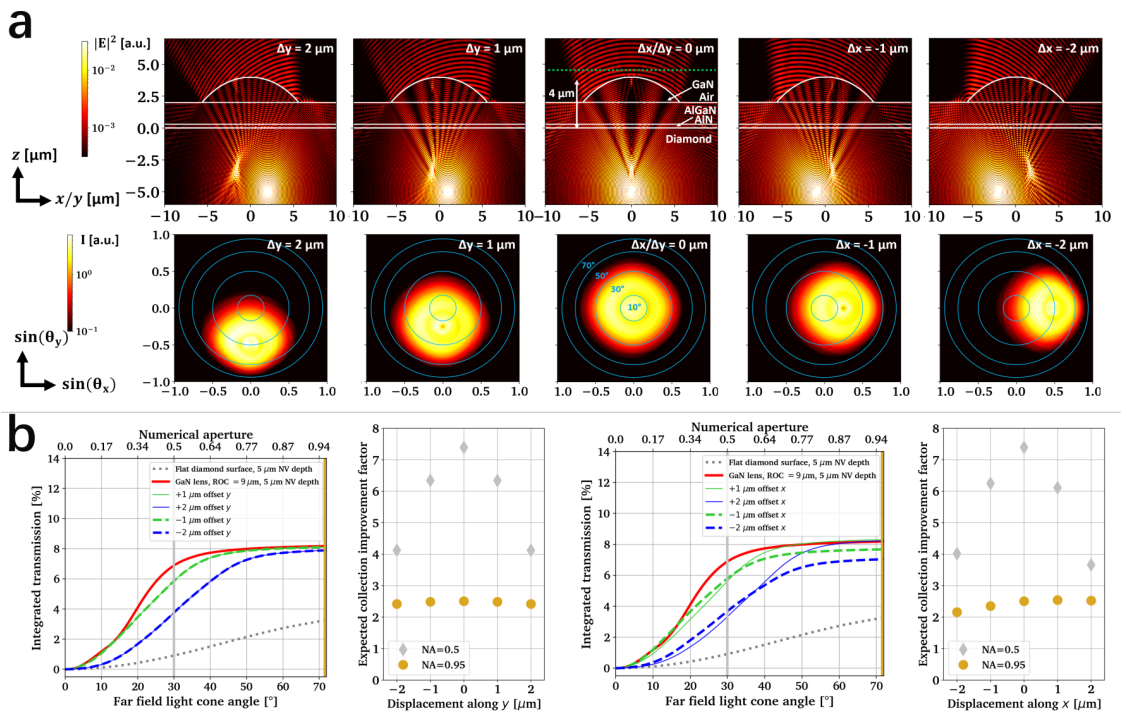


Figure 5.14: FDTD simulation of the influence of x and y displacement on the expected collection efficiency from the two dipole emitter. The radius of curvature of the GaN micro−lens is matched to the emitter depth of 5 μm. Cross sections are taken at $\lambda = 700$ nm wavelength and the transmission is averaged between $\lambda = 650 - 750$ nm wavelength. **a**, Cross−sectional field intensity profiles for lateral displacements of (Δx and Δy) of 0, 1, and 2 μm along the x−axis and y−axis. **b**, Integrated transmission versus far−field light cone angle (equivalent to numerical aperture) for different lateral displacements.

two saturation curves derived for two-level quantum systems, allowing each emitter in the focal volume its own saturation power P_{sat} and intensity I_{sat}:

$$I(P) = \frac{I_{\text{sat1}} \cdot P}{P + P_{\text{sat1}}} + \frac{I_{\text{sat2}} \cdot P}{P + P_{\text{sat2}}} \tag{5.1}$$

A single saturation curve fit describes the data equally well. This analysis yields a $(2.2 \pm 0.1)\times$ and $(1.8 \pm 0.1)\times$ enhancement of I_{sat} for pair 1 and pair 2, respectively. Similarly, a slight reduction in saturation pump power by a factor of $(1.7 \pm 0.3)\times$ for pair 1 and $(1.2 \pm 0.2)\times$ for pair 2 is observed. This is likely due to the reduction in spherical aberration that occurs at a planar interface with high index contrast [109]. We do not expect significant additional narrowing of the point spread function of the pump laser due to the transfer-printed GaN SIL, as the objective lens and SIL exhibit similar numerical apertures. However, pump

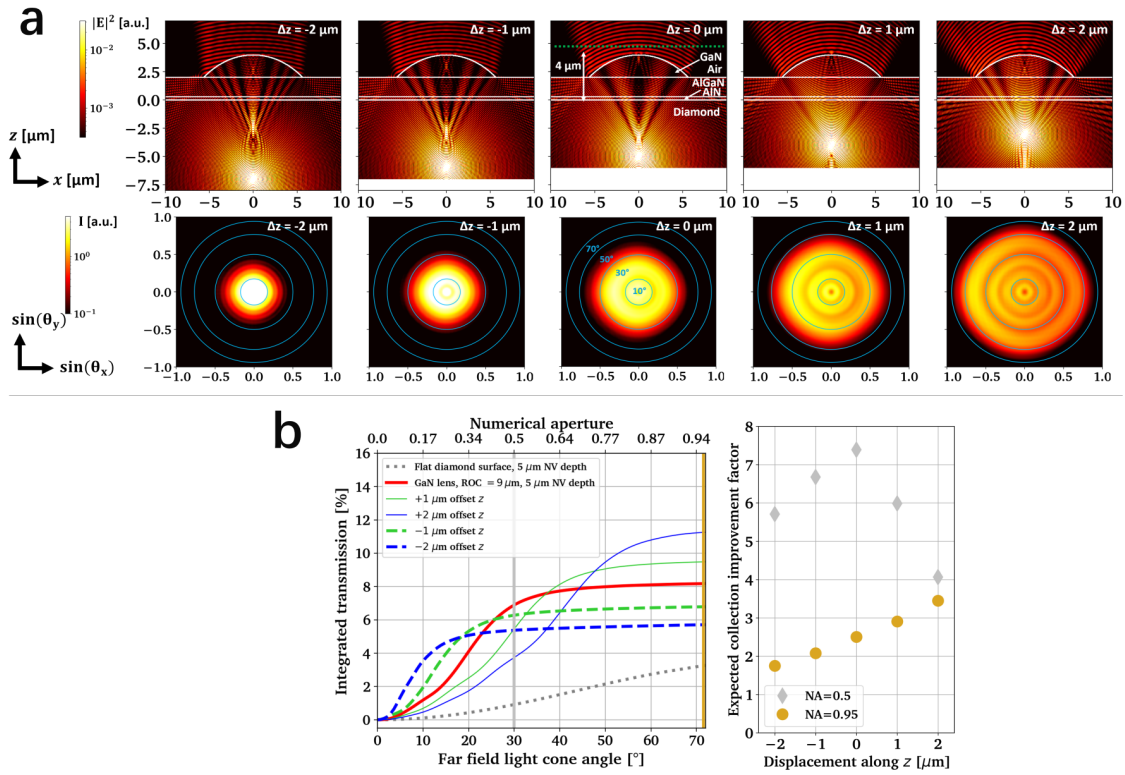


Figure 5.15: FDTD simulation of the influence of z displacement on the expected collection efficiency from the two dipole emitter. **a**, Cross−sectional field intensity profiles for axial displacements of (Δz) of 0, 1, and 2 μm along the z−axis. **b**, Integrated transmission versus far−field light cone angle (equivalent to numerical aperture) for different axial displacements.

efficiency enhancement would likely be more noticeable when using a lower NA objective, as the SIL is expected to reduce the diffraction−limited spot size.

These measurement results are compared to the expected collection enhancement derived from the simulations shown in Fig. 5.12. The transmitted light through the detector surfaces (green lines) in the air above the diamond substrate/GaN SIL is averaged over wavelengths between 650 and 750 nm. The far-field projection is similarly averaged over 650, 700, and 750 nm wavelengths. As neither transmission nor angular dependency varies strongly with wavelength, both can be multiplied to estimate light collection efficiency as a function of the acceptance angle/NA of the collection optics, without needing to weight the simulation results with the spectral density of NV^- emission. The simulation result is shown in Fig. 5.13, comparing the planar diamond surface to a GaN micro-lens with its radius of curvature matched

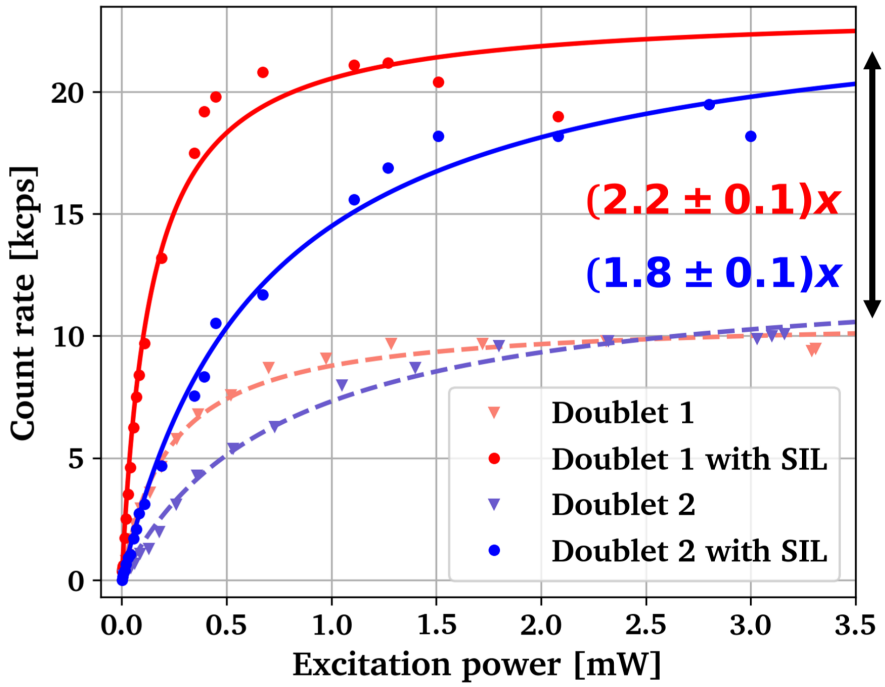


Figure 5.16: Fitted power saturation measurements of two suspected NV^- centre pairs with and without GaN SIL using an objective with NA = 0.95. Results yields a $(2.2\pm0.1)\times$ and $(1.8\pm0.1)\times$ enhancement of I_{sat} for pair 1 and pair 2, respectively.

to the emitter depth and ideal lateral alignment. The integrated transmission refers to the percentage of total light emitted by the dipole that is captured within the respective angular acceptance cone. The simulations account for Purcell enhancement, which is found to be less than 5% within the specified spectral range.

The simulations predict an improvement factor of around 2.5× for an objective lens with NA = 0.95, which is slightly higher than the experimental findings. As discussed, lateral misalignment is unlikely to explain this discrepancy, but vertical misalignment could lead to lower collection enhancement if the emitter is positioned deeper within the crystal than intended. Based on previous findings from laser writing of NV^- centres [70], the axial positioning accuracy should be within 500 nm. We estimate that an emitter located 1 μm too low could reduce the enhancement to approximately a factor of 2×, as shown in Fig. 5.15. Notably, the SIL above NV^- centre pair 1 was chosen to have a slightly larger diameter, leading to a larger ROC, which simulations predict would increase collection at larger collection NA.

Fig. 5.17 presents the power saturation results for an NV^- ensembles from the upper quadrant with and without a square−shaped SIL in Region D, as discussed in Fig. 5.6. As expected, no saturation plateau is observed for these ensemble emitters; however, the enhancement factor of approximately 2 agrees well with the simulation. Overall, the derived collection efficiency for the planar diamond surface and the monolithic diamond SIL aligns well with previous experimental and theoretical work [33, 35, 101, 107, 109, 111, 186, 188], supporting the validity of the simulations.

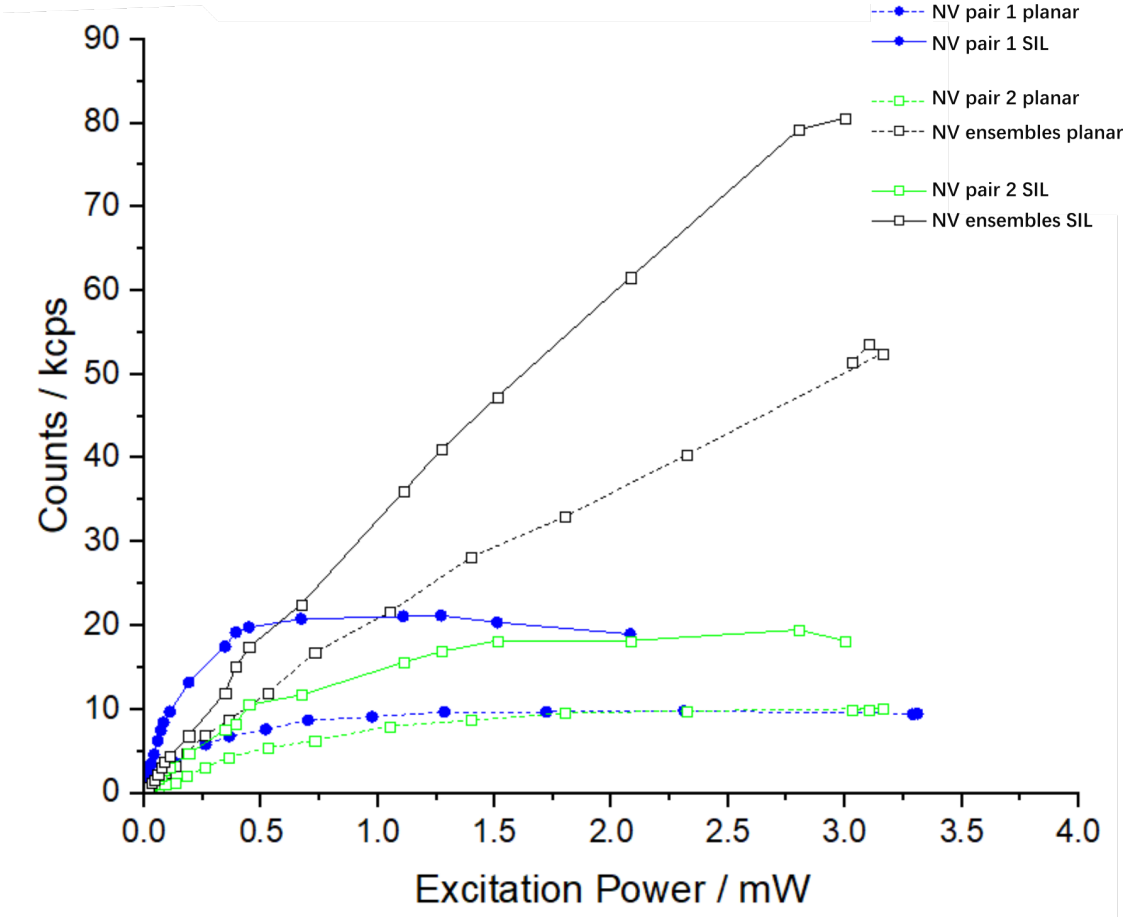


Figure 5.17: Raw power saturation measurements data of NV^- centre pairs (in green and blue) and NV^- ensembles (in black) with (solid line) and without (dashed line) GaN SIL using an objective with NA = 0.95.

5.3.3 Background analysis

As observed in the 2D PL maps, the background level within the GaN SIL is significantly higher than the baseline background from diamond without a SIL. To

better understand this, room temperature spectral analyses were conducted on the background emission from 550 nm to 800 nm for three cases: diamond without a SIL, diamond with a transfer−printed GaN SIL (as discussed in the previous section), and diamond with an AlGaN/AlN buffer layer (mesa structures). The results are shown in Fig. 5.18 (note: spectral data is uncalibrated and exhibits a 4 nm red shift).

For the pure diamond substrate, background noise primarily arises from the first-order (1332 cm^{-1}, 573 nm) and second-order (2460 cm^{-1}, 612 nm) Raman lines of diamond [189].

Apart from photoluminescence signal from these III−Nitride materials, Raman scattering must also be considered when analysing background spectral contributions. Under excitation with a 532 nm laser, characteristic Raman modes of III-Nitrides appear at specific spectral positions:

According to Raman study at room temperature by Kuball et al. [190]: For GaN, the dominant Raman modes appear at:

- E_2(high): 567 cm^{-1} (548.5 nm)
- A_1(LO): 734 cm^{-1} (552.7 nm)
- E_1(LO): 741 cm^{-1} (552.9 nm)

The AlN buffer layers contribute additional Raman features at:

- E_2(low): 248 cm^{-1} (541.7 nm)
- E_2(high): 657 cm^{-1} (550.8 nm)
- A_1(LO): 890 cm^{-1} (556.0 nm)
- E_1(TO): 670 cm^{-1} (551.1 nm)

For the $Al_xGa_{1-x}N$, the Raman depends upon composition. In the case of $Al_{0.5}Ga_{0.5}N$, the characteristic modes appear at:

- E_2(high): 615 cm^{-1} (549.7 nm)
- A_1(LO): 805 cm^{-1} (554.7 nm)

These diamond and III-Nitride Raman signals explain the sharp peaks observed in the spectra. The broad emission from 550 nm to 750 nm is attributed to photoluminescence from the GaN SIL itself, which cannot be fully excluded when using spectral filters during measurements, unless with an excitation wavelength that excited NV^- but not the GaN fluorescence. However, despite this increased background, the signal-to-noise ratio (SNR) of the NV^- centres with integrated SIL remains higher than in measurements without SIL.

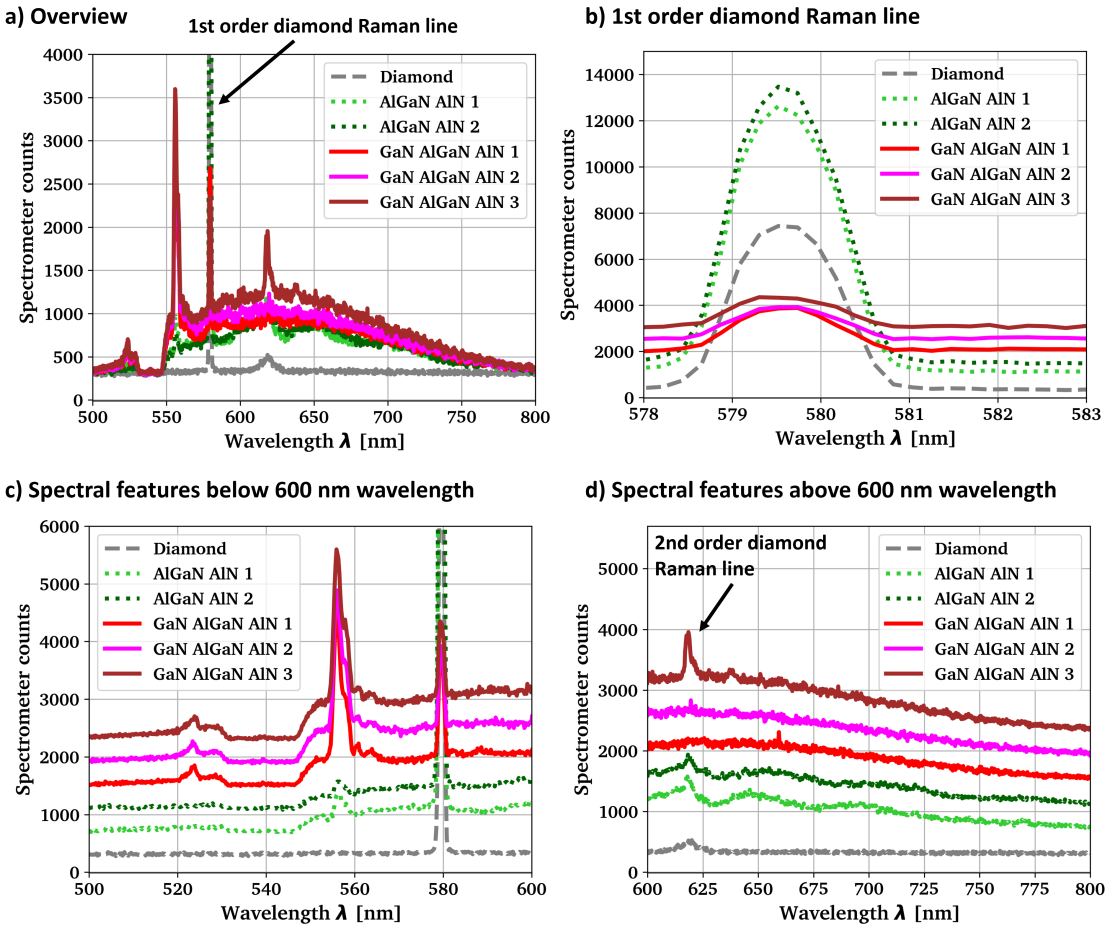


Figure 5.18: Room temperature photoluminescence spectra of transferprinted GaN lenses on AlGaN/AlN mesa structures on a single crystalline CVD grown polished diamond sample. **a**– **d** show the same spectra, which are separated linearly in **b**– **d** for better visibility.FDTD simulation of the influence of z displacement on the expected collection efficiency from the two dipole emitter.

5.3.4 Summary

This section has demonstrated the effectiveness of additive GaN micro-lenses in enhancing photon collection from diamond colour centres, using laser-written NV^- centres as a model system. This study represents the first deterministic integration of semiconductor micro-lenses, approximately 10 μm in size, with colour centres hosted in an external crystal. These results underscore the potential of high-NA, additive micro-optical components for advancing quantum technology. Experimental results reveal a photon collection efficiency enhancement of approximately 2×, which aligns well with FDTD simulations. However, the reported second-order correlation values, $g^{(2)}(0)$, were measured without background subtraction. As shown in Fig. 5.11, the spectrum includes a strong second-order Raman component that could artificially produce a dip near 0.5. Also, a single NV^- centre has two dipole orientations (associated with the E_x and E_y excited states) but remains a single emitter rather than a doublet. Thus, we cannot rule out the possibility that the NV^- centres examined are single emitters. Additionally, transfer-printed GaN SILs offer significant advantages over monolithic diamond hemispheres fabricated via FIB milling. The transfer-printing process is non-destructive and reversible, preserving the intrinsic properties of the colour centres while expediting fabrication. By avoiding lattice damage, GaN SILs maintain the optical and quantum properties of the diamond colour centres, further establishing their utility for scalable quantum technologies.

Photon collection efficiency could be further increased by positioning the colour centre closer to the diamond−air interface. According to our simulations, an emitter positioned within 1 μm of the surface could achieve an enhancement factor in the range of 4−7×. However, the collection efficiency achievable with additive GaN lenses is limited by the presence of a 2 μm thick buffer layer, a factor that does not affect monolithic hemispheres to the same extent.

A promising direction for future research is to scale the GaN micro−lens platform for transferable arrays, integrated with laser writing through the lenses themselves. This approach would enable the precise alignment of each colour centre at the midpoint of the lens sphere and reduce the depth of vacancy generation, facilitating

greater control over emitter placement[191]. Moreover, if a DBR mirror is applied to the back of a diamond membrane, with GaN SILs transfer printed on the top, it could enable cavity−enhanced emission from NV^- centres. This configuration would help address the challenge of diamond surface graphitisation when creating shallow NV^- centres.

5.4 Laser writing through monolithic SILs in 4H-SiC

5.4.1 Introduction

As described in the previous section, transfer−printing SIL structures onto pre-fabricated quantum emitters was achieved with high positional accuracy, attributed to precise alignment between emitters and alignment markers. In this section, we shift our focus to monolithic SILs.

Monolithic SILs show significant potential for enhancing photon extraction, especially with objective lens of high NA, as discussed in previous section; however, a primary challenge in scaling up the integration of quantum emitters within these structures lies in accurately positioning the emitters within the SIL region that maximises optical enhancement. Two main approaches have been developed to align single quantum emitters with photonic structures.

The first approach involves mapping the position of pre−existing emitters against an array of markers and subsequently fabricating the photonic structures based on this marker array [34], as discussed in the previous section. This method, in principle, provides positional accuracy down to a few nanometres, sufficient to achieve the strong coupling regime, and allows for the pre−selection of emitters with optimal properties for specific applications. However, this approach is time−intensive and not easily scalable for large arrays. Additionally, depending on the fabrication method, there may be concerns regarding residual damage or the introduction of high local strain around the defect sites, potentially impacting emitter performance.

A second approach involves implanting ion species to create the emitter directly within pre-existing photonic structures, typically via focused ion beam

implantation [108, 109]. This technique is effective for creating shallow emitters (less than approximately 1 μm in depth); however, it is limited by the lateral accuracy of ion placement, which is comparable to the implantation depth due to straggle effects within the material. Higher ion energies required for deeper implantation can induce substantial lattice damage, which may compromise the quantum properties of the emitters.

In this section, we demonstrate a method for registering quantum emitters at the focal points of SILs by laser−writing directly through the SIL interface, focusing the laser precisely at the desired positions. This approach eliminates the need for alignment markers, enabling a faster, scalable process suitable for wafer−level applications. Additionally, the photonic structure can enhance the electric field during laser writing, potentially removing the requirement for manual registration.

Thus far, the primary focus has been on diamond substrates. However, as discussed in Chapter 1, SiC substrates offer complementary advantages for quantum technologies, including compatibility with existing semiconductor infrastructure and greater ease of engineering, such as the fabrication of monolithic SIL arrays.

5.4.2 Scalable fabrication of monolithic SILs

The fabrication of monolithic SIL arrays were carried out by Bekker et al. [192], and the results displayed here are reproduced with permission for clarity. Their novel fabrication protocol combines greyscale lithography with hard-mask techniques to create nearly hemispherical lenses with 5 μm radius etched directly into silicon carbide substrates. The fabrication process comprises several crucial steps. Initially, a 5 μm thick silica (SiO_2) layer was deposited on 5 $\times$ 5 mm SiC chips using plasma-enhanced chemical vapour deposition. Subsequently, greyscale photoresist (ma-P 1275G) was spin-coated at 3000 rpm to achieve 8 μm thickness, followed by soft-baking at temperatures up to 100°C over 50 minutes. The exposure process utilised a Heidelberg Instruments DWL 66+ direct−writing laser lithography system, where the resist was exposed with variable dose patterns. The resist was then developed using TMAH-based solvent for 5 minutes and baked at 60°C.

A two-step etching process was then employed:

- The first step involved etching the SiO_2 layer using reactive ion etching (RIE) with $CHF_3/Ar/O_2$ gas chemistry, utilising the greyscale photoresist as a mask
- The second step consisted of etching the SiC substrate using $SF_6/Ar/O_2$ chemistry, with the patterned SiO_2 acting as a greyscale hard-mask

The entire fabrication process requires approximately 12 hours for fabricating 20,000 lenses, with 8 hours dedicated to etching. Fig. 5.19 shows a sequence of SEM image taken by Bekker et al., demonstrating a reproducable arrays of monolithic SILs fabricated. Fig. 5.19a shows a large-area view of the SIL array, revealing uniformity across hundreds of devices over a 100 μm scale. A closer examination of a 5 $\times$ 5 subset of the array (shown in b) confirms the consistency in both shape and spacing between individual SILs. The high-resolution image of a single SIL (c) reveals the hemispherical profile achieved through greyscale lithography and two-step etching process. The scanning electron microscopy (SEM) characterisation of the fabricated SIL arrays demonstrates the high quality and reproducibility of the fabrication process. Fig. 5.19a shows a large-area view of the SIL array, revealing excellent uniformity across hundreds of devices over a 100 μm scale. A closer examination of a 5 $\times$ 5 subset of the array (b) confirms the consistency in both shape and spacing between individual SILs. The high-resolution image of a single SIL (c) reveals the smooth, hemispherical profile achieved through our greyscale lithography and two-step etching process. To quantitatively evaluate the reproducibility of the fabrication method, cross-sectional profiles of multiple SILs across the array were measured. As shown in Fig. 5.19d, the profile measurements exhibit consistent height and curvature, with a maximum height of approximately 5 μm and a base width of about 12 μm. Variations between different SILs were found to be below 30%, indicating good reproducibility. While this technique is applicable to diamond, there are specific considerations and potential challenges associated with its use. Diamond's exceptional hardness and chemical resistance make it significantly more difficult to etch compared to materials such as SiC. Specialized etching methods,

such as reactive ion etching with oxygen or hydrogen plasma [193], have been developed for diamond and could be adapted for this purpose. However, due to the slower etch rate of diamond relative to SiC, the process may require longer etching times or more advanced etching equipment. Additionally, maintaining uniformity across a large array of SILs could be more challenging when using diamond, given the inherent difficulties in processing it uniformly.

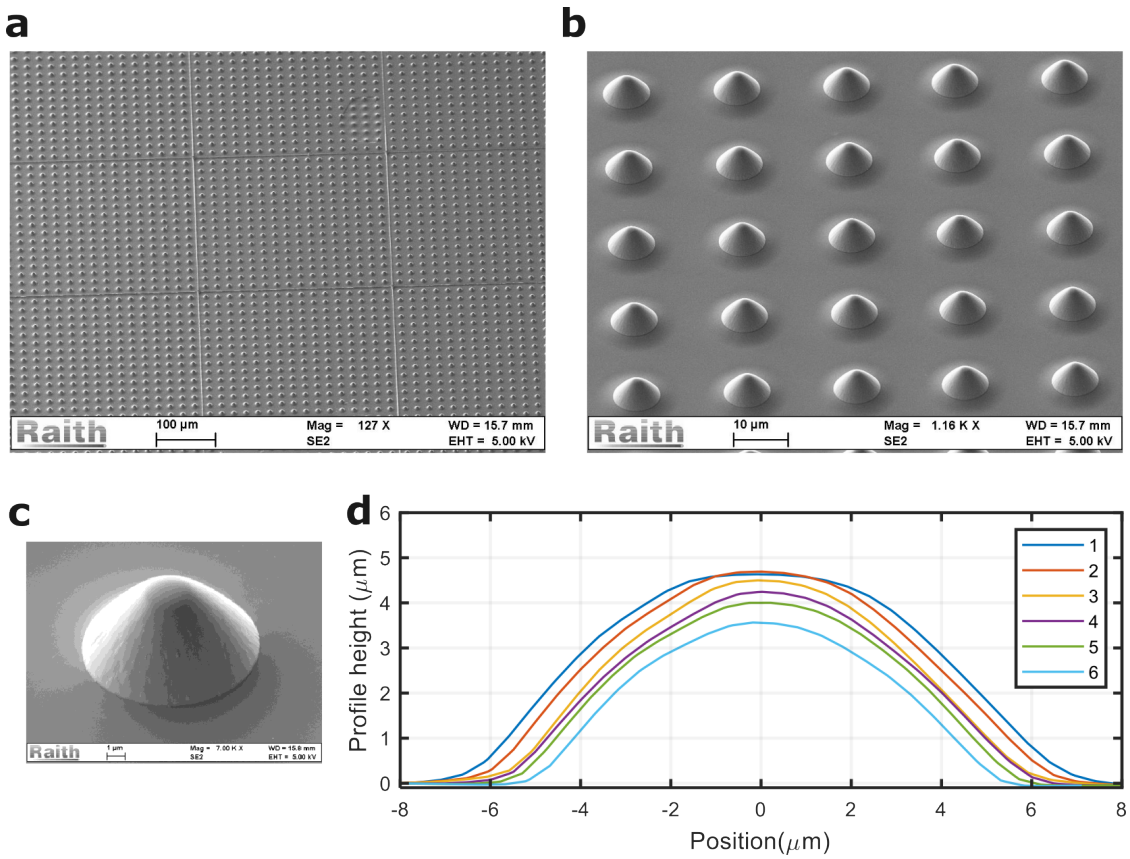


Figure 5.19: SEM characterisation of fabricated SIL arrays (adapted with permission from Bekker et al., University of Heriot-Watt). **a** Large-area SEM image showing the uniformity of the fabricated SIL array over a 100 μm scale. **b** Higher magnification SEM image displaying a 5×5 array of SILs with consistent shape and spacing. **c** High-resolution SEM image of a single SIL showing the hemispherical profile. **d**Cross-sectional profile measurements of different SILs, The measured profiles exhibit a maximum height of approximately 5 μm and a base width of about 12 μm, with variations between different SILs remaining below 30%.

5.4.3 Laser writing process

The laser fabrication process for creating quantum defects in 4H-SiC is illustrated in Fig. 5.20. This method utilises a 4H−SiC sample with arrays of pre−fabricated SILs, as outlined in the previous section. As discussed in Chapter 3, laser writing is conducted using a regeneratively amplified Ti:Sapphire laser source, which produces 250 fs pulses at a wavelength of 790 nm and a repetition rate of 1 kHz. The laser is focused through a high−NA oil immersion objective lens (Olympus 60×, 1.4 NA).

Two laser writing techniques were implemented:

- **Single seed pulse:** A single femtosecond laser pulse with adjustable pulse energy was directed to selected focal points within the 4H-SiC sample, with optimised abberation correction inside the 4H-SiC. The level of lattice damage introduced was controlled by adjusting the pulse energy, this applies to both planar and SIL interfaces. This single seed pulse was used to generate V_{Si} defects within the lattice.

- **Single seed pulse with additional diffusion pulses:** Following the initial seed pulse, additional diffusion pulses with lower energy were applied to the same focal point, monitored via a live SPAD fluorescence feedback loop. The diffusion pulses were ceased upon detecting a step up in the SPAD trace, accompanied by a brightness increase in the CCD signal at the focal point (see Fig. 5.21). This rise in SPAD counts indicated successful creation of fluorescent defects. The aim of the process is to stabilise the V_{Si} defects by the diffusion pulses, which act as an annealing mechanism to remove nearby unwanted defects, enhancing the stability of the V_{Si} defects [194].

For single seed pulse mode, when writing through a planar interface, the depth was set to 5 μm to match the radius of the hemispherical monolithic SILs (illustrated by the red spots in Fig. 5.20), with aberration corrections optimised to shape the focus into a diffraction-limited Gaussian spot as seen on the CCD camera. The pulse energy was adjusted through the HWP and a Glan-laser polariser to achieve minimal visible lattice damage. For writing through the SIL, during fabrication,

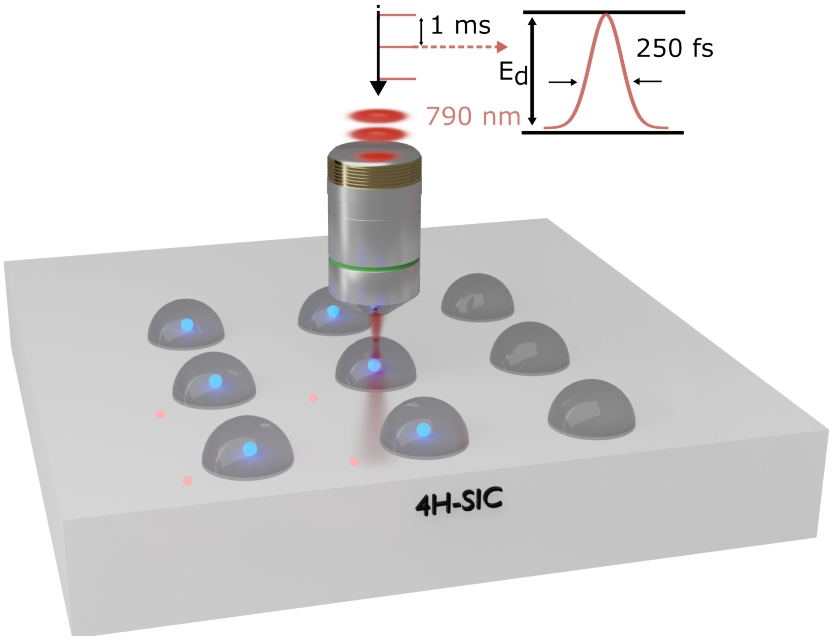


Figure 5.20: Schematic illustrating the process of femtosecond laser writing through planar and SIL interfaces inside 4H−SiC substrate. The target depth for writing through planar interface is 5 μm (indicating in red spots), mathching the radius of the monolithic SILs., which is the target depth for writing through SIL interface is the radius of the SIL (indicating in blue spots).

the laser was focused through the SIL to its central axis at a depth corresponding to the sample's planar surface, as shown by the blue spots in Fig. 5.20.

In the single seed pulse with diffusion pulses mode, the focal position of the diffusion pulses remained consistent with that of the seed pulse, but the pulse energy was reduced by approximately 70% to prevent additional defect generation while providing sufficient energy to mobilise local defects. Fig. 5.21a and b display CCD images of a SIL taken live in the laser processing system, during the seed pulse and the diffusion pulses. The green square marks the laser focus position, and the diffusion pulses were turned off once a bright signal appeared in Fig. 5.21b. Fig. 5.21c shows the corresponding SPAD trace captured during the laser writing process. A step increase in PL count rates was observed when the single seed pulse was applied to the SiC lattice, followed by a further step increase after approximately 10 s of diffusion pulses. Further details of this process are discussed in a later section.

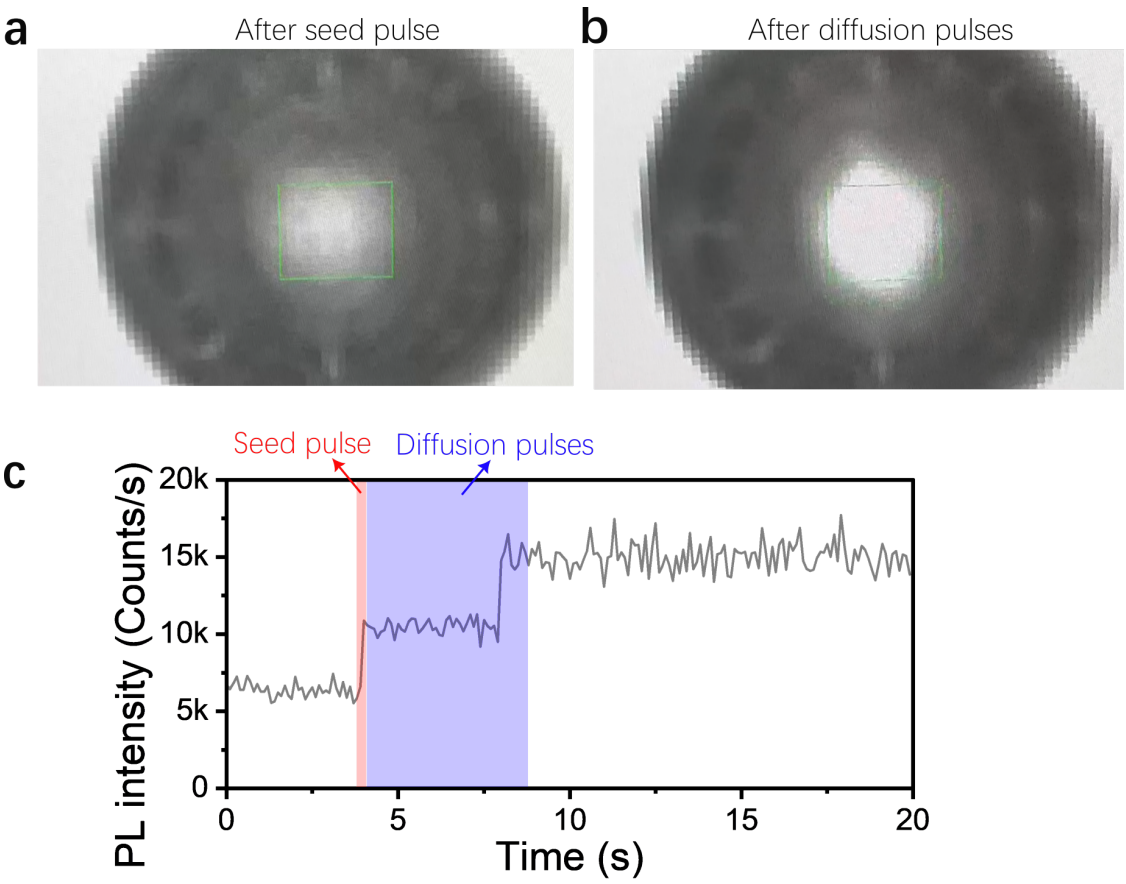


Figure 5.21: CCD images during the laser fabrication of a SIL in the 4H−SiC sample, the green box indicates the position of the fabrication laser focus, where **a** shows the image after seed pulse and **b** shows the CCD image after diffusion pusles. The diffusion pulses were turned off once this bright signal was observed. **c**, SPAD trace recorded during the fabrication with a sampling time of 50 ms, the red square indicates the time where single seed pulse was delivered to the lattice and the blue square indicates the operation window of the diffusion pulses.

5.4.4 Characterisation of laser written array with 532 nm excitation source

PL image

A custom-built confocal microscope with 532 nm excitation was used to investigate the PL of the single pulse−damaged array at room temperature. Fig. 5.22 presents a series of XY and XZ 2D PL images for defects created with high pulse energy (a,b) and low pulse energy (c,d). These PL images indicate that the defect centres are located near the centre of the SIL, both laterally and axially, approximately aligned with the SIL's focal plane.

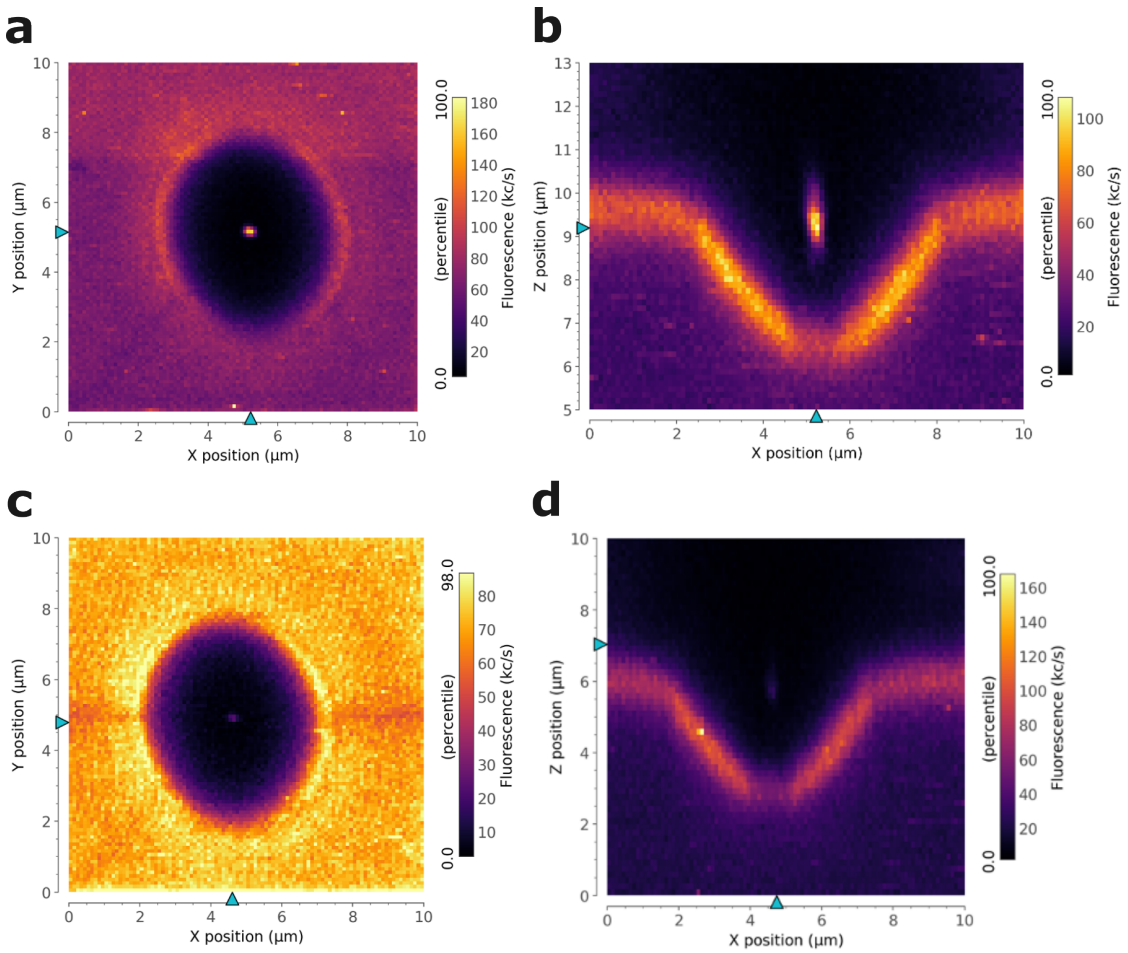


Figure 5.22: 2D PL images of laser written defect centres through SIL interface excited with 532 nm CW laser. **a,b** XY and XZ spatial maps, respectively, of PL intensity distribution for defects created using high pulse energy. **c,d** Corresponding XY and XZ PL intensity maps for defects generated with low pulse energy. The defect centres are spatially localised near the geometric centre of the SIL in both lateral (XY) and axial (XZ) dimensions, demonstrating alignment with the SIL's focal plane.

The elongated point spread function (PSF) in the XZ scan is attributed to the increased Abbe resolution (as discussed in Chapter 2), as described in Eqn 5.2.

$$d_{\text{resolution}} = \begin{cases} \frac{\lambda}{2(\text{NA}\times n_{\text{SiC}})} & \text{for lateral (XY) plane} \\ \frac{2\lambda}{(\text{NA}\times n_{\text{SiC}})^2} & \text{for axial (Z) direction} \end{cases} \tag{5.2}$$

where:

λ = wavelength of light

NA = numerical aperture of objective

n_{SiC} = refractive index of SiC

With monolithic SIL, $\mathrm{NA_{eff}} \approx n_{\mathrm{SiC}} \approx 2.6$ and $\lambda = 532$ nm:

$$\begin{aligned} d_{\mathrm{lateral}} &= \frac{\lambda}{2\mathrm{NA_{eff}}} \\ &= \frac{532 \text{ nm}}{2(2.6)} \\ &\approx 102 \text{ nm} \\ d_{\mathrm{axial}} &= \frac{2\lambda}{(\mathrm{NA_{eff}})^2} \\ &= \frac{2(532 \text{ nm})}{(2.6)^2} \\ &\approx 158 \text{ nm} \end{aligned} \tag{5.3}$$

The estimated resolution aligns well with the PL images of defect centres created at low pulse energy, demonstrating diffraction-limited behaviour. For high pulse energy, however, increased lattice damage produces an extended emission region, deviating from a diffraction-limited point source.

To investigate the impact of pulse energy, both SIL and planar interfaces were studied. For the SIL interface, Fig. 5.23a shows a 2D PL map of an array of SILs before any laser fabrication. Figs 5.23b and c display SIL arrays fabricated with decreasing pulse energies from left to right. Only selected SILs are shown, with panel (b) representing the array created at the highest pulse energy (5.51 nJ) and panel (c) showing the array fabricated at the lowest pulse energy (1.65 nJ), where PL emission is still detectable under 532 nm excitation.

For the planar interface, the results are presented in Fig. 5.24. The written array is located within box-shaped alignment markers, with each row aligned to point-shaped markers to indicate consistent pulse energy across the array. Pulse energy is higher in the right panel and decreases from top to bottom within each panel, ranging from 20 nJ to 3.24 nJ.

Comparing the PL maps of SIL and planar interfaces reveals a common trend: increasing pulse energy results in higher PL intensities. Additionally, the monolithic SILs allow for defect creation at lower pulse energies and offer enhanced light extraction, as evidenced by the generally higher PL intensities of defect centres within the SIL compared to the planar interface. Since the monolithic SIL influences

both the writing process and light collection, a direct comparison to extract an enhancement factor is not feasible. However, plotting the single seed pulse energy against the PL intensities provides further insight into the laser writing mechanisms with single seed pulse, which will be discussed in the following sections.

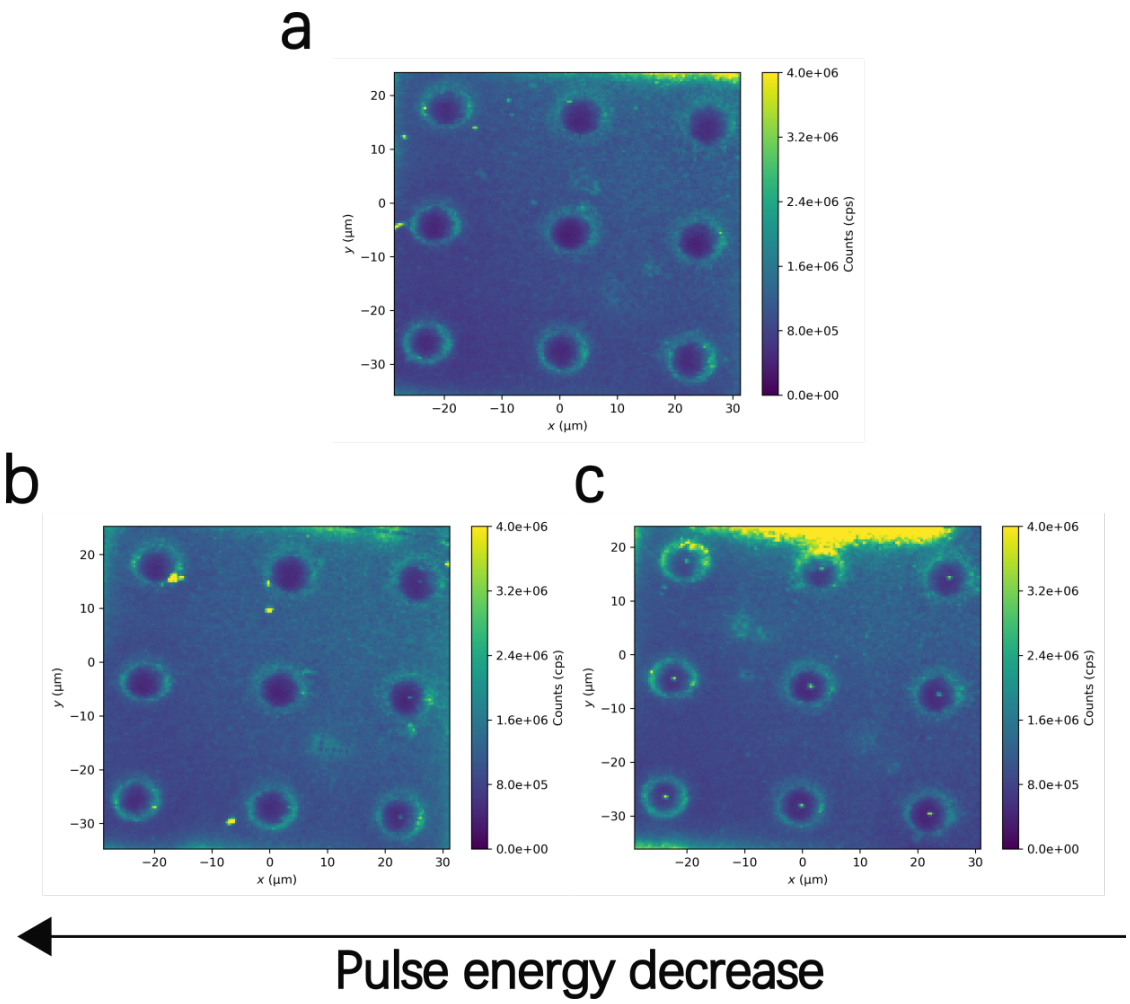


Figure 5.23: 2D PL mapping of SIL arrays under 532 nm excitation with various written pulse energy. **a** Reference PL map of the SIL array prior to laser fabrication. **b,c** PL intensity distributions of laser written SIL arrays fabricated with decreasing pulse energies from right to left: **b** The very right column indicates highest pulse energy of 5.51 nJ and the very left column in panel **c** indicates lowest pulse energy of 1.65 nJ.

Laser writing mechanism

Throughout these measurements, the excitation power of the 532 nm CW laser was maintained at 1 mW. In both SIL and planar configurations, a consistent trend was observed: the PL emission brightness decreased with decreasing pulse energy.

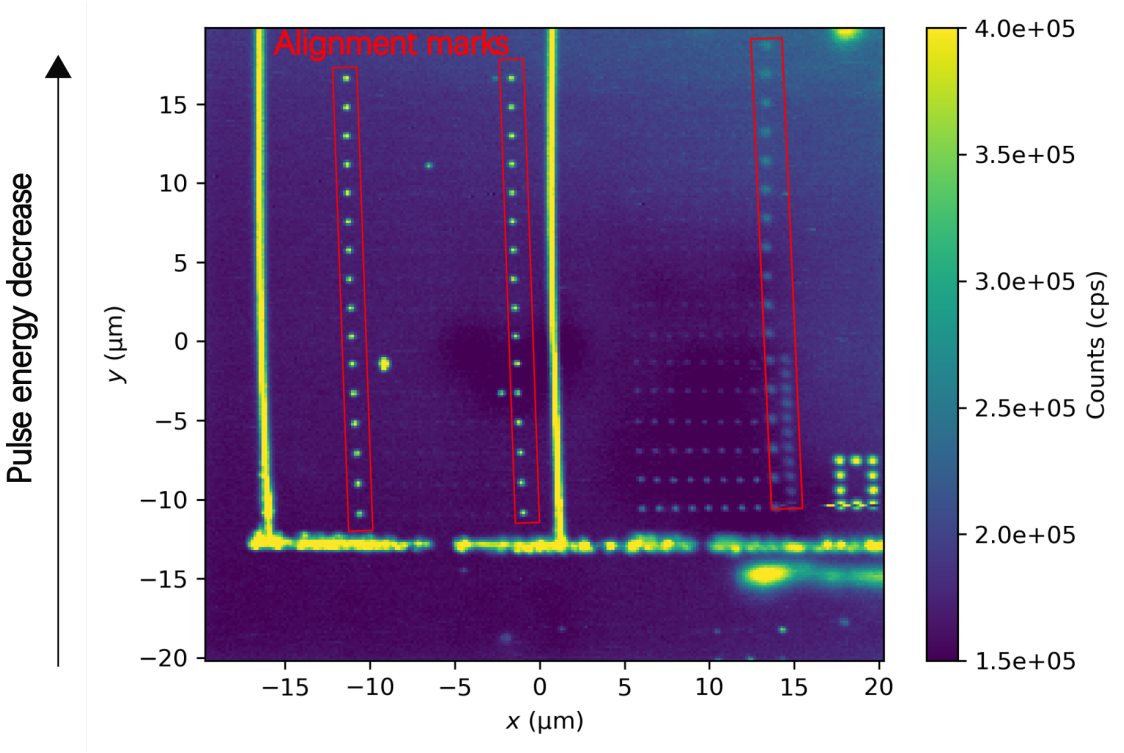


Figure 5.24: 2D PL map showing laser-written defect arrays through a planar interface.The arrays are positioned within box-shaped alignment markers, with individual rows aligned to point markers. Each row corresponds to a constant pulse energy, with energy decreasing from top to bottom within each panel. The pulse energy ranges from 20 nJ to 3.24 nJ, with higher energies used in the right panel.

This correlation between pulse energy and PL emission is illustrated in Fig. 5.25, where the blue and red curves represent the PL intensities as a function of pulse energy for defects fabricated through the SIL and planar interfaces, respectively. The data clearly show that defect formation shifts to lower pulse energies in the SIL configuration, attributed to the NA enhancement provided by the SIL. Additionally, higher PL intensities are observed in the SIL configuration, which is attributed to the enhanced PL collection efficiency enabled by the SIL. For each pulse energy level, data were collected from five SILs written in a single column, each fabricated using the same pulse energy. The recorded intensities represent the arithmetic mean across these five SILs.

The hypothesis is that the laser writing process generates silicon vacancies (V_{Si}^{-}s) in the 4H-SiC sample. While 532 nm excitation cannot effectively excite V_{Si}^{-}, broad emission is still observed [195]. As discussed in Chapter 2, defect

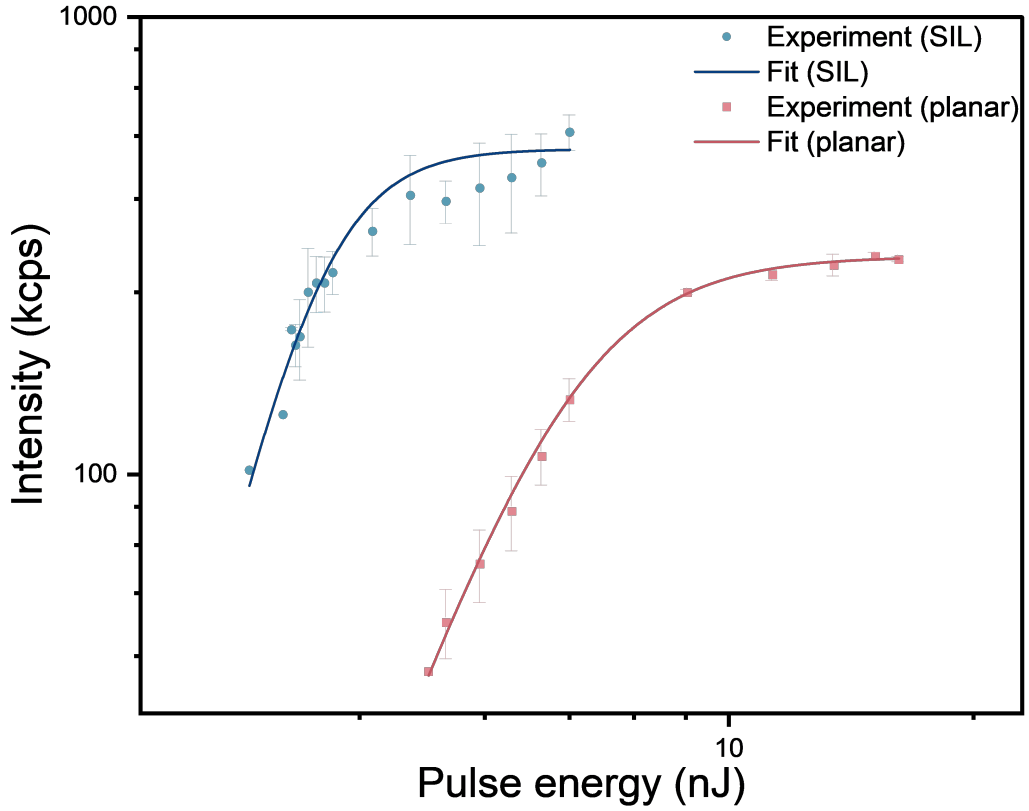


Figure 5.25: PL intensity as a function of pulse energy for defect fabrication through SIL (blue) and planar (red) interfaces. Data points represent experimental measurements with associated uncertainties, whilst solid lines show power law fits incorporating a saturation model. The planar interface data demonstrates excellent agreement with the model ($R^2 = 0.999$), exhibiting PL intensity saturation at approximately 8 nJ with a power law exponent of $n = 3.67 \pm 0.15$ and maximum intensity of 200 kcps. The SIL interface data ($R^2 = 0.983$) yields a higher power law exponent of $n = 5.75 \pm 0.21$ and reaches a maximum intensity of 515 kcps at saturation. Both y-axis (PL intensity) and x-axis (pulse energy) are plotted on logarithmic scales.

generation by ultrafast laser pulses in transparent materials is typically modelled by three mechanisms: multi-photon ionisation (MPI), tunnelling ionisation (Zener breakdown), and avalanche ionisation, as detailed in Chapter 3. Based on Chen's model for GR1 generation [196], the 250 fs laser pulses used here are shorter than the characteristic timescales of thermal diffusion (ns) [82], allowing thermal effects to be neglected. The transition between MPI and tunnelling ionisation is described by the Keldysh parameter [123]. MPI dominates over tunnelling ionisation when $\gamma > 1$, corresponding to:

$$I < \frac{mcn\epsilon_0 E_g \omega^2}{e^2} \tag{5.4}$$

The material constants are first substituted: $m = 0.37, m_\mathrm{e} = 3.370 \times 10^{-31}\,\mathrm{kg}$, $n = 2.6$, $E_g = 4.46\,\mathrm{eV} = 7.150 \times 10^{-19}\,\mathrm{J}$, and $\omega = 2.4 \times 10^{15}\,\mathrm{s}^{-1}$. The intensity threshold is then calculated:

$$I < \frac{(0.37 \times 3.370 \times 10^{-31})(2.6)(8.854 \times 10^{-12})(7.150 \times 10^{-19})(2.4 \times 10^{15})^2}{(1.602 \times 10^{-19})^2}$$

yielding

$$I < 1.382 \times 10^{17}\,\mathrm{W/m^2}$$

The pulse energy E is derived from the intensity threshold I_th and pulse duration τ:

$$E = I_\mathrm{th} \times \tau \times \pi w^2 \tag{5.5}$$

Substituting $I_\mathrm{th} = 1.382 \times 10^{17}\ \mathrm{W/m^2}$, $\tau = 300 \times 10^{-15}\ \mathrm{s}$, and $w = 350 \times 10^{-9}\ \mathrm{m}$:

$$E = (5.34 \times 10^{12})(300 \times 10^{-15})\pi(350 \times 10^{-9})^2 \tag{5.6}$$

$$E \approx 1.59 \times 10^{-8}\ \mathrm{J} = 16\ \mathrm{nJ} \tag{5.7}$$

For comparison, key parameters affecting this threshold between diamond and 4H-SiC are summarised in Table 5.1.

Parameter	Diamond	4H-SiC	Unit
Effective mass (m)	$0.40m_\mathrm{e}$	$0.37m_\mathrm{e}$	–
Refractive index (n)	2.4	2.6	–
Band gap (E_g)	7.1	3.23	eV
Threshold energy	68.0	16	nJ

Table 5.1: Comparison of material parameters and calculated threshold energies for diamond and 4H-SiC

For very high pulse energies, the MPI effect does not dominate, and additional energy may not create new defects due to saturation of available defect sites (at this stage, defect recovery processes may actively counteract defect creation upon high pulse energy). Unlike Chen's approach, I consider an additional saturation model alongside the power law to better capture the defect generation behavior at high pulse energies:

$$I(E) = \frac{aE^n}{1 + kE^n} \tag{5.8}$$

where:

- $I(E)$ represents the intensity of defect generation or the extent of material modification as a function of pulse energy E, correlating with the number of defects created or the degree of damage induced by the pulse energy.
- aE^n, describes a standard power-law relationship, where a is a scaling factor and n is the power-law exponent. This term models the initial rapid increase in defect generation with increasing pulse energy, typical of MPI and defect creation processes when saturation effects are negligible.
- $1 + kE^n$, accounts for the saturation effect. As pulse energy increases, the term kE^n becomes significant, reducing the rate at which new defects are generated. This models the physical limitation where available defect sites are exhausted or damage saturation occurs, meaning that further increases in energy yield diminishing returns in defect generation.
- k is the saturation parameter, determining how quickly the saturation effect becomes significant. A larger value of k indicates that saturation occurs at lower pulse energies.

At low pulse energies ($E \ll 1$), the denominator approaches unity, and the equation simplifies to a standard power law, $I(E) \approx aE^n$, indicating a rapid increase in defect generation with increasing energy. At high pulse energies ($E \gg 1$), the denominator grows significantly due to the term kE^n, causing $I(E)$ to asymptotically

approach a limiting value of a/k. This limiting behaviour reflects the saturation of defect generation, where additional increases in pulse energy produce negligible new defects. In this regime, the reduction in defect generation may also be attributed to laser-induced lattice recovery or localised melting, which counteracts further damage.

The experimental results show the following for the SIL interface:

- Power law exponent $n = 5.75 \pm 0.15$
- Saturation parameter $k = (12.5 \pm 1.26) \times 10^{-3}$

and for the planar interface:

- Power law exponent $n = 3.67 \pm 0.15$
- Saturation parameter $k = (1.83 \pm 0.43) \times 10^{-3}$

As shown in Fig. 5.25, the fit agrees very well ($R^2 = 0.999$) with data obtained from the planar interface, showing PL intensity saturation around 8 nJ. This aligns with the Keldysh prediction of MPI dominance below 8.7 nJ. The number of photons involved in defect generation was $n = 3.67 \pm 0.15$, with each photon energy of 1.57 eV, resulting in a combined energy of 5.8 ± 0.24 eV. This value, below the displacement energy for Si (66 eV) and C (24 eV) in 4H-SiC [197], suggests defect formation through electronic excitation, phonon generation, or point defects without direct atomic displacement. An alternative explaination would be that the defect generated is not or not only V_{Si}^{-} but a combination of different defects, thus the PL spectra is studied in the later session.

The discrepancy in the extracted n values may be attributed to the higher effective NA when writing through the SIL interface. This higher NA results in underestimation of the total photon flux in the model, thereby yielding a higher effective photon absorption. The observed data shift for writing through SILs indicates additional focusing effects and photon collection enhancement provided by the SILs. This observation supports the dual role of SILs in enhancing both photon collection and laser writing.

Spectral analysis

To investigate the origin of the observed PL emission, room temperature spectroscopy was performed on the laser-written arrays. The spectral features were similar for both the planar and SIL interfaces across different pulse energies; only the intensities varied, while the spectral shape remained consistent for defect centres fabricated with a single seed pulse. However, the spectral features differed for defect centres created using a seed pulse followed by additional diffusion pulses. Fig. 5.26a shows a representative spectrum for a defect centre fabricated with both seed and diffusion pulses, while Fig. 5.26b shows the spectrum for a defect centre created with a single seed pulse.

The spectra from sites fabricated with both a seed pulse and additional diffusion pulses exhibit a broad emission peak centred at 730 nm, ranging from 600 nm to 800 nm. The cut off at 800 nm attributes to the dichroic mirror used during the measurements and the decrease in quantum efficiency of the spectrometer at red wavelengths. This emission profile aligns with the reported characteristics of the carbon antisite-vacancy pair ($C_{Si}V_C$) [61] ensembles. The $C_{Si}V_C$ defect centre consists of a carbon atom occupying a silicon site (C_{Si}, the antisite) adjacent to a carbon vacancy (V_C), shedding light on the formation mechanism during laser fabrication. The initial seed pulse generates V_{Si}^- and V_C vacancies, which are generally optically inactive under 532 nm excitation. The subsequent diffusion pulses provide enough energy to overcome a small energy barrier [198], allowing these vacancies to transform into the $C_{Si}V_C$ structure.

In contrast, spectra from sites fabricated with only a single seed pulse display a broad emission ranging from 600 nm to 750 nm (with a sharp cut-off at 580 nm due to the dichroic mirror's forbidden band). This emission does not align well with the reported characteristics of V_{Si}^- under 532 nm excitation [195], prompting further investigation with a 780 nm CW laser in the next section.

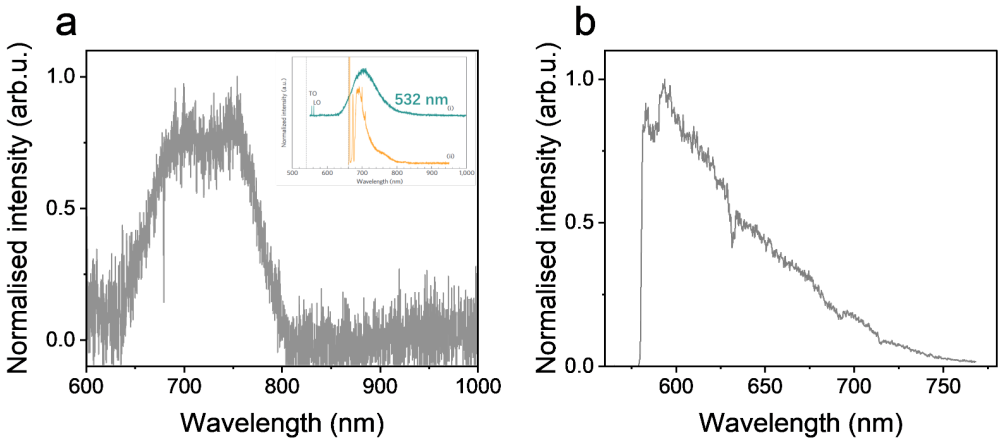


Figure 5.26: Normalised PL spectra of laser written defect centres. **a** Representative spectrum from a defect centre created using both seed and diffusion pulses, showing a broad emission peak centred at 730 nm (ranging from 600 nm to 800 nm), characteristic of the carbon antisite-vacancy pair ($C_{Si}V_C$). Inset shows results from Castelletto et al. [61] spectrum of ($C_{Si}V_C$) centres under 532 nm CW excitation. **b**Spectrum from a defect centre fabricated using a single seed pulse, exhibiting broad emission between 600 nm and 750 nm, with emission below 580 nm suppressed by the dichroic mirror's forbidden band.

5.4.5 Characterisation of laser written array with 780 nm excitation source

Measurements using a 780 nm CW laser as the excitation source were conducted by Alexander Jones and Christiaan Bekker from the University of Heriot-Watt and reproduced and analysed by myself with their permission.

As discussed in the previous section, 532 nm excitation of single seed pulse-written centres did not yield the characteristic spectral features of V_{Si}^- emission. Therefore, a 780 nm CW laser was employed as an alternative excitation source. Optical characterisation, including PL mapping, power saturation, spectroscopy, and HBT measurements, was performed using a custom-built cryostat confocal microscope.

The array under study is a single seed pulse region written through the SIL interface, which remained undetectable with green laser excitation at a pulse energy of 1.8 nJ. Fig. 5.27a shows a PL image of a representative SIL at 4 K, and Fig. 5.27b illustrates the saturation behaviour of the colour centre. A fitting curve for a single emitter, described by Eqn 5.9, shows that the count rate of the emitter

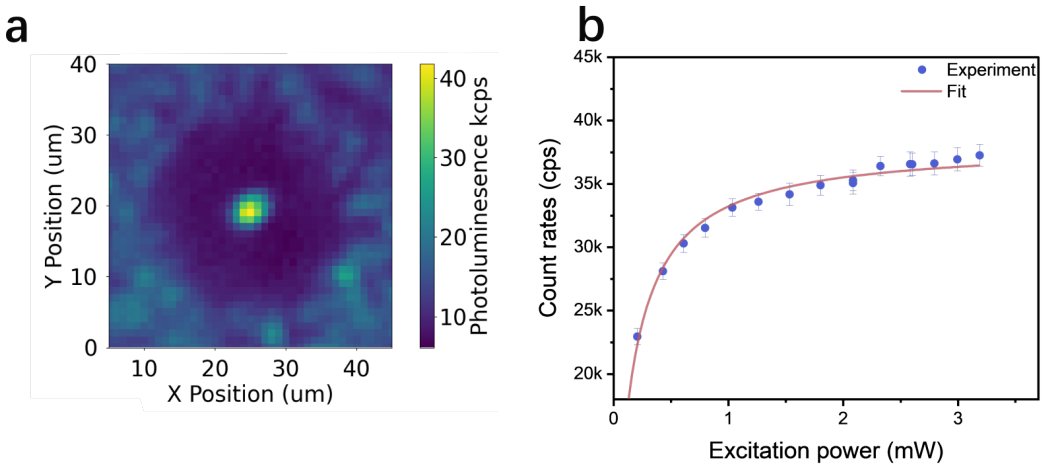


Figure 5.27: Characterisation of a single seed pulse laser written defect centre through SIL interface at 4 K using 780 nm CW excitation. **a** 2D PL image showing localised emission from the defect centre. **b** Power-dependent emission characteristics displaying saturation behaviour typical of a single emitter. The solid line represents a fit to the experimental data (blue dots), yielding a saturation intensity $I_{\text{sat}} = (38.1 \pm 0.37)$ kcps and saturation power $P_{\text{sat}} = (0.15 \pm 0.01)$ mW.

increases with laser power until reaching a saturation level, beyond which the rate plateaus. Fitting results yield a saturation intensity I_{sat} of (38.1 ± 0.37) kcps and a saturation power P_{sat} of (0.15 ± 0.01) mW.

$$I(P) = \frac{I_{\text{sat}} \cdot P}{P + P_{\text{sat}}} \tag{5.9}$$

To further verify the identity of the emitter, a 4 K spectrum was taken, with the background-subtracted result displayed in Fig. 5.28. A sharp ZPL at 861 nm was observed, characteristic of V1 emission [56] from the V_{Si}^- centre in 4H-SiC, thus confirming the presence of a V_{Si}^- centre. To confirm that this V_{Si}^- centre corresponds to a single emitter, an HBT measurement was performed, as shown in Fig. 5.29. The second-order autocorrelation function, $g^{(2)}(\delta t)$, reveals a dip at $\delta t = 0$, with $g^{(2)}(0) = 0.35$, indicative of single photon emission as expected for a Fock state (discussed in Chapter 2). Fitting an analytic function for a three-level system (according to Eqn 4.2) to the $g^{(2)}(\delta t)$ histogram yields $\tau_1 = 7.0$, corresponding to an estimated lifetime of 7.0 ns. This value is slightly higher than the previously reported 5.5 ns lifetime for V_{Si}^- centres [56], potentially due to local strain variations introduced by the fabricated SIL.

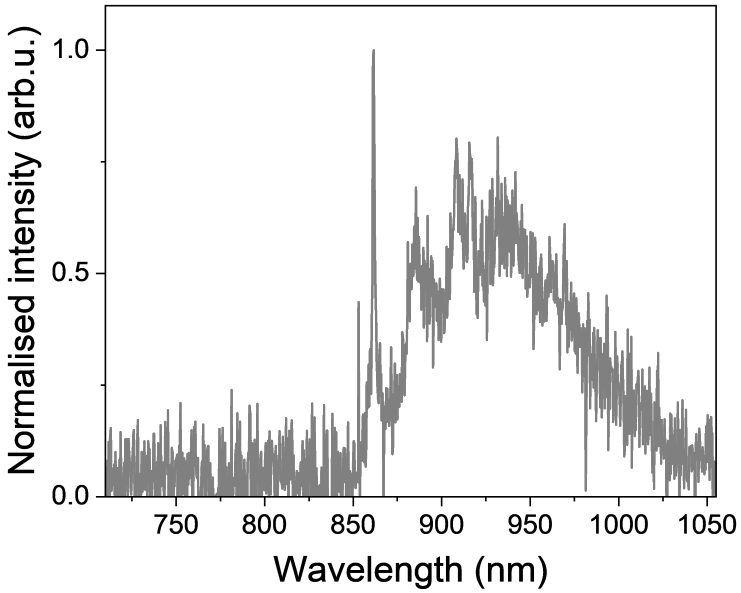


Figure 5.28: Normalised cryogenic PL spectrum of a single seed pulse laser written defect centre through SIL interface. A sharp ZPL presents at 861 nm and correponding PSB ranges up to 1050 nm, characteristic of V1 emission from the V_{Si}^{-} centre in 4H-SiC.

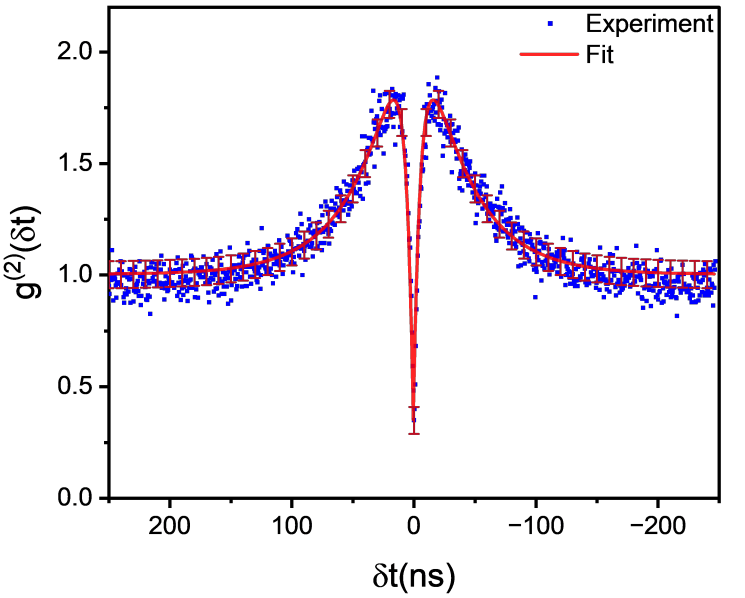


Figure 5.29: Second−order autocorrelation measurement and corresponding three−level fit for a V_{Si}^{-} centre inside SIL. A dip is observed with $g^{(2)}(0) = 0.35$, indicating single photon emission behaviour. The red curve correponds to a three−level model fitting with fitted values $\tau_1 = 7.0$ ns. The red shaded region represents one sigma standard error.

5.4.6 Summary

In this section, we explored the laser fabrication of quantum defects in 4H-SiC, focusing on the effects of pulse energy and the role of SILs in enhancing both defect creation and photon collection efficiency. Our study involved both planar and SIL interfaces, with systematic examination of laser parameters and defect formation mechanisms.

We initially investigated defect centre fabrication using single seed pulses and single seed pulses followed by diffusion pulses with live PL feedback during fabrication. SIL structures enabled the creation of defects at lower pulse energy thresholds and enhanced PL intensities compared to the planar interface. Detailed PL mapping and spectroscopy revealed that defects created with both seed and diffusion pulses exhibited distinct spectral features, suggesting the formation of carbon antisite-vacancy ($C_{Si}V_C$) centres, in agreement with previous studies [61].

Further characterisation with a 780 nm CW laser confirmed the presence of V_{Si}^- centres in defects created with only a single seed pulse in the SIL interface. Power saturation measurements showed typical single-photon emission behaviour, with saturation intensities and power values indicating efficient excitation of V_{Si}^- centres. The observed zero-phonon line (ZPL) at 861 nm confirmed the V1 emission characteristic of V_{Si}^- centres [56]. HBT measurements further validated these centres as single-photon emitters, with a second-order autocorrelation value of $g^{(2)}(0) = 0.35$.

The effect of pulse energy on PL emission was consistent for both SIL and planar interfaces, with higher pulse energies generally leading to stronger PL intensities. However, SIL structures allowed for defect creation at lower pulse energies and significantly enhanced photon extraction, with PL intensities within SILs surpassing those of the planar interface. Although direct calculation of enhancement factors was limited by the dual influence of SILs on both writing and collection, plotting pulse energy against PL intensity offered further insights into laser writing mechanisms. This suggests that defect formation occurs through electronic excitation and hot charge carriers generation without direct atomic displacement.

Overall, this section has demonstrated the effectiveness of SILs in enhancing both defect creation and photon collection in 4H-SiC, supporting the potential of SIL-assisted laser fabrication for scalable quantum technologies. This work represents the first demonstration of laser-written single defects inside monolithic SILs and only the second reported demonstration of single V_{Si}^{-} centres in SiC, following the work by Chen et al. [86]. In addition to replicating prior results, this study provided further insights into key defect formation mechanisms and the influence of laser parameters, thereby establishing a foundation for optimising the production of quantum emitters in wide bandgap materials.

Furthermore, the findings highlight the potential for employing laser diffusion in SiC to fabricate carbon antisite-vacancy pairs. Future work could focus on using 780 nm laser excitation within a live fluorescence feedback loop to deterministically generate single V_{Si}^{-} centres inside SILs, further demonstrating 4H-SiC's viability for scalable quantum networks.

5.5 Discussion

This chapter has described the idea of combining the unique advantages of 3D spatial control with high positioning accuracy and for both defect centres and alignment marks inside bulk transparent materials of laser writing and enhanced light collection efficiency of SIL by reducing the total internal reflection. Two different approaches are discussed: (a) a top−down approach where emitters were fabricated with alignment marks that visible with normal transmission microscope, SILs were then integrated with the bulk lattice via transfer printing with the aid of alignment marks pointing out the position of written defects and reaches sub−micron positioning accuracy of the transfer printed SIL. (b) a bottom−up approach where arrays of monolithic hemispherical SILs were fabricated in advance via greyscale lithography with hard−mask techniques. Subsequent laser writing allows addressing defect centres that aligns well with the SIL focus spatially. Both approaches were first carried out down to a single emitter level, and address the issues that is currently facing: scalable approahc of arrays of quantum emitters with high yields.

This chapter has presented the integration of quantum emitters with SILs inside bulk transparent materials, combining the unique advantages of three-dimensional spatial control and high positioning accuracy aided by femtosecond laser writing techniques. By enhancing light collection efficiency through the reduction of total internal reflection, these methods aim to improve the performance of quantum emitters for applications in quantum technologies.

Two different approaches were discussed:

(a) **Top-down approach:** Emitters were fabricated alongside alignment marks that are visible under normal transmission microscopy. SILs were then integrated with the bulk lattice via transfer printing, utilizing the alignment marks to indicate the positions of the written defects. This method achieved submicron positioning accuracy for the transfer-printed SILs. The enhancement factors are validated with good agreement between experimental and FDTD simulation results.

(b) **Bottom-up approach:** Arrays of monolithic hemispherical SILs were prefabricated using greyscale lithography with hard-mask techniques. Subsequent laser writing was then employed to create defect centres that were precisely aligned with the focal points of the SILs. In this configuration, the SILs not only facilitated spatial alignment but also enhanced the writing process by reducing the pulse energy required to generate defect centres. Additionally, the SILs helped refocus the fabrication laser, directing it to the SIL focal positions for optimal precision.

To our knowledge, both approaches were the first work demonstrating at the single-emitter level, addressing the current challenges in developing scalable arrays of quantum emitters with high yields. By demonstrating precise spatial alignment and enhanced light collection efficiency, these methods represent significant progress toward the practical integration of quantum emitters for quantum technology applications.

The top-down approach benefits from the direct integration of SILs with predefined emitters, achieving high positioning accuracy through the use of visible alignment marks. However, scalability may be limited due to the complexity of the transfer printing process when applied to large-scale fabrication. Conversely, the bottom-up approach inherently supports scalability by creating SIL arrays before emitter fabrication, though it demands precise control over both lithography and laser writing processes to ensure accurate alignment.

Future work will focus on optimizing these techniques for scalability and integration into complex quantum systems. This includes refining fabrication processes to improve yield and uniformity, exploring automated alignment methods, and investigating new materials and defect centres with enhanced performance. This leads to scalable arrays of quantum emitters with high yields, contributing significantly to the progress of quantum computing, communication, and sensing technologies.

6

Laser written interdigitated electrode devices

Contents

6.1 Introduction 181
6.2 Device Fabrication 183
6.2.1 Design 183
6.2.2 Device characterisation 186
6.3 Surface electrode patterning 188
6.4 Discussion 195

6.1 Introduction

To investigate further, we base our study on Griffiths's hypothetical model [83], which suggests that self-trapped biexciton recombination induces Frenkel defect formation during femtosecond laser writing. Supported by rate-equation simulations consistent with experimental data, this model describes a multi-stage process of defect formation triggered by femtosecond laser pulses:

(i) **Carrier Generation**: Upon exposure to an ultrafast laser pulse, electrons are excited from the valence to the conduction band through multiphoton

absorption and avalanche ionisation. This process generates a dense electron-hole plasma over a few femtoseconds.

(ii) **Carrier Relaxation and Thermalisation**: After excitation, high-energy carriers rapidly thermalise via carrier-carrier scattering, forming a high-temperature electron-hole gas. This gas cools as energy transfers to the lattice through electron-phonon scattering, bringing carriers and lattice to a quasi-equilibrium state within approximately 30 picoseconds.

(iii) **Biexciton Formation and Self-Trapping**: As carriers cool further, excitons (bound electron-hole pairs) form. At sufficient densities, biexcitons (bound pairs of excitons) develop, self-trapping and localising energy near the defect site. This self-trapping creates a deformation potential of approximately 1.74 eV, straining atomic bonds within the diamond lattice.

(iv) **Nonradiative Biexciton Recombination and Energy Transfer**: The self-trapped biexcitons undergo nonradiative recombination, transferring energy directly to the lattice without photon emission. This localised energy transfer reaches around 8.9 eV, sufficient to break a carbon-carbon bond, thus forming the Frenkel defect. This energy surpasses the 7.14 eV threshold required for defect formation in diamond.

(v) **Barrier Crossing and Defect Formation**: For complete Frenkel defect formation, an additional energy barrier of roughly 0.5 eV must be crossed. This barrier is overcome via localised lattice heating from carrier-phonon scattering, resulting in a vacancy at the original atomic site and an interstitial carbon atom nearby, finalising the defect.

Although experimental data strongly support these theoretical predictions from a coupled rate-equation model, it is important to recognise that these data provide indirect, rather than direct, evidence for the model's validity. The experiments rely on fluorescence imaging of the GR1 peak associated with vacancy formation in diamond, which serves as a proxy measure for defect presence but does not capture

real-time carrier dynamics. Such dynamics are essential for directly observing the processes proposed in the model, especially the charge carrier concentration.

A more direct approach, such as monitoring the photocurrent generated during laser interaction, could offer definitive insights into carrier behaviour and recombination dynamics. Photocurrent measurements would provide real-time data on electron-hole generation, transport, and recombination, enabling quantitative validation of the rate and energy distribution among charge carriers. This technique would allow for a more precise alignment of theoretical predictions with experimental observations and, if validated, could enable control over light-matter interactions through applied bias to modulate charge carrier concentration around the interaction regions.

These considerations motivate the design and fabrication of a device with optical access for laser fabrication and electrical access for in-situ photocurrent measurements. Such a device would enable the application of bias to control light-matter interaction dynamics effectively.

6.2 Device Fabrication

6.2.1 Design

For diamond, despite being a wide-bandgap material, the Wannier-Mott exciton model is appropriate due to its band structure and high dielectric constant. The Bohr radius can be calculated using:

$$r_{ex} = \frac{\varepsilon_0 h^2}{2\mu e^2} = 2.49 \times 10^{-10} \text{ m} \tag{6.1}$$

where:

- $\varepsilon_0 = 8.854 \times 10^{-12}$ F/m (vacuum permittivity)
- $h = 6.626 \times 10^{-34}$ J·s (Planck's constant)
- $\mu = 2.256 \times 10^{-31}$ kg (reduced mass, assuming 0.57m_e)
- $e = 1.602 \times 10^{-19}$ C (elementary charge)

The electric field required to dissociate the exciton with a binding energy of 80 meV [199] is:

$$E = \frac{E_{bind}}{qr_{ex}} = \frac{80 \text{ meV} \times 1.602 \times 10^{-19} \text{ J}}{1.602 \times 10^{-19} \text{ C} \times 2.49 \times 10^{-10} \text{ m}} = 3.21 \times 10^{8} \text{ V/m} \tag{6.2}$$

At room temperature (25 meV), the required field reduces to 2.2×10^8 V/m. For electrode separations of 5 and 10 microns, the required bias voltages are:

An operating voltage of 2.2 kV exceeds the safe operational window. Additionally, if the separation between the interdigitated electrodes is set at 1 μm, the intact area available for laser writing becomes insufficient. Therefore, a spacing of 2 μm was chosen for the interdigitated electrodes.

Due to the limitations of laser writing techniques in fabricating shallow (<2 μm) Frenkel defects, the defects created would be at a minimum depth of 5 μm within the diamond. Consequently, it is necessary to embed the interdigitated electrodes within the bulk of the diamond rather than on its surface, which restricts the options available for electrode material.

Previous studies [200–202] have demonstrated the creation of graphitic wires as conductive pathways by using femtosecond lasers to locally convert sp^3 hybridised carbon into sp^2 hybridised carbon, thereby altering the diamond's properties to resemble those of graphite locally. The application of adaptive optics corrections during laser fabrication improves wire quality by reducing resistance and barrier potential through consistent laser focus across the depth of the diamond.

The proposed device design is illustrated in Fig. 6.1. Fig. 6.1a presents a top view at the depth of the laser-written electrode, indicated by the black and purple solid lines. Five arrays of interdigitated electrodes are patterned, with pulse energy decreasing incrementally from array 1 to array 5, yielding electrodes with varying resistance. The red-squared regions represent laser-written axial electrodes that extend to connect with the coated surface electrode layers on both sides, as shown in Fig. 6.1b. This configuration provides electrical access from both sides of the surface, depending on which side is utilised for optical access.

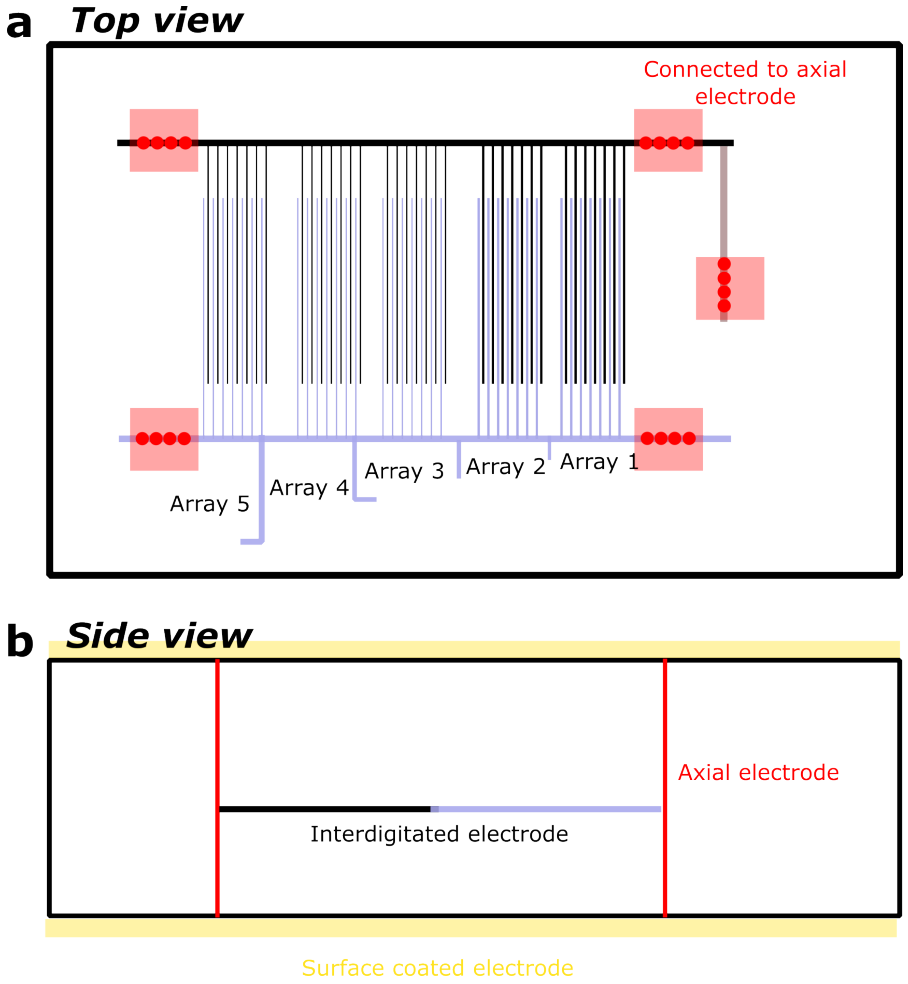


Figure 6.1: Schematic representation of the device configuration. a Top view illustrating the laser-written electrode layer, denoted by the black and purple lines. Five arrays of interdigitated electrodes are fabricated, with decreasing pulse energy from Array 1 to Array 5, resulting in electrodes of varying resistance. The red-highlighted regions correspond to laser-written axial electrodes that extend to connect with the coated surface electrode layers. **b** Side view showing the axial electrodes bridging the interdigitated electrodes to the surface-coated layers on both sides. This dual-access design permits electrical connectivity from either surface, depending on the orientation used for optical access.

For ease of device connection, the surface is coated with a conductive layer consisting of 10 nm of chromium and 100 nm of gold. This layer is patterned using a femtosecond laser (detailed in later section), creating five pads (regions A to E), each connected to the laser-written axial electrodes, as shown in Fig. 6.2 b. Additionally, a large square region is patterned to isolate any potential short circuits along the edge of the coating layer. These five pads enable independent control and measurement of different sections of the interdigitated electrode device. The structure is designed to be flip-chip bonded onto a carrier wafer containing a reciprocal electrode structure, which is connected to an external biasing system via wire bonds. Optical access is provided from the top, ensuring compatibility with optical measurement techniques.

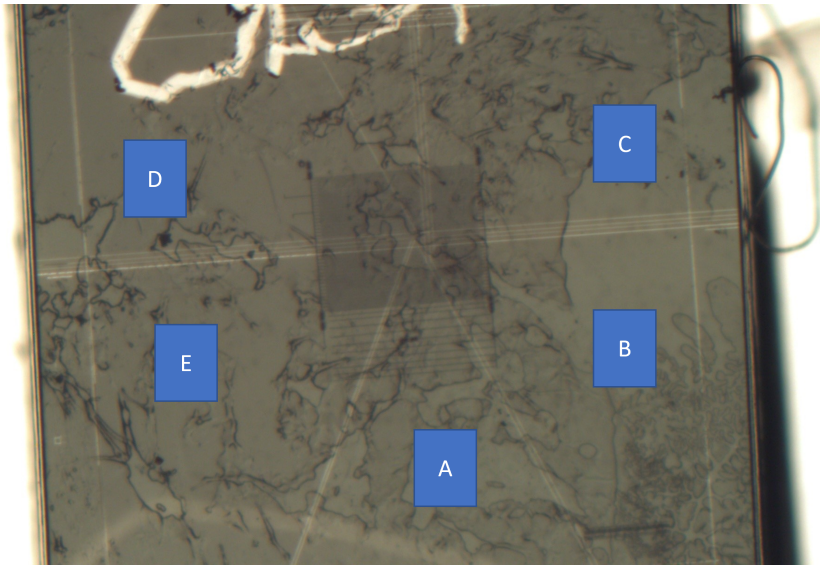


Figure 6.2: Patterned conductive layer and electrode pads. The device surface is coated with a conductive layer comprising 10nm chromium and 100nm gold. This layer is patterned using a femtosecond laser to create five distinct pads (A–E), each connected to the laser-written axial electrodes (see Fig. 6.2b). A large square region is also patterned to prevent potential short circuits along the coating's edges. The five pads allow for independent electrical control and measurement of different sections of the interdigitated electrode device.

6.2.2 Device characterisation

The device consists of two types of electrodes: those embedded within the bulk diamond and surface electrodes located on the diamond surface. The primary

purpose of the device is to connect the laser-written electrodes inside the bulk diamond to the coated surface electrodes. The surface electrode pads are then linked to an external bonder substrate, which can be connected to a PCB board for ease of integration. Before bonding to an external bonder, characterisation was performed on the surface electrodes patterned by the femtosecond laser.

Although optical microscope images (Fig. 6.2) show that the femtosecond laser successfully removed the surface coating, revealing the diamond surface and confirming successful patterning, the possibility of short circuits remained uncertain. To address this, optical profilometry measurements were carried out on the device centre. Fig. 6.3 presents data acquired in phase scanning mode of the junction regions. While phase scanning has height limitations, restricted to differences within a single fringe cycle (in this case ±20 nm) unless phase unwrapping techniques are employed, it offers a larger lateral scan range with sufficient accuracy for lateral dimensions. Fig. 6.3b shows the vertical line profile indicated by the red line in Fig. 6.3a. The results reveal that four edges were consistently cut to disconnect the surface electrodes from the pads. The width of the removal trace was measured to be consistently 2 μm, demonstrating the precision and repeatability of the technique. However, since the height limitation prevented confirmation of whether the coated materials were completely removed within the traces, further electrical characterisation was performed.

To evaluate the electrical performance of the device, probe measurements were conducted using a Keithley sourcemeter as the voltage supply. Different tips were connected to various pads, and a bias of ±50 V was applied to two of the five pads while measuring the resulting current. As illustrated in Fig. 6.2, pad ED is connected via the interdigitated electrode (represented by the purple line in Fig. 6.1) embedded within the diamond. Pads AB, BC, and AC are connected via the interdigitated electrode (shown by the black line in Fig. 6.1). Figure 6.4 displays the measured IV curves for different pad connections. As expected, closed-circuit behaviour was observed for pads connected by the laser-written electrodes (ED, BC, and AB), while open-circuit behaviour was recorded for unconnected pads

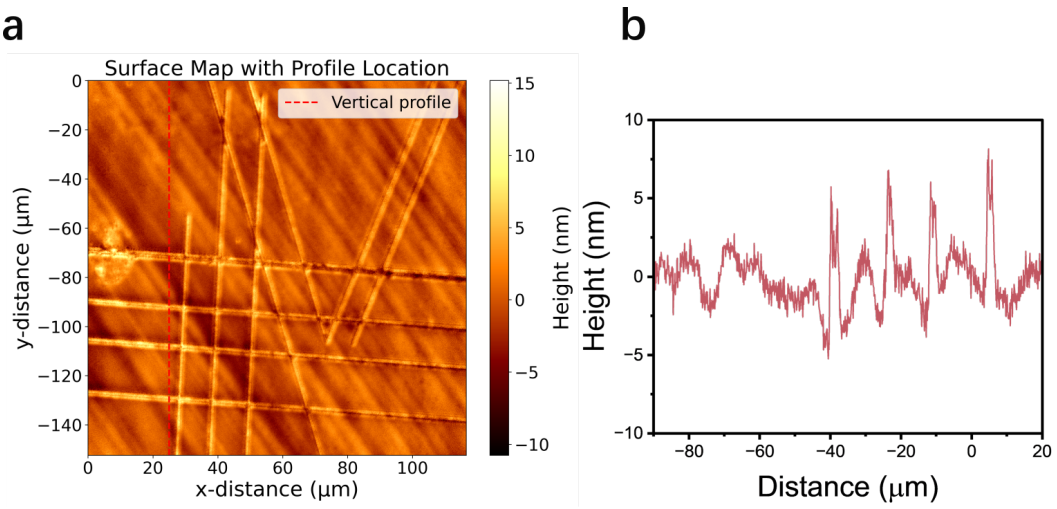


Figure 6.3: Optical profilometry surface map and profile of junction regions. a Phase scanning mode surface map of the junction regions, showing the vertical profile location (red line). **b** Vertical line profile corresponding to the red line in (a), revealing four consistent edge cuts that disconnect the surface electrodes from the pads. The removal trace width was consistently measured at 2μm, demonstrating high precision and repeatability.

(BD). For the closed-circuit configurations, a resistance of approximately 0.6 MΩ was measured, consistent across all pad connections.

These results indicate that with a 2 μm separation, the interdigitated electrodes show no signs of short-circuiting. Furthermore, the femtosecond laser surface patterning of the electrode was successfully achieved, demonstrating the potential for an entirely optical-based device fabrication technique.

6.3 Surface electrode patterning

In this section, we perform an edge roughness analysis of laser-written patterns on the sample surface to quantitatively assess the quality of the laser writing process. This approach parallels the dose test commonly used in lithography [203], where edge quality variations are evaluated to determine optimal exposure parameters. We apply a similar methodology here to investigate the quality of laser-patterned surface electrodes. A regeneratively amplified Ti:Sapphire source, operating at a wavelength of 790 nm with a pulse duration of 250 fs and a repetition rate of 1 kHz, was used to pattern the surface electrodes. A commercially available electronic-grade single-

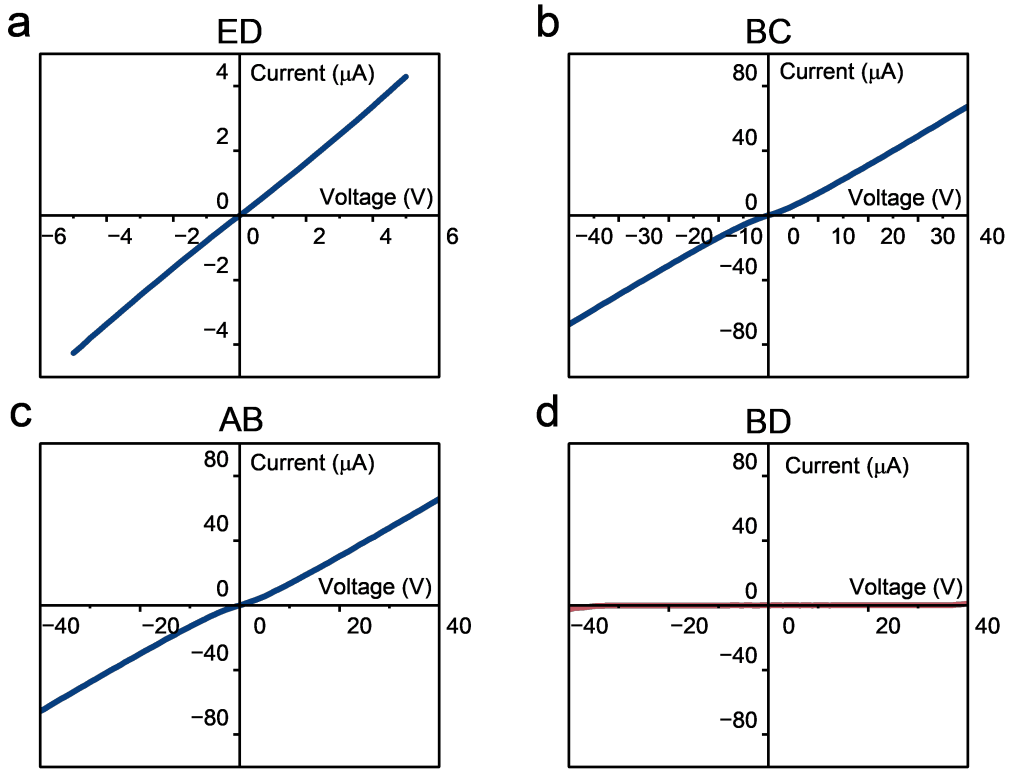


Figure 6.4: IV curves for different pad connections. Electrical performance of the device was evaluated using a Keithley sourcemeter to supply a voltage bias of ±50V between selected pads, with the resulting current measured. **a** Pad ED, connected via the interdigitated electrode embedded within the diamond, exhibits closed-circuit behaviour. Bias was applied up to ±5V. **b,c** Pads BC and AB, connected by the laser-written interdigitated electrode, also show closed-circuit behaviour. **d** Pad BD, not connected by any electrode, demonstrates open-circuit behaviour. For the closed-circuit configurations (ED, BC, and AB), a consistent resistance of approximately 0.6 MΩ was measured, confirming the precision and uniformity of the device's electrical connections.

crystalline ⟨100⟩ diamond, grown by chemical vapour deposition with a nitrogen density below 5 ppb (sourced from Element Six), was used as the substrate. The diamond surface was coated with a 10 nm chromium adhesion layer and a 100 nm gold layer (prepared by Gareth S. Jones). The femtosecond laser was used to pattern electrodes by scanning a box shape with a width of 20 μm and variable heights of 5 μm, 2 μm, and 1 μm. An objective lens with a NA of 0.5 was used throughout the test, yielding a Rayleigh diffraction limit of 964 nm. Consequently, the electrode box of 1 μm height lacked residual surface gold within the box. Unlike lithography, the parameters controlling the quality of laser-patterned electrodes were the pulse energy

and the scanning speed (patterning speed). Nine arrays with varying parameters were fabricated and studied, with pulse energies ranging from 30 nJ to 16.5 nJ and patterning speeds from 0.5 mm/s to 0.1 mm/s (with a step size of 0.3 μm).

Optical microscope images (taken with Keyence VHX-7000 Digital Microscope) of the dose test for the laser-patterned electrodes are shown in Fig. 6.6. Figs 6.6 a and b present bright and dark field images of the dose test arrays, respectively, with laser-induced redeposition clearly visible in the dark field mode. This redeposition results in a rougher surface, as indicated by the optical profilometry data in Fig. 6.5.

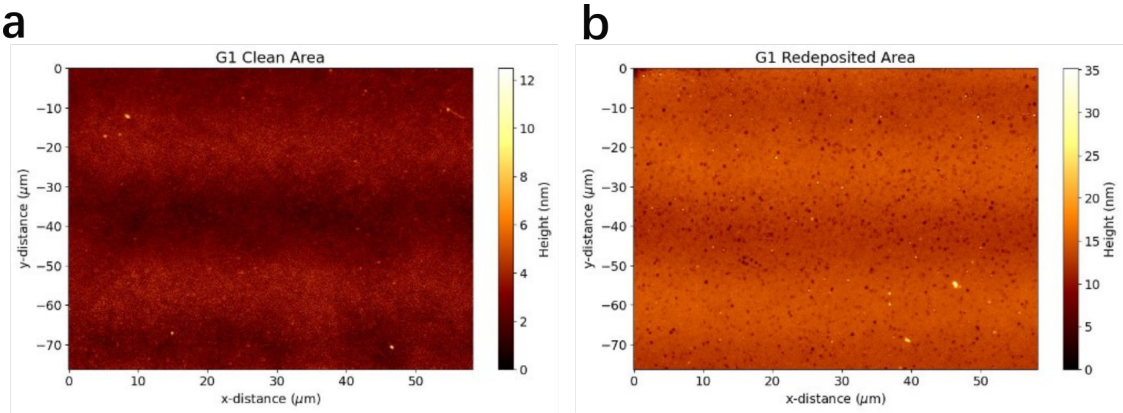


Figure 6.5: Surface roughness comparison between pristine and redeposited regions. a Surface map of a pristine region unaffected by laser patterning. **b** Surface map of a redeposited region affected by laser processing. The fringes observed here are likely attributable to back-surface reflections, which artificially elevate the measured surface roughness. Even so, the data clearly show that redeposition has indeed produced a markedly rougher surface.

Fig. 6.6c and d show two example arrays (array 4 and array 7), illustrating clear electrode patterning and incomplete patterning, respectively. A summary of these results is provided in Table 6.1, where we identified an optimal operating pulse energy is 20.25 nJ. To quantitatively evaluate the electrode quality, a Python-based computer vision approach was employed to analyse the microscope images of the electrode boxes patterned of a width of 20 μm and a height of 5 μm for the clearest contrast.

First, the original image (Fig. 6.7) was converted to greyscale, and Gaussian blurring was applied to reduce noise, improving the thresholding process. For thresholding, Otsu's method [204] was used to automatically determine an optimal

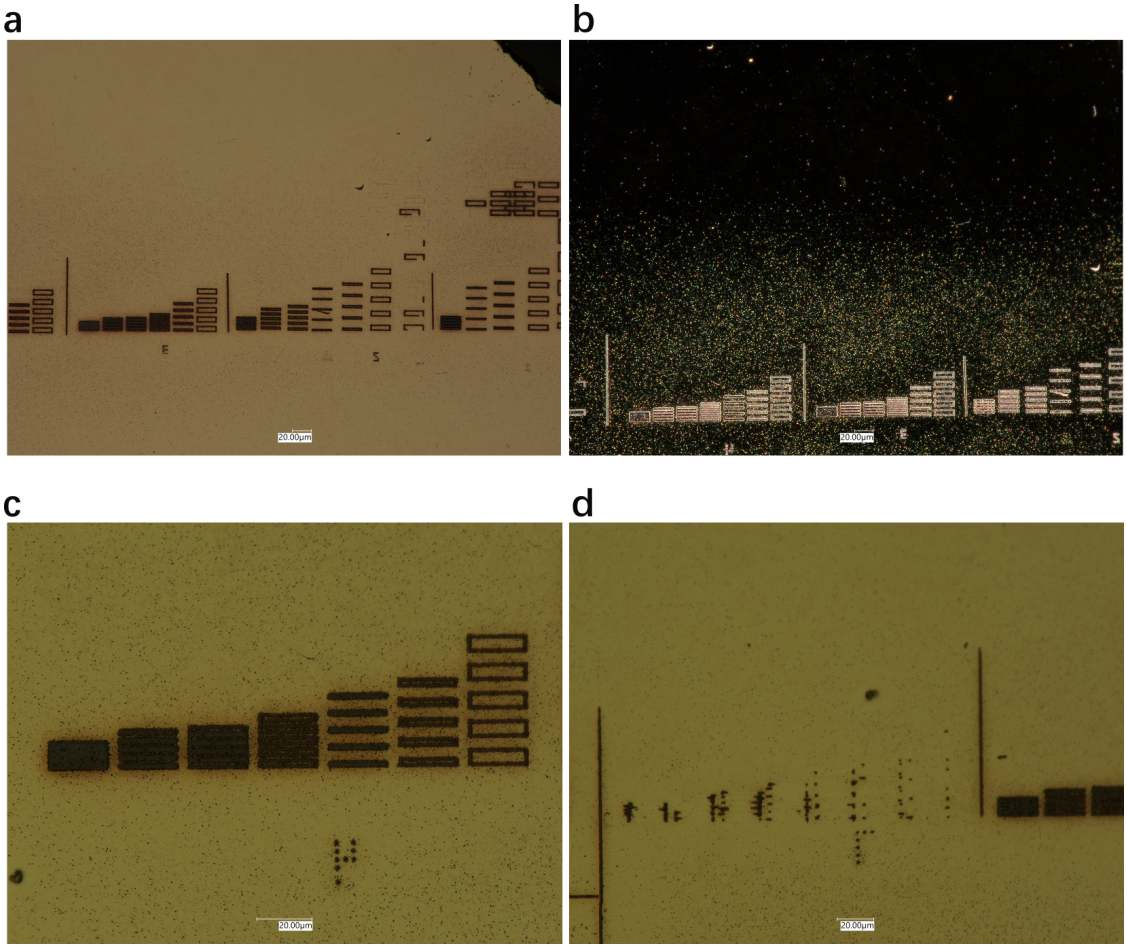


Figure 6.6: Optical microscope images of laser-patterned electrode dose test. a,b Bright field and dark field images of the dose test arrays, respectively. Laser-induced redeposition is clearly visible in the dark field mode. **c** Example of a successfully patterned array (Array 4), showing clear and uniform electrode structures. **d** Example of incomplete patterning (Array 7), illustrating areas where the laser parameters were insufficient for complete electrode formation. These images demonstrate the effect of varying laser doses on the quality and completeness of the patterned electrodes.

Array number	Pulse energy (nJ)	Patterning speed (mm/s)	Electrode pattern	Redeposition
1	25.5	0.1	Clear	Strong
2	20.25	0.1	N/A	N/A
3	20.25	0.1	Clear	Moderate
4	20.25	0.1	Clear	Moderate
5	16.5	0.1	Partially incomplete	Weak
6	20.25	0.2	Clear	Moderate
7	20.25	0.5	Incomplete	Weak
8	20.25	0.3	Partially incomplete	Weak
9	20.25	0.28	Clear	Weak

Table 6.1: Array parameters and resulting pattern characteristics

threshold value by maximising the variance between background and foreground pixel intensities. However, due to complexities and variations in the electrode patterns and background, a single automatic threshold often failed to clearly isolate the patterned regions. To address this, I adjusted the threshold iteratively, visually inspecting each binary image to ensure a clear separation of the electrode pattern from the background. This iterative adjustment process allowed for optimised contrast in the binary image (shown in Fig. 6.8), emphasising the patterned regions and enabling clearer contour identification.

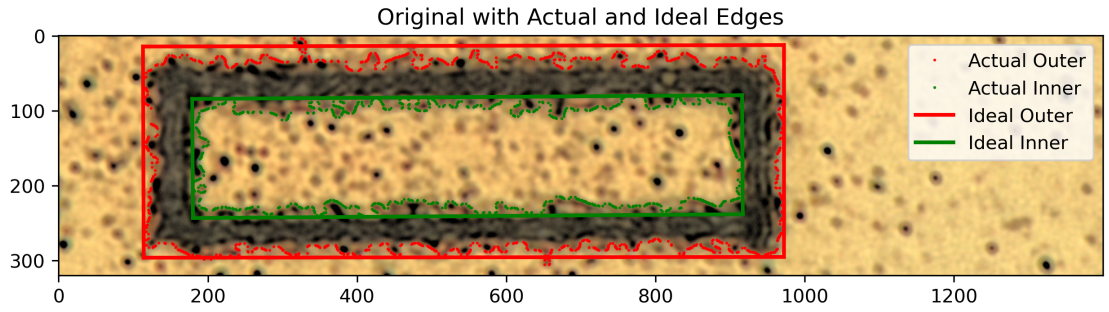


Figure 6.7: Visualisation of actual and ideal contours with pixel-based axes. The image displays the original surface with overlaid contours representing the inner and outer edges of the electrode pads. The x- and y-axes are presented in pixel numbers. Actual contours (dotted red and black lines) are compared to ideal contours (solid red and green lines) to evaluate the alignment and precision of the laser-patterned structures.

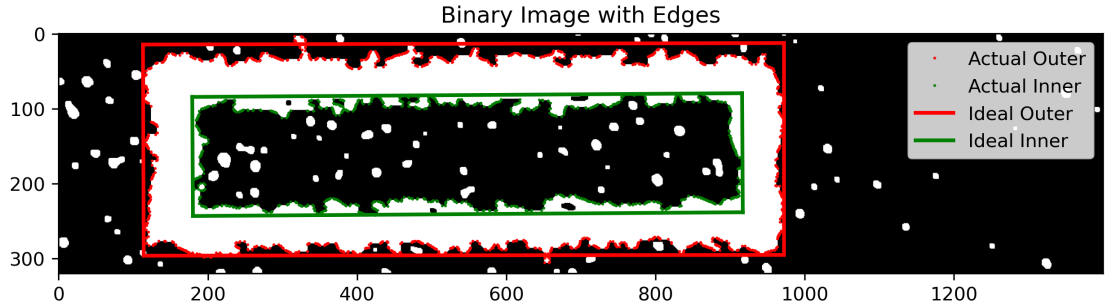


Figure 6.8: Binary image processing and contour identification for electrode patterns. The original greyscale image was processed using Gaussian blurring to reduce noise, improving the thresholding process. The resulting binary image effectively highlights the patterned regions, as shown, and facilitates accurate contour identification by comparing actual (dotted red and black) and ideal (solid red and green) contours. The x- and y-axes represent pixel numbers.

With the optimised threshold, a binary image emphasising the patterned regions

was generated, providing a distinct view of the contours. To refine the edges, I applied a series of morphological operations. Specifically, a closing operation (dilation (the dilation operation expands the boundaries of the white regions in the binary image) followed by erosion (it shrinks the white regions back slightly, which restores the original shape of the regions but leaves the small gaps or holes filled in.)) with a 5×5 kernel (a square matrix with dimensions of 5 pixels by 5 pixels) was used to fill small gaps and holes within the patterned regions, ensuring solid and continuous edges. This step was essential for bridging any gaps or minor imperfections present in the binary image. Following this, an opening operation (erosion followed by dilation) was applied to remove small, isolated noise elements from the background while preserving the main contour shapes. These combined operations resulted in a cleaner, more refined binary mask, enabling accurate detection of the main contours, as seen in the final binary image.

Using the cleaned binary mask, we identified the contours, isolating both the outer and inner edges of the pattern. These contours, representing the actual edges, are shown as dotted lines in red (outer edges) and green (inner edges) in both the original and binary images.

To quantify roughness, ideal rectangles approximating the intended outer and inner boundaries of the pattern were fitted. These ideal boundaries are depicted as solid red and green lines for the outer and inner edges, respectively, serving as reference points for roughness analysis. By measuring the deviation of each point on the actual contour from the nearest point on the ideal rectangle, edge deviation values (RMS) were calculated, representing surface roughness. These deviations were then converted from pixel units to nanometres for physical relevance, based on the scale bar in each image.

Fig. 6.9 illustrates the distribution of RMS roughness values, presenting histograms for both the outer and inner edges of two arrays patterned at the optimal operating pulse energy of 20.25 nJ but with different patterning speeds. The RMS roughness distributions are fitted to normal distributions. Notably, array 9 was selected for its patterning speed of 0.28 mm/s, a step size of 0.3 μm, and a spot

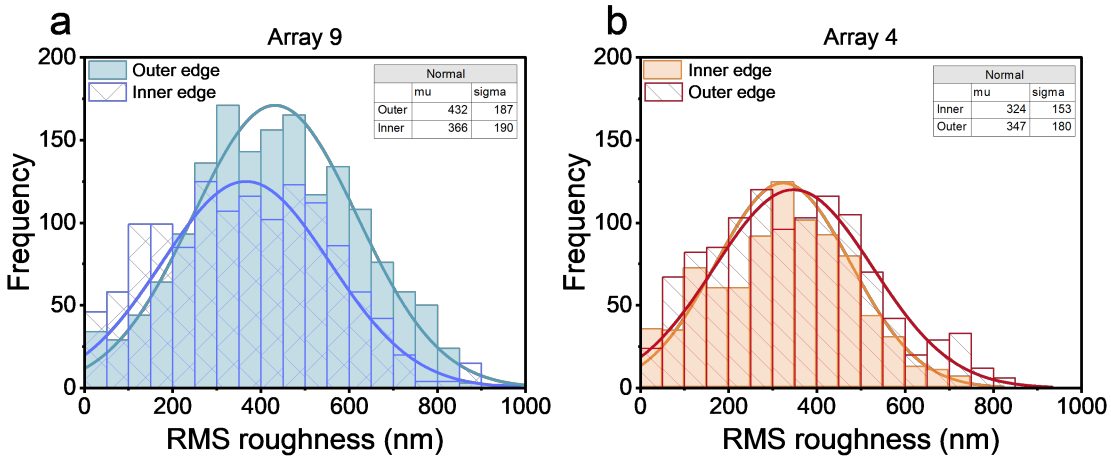


Figure 6.9: RMS roughness distributions for patterned arrays. a Histogram of RMS roughness for the outer and inner edges of Array 9, fitted to $Outer \sim \mathcal{N}(432, 187^2)$ and $Inner \sim \mathcal{N}(366, 190^2)$. **b** Histogram of RMS roughness for the outer and inner edges of Array 4, fitted to $Outer \sim \mathcal{N}(347, 180^2)$ and $Inner \sim \mathcal{N}(324, 153^2)$.

size of 0.96 μm, which collectively enable a near-continuous trace with slight pulse overlap. This configuration is theoretically expected to minimise redeposition while maintaining a continuous patterned shape for the electrode. The fitted normal distributions yield $Outer \sim \mathcal{N}(432, 187^2)$ and $Inner \sim \mathcal{N}(366, 190^2)$ for array 9, and $Outer \sim \mathcal{N}(347, 180^2)$ and $Inner \sim \mathcal{N}(324, 153^2)$ for array 4. These results indicate that a lower patterning speed leads to improved surface roughness for the patterned electrode. This improvement is likely due to increased pulse overlap at lower patterning speeds, which enhances local redeposition, effectively smoothing rough edges with redeposited Au and Cr.

The dimensions of the ideal rectangles for both arrays were measured as 22 μm in width and 8 μm in height for the outer edges, and 19 μm in width and 5 μm in height for the inner edges. These measurements align closely with the target dimensions of the patterned regions, consistent with the design specifications.

To our knowledge, this is the first demonstration of using femtosecond laser surface patterning on a coated surface. In summary, an optimal operating pulse energy of 20.25 nJ was identified based on the microscope images of the patterned electrode. Quantitative analysis indicates that lower patterning speeds result in improved lateral RMS edge roughness, likely due to increased redeposition from

overlapping femtosecond laser pulses. However, this stronger redeposition could potentially impact the functional performance of the patterned electrode. Further investigation into patterning speed could help identify an optimal value, while employing a higher NA objective lens or a femtosecond laser with a shorter wavelength could reduce the spot size, potentially yielding finer edge roughness and enabling the creation of narrower electrode pads on a coated surface. This advancement is particularly significant because it facilitates the processing of membranes and other small samples, which is challenging with conventional photolithography systems that are typically optimized for large wafers.

6.4 Discussion

This chapter presents a novel approach to device fabrication, marking the first example of a fully optical method for creating all electrodes within a device. Using femtosecond laser writing, we successfully fabricated interdigitated electrode arrays embedded within a diamond substrate, achieving precise spatial control and flexibility in patterning hard, wide bandgap materials. This technique eliminates the need for conventional lithographic processes, enabling robust electrode placement and simplifying alignment within the bulk material.

The laser-written interdigitated electrodes, fabricated with a 2 μm spacing, demonstrated reliable electrical performance without evidence of short-circuiting. Probe measurements under a $\pm$50 V bias showed consistent closed-circuit behaviour across connected pads, with an average resistance of approximately 0.6 MΩ, indicating effective electrode isolation and connectivity at the micron scale. The precision of femtosecond laser writing is evident in the well-defined electrode structures achieved within the diamond substrate.

The surface electrodes were patterned using femtosecond laser pulses, achieving resolution and fabrication speeds comparable to those of a commercial Direct Laser Writer (DWL) lithography tool. However, this technique offers significant advantages, including the elimination of alignment, bonding, and sample mounting requirements. These features make the fabrication of delicate samples, such as

membranes or other two-dimensional materials, more feasible. With an optimised SLM pattern, two-dimensional patterning is achievable, enabling the fabrication of entire electrodes through a faster and more efficient process. A detailed dose test was conducted to evaluate the quality of the laser-patterned surface electrodes, revealing an edge roughness of less than 500 nm. This roughness could be further minimised by using a higher NA objective lens or a femtosecond laser with a shorter wavelength.

Several directions for future work could extend these findings. First, laser-induced generation of Frenkel defects between the interdigitated electrodes, combined with in-situ photocurrent measurements, could yield valuable insights into the mechanisms of laser writing, enabling direct comparison with Griffiths's hypothetical model [83] and potentially validating theoretical predictions. Additionally, applying a bias between electrodes to control charge carrier density could enable the examination of its influence on the threshold pulse energy required for visible damage and Frenkel defect densities. Such investigation could offer greater control over defect formation, refining the laser-writing process to enhance pattern fidelity. The ability to position electrodes close to emitters could also improve contrast in the Stark tuning of defect centres within bulk materials [205].

This device also enables more controlled laser writing and laser annealing by modulating charge carrier densities. By managing these parameters, it may be possible to fine-tune light-matter interactions, allowing precise control over defect generation and pattern characteristics. Together, these advancements position this fully optical fabrication technique as a powerful tool for future applications in quantum and electronic devices, where traditional methods face inherent limitations.

7 Conclusion and outlook

Contents

7.1 Conclusion 197
7.2 Outlook 199

7.1 Conclusion

This thesis addressed the core challenge of bridging the gap between fundamental defect formation and practical device engineering in diamond and SiC, aiming to advance spin-photon interfaces suitable for large-scale quantum applications. Femtosecond-laser processing underpins three interlinked achievements. First, it offers a deterministic route for generating single group-IV colour centres, yielding site-selective spectral tuning that conventional thermal annealing cannot attain. Secondly, it introduces a scalable strategy for embedding these quantum defects within solid-immersion lenses—realised both by the top-down transfer of GaN micro-lenses and by bottom-up fabrication of laser-written hemispherical arrays in 4H-SiC substrate, thus enhancing photon collection. Thirdly, the same laser platform integrates the engineered defects directly into chip-scale photonic and electronic architectures, dispensing with lithographic masks. Collectively, these

advances bring spin-photon interfaces markedly closer to the performance and scalability demanded by future quantum networks and sensing applications.

Chapter 4 introduced a site-controlled activation method for SnV^- and SiV^- centres in diamond, supported by in-situ spectral monitoring of defect activation. This method uncovered new insights into the dynamics of defect formation, including the identification of Type II Sn centres, characterised by a ZPL at 595 nm. These centres likely represent Sn atoms bonded to carbon interstitials, serving as precursors to stable SnV^- centres. These findings elucidate the defect formation mechanism, highlighting the roles of exciton-mediated annealing and charge carrier dynamics during laser activation. This work constitutes the first demonstration of laser annealing for activating Group-IV defects in diamond. The systematic investigation of laser annealing times and pulse energies, which shows that the lateral span of the activated region expands to a size comparable with the exciton diffusion length in diamond at room temperature, supports the hypothesis that this process is exciton-mediated.

Chapter 5 outlined substantial advancements in enhancing light collection from solid-state defects across various defects and host materials, achieved through the integration of SILs with laser writing. Two complementary approaches were developed: a top-down integration of micro-transfer printed SILs and a bottom-up fabrication of hemispherical SIL arrays. FDTD simulations validated the top-down approach, predicting a twofold enhancement in light collection for an objective lens with a NA of 0.95, validated by experimental power saturation measurements. These experiments also confirmed that SILs do not alter the photon statistics or spectra of the emitters, apart from Raman features arising from the SIL material. In the bottom-up approach, the laser writing mechanism in 4H-SiC was studied under the multiphoton ionisation regime, showing that SILs enhance photon collection and improve laser writing precision. This study represents the first demonstration of laser writing through SIL structures at the single-defect level, achieving enhanced light extraction and precise spatial alignment.

Additionally, Chapter 6 presented a fully optical method for fabricating interdigitated electrodes within diamond substrates using femtosecond laser writing. This approach serves as a strong alternative to conventional lithography, providing benefits in scalability and ease of integration. The method provides a robust technique for future quantum and electronic device applications. The results presented here have the potential to impact multiple aspects of solid-state quantum technologies.

The demonstrated ability to deterministically generate and activate colour centres at single-defect level establishes a foundation for building large-scale quantum networks. Enhanced photon collection through SILs, together with the prospect of on-chip electrodes, promises more efficient readout and control of single spins. This is a critical step toward realising robust, device-level quantum architectures. Together, these developments represent significant progress toward industrially viable quantum sensors and communication nodes.

7.2 Outlook

Building on these findings, several directions for future research emerge. For SnV^- centres, further PLE and coherence measurements are essential to evaluate whether additional laser annealing can improve coherence times or other optical properties. Investigating whether Type II Sn centres can be reverted to SnV^- centres via laser annealing, and comparing their properties to the original centres, could yield valuable insights into defect formation mechanisms and tunability. Combining deterministic single-ion implantation with laser activation may enable precise control over individual SnV^- centres. Additionally, cryogenic laser activation with spectral feedback offers a promising approach. At cryogenic temperatures, SnV^- spectral lines can be resolved with acquisition times as short as one second, providing a 100-fold increase in temporal resolution over room temperature. This technique could enable deterministic activation and exploration of strain tuning effects by monitoring spectral splitting in the optical transitions. However, cryogenic conditions may increase exciton diffusion, broadening the laser-annealed region and requiring adjustments in operational parameters.

For Type II Sn centres, DFT simulations are needed to study the energy levels and transitions within their ZPL windows. At room temperature, Type II Sn centres exhibit similar ZPL features, but at cryogenic temperatures, site-specific variations and multiple optical transitions appear within the ZPL window. ODMR and polarisation studies of the ZPL optical lines could further clarify the structural symmetry and electronic characteristics of these defects.

In enhancing light extraction, future experiments could explore laser writing through transfer-printed SILs on diamond membranes. This approach may address challenges associated with shallow or surface NV^- centres, where laser writing risks graphitising the diamond surface. Integrating SILs with diamond membranes and distributed Bragg reflector (DBR) mirrors could facilitate scalable quantum devices, such as single NV^- centres embedded in Fabry Perot microcavities. In SiC, incorporating an 795 nm laser during SIL-assisted writing could improve the yield of single V_{Si}^- defects and enable defect annealing to desired configurations. This additional excitation source could also optimise the laser annealing of defects in 4H-SiC.

For interdigitated devices, photon-current measurements during laser writing of GR1 defects could validate theoretical models, such as those proposed by Griffiths et al [83]. Applying an external bias during laser writing may alter the graphitisation threshold, confining the laser-affected volume by creating a charge-depleted region. This technique could also be applied to Sn-implanted samples, potentially enabling precise localisation of annealing effects. Post-fabrication, interdigitated devices could facilitate Stark tuning with improved resolution, allowing precise electric field application within micrometre-scale distances to the defects.

Taken together, these pursuits open new avenues for both fundamental studies of solid-state defects and the development of integrated quantum technologies that are poised to move from proof-of-concept devices to real-world applications.

8 Appendix

Contents

8.1 List of publications 201
8.1.1 Journal Articles 201
8.1.2 Conference Presentations 202

8.1 List of publications

8.1.1 Journal Articles

1. **Laser activation of single group-IV colour centres in diamond**, *Nature Communications* **16**, 5124 (2025), **X. Cheng**, A. Thurn, G. Chen, G. S. Jones, J. E. Bennett, M. Coke, M. Adshead, C. P. Michaels, O. Balci, A. C. Ferrari, M. Atatüre, R. J. Curry, J. M. Smith, P. S. Salter, D. A. Gangloff

2. **Scalable registration of single quantum emitters within solid immersion lenses through femtosecond laser writing**, *Nano Letters* (2025), DOI: 10.1021/acs.nanolett.5c01325, A. R. Jones, **X. Cheng**, S. K. Parthasarathy, M. J. Arshad, P. Cilibrizzi, R. Nagy, P. S. Salter, J. Smith, C. Bonato, C. Bekker

3. **Laser-written nitrogen vacancy centres in diamond integrated with transfer-printed GaN solid immersion lenses**, *Proc. SPIE 12874, Nanoscale*

and Quantum Materials: From Synthesis and Laser Processing to Applications 2024, 1287405 (12 March 2024) **X. Cheng**, N. K. Wessling, S. Ghosh, A. R. Kirkpatrick, M. J. Kappers, Y. N. D. Lekhai, G. W. Morley, R. A. Oliver, M. D. Dawson, J. M. Smith, P. S. Salter, M. J. Strain

4. **AAdditive GaN solid immersion lenses for enhanced photon extraction efficiency from diamond colour centres**, *ACS Photonics 2023, 10 (9), 3374-3383* **X. Cheng**, N. K. Wessling, S. Ghosh, A. R. Kirkpatrick, M. J. Kappers, Y. N. D. Lekhai, G. W. Morley, R. A. Oliver, M. D. Dawson, J. M. Smith, P. S. Salter, M. J. Strain

8.1.2 Conference Presentations

1. **QCS End of Hub Event**, November 2024: Laser Writing of Quantum Defects in Diamond

2. **34th International Conference on Diamond and Carbon Materials**, September 2024: Laser Activation of Tin-Vacancy Quantum Emitters in Electronic-Grade Diamond

3. **QCS Forum**, June 2024: Poster: Laser Activation of Tin-Vacancy Centres (SnV^-) in Diamond

4. **SPIE Photonics West**, February 2024: Laser-Written Nitrogen Vacancy Centres in Diamond Integrated with Transfer-Printed GaN Solid Immersion Lenses

5. **M4QN Solid-State Defects Workshop on Facilities Access and Development**, June 2023: Poster: Laser Annealing of Group IV Colour Centres in Diamond

6. **Oxford Photonics Day**, September 2022: Poster: Laser Writing for Solid-State Quantum Defects

References

[1] Gary Wolfowicz et al. "Quantum guidelines for solid-state spin defects". In: *Nature Reviews Materials* 6.October (2021). arXiv: 2010.16395. URL: http://dx.doi.org/10.1038/s41578-021-00306-y.

[2] J. R. Weber et al. "Quantum computing with defects". In: *Proceedings of the National Academy of Sciences of the United States of America* 107.19 (2010), pp. 8513–8518.

[3] Lilian Childress and Ronald Hanson. "Diamond NV centers for quantum computing and quantum networks". In: *MRS bulletin* 38.2 (2013), pp. 134–138.

[4] S.C. Benjamin, B.W. Lovett, and J.M. Smith. "Prospects for measurement-based quantum computing with solid state spins". In: *Laser & Photonics Reviews* 3.6 (2009), pp. 556–574. eprint: https://onlinelibrary.wiley.com/doi/pdf/10.1002/lpor.200810051. URL: https://onlinelibrary.wiley.com/doi/abs/10.1002/lpor.200810051.

[5] Brahim Lounis and Michel Orrit. "Single-photon sources". In: *Reports on Progress in Physics* 68.5 (2005), pp. 1129–1179.

[6] John F. Barry et al. "Sensitivity optimization for NV-diamond magnetometry". In: *Reviews of Modern Physics* 92.1 (2020). arXiv: 1903.08176.

[7] Valerio Scarani et al. "The security of practical quantum key distribution". In: *Rev. Mod. Phys.* 81 (3 2009), pp. 1301–1350. URL: https://link.aps.org/doi/10.1103/RevModPhys.81.1301.

[8] Shi-Hai Wei et al. "Towards Real-World Quantum Networks: A Review". In: *Laser & Photonics Reviews* 16.3 (2022), p. 2100219.

[9] Charles H. Bennett and David P. DiVincenzo. "Quantum information and computation". In: *Nature* 404.6775 (2000), pp. 247–255.

[10] W. B. Gao et al. "Coherent manipulation, measurement and entanglement of individual solid-state spins using optical fields". In: *Nature Photonics* 9.6 (2015), pp. 363–373.

[11] S. Pirandola et al. "Advances in quantum cryptography". In: *Adv. Opt. Photon.* 12.4 (2020), pp. 1012–1236. URL: https://opg.optica.org/aop/abstract.cfm?URI=aop-12-4-1012.

[12] Bernd Fröhlich et al. "A quantum access network". In: *Nature* 501.7465 (2013), pp. 69–72. URL: https://doi.org/10.1038/nature12493.

[13] H. J. Kimble. "The quantum internet". In: *Nature* 453.7198 (2008), pp. 1023–1030. URL: https://doi.org/10.1038/nature07127.

[14] Christoph Simon. “Towards a global quantum network”. In: *Nature Photonics* 11.11 (2017), pp. 678–680. URL: https://doi.org/10.1038/s41566-017-0032-0.

[15] Sheng-Kai Liao et al. “Satellite-to-ground quantum key distribution”. In: *Nature* 549.7670 (2017), pp. 43–47.

[16] Charles H. Bennett and Gilles Brassard. “Quantum cryptography: Public key distribution and coin tossing”. In: *Theoretical Computer Science* 560 (2014). Theoretical Aspects of Quantum Cryptography – celebrating 30 years of BB84, pp. 7–11. URL: https://www.sciencedirect.com/science/article/pii/S0304397514004241.

[17] Chris J.H. Wort and Richard S. Balmer. “Diamond as an electronic material”. In: *Materials Today* 11.1 (2008), pp. 22–28. URL: https://www.sciencedirect.com/science/article/pii/S1369702107703498.

[18] Christoph E. Nebel. “CVD diamond: a review on options and reality”. In: *Functional Diamond* 3.1 (2023), p. 2201592. eprint: https://doi.org/10.1080/26941112.2023.2201592. URL: https://doi.org/10.1080/26941112.2023.2201592.

[19] T. Joas et al. “High-Fidelity Electron Spin Gates for Scaling Diamond Quantum Registers”. In: *Phys. Rev. X* 15 (2 2025), p. 021069. URL: https://link.aps.org/doi/10.1103/PhysRevX.15.021069.

[20] Sam Johnson, Philip R Dolan, and Jason M Smith. “Diamond photonics for distributed quantum networks”. In: *Progress in Quantum Electronics* 55 (2017), pp. 129–165.

[21] F. Jelezko and J. Wrachtrup. “Single defect centres in diamond: A review”. In: *physica status solidi (a)* 203.13 (2006), pp. 3207–3225. URL: https://onlinelibrary.wiley.com/doi/abs/10.1002/pssa.200671403.

[22] Marcus W. Doherty et al. “The nitrogen-vacancy colour centre in diamond”. In: *Physics Reports* 528.1 (2013). The nitrogen-vacancy colour centre in diamond, pp. 1–45. URL: https://www.sciencedirect.com/science/article/pii/S0370157313000562.

[23] H. J. Briegel et al. “Measurement-based quantum computation”. In: *Nature Physics* 5.1 (2009), pp. 19–26.

[24] D. D. Bhaktavatsala Rao, Sen Yang, and Jörg Wrachtrup. “Generation of entangled photon strings using NV centers in diamond”. In: *Phys. Rev. B* 92 (8 2015), p. 081301. URL: https://link.aps.org/doi/10.1103/PhysRevB.92.081301.

[25] G. Davies. “The Jahn-Teller effect and vibronic coupling at deep levels in diamond”. In: *Reports on Progress in Physics* 44.7 (July 1981), p. 787. URL: https://dx.doi.org/10.1088/0034-4885/44/7/003 (visited on 03/06/2024).

[26] I Aharonovich et al. “Diamond-based single-photon emitters”. In: *Reports on Progress in Physics* 74.7 (2011), p. 076501. URL: https://dx.doi.org/10.1088/0034-4885/74/7/076501.

[27] Paul E. Barclay et al. “Coherent interference effects in a nano-assembled diamond NV center cavity-QED system”. In: *Optics Express* 17.10 (2009), p. 8081.

[28] Sam Johnson et al. “Tunable cavity coupling of the zero phonon line of a nitrogen-vacancy defect in diamond”. In: *New Journal of Physics* 17.12 (2015), p. 122003.

[29] Michael Gould et al. “Efficient extraction of zero-phonon-line photons from single nitrogen-vacancy centers in an integrated gap-on-diamond platform”. In: *Physical Review Applied* 6.1 (2016), p. 011001.

[30] P. R. Dolan et al. “Robust, tunable, and high purity triggered single photon source at room temperature using a nitrogen-vacancy defect in diamond in an open microcavity”. In: *Optics Express* 26.6 (2018), p. 7056.

[31] Thomas M Babinec et al. “A diamond nanowire single-photon source”. In: *Nature nanotechnology* 5.3 (2010), pp. 195–199.

[32] Stefania Castelletto et al. “Diamond-based structures to collect and guide light”. In: *New Journal of Physics* 13.2 (2011), p. 025020.

[33] JP Hadden et al. “Strongly enhanced photon collection from diamond defect centers under microfabricated integrated solid immersion lenses”. In: *Applied Physics Letters* 97.24 (2010), p. 241901.

[34] Xingrui Cheng et al. “Additive GaN Solid Immersion Lenses for Enhanced Photon Extraction Efficiency from Diamond Color Centers”. In: *ACS Photonics* 10.9 (2023), pp. 3374–3383. eprint: https://doi.org/10.1021/acsphotonics.3c00854. URL: https://doi.org/10.1021/acsphotonics.3c00854.

[35] Lachlan J. Rogers et al. “Electronic structure of the negatively charged silicon-vacancy center in diamond”. In: *Phys. Rev. B* 89 (23 2014), p. 235101. URL: https://link.aps.org/doi/10.1103/PhysRevB.89.235101.

[36] M. K. Bhaskar et al. “Quantum Nonlinear Optics with a Germanium-Vacancy Color Center in a Nanoscale Diamond Waveguide”. In: *Phys. Rev. Lett.* 118 (22 2017), p. 223603. URL: https://link.aps.org/doi/10.1103/PhysRevLett.118.223603.

[37] Tina Müller et al. “Optical signatures of silicon-vacancy spins in diamond”. In: *Nature Communications* 5.1 (Feb. 2014), p. 3328. URL: https://www.nature.com/articles/ncomms4328 (visited on 09/11/2024).

[38] Benjamin Pingault et al. “Coherent control of the silicon-vacancy spin in diamond”. In: *Nature Communications* 8.1 (2017), p. 15579.

[39] Takayuki Iwasaki et al. “Tin-Vacancy Quantum Emitters in Diamond”. In: *Phys. Rev. Lett.* 119 (25 2017), p. 253601. URL: https://link.aps.org/doi/10.1103/PhysRevLett.119.253601.

[40] N. Bar-Gill et al. “Solid-state electronic spin coherence time approaching one second”. In: *Nature Communications* 4.1 (2013), p. 1743.

[41] Romain Debroux. “Developing the Spin Qubit of the Tin-Vacancy Center in Diamond for Quantum Networks”. PhD thesis. University of Cambridge, 2022. URL: https://www.repository.cam.ac.uk/handle/1810/343543.

[42] Ioannis Karapatzakis et al. “Microwave Control of the Tin-Vacancy Spin Qubit in Diamond with a Superconducting Waveguide”. In: *Phys. Rev. X* 14 (3 2024), p. 031036. URL: https://link.aps.org/doi/10.1103/PhysRevX.14.031036.

[43] Kay D. Jahnke et al. “Electron-phonon processes of the silicon-vacancy centre in diamond”. In: *New Journal of Physics* 17 (Apr. 2015).

[44] Gergő Thiering and Adam Gali. “The (eg x eu) x Eg product Jahn–Teller effect in the neutral group-IV vacancy quantum bits in diamond”. In: *npj Comput. Mater.* 5.1 (2019), p. 18. URL: https://www.nature.com/articles/s41524-019-0158-3.

[45] Johannes Görlitz et al. “Spectroscopic investigations of negatively charged tin-vacancy centres in diamond”. In: *New Journal of Physics* 22.1 (2020), p. 13048. URL: https://dx.doi.org/10.1088/1367-2630/ab6631.

[46] J. P. Goss et al. “The Twelve-Line 1.682 eV Luminescence Center in Diamond and the Vacancy-Silicon Complex”. In: *Phys. Rev. Lett.* 77 (14 1996), pp. 3041–3044. URL: https://link.aps.org/doi/10.1103/PhysRevLett.77.3041.

[47] Matthew E. Trusheim et al. “Transform-Limited Photons From a Coherent Tin-Vacancy Spin in Diamond”. In: *Phys. Rev. Lett.* 124.2 (2020), p. 023602. URL: https://link.aps.org/doi/10.1103/PhysRevLett.124.023602.

[48] Christian Hepp et al. “Electronic Structure of the Silicon Vacancy Color Center in Diamond”. In: *Phys. Rev. Lett.* 112 (3 2014), p. 036405. URL: https://link.aps.org/doi/10.1103/PhysRevLett.112.036405.

[49] Alan T. Collins et al. “The annealing of radiation damage in De Beers colourless CVD diamond”. In: *Diamond and Related Materials* 3.4 (1994). Proceedings of the 4th European Conference on Diamond, Diamond-like and Related Materials, pp. 932–935.

[50] Stefano Lagomarsino et al. “Optical properties of silicon-vacancy color centers in diamond created by ion implantation and post-annealing”. In: *Diamond and Related Materials* 84 (2018), pp. 196–203.

[51] Elke Neu et al. “Single photon emission from silicon-vacancy colour centres in chemical vapour deposition nano-diamonds on iridium”. In: *New Journal of Physics* 13.2 (Feb. 2011), p. 025012. URL: https://dx.doi.org/10.1088/1367-2630/13/2/025012 (visited on 08/30/2024).

[52] G. R. Fisher and P. Barnes. “Towards a unified view of polytypism in silicon carbide”. In: *Philosophical Magazine B* 61.2 (1990), pp. 217–236.

[53] A. Lohrmann et al. “A review on single photon sources in silicon carbide”. In: *Reports on Progress in Physics* 80.3 (Jan. 2017), p. 034502. URL: https://dx.doi.org/10.1088/1361-6633/aa5171.

[54] Matthias Widmann et al. “Coherent control of single spins in silicon carbide at room temperature”. In: *Nature Materials* 14.2 (2015), pp. 164–168.

[55] David J. Christle et al. “Isolated electron spins in silicon carbide with millisecond coherence times”. In: *Nature Materials* 14.2 (2015), pp. 160–163.

[56] Roland Nagy et al. “High-fidelity spin and optical control of single silicon-vacancy centres in silicon carbide”. In: *Nature Communications* 10.1 (Apr. 2019), p. 1954.

[57] Stefania Castelletto, Brett C. Johnson, and Alberto Boretti. “Quantum Effects in Silicon Carbide Hold Promise for Novel Integrated Devices and Sensors”. In: *Advanced Optical Materials* 1.9 (2013), pp. 609–625.

[58] Stefania Castelletto et al. “Room Temperature Quantum Emission from Cubic Silicon Carbide Nanoparticles”. In: *ACS Nano* 8.8 (2014), pp. 7938–7947.

[59] A. Lohrmann et al. “Activation and control of visible single defects in 4H-, 6H-, and 3C-SiC by oxidation”. In: *Applied Physics Letters* 108.2 (Jan. 2016), p. 021107.

[60] A. Lohrmann et al. “Single-photon emitting diode in silicon carbide”. In: *Nature Communications* 6.1 (2015), p. 7783.

[61] S. Castelletto et al. “A silicon carbide room-temperature single-photon source”. In: *Nature Materials* 13.2 (2014), pp. 151–156. URL: https://doi.org/10.1038/nmat3806.

[62] Jason M. Smith et al. “Colour centre generation in diamond for quantum technologies”. In: *Nanophotonics* 8.11 (2019), pp. 1889–1906. URL: https://www.degruyter.com/document/doi/10.1515/nanoph-2019-0196/html (visited on 02/19/2024).

[63] Mason Adshead et al. “A High-Resolution Versatile Focused Ion Implantation Platform for Nanoscale Engineering”. In: *Advanced Engineering Materials* 25.22 (2023), p. 2300889. URL: https://onlinelibrary.wiley.com/doi/abs/10.1002/adem.202300889 (visited on 09/11/2024).

[64] Igor Aharonovich and Elke Neu. “Diamond Nanophotonics”. In: *Advanced Optical Materials* 2.10 (2014), pp. 911–928.

[65] Ariful Haque and Sharaf Sumaiya. “An Overview on the Formation and Processing of Nitrogen-Vacancy Photonic Centers in Diamond by Ion Implantation”. In: *Journal of Manufacturing and Materials Processing* 1.1 (2017), p. 6.

[66] I Kiflawi et al. “Electron irradiation and the formation of vacancy–interstitial pairs in diamond”. In: *Journal of Physics: Condensed Matter* 19.4 (Jan. 2007), p. 046216.

[67] Richard D Simmonds et al. “Three dimensional laser microfabrication in diamond using a dual adaptive optics system”. In: *Optics express* 19.24 (2011), pp. 24122–24128.

[68] U. F. S. D’Haenens-Johansson et al. “Optical properties of the neutral silicon split-vacancy center in diamond”. In: *Phys. Rev. B* 84.24 (Dec. 2011), p. 245208. URL: https://link.aps.org/doi/10.1103/PhysRevB.84.245208.

[69] Chris B Schaffer, André Brodeur, and Eric Mazur. “Laser-induced breakdown and damage in bulk transparent materials induced by tightly focused femtosecond laser pulses”. In: *Measurement Science and Technology* 12.11 (2001), p. 1784. URL: https://dx.doi.org/10.1088/0957-0233/12/11/305.

[70] Yu-Chen Chen et al. “Laser writing of coherent colour centres in diamond”. In: *Nature Photonics* 11.2 (2017), pp. 77–80. URL: https://www.nature.com/articles/nphoton.2016.234 (visited on 08/14/2024).

[71] J. P. Hadden et al. “Integrated waveguides and deterministically positioned nitrogen vacancy centers in diamond created by femtosecond laser writing”. In: *Opt. Lett.* 43.15 (2018), pp. 3586–3589. URL: https://opg.optica.org/ol/abstract.cfm?URI=ol-43-15-3586.

[72] Aaron M. Day et al. “Laser writing of spin defects in nanophotonic cavities”. In: *Nature Materials* (Apr. 2023), pp. 1–7. URL: https://www.nature.com/articles/s41563-023-01544-x (visited on 05/26/2023).

[73] Xiao-Jie Wang et al. “Laser manufacturing of spatial resolution approaching quantum limit”. In: *Light: Science & Applications* 13.1 (Jan. 2024), p. 6. URL: https://www.nature.com/articles/s41377-023-01354-5 (visited on 09/11/2024).

[74] Yu-Chen Chen et al. “Laser writing of individual nitrogen-vacancy defects in diamond with near-unity yield”. In: *Optica* 6.5 (2019), pp. 662–667. URL: https://opg.optica.org/optica/abstract.cfm?URI=optica-6-5-662.

[75] Johannes Engel et al. “Combining femtosecond laser annealing and shallow ion implantation for local color center creation in diamond”. In: *Applied Physics Letters* 122.23 (June 2023), p. 234002. URL: https://doi.org/10.1063/5.0143922.

[76] Yan-Kai Tzeng et al. “Improving the creation of SiV centers in diamond via sub-us pulsed annealing treatment”. In: *Nature Communications* 15.1 (Aug. 2024), p. 7251. URL: https://www.nature.com/articles/s41467-024-51523-2 (visited on 09/11/2024).

[77] Jingmin Wu et al. “Pulsed Laser Annealing of Phosphorous-Implanted 4H-SiC: Electrical and Structural Characteristics”. In: *Journal of Electronic Materials* 50 (2021), pp. 3051–3058.

[78] M. N. Gadalla et al. “Enhanced cavity coupling to silicon vacancies in 4H silicon carbide using laser irradiation and thermal annealing”. In: *Proceedings of the National Academy of Sciences* 118.12 (2021), e2021768118.

[79] Sen Yang et al. “Study of photoinduced nonthermal melting of 4H-SiC under femtosecond pulse laser irradiation based on time-dependent density functional theory simulations”. In: *J. Appl. Phys.* 136.24 (2024), p. 245701.

[80] Yan Liu et al. “Fabrication of nitrogen vacancy color centers by femtosecond pulse laser illumination”. In: *Opt. Express* 21 (2013), pp. 12843–12848.

[81] P. Sprangle, J. R. Peñano, and B. Hafizi. “Propagation of intense short laser pulses in the atmosphere”. In: *Phys. Rev. E* 66.4 (Oct. 2002), p. 046418. URL: https://link.aps.org/doi/10.1103/PhysRevE.66.046418.

[82] Rafael R. Gattass and Eric Mazur. “Femtosecond laser micromachining in transparent materials”. In: *Nature Photonics* 2.4 (Apr. 2008), pp. 219–225. URL: https://www.nature.com/articles/nphoton.2008.47 (visited on 09/06/2024).

[83] Benjamin Griffiths et al. “Microscopic processes during ultrafast laser generation of Frenkel defects in diamond”. In: *Phys. Rev. B* 104 (17 2021), p. 174303. URL: https://link.aps.org/doi/10.1103/PhysRevB.104.174303.

[84] Sergei M. Pimenov et al. "Picosecond-laser bulk modification induced enhancement of nitrogen-vacancy luminescence in diamond". In: *J. Opt. Soc. Am. B* 33.3 (Mar. 2016), B49–B55. URL: https://opg.optica.org/josab/abstract.cfm?URI=josab-33-3-B49.

[85] Torataro Kurita et al. "Efficient generation of nitrogen-vacancy center inside diamond with shortening of laser pulse duration". In: *Applied Physics Letters* 113.21 (Nov. 2018), p. 211102. URL: https://doi.org/10.1063/1.5054730.

[86] Yu-Chen Chen et al. "Laser Writing of Scalable Single Color Centers in Silicon Carbide". In: *Nano Lett.* 19.4 (2019), pp. 2377–2383. URL: https://doi.org/10.1021/acs.nanolett.8b05070.

[87] Xingyu Gao et al. "Femtosecond Laser Writing of Spin Defects in Hexagonal Boron Nitride". In: *ACS Photonics* 8.4 (2021), pp. 994–1000. URL: https://doi.org/10.1021/acsphotonics.0c01847.

[88] Umar Saleem et al. "Light emission from localised point defects induced in GaN crystal by a femtosecond-pulsed laser". In: *Opt. Mater. Express* 8.9 (Sept. 2018), pp. 2703–2712. URL: https://opg.optica.org/ome/abstract.cfm?URI=ome-8-9-2703.

[89] Stefania Castelletto et al. "Color Centers Enabled by Direct Femto-Second Laser Writing in Wide Bandgap Semiconductors". In: *Nanomaterials* 11.1 (2021). URL: https://www.mdpi.com/2079-4991/11/1/72.

[90] D. J. Twitchen et al. "The production and annealing stages of the self-interstitial (R2) defect in diamond". In: *Physica B: Condensed Matter* 273-274 (1999), pp. 644–646.

[91] Alison Mainwood. "Nitrogen and nitrogen-vacancy complexes and their formation in diamond". In: *Phys. Rev. B* 49 (12 1994), pp. 7934–7940. URL: https://link.aps.org/doi/10.1103/PhysRevB.49.7934.

[92] Peter Deák et al. "Formation of NV centers in diamond: A theoretical study based on calculated transitions and migration of nitrogen and vacancy related defects". In: *Physical Review B* 89.7 (Feb. 2014), p. 075203.

[93] Bernhard Dischler. *Intrinsic Defects and Their Associates in Diamond*. Springer, 2012, pp. 269–302.

[94] Sébastien Pezzagna et al. "Creation and nature of optical centres in diamond for single-photon emission—overview and critical remarks". In: *New Journal of Physics* 13.3 (Mar. 2011), p. 035024. URL: https://dx.doi.org/10.1088/1367-2630/13/3/035024.

[95] CJ Stephen et al. "Deep three-dimensional solid-state qubit arrays with long-lived spin coherence". In: *Physical Review Applied* 12.6 (2019), p. 064005.

[96] Inga A. Dobrinets, Victor G. Vins, and Alexander M. Zaitsev. *HPHT-Treated Diamonds: Diamonds Forever*. Vol. 181. Springer Series in Materials Science. Berlin, Heidelberg: Springer-Verlag, 2013. URL: https://link.springer.com/book/10.1007/978-3-642-37484-5.

[97] Luozhou Li et al. "Efficient photon collection from a nitrogen vacancy center in a circular bullseye grating". In: *Nano letters* 15.3 (2015), pp. 1493–1497.

[98] Alp Sipahigil et al. “An integrated diamond nanophotonics platform for quantum-optical networks”. In: *Science* 354.6314 (2016), pp. 847–850.

[99] Mariusz Radtke et al. “Nanoscale sensing based on nitrogen vacancy centers in single crystal diamond and nanodiamonds: achievements and challenges”. In: *Nano Futures* 3.4 (2019), p. 042004.

[100] Seong-Woo Jeon et al. “Bright nitrogen-vacancy centers in diamond inverted nanocones”. In: *Acs Photonics* 7.10 (2020), pp. 2739–2747.

[101] L Marseglia et al. “Nanofabricated solid immersion lenses registered to single emitters in diamond”. In: *Applied Physics Letters* 98.13 (2011), p. 133107.

[102] Kerry J. Vahala. “Optical microcavities”. In: *Nature* 424.6950 (2003), pp. 839–846. URL: https://doi.org/10.1038/nature01939.

[103] Andrei Faraon et al. “Coupling of Nitrogen-Vacancy Centers to Photonic Crystal Cavities in Monocrystalline Diamond”. In: *Phys. Rev. Lett.* 109.3 (July 2012), p. 033604. URL: https://link.aps.org/doi/10.1103/PhysRevLett.109.033604.

[104] Viktoria Yurgens et al. “Cavity-assisted resonance fluorescence from a nitrogen-vacancy center in diamond”. In: *npj Quantum Information* 10.1 (2024), p. 112.

[105] Gregor Bayer et al. “Optical driving, spin initialization and readout of single SiV centers in a Fabry Perot resonator”. In: *Communications Physics* 6.1 (2023), p. 300.

[106] W. L. Barnes et al. “Solid-state single photon sources: light collection strategies”. In: *Eur. Phys. J. D* 18.2 (2002), pp. 197–210.

[107] P Siyushev et al. “Monolithic diamond optics for single photon detection”. In: *Applied physics letters* 97.24 (2010), p. 241902.

[108] Lucio Robledo et al. “High-fidelity projective read-out of a solid-state spin quantum register”. In: *Nature* 477.7366 (2011), pp. 574–578.

[109] Mohammad Jamali et al. “Microscopic diamond solid-immersion-lenses fabricated around single defect centers by focused ion beam milling”. In: *Review of Scientific Instruments* 85.12 (2014), p. 123703.

[110] D. Riedel et al. “Low-Loss Broadband Antenna for Efficient Photon Collection from a Coherent Spin in Diamond”. In: *Phys. Rev. Appl.* 2.6 (2014), p. 064011.

[111] Qianqing Jiang et al. “Focused-ion-beam overlay-patterning of three-dimensional diamond structures for advanced single-photon properties”. In: *Journal of Applied Physics* 116.4 (2014), p. 044308.

[112] Xiaoche Wang et al. “Electrical control of coherent spin rotation of a single-spin qubit”. In: *npj Quantum Information* 6.1 (2020). URL: http://dx.doi.org/10.1038/s41534-020-00308-8.

[113] Sebastian Knauer, John P. Hadden, and John G. Rarity. “In-situ measurements of fabrication induced strain in diamond photonic-structures using intrinsic colour centres”. In: *npj Quantum Information* 6.1 (2020), pp. 2–7. URL: http://dx.doi.org/10.1038/s41534-020-0277-1.

[114] MH Abobeih et al. "Fault-tolerant operation of a logical qubit in a diamond quantum processor". In: *Nature* 606.7916 (2022), pp. 884–889.

[115] Matteo Pompili et al. "Realization of a multinode quantum network of remote solid-state qubits". In: *Science* 372.6539 (2021), pp. 259–264.

[116] Gordon S. Kino. "Applications and theory of the solid immersion lens". In: *Optical Pulse and Beam Propagation*. Ed. by Yehuda B. Band. Vol. 3609. 1999, pp. 56–66.

[117] P. Scholz et al. "A Versatile Design of Solid Immersion Lenses in Bulk Silicon Using Focused Ion Beam Techniques". In: *ISTFA 2009: Conference Proceedings from the 35th International Symposium for Testing and Failure Analysis*. 2009, pp. 119–125.

[118] George Davidson. "Symmetry-adapted linear combinations". In: *Group Theory for Chemists*. London: Palgrave Macmillan, 1991, pp. 81–90.

[119] Cathryn Michaels. "Group-IV Colour Centres in Diamond for Multi-Photon Entangled State Generation". PhD thesis. University of Cambridge, 2023.

[120] Christopher J. Ciccarino et al. "Strong spin–orbit quenching via the product Jahn–Teller effect in neutral group IV qubits in diamond". In: *npj Quantum Mater.* 5.1 (2020), p. 75.

[121] Jason M Smith et al. "Optical properties of a single-colour centre in diamond with a green zero-phonon line". In: *New Journal of Physics* 13.4 (2011), p. 45005. URL: https://dx.doi.org/10.1088/1367-2630/13/4/045005.

[122] Wataru Watanabe et al. "Space-selective laser joining of dissimilar transparent materials using femtosecond laser pulses". In: *Applied Physics Letters* 89.2 (July 2006), p. 021106. eprint: https://pubs.aip.org/aip/apl/article-pdf/doi/10.1063/1.2221393/14352530/021106_1_online.pdf. URL: https://doi.org/10.1063/1.2221393.

[123] L. V. Keldysh. "Ionization in the Field of a Strong Electromagnetic Wave". In: *J. Exp. Theor. Phys.* 20.5 (1965), pp. 1307–1314.

[124] B. N. Chichkov et al. "Femtosecond, picosecond and nanosecond laser ablation of solids". In: *Applied Physics A* 63.2 (1996), pp. 109–115.

[125] Andrew Kirkpatrick. "Optical Engineering of Colour Centres in Diamond". PhD thesis. University of Oxford, 2023.

[126] Carlo Bradac et al. "Quantum nanophotonics with group IV defects in diamond". In: *Nature Communications* 10 (1 2019), p. 5625. URL: https://doi.org/10.1038/s41467-019-13332-w.

[127] U. Wahl et al. "Direct Structural Identification and Quantification of the Split-Vacancy Configuration for Implanted Sn in Diamond". In: *Phys. Rev. Lett.* 125.4 (2020), p. 045301. URL: https://link.aps.org/doi/10.1103/PhysRevLett.125.045301.

[128] Emilio Corte et al. "Spectral Emission Dependence of Tin-Vacancy Centers in Diamond from Thermal Processing and Chemical Functionalization". In: *Advanced Photonics Research* 3.1 (2022), p. 2100148. URL: https://onlinelibrary.wiley.com/doi/abs/10.1002/adpr.202100148.

[129] Tobias Lühmann et al. “Coulomb-driven single defect engineering for scalable qubits and spin sensors in diamond”. In: *Nature Communications* 10.1 (Oct. 2019), p. 4956. URL: https://www.nature.com/articles/s41467-019-12556-0 (visited on 06/04/2024).

[130] Gordon Davies. “Charge states of the vacancy in diamond”. In: *Nature* 269.5628 (1977), pp. 498–500. URL: https://www.nature.com/articles/269498a0 (visited on 03/07/2024).

[131] Xin Qi et al. “Modelling the Impact of Graphene Coating of Different Thicknesses on Polyimide Substrate on the Secondary Electron Yield”. In: *Coatings* 14.1 (2024), p. 13.

[132] Gary Wan et al. “Graphene-diamond junction photoemission microscopy and electronic interactions”. In: *Nano Express* 1.2 (2020), p. 020011.

[133] Sally Eaton-Magaña et al. “Raman and Photoluminescence Mapping of Gem Materials”. In: *Minerals* 11.2 (2021), p. 177. URL: https://doi.org/10.3390/min11020177.

[134] D. Gatto Monticone et al. “Systematic study of defect-related quenching of NV luminescence in diamond with time-correlated single-photon counting spectroscopy”. In: *Physical Review B* 88.15 (2013), p. 155201. URL: https://link.aps.org/doi/10.1103/PhysRevB.88.155201.

[135] Tobias Lühmann et al. “Charge-State Tuning of Single SnV Centers in Diamond”. In: *ACS Photonics* 7.12 (2020), pp. 3376–3385. eprint: https://doi.org/10.1021/acsphotonics.0c01123. URL: https://doi.org/10.1021/acsphotonics.0c01123.

[136] Hikaru Morimoto et al. “Exciton lifetime and diffusion length in high-purity chemical-vapor-deposition diamond”. In: *Diamond and Related Materials* 63 (2016). 9th International Conference on New Diamond and Nano Carbons – NDNC 2015, pp. 47–50. URL: https://www.sciencedirect.com/science/article/pii/S0925963515300893.

[137] Srujan Meesala et al. “Strain engineering of the silicon-vacancy center in diamond”. In: *Phys. Rev. B* 97.20 (2018), p. 205444. URL: https://link.aps.org/doi/10.1103/PhysRevB.97.205444.

[138] R. Hanbury Brown and R. Q. Twiss. “A Test of a New Type of Stellar Interferometer on Sirius”. In: *Nature* 178.4541 (Nov. 1956), pp. 1046–1048. URL: https://www.nature.com/articles/1781046a0 (visited on 09/11/2024).

[139] Rosa Brouri et al. “Photon antibunching in the fluorescence of individual color centers in diamond”. In: *Opt. Lett.* 25.17 (2000), pp. 1294–1296. URL: https://opg.optica.org/ol/abstract.cfm?URI=ol-25-17-1294.

[140] Ivan Yu. Eremchev et al. “Detection of Single Charge Trapping Defects in Semiconductor Particles by Evaluating Photon Antibunching in Delayed Photoluminescence”. In: *Nano Letters* 23.6 (Mar. 2023), pp. 2087–2093. URL: https://doi.org/10.1021/acs.nanolett.2c04004 (visited on 09/11/2024).

[141] D. V. Regelman et al. “Semiconductor Quantum Dot: A Quantum Light Source of Multicolor Photons with Tunable Statistics”. In: *Phys. Rev. Lett.* 87 (25 2001), p. 257401. URL: https://link.aps.org/doi/10.1103/PhysRevLett.87.257401.

[142] P. Michler et al. “Nonclassical Radiation from a Single Quantum Dot”. In: *physica status solidi (b)* 229.1 (2002), pp. 399–405. URL: https://onlinelibrary.wiley.com/doi/abs/10.1002/1521-3951%28200201%29229%3A1%3C399%3A%3AAID-PSSB399%3E3.0.CO%3B2-P (visited on 09/11/2024).

[143] S. Ditalia Tchernij et al. “Single-Photon-Emitting Optical Centers in Diamond Fabricated upon Sn Implantation”. In: *ACS Photonics* 4.10 (Oct. 2017), pp. 2580–2586. URL: https://doi.org/10.1021/acsphotonics.7b00904 (visited on 05/24/2024).

[144] Alison E. Rugar et al. “Characterization of optical and spin properties of single tin-vacancy centers in diamond nanopillars”. In: *Phys. Rev. B* 99 (20 2019), p. 205417. URL: https://link.aps.org/doi/10.1103/PhysRevB.99.205417.

[145] Gerg ő Thiering and Adam Gali. “Ab Initio Magneto-Optical Spectrum of Group-IV Vacancy Color Centers in Diamond”. In: *Phys. Rev. X* 8 (2 2018), p. 021063. URL: https://link.aps.org/doi/10.1103/PhysRevX.8.021063.

[146] J. Kulda et al. “Overbending of the longitudinal optical phonon branch in diamond as evidenced by inelastic neutron and x-ray scattering”. In: *Phys. Rev. B* 66 (24 2002), p. 241202. URL: https://link.aps.org/doi/10.1103/PhysRevB.66.241202.

[147] William M. Yen and Peter M. Selzer. *Laser Spectroscopy of Solids*. 2nd ed. Berlin: Springer, 2021.

[148] P. Neumann et al. “Multipartite Entanglement Among Single Spins in Diamond”. In: *Science* 320.5881 (2009), pp. 1326–1329.

[149] Petr Siyushev et al. “Optical and microwave control of germanium-vacancy center spins in diamond”. In: *Physical Review B* 96.8 (Aug. 2017), p. 081201. URL: https://link.aps.org/doi/10.1103/PhysRevB.96.081201 (visited on 09/05/2024).

[150] Johannes Görlitz et al. “Coherence of a charge stabilised tin-vacancy spin in diamond”. In: *npj Quantum Information* 8.1 (2022), p. 45. URL: https://doi.org/10.1038/s41534-022-00552-0.

[151] Xingrui Cheng et al. “Laser activation of single group-IV colour centres in diamond”. In: *Nature Communications* 16.1 (2025), p. 5124. URL: https://doi.org/10.1038/s41467-025-60373-5.

[152] Chunlang Wang et al. “Single photon emission from SiV centres in diamond produced by ion implantation”. In: *Journal of Physics B: Atomic, Molecular and Optical Physics* 39.1 (2005), p. 37. URL: https://dx.doi.org/10.1088/0953-4075/39/1/005.

[153] Tobias Lühmann et al. “Screening and engineering of colour centres in diamond”. In: *Journal of Physics D: Applied Physics* 51.48 (Oct. 2018), p. 483002. URL: https://dx.doi.org/10.1088/1361-6463/aadfab (visited on 02/14/2024).

[154] N. M. Kazuchits et al. “Luminescence of negatively charged single vacancies in diamond: ND1 center”. In: *Diamond and Related Materials* 121 (Jan. 2022), p. 108741. URL: https://www.sciencedirect.com/science/article/pii/S0925963521005045 (visited on 06/13/2023).

[155] Gordon Davies and Alan T. Collins. "Vacancy complexes in diamond". In: *Diamond and Related Materials*. Diamond 1992 Proceedings of the Third International Conference on the New Diamond Science and Technology 2.2 (Mar. 1993), pp. 80–86. URL: https://www.sciencedirect.com/science/article/pii/092596359390035Z (visited on 06/13/2023).

[156] Alison Mainwood and A M Stoneham. "Stability of electronic states of the vacancy in diamond". In: *Journal of Physics: Condensed Matter* 9.11 (Mar. 1997), pp. 2453–2464. URL: https://iopscience.iop.org/article/10.1088/0953-8984/9/11/013 (visited on 05/19/2023).

[157] J. Isoya et al. "EPR identification of the negatively charged vacancy in diamond". In: *Physical Review B* 45.3 (Jan. 1992), pp. 1436–1439. URL: https://link.aps.org/doi/10.1103/PhysRevB.45.1436 (visited on 03/07/2024).

[158] A. Pu, V. Avalos, and S. Dannefaer. "Negative charging of mono-and divacancies in IIa diamonds by monochromatic illumination". In: *Diamond and Related Materials*. 11th European Conference on Diamond, Diamond-like Materials, Carbon Nanotubes, Nitrides and Silicon Carbide 10.3 (Mar. 2001), pp. 585–587. URL: https://www.sciencedirect.com/science/article/pii/S0925963500004416 (visited on 03/18/2024).

[159] I. N. Kupriyanov et al. "Photochromic effect in irradiated and annealed nearly IIa type synthetic diamond". In: *Journal of Physics: Condensed Matter* 12.35 (Sept. 2000), p. 7843. URL: https://dx.doi.org/10.1088/0953-8984/12/35/318 (visited on 06/13/2023).

[160] S. Dannefaer. "Defects in diamond". In: *physica status solidi c* 4.10 (2007), pp. 3605–3613. URL: https://onlinelibrary.wiley.com/doi/abs/10.1002/pssc.200675790 (visited on 04/11/2024).

[161] J.-M. Mäki et al. "Time Dependence of Charge Transfer Processes in Diamond Studied with Positrons". In: *Physical Review Letters* 107.21 (Nov. 2011), p. 217403. URL: https://link.aps.org/doi/10.1103/PhysRevLett.107.217403 (visited on 04/15/2024).

[162] T. Ichii et al. "Study of detailed balance between excitons and free carriers in diamond using broadband terahertz time-domain spectroscopy". In: *Applied Physics Letters* 116.23 (June 2020), p. 231102. URL: https://doi.org/10.1063/5.0006993 (visited on 09/06/2024).

[163] V. V. Kononenko et al. "Observation of fs laser-induced heat dissipation in diamond bulk". In: *Laser Physics Letters* 10.3 (Jan. 2013), p. 036003. URL: https://dx.doi.org/10.1088/1612-2011/10/3/036003 (visited on 05/15/2023).

[164] J. R. Olson et al. "Thermal conductivity of diamond between 170 and 1200 K and the isotope effect". In: *Phys. Rev. B* 47 (22 1993), pp. 14850–14856. URL: https://link.aps.org/doi/10.1103/PhysRevB.47.14850.

[165] Robert R. Reeber and Kai Wang. "Thermal Expansion, Molar Volume and Specific Heat of Diamond from 0 to 3000k". In: *Journal of Electronic Materials* 25.1 (Jan. 1996), pp. 63–67. (Visited on 02/13/2025).

[166] Martin Kozák et al. "Two- and Three-Photon Absorption in Chemical Vapor Deposition Diamond". In: *JOSA B* 29.5 (May 2012), pp. 1141–1145. (Visited on 02/13/2025).

[167] F. N. Li et al. "Thermal Annealing Induced Graphite/Diamond Structure Processed by High-Voltage Hydroxide Ion Treatments". In: *Applied Surface Science* 657 (June 2024), p. 159753. (Visited on 02/16/2025).

[168] David C. Palmer. "Visualization and analysis of crystal structures using CrystalMaker software". In: *Zeitschrift für Kristallographie - Crystalline Materials* 230.9-10 (Sept. 2015), pp. 559–572. URL: https://www.degruyter.com/document/doi/10.1515/zkri-2015-1869/html?lang=en (visited on 09/11/2024).

[169] Stewart J. Clark et al. "First principles methods using CASTEP". In: *Zeitschrift für Kristallographie - Crystalline Materials* 220.5-6 (May 2005). Publisher: De Gruyter (O), pp. 567–570. URL: https://www.degruyter.com/document/doi/10.1524/zkri.220.5.567.65075/html?lang=en (visited on 09/11/2024).

[170] John P. Perdew, Matthias Ernzerhof, and Kieron Burke. "Rationale for mixing exact exchange with density functional approximations". In: *The Journal of Chemical Physics* 105.22 (Dec. 1996), pp. 9982–9985. URL: https://doi.org/10.1063/1.472933 (visited on 09/11/2024).

[171] Andrew R. Kirkpatrick et al. "Ab initio study of defect interactions between the negatively charged nitrogen vacancy centre and the carbon self-interstitial in diamond". In: *Philosophical Transactions of the Royal Society A: Mathematical, Physical and Engineering Sciences* 382.2265 (2023), p. 20230174. URL: https://royalsocietypublishing.org/doi/10.1098/rsta.2023.0174 (visited on 09/11/2024).

[172] Nils Kolja Wessling et al. "Fabrication and transfer printing based integration of free-standing GaN membrane micro-lenses onto semiconductor chips". In: *Optical Materials Express* 12.12 (2022), p. 4606. arXiv: 2208.05275.

[173] BF Spiridon et al. "Method for inferring the mechanical strain of GaN-on-Si epitaxial layers using optical profilometry and finite element analysis". In: *Optical Materials Express* 11.6 (2021), pp. 1643–1655.

[174] Saptarsi Ghosh et al. "Origin (s) of anomalous substrate conduction in MOVPE-Grown GaN HEMTs on highly resistive silicon". In: *ACS Applied Electronic Materials* 3.2 (2021), pp. 813–824.

[175] Saptarsi Ghosh et al. "Design of step-graded AlGaN buffers for GaN-on-Si heterostructures grown by MOCVD". In: *Semiconductor Science and Technology* 38.4 (2023), p. 044001.

[176] John McPhillimy et al. "High accuracy transfer printing of single-mode membrane silicon photonic devices". In: *Optics Express* 26.13 (2018), pp. 16679–16688.

[177] Xue Feng et al. "Competing fracture in kinetically controlled transfer printing". In: *Langmuir* 23.25 (2007), pp. 12555–12560.

[178] Benoit Guilhabert et al. “Advanced Transfer Printing With In-Situ Optical Monitoring for the Integration of Micron-Scale Devices”. In: *IEEE Journal of Selected Topics in Quantum Electronics* 29.3: Photon. Elec. Co-Inte. and Adv. Trans. Print. (2022), pp. 1–11.

[179] R Hanbury Brown and Richard Q Twiss. “LXXIV. A new type of interferometer for use in radio astronomy”. In: *The London, Edinburgh, and Dublin Philosophical Magazine and Journal of Science* 45.366 (1954), pp. 663–682.

[180] J. R. Maze et al. “Nanoscale magnetic sensing with an individual electronic spin in diamond”. In: *Nature* 455.7213 (2008), pp. 644–647.

[181] Martin Berthel et al. “Photophysics of single nitrogen-vacancy centers in diamond nanocrystals”. In: *Physical Review B - Condensed Matter and Materials Physics* 91.3 (2015), pp. 1–13. arXiv: 1501.03714.

[182] Christian Kurtsiefer et al. “The breakdown flash of silicon avalanche photodiodes-back door for eavesdropper attacks?” In: *Journal of Modern Optics* 48.13 (2001), pp. 2039–2047.

[183] Jelle Storteboom et al. “Lifetime investigation of single nitrogen vacancy centres in nanodiamonds”. In: *Opt. Express* 23.9 (2015), pp. 11327–11333. URL: https://opg.optica.org/oe/abstract.cfm?URI=oe-23-9-11327.

[184] A Gruber et al. “Scanning confocal optical microscopy and magnetic resonance on single defect centers”. In: *Science* 276.5321 (1997), pp. 2012–2014.

[185] F. Jelezko and J. Wrachtrup. “Single defect centres in diamond: A review”. In: *Physica Status Solidi (A) Applications and Materials Science* 203.13 (2006), pp. 3207–3225.

[186] Motoyoshi Baba et al. “Aberrations and allowances for errors in a hemisphere solid immersion lens for submicron-resolution photoluminescence microscopy”. In: *Journal of applied physics* 85.9 (1999), pp. 6923–6925.

[187] Ian Christen et al. “An integrated photonic engine for programmable atomic control”. In: *arXiv preprint arXiv:2208.06732* (2022).

[188] Valery Zwiller and Gunnar Björk. “Improved light extraction from emitters in high refractive index materials using solid immersion lenses”. In: *Journal of Applied Physics* 92.2 (2002), pp. 660–665.

[189] S. A. Solin and A. K. Ramdas. “Raman Spectrum of Diamond”. In: *Phys. Rev. B* 1 (4 1970), pp. 1687–1698. URL: https://link.aps.org/doi/10.1103/PhysRevB.1.1687.

[190] M. Kuball. “Raman spectroscopy of GaN, AlGaN and AlN for process and growth monitoring/control”. In: *Surface and Interface Analysis* 31.10 (2001), pp. 987–999. eprint: https://analyticalsciencejournals.onlinelibrary.wiley.com/doi/pdf/10.1002/sia.1134. URL: https://analyticalsciencejournals.onlinelibrary.wiley.com/doi/abs/10.1002/sia.1134.

[191] Viktoria Yurgens et al. “Low-charge-noise nitrogen-vacancy centers in diamond created using laser writing with a solid-immersion lens”. In: *ACS Photonics* 8.6 (2021), pp. 1726–1734.

[192] Christiaan Bekker et al. "Scalable fabrication of hemispherical solid immersion lenses in silicon carbide through grayscale hard-mask lithography". In: *Applied Physics Letters* 122.17 (Apr. 2023), p. 173507. eprint: https://pubs.aip.org/aip/apl/article-pdf/doi/10.1063/5.0144684/18151708/173507_1_5.0144684.pdf. URL: https://doi.org/10.1063/5.0144684.

[193] Jingxiang Xu et al. "Different Etching Mechanisms of Diamond by Oxygen and Hydrogen Plasma: A Reactive Molecular Dynamics Study". In: *J. Phys. Chem. C* 125.30 (2021), pp. 16711–16718.

[194] Takeshi Ohshima et al. "Creation of silicon vacancy in silicon carbide by proton beam writing toward quantum sensing applications". In: *Journal of Physics D: Applied Physics* 51.33 (2018), p. 333002. URL: https://dx.doi.org/10.1088/1361-6463/aad0ec.

[195] Stefania Castelletto, Brett C Johnson, and Alberto Boretti. "Visible and Infrared Photoluminescence in Hexagonal Silicon Carbide by Direct Femtosecond Laser Writing". In: *IOP Conference Series: Materials Science and Engineering* 840.1 (2020), p. 012010. URL: https://dx.doi.org/10.1088/1757-899X/840/1/012010.

[196] Y.-C. Chen. "Laser writing of coherent colour centres in diamond". PhD thesis. University of Oxford, 2017.

[197] Weimin Li et al. "Threshold displacement energies and displacement cascades in 4H-SiC: Molecular dynamic simulations". In: *AIP Advances* 9.5 (May 2019), p. 055007. eprint: https://pubs.aip.org/aip/adv/article-pdf/doi/10.1063/1.5093576/12932441/055007_1_online.pdf. URL: https://doi.org/10.1063/1.5093576.

[198] Michel Bockstedte, Alexander Mattausch, and Oleg Pankratov. "Ab initio study of the annealing of vacancies and interstitials in cubic SiC: Vacancy-interstitial recombination and aggregation of carbon interstitials". In: *Phys. Rev. B* 69 (23 2004), p. 235202. URL: https://link.aps.org/doi/10.1103/PhysRevB.69.235202.

[199] C. D. Clark, P. J. Dean, and P. V. Harris. "Intrinsic edge absorption in diamond". In: *Proceedings of the Royal Society of London. Series A. Mathematical and Physical Sciences* 277 (1964), pp. 312–329.

[200] Patrick S. Salter et al. "High resolution structural characterisation of laser-induced defect clusters inside diamond". In: *Applied Physics Letters* 111.8 (Aug. 2017), p. 081103. eprint: https://pubs.aip.org/aip/apl/article-pdf/doi/10.1063/1.4993118/13937501/081103_1_online.pdf. URL: https://doi.org/10.1063/1.4993118.

[201] Patrick S. Salter and Martin J. Booth. "Adaptive optics in laser processing". In: *Light: Science & Applications* 8.1 (2019), p. 110. URL: https://doi.org/10.1038/s41377-019-0215-1.

[202] I. Haughton et al. "Barrier potential for laser written graphitic wires in diamond". In: *Diamond and Related Materials* 111 (2021), p. 108164. URL: https://www.sciencedirect.com/science/article/pii/S0925963520307172.

[203] O. Dial, C. C. Cheng, and A. Scherer. “Fabrication of high-density nanostructures by electron beam lithography”. In: *J. Vac. Sci. Technol. B* 16.6 (Nov. 1998), pp. 3887–3890. URL: https://doi.org/10.1116/1.590428.

[204] Dongju Liu and Jian Yu. “Otsu Method and K-means”. In: *Proc. 9th Int. Conf. Hybrid Intelligent Systems*. 2009, pp. 344–349.

[205] L. C. Bassett et al. “Electrical Tuning of Single Nitrogen-Vacancy Center Optical Transitions Enhanced by Photoinduced Fields”. In: *Phys. Rev. Lett.* 107 (26 2011), p. 266403. URL: https://link.aps.org/doi/10.1103/PhysRevLett.107.266403.